

Mechanical Immunoengineering of T Cells for Enhanced Cancer Immunotherapy

Présentée le 25 février 2022

Faculté des sciences et techniques de l'ingénieur
Laboratoire de biomatériaux pour Immunoengineering
Programme doctoral en science et génie des matériaux

pour l'obtention du grade de Docteur ès Sciences

par

Kewen LEI

Acceptée sur proposition du jury

Prof. D. Grundler, président du jury
Prof. L. Tang, directeur de thèse
Prof. M. David, rapporteur
Prof. H. Morgan, rapporteur
Prof. S. Francesco, rapporteur

Acknowledgements

The Ph.D. study is a journey full of uncertainties and also surprises. Gaining fruits from the tree of science is never a job that can be done alone. I want to thank my supervisor, Prof. Li Tang, for offering me the opportunity to enter his lab to pursue my Ph.D. research. During the last four years, he was always there to discuss research, answer questions, and offer valuable advice on scientific projects and future careers. I learned a lot from his commitment to science, openness to new things, and ways of logical thinking to solve problems. I am very grateful for his great guidance and unreserved support in my Ph.D. study. Without his supervision, it is hard to imagine if I could accomplish what has been shown in this thesis.

I want to thank all the group members in Tang Lab. It is a great honor to work with these outstanding scientists and share daily life with them. Thank Armand Kurum for his great help in performing the cell biomechanics-related experiments, inspiring discussions about research, and dealing with French-only staff. Thank my officemate Lucia Bonati for her help with cell transfection and talking about life and politics. Thank Dr. Yugang Guo and Dr. Yuqing Xie for leading me to immunology and their valuable advice on my research projects. Thank Min Gao for her help in producing cytokines and sharing her snacks unselfishly. Thank all the other Tang Lab members for your help and concern.

Thank my collaborators for their significant contribution to my research projects. They are professional and knowledgeable in their fields and always give valuable suggestions for approaching the truths with scientific insights. I want to give special thanks to Dr. Murat Kaynak and Prof. Mahmut S. Sakar for designing, fabricating, and optimizing microfluidic devices from scratch and their great help in measuring the cellular stiffness of many cell types. Thank Dr. Yulong Han and Prof. Ming Guo for teaching me about the optical tweezer and their help in measuring cell stiffness. Thank Veronika Cencen, Dr. Melanie T.M. Hannebelle, and Prof. Georg E. Fantner for showing me the beauty of atomic force microscopy and their help in measuring cell stiffness. Thank Guanyu Zhou and Prof. Yangping Wu for collecting tumor biopsies for histological analysis and providing their clinical insights.

Finally, I would like to thank my family, especially my wife Yiran Cao, for their endless love all the time. For me, love is as important as science that makes the world better. My family is always there when I meet difficulties or feel upset. They are my strength to overcome the hard times during my Ph.D. journey. I dedicate this thesis to everyone who has ever offered me help and concern.

Lausanne, 08 November 2021

Abstract

Cancer is one of the leading causes of death globally. In the campaign conquering cancer, immunotherapy represents one of the most promising treatments inducing complete and durable responses in a fraction of cancer patients. T cells play a central role in anti-cancer immunity and are at the core of the development of cancer immunotherapy. For example, immune checkpoint blockade and chimeric antigen receptor (CAR)-T cell therapies have been approved by the U.S. Food and Drug Administration (FDA) to treat a variety of cancers. Despite the unprecedented clinical success achieved by T cell-based cancer immunotherapies, there are tremendous outstanding challenges, including low response rate and severe toxicities, which substantially limit the clinical benefits in a majority of cancer patients.

Immunoengineering is an emerging field applying bioengineering techniques (e.g., genetic engineering and biomaterial engineering) to precisely manipulate immunity, which provides numerous opportunities to enhance current cancer immunotherapy. At present, enormous efforts have been spent on modulating biochemical interactions for improving the efficacy and safety of T cell-based cancer immunotherapy. Besides biochemical exchanges, mechanical interactions are universal in every step of T cell immunity and have been shown to be crucial in regulating T cell fate and function. Therefore, immunoengineering approaches that modulate mechanical interactions in T cell immunity hold great promise to further improve current cancer immunotherapy. This thesis aims to develop novel mechanical immunoengineering approaches for improving T cell-based cancer immunotherapy. Specifically, it includes the following parts:

Developing a spiky artificial antigen-presenting cell (aAPC) to enhance ex vivo T cell expansion. Ex vivo expansion of T cells is critical in adoptive T cell therapy (ACT) to ensure an effective therapeutic dosage for cancer treatment. By mimicking the dendritic morphology of dendritic cells, a potent natural APC, I developed a spiky titanium dioxide (TiO₂) microparticle presenting T cell stimulatory ligands as an aAPC to enhance ex vivo T cell expansion. The spiky aAPC outperformed smooth counterpart, as well as Dynabead®, a golden standard aAPC currently used in clinical manufacturing of ACT therapy, for T cell activation and expansion in a manner dependent on F-actin polymerization but independent of mechanosensitive channels including Piezo1 and TRPV4. Therefore, this finding identifies the morphology of aAPCs as a critical parameter to control for improved ex vivo T cell manufacturing for ACT therapy.

Boosting T cell-mediated cytotoxicity by stiffening cancer cells. Cancer progressions are typically associated with cancer cell softening. I discovered that cancer cell softening owing to cholesterol enrichment in the plasma membrane led to resistance to T cell-mediated cytotoxicity. Stiffening cancer cells via membrane cholesterol depletion substantially enhanced T cell-mediated cytotoxicity against cancer cells through augmenting T cell mechanical force but not any known biochemical pathways of T cell-mediated cytotoxicity. Cancer cell stiffening intervention in vivo enhanced the efficacy of ACT therapy in multiple preclinical solid tumor models. Cancer cell softness thus represents a new immune checkpoint of mechanical basis, and therapeutically targeting this mechanical immune checkpoint has the potential to improve the clinical response of T cell-based cancer immunotherapy.

Utilizing T cell force as a trigger to achieve specific release of anti-cancer drugs. Specific delivery of T cell supporting drugs and/or anti-cancer drugs into tumors has the potential to increase the response rate of ACT therapy without causing systemic toxicity. To this end, I developed a T cell force-responsive drug release system based on a mesoporous

silica microparticle with DNA force sensors as gatekeepers. T cell force as a highly specific signal upon recognizing cancer cells presenting cognate antigens was shown to trigger specific drug release when T cell receptor signaling was activated. Further, the T cell force-responsive drug release system could deliver anti-cancer drugs in vitro and in vivo in a T cell force-dependent manner and hold promise to enhance cancer immunotherapy.

In the end, future directions are discussed from three perspectives: 1) a deeper understanding of mechanobiology of T cell immunity is crucial; 2) it is promising to engineer the mechanics of other steps of T cell immunity such as T cell infiltration and differentiation; and 3) mechanical immunoengineering of immune cells other than T cells (e.g., B cells and macrophage) also holds promise for enhancing cancer immunotherapy.

Keywords

Cancer immunotherapy; anti-cancer immunity; T cell; mechanical immunoengineering; spiky microparticles; ex vivo T cell expansion; cancer cell softness; cholesterol depletion; mechanical immune checkpoint; cancer cell stiffening; T cell force; T cell-mediated cytotoxicity; DNA force sensor; mesoporous silica microparticles; T cell force-responsive release

Résumé

Le cancer est l'une des principales causes de décès dans le monde. Dans la campagne de conquête des cancers, l'immunothérapie représente l'un des traitements les plus prometteurs, induisant des réponses complètes et durables chez une fraction des patients atteints de cancer. Les cellules T jouent un rôle central dans l'immunité anticancéreuse et sont au cœur du développement de l'immunothérapie anticancéreuse. Par exemple, le blocage des points de contrôle immunitaire et les thérapies cellulaires à récepteur d'antigène chimérique (CAR)-T ont été approuvés par la Food and Drug Administration (FDA) des États-Unis pour traiter une variété de cancers. Malgré le succès clinique considérable obtenu avec les immunothérapies anticancéreuses à base de cellules T, il existe d'énormes défis à relever, notamment un faible taux de réponse et des toxicités graves, qui limitent considérablement les avantages cliniques chez la majorité des patients atteints de cancer.

L'immuno-ingénierie est un domaine émergent appliquant des techniques de bio-ingénierie (par exemple, le génie génétique et l'ingénierie des biomatériaux) pour la manipulation thérapeutique de l'immunité, ce qui offre de nombreuses opportunités pour améliorer l'immunothérapie du cancer. À l'heure actuelle, d'énormes efforts sont consacrés à la modulation des interactions biochimiques pour améliorer l'efficacité et le profil d'innocuité de l'immunothérapie du cancer à base de cellules T. Outre les échanges biochimiques, les interactions mécaniques sont présentes à chaque étape de l'immunité des cellules T et se sont avérées cruciales pour réguler le destin et la fonction des cellules T. Par conséquent, les approches d'immuno-ingénierie cherchant à moduler les interactions mécaniques durant la réponse immunitaire des cellules T sont très prometteuses pour améliorer encore l'immunothérapie actuelle du cancer. Cette thèse vise à développer de nouvelles approches d'immuno-ingénierie mécanique pour améliorer l'immunothérapie du cancer à base de cellules T et comprend les parties suivantes :

Développer une cellule présentatrice d'antigène artificielle hérissée (aAPC) pour améliorer l'expansion des cellules T *ex vivo*. L'expansion *ex vivo* des cellules T est essentielle dans la thérapie adoptive des cellules T (ACT) pour assurer un dosage thérapeutique efficace pour le traitement du cancer. En imitant la morphologie des cellules dendritiques, un puissant APC naturel, j'ai développé une microparticule hérissée de dioxyde de titane (TiO₂) présentant des ligands stimulateurs des lymphocytes T comme un aAPC pour améliorer l'expansion des lymphocytes T *ex vivo*. L'aAPC hérissé a surpassé Dynabead®, un aAPC de référence actuellement utilisé dans la fabrication clinique de thérapie ACT, et une microparticule lisse de TiO₂ avec une modification de surface similaire pour l'activation et l'expansion des cellules T grâce à une polymérisation accrue de l'actine F dans les cellules T. Par conséquent, ma découverte identifie la morphologie comme un paramètre critique pour contrôler l'amélioration de la fabrication de cellules T *ex vivo* pour la thérapie cellulaire.

Stimuler la cytotoxicité des lymphocytes T en rigidifiant les cellules cancéreuses. Les progressions du cancer sont généralement associées à un ramollissement des cellules cancéreuses. J'ai découvert que le ramollissement cortical résultant de l'enrichissement en cholestérol de la membrane plasmique contribuait au ramollissement des cellules cancéreuses et conduisait à une résistance à la cytotoxicité induite par les lymphocytes T. Le durcissement des cellules can-

céreuses via la réduction du cholestérol membranaire a considérablement amélioré la cytotoxicité médiée par les cellules T contre les cellules cancéreuses en augmentant la force mécanique des cellules T et sans changement des propriétés biochimiques de la cytotoxicité des cellules T. L'intervention de rigidification des cellules cancéreuses *in vivo* a amélioré l'efficacité de la thérapie ACT contre plusieurs modèles de tumeurs solides précliniques. La faible rigidité des cellules cancéreuses représente donc un nouveau point de contrôle immunitaire de base mécanique, et le ciblage thérapeutique de ce point de contrôle immunitaire mécanique a le potentiel d'améliorer la réponse clinique de l'immunothérapie du cancer à base de cellules T.

Utilisation de la force des cellules T comme déclencheur pour obtenir une libération spécifique de médicaments anticancéreux. L'administration spécifique de médicaments soutenant les lymphocytes T et/ou de médicaments anticancéreux dans les tumeurs a le potentiel d'augmenter le taux de réponse de la thérapie ACT sans provoquer de toxicité systémique. À cette fin, j'ai développé un système de libération de médicament basé sur une microparticule de silice mésoporeuse avec des capteurs de force d'ADN permettant la libération du médicament une fois que les cellules T ont excédé la tension maximale de ces capteurs. La force des cellules T est un signal hautement spécifique lors de la reconnaissance des cellules cancéreuses présentant des antigènes et peut donc déclencher une libération spécifique lorsque les cellules T rencontrent des cellules tumorales. J'ai montré que le système de libération de médicaments « force-réponse » des cellules T pouvait libérer des médicaments anticancéreux d'une manière dépendante de la force des cellules T *in vitro* et *in vivo* et offrait une nouvelle avenue thérapeutique pour l'immunothérapie anticancéreuse.

Pour conclure, les prochaines étapes sont discutées à partir de trois perspectives: 1) une meilleure compréhension de la mécanobiologie de l'immunité des cellules T; 2) l'immuno-ingénierie mécanique d'autres étapes de l'immunité des cellules T telles que l'infiltration des cellules T et leur différenciation; et 3) l'immuno-ingénierie mécanique de cellules immunitaires autres que les cellules T (par exemple, les cellules B et les macrophages) pour l'immunothérapie du cancer.

Mots-clés

Immunothérapie anticancéreuse; immunité anticancéreuse; cellule T; immuno-ingénierie mécanique; microparticules hérissées; expansion des cellules T *ex vivo*; mollesse des cellules cancéreuses; réduction du cholestérol; point de contrôle immunitaire mécanique; raidissement des cellules cancéreuses; force des lymphocytes T; cytotoxicité médiée par les lymphocytes T; capteur de force ADN; microparticules de silice mésoporeuses; Libération sensible à la force des cellules T

Contents

Acknowledgements	v
Abstract	vi
Keywords	vii
Résumé	viii
Mots-clés	ix
List of Figures	xii
List of Tables	xv
Chapter 1 Introduction.....	17
1.1 The cancer-immunity cycle and cancer immunotherapy.....	19
1.1.1 Immune checkpoint blockade (ICB) therapy	20
1.1.2 Adoptive T cell (ACT) therapy.....	22
1.2 T cell mechanobiology	24
1.3 Mechanical immunoengineering of T cells	26
1.3.1 Passive mechanical cues for mechanical immunoengineering of T cells.....	27
1.3.1.1 Substrate/cell stiffness	28
1.3.1.2 Topography and ligand patterning	31
1.3.2 Active forces for mechanical immunoengineering of T cells.....	34
1.3.2.1 Forces exerted by T cells	34
1.3.2.2 External forces applied on T cells	35
Chapter 2 Spiky microparticles provide mechanical stimulation for enhanced T cell expansion	39
2.1 Abstract	40
2.2 Introduction.....	40
2.3 Results	42
2.3.1 Fabrication and characterization of aCD3/28-coated spiky TiO ₂ microparticles	42
2.3.2 Ex vivo expansion of Pmel splenocytes with aCD3/28-coated spiky microparticles	43
2.3.3 Ex vivo expansion of Pmel CD8 ⁺ T cells with aCD3/28-coated spiky microparticles.....	44
2.3.4 Ex vivo expansion of polyclonal CD3 ⁺ T cells with aCD3/28-coated spiky microparticles	46
2.4 Conclusion	48
2.5 Supplementary materials	49
2.5.1 Experimental methods.....	49
2.5.2 Supplementary figures	51
Chapter 3 Stiffening cancer cells enhances T cell mechanical forces and anti-tumor efficacy	53
3.1 Abstract	54
3.2 Introduction.....	54
3.3 Results	55
3.3.1 Cancer cells enrich cholesterol in the plasma membrane.....	55

3.3.2	Controlling cancer cell stiffness by manipulating membrane cholesterol levels.....	56
3.3.3	Cancer cell softness as a mechanical immune checkpoint impairs T cell-mediated cytotoxicity.....	58
3.3.4	Cancer-cell stiffening enhances the efficacy of ACT therapies.....	60
3.3.5	Biochemical pathways of T cell-mediated cytotoxicity are not affected by cancer-cell stiffening.....	62
3.3.6	Cancer-cell stiffening augments cellular forces and cytotoxicity mediated by T cells	66
3.4	Conclusion	69
3.5	Supplementary materials	71
3.5.1	Supplementary methods.....	71
3.5.2	Supplementary figures	83
3.6	Acknowledgements	102
Chapter 4	T cell force-responsive delivery of anti-cancer drugs	103
4.1	Abstract	104
4.2	New concepts	104
4.3	Introduction.....	104
4.4	Results	106
4.4.1	Screening of force-sensitive gatekeepers for mesoporous silica microparticle system	106
4.4.2	Fabrication and characterization of T cell force-responsive drug release system using DNA-based force-sensitive gatekeepers.....	107
4.4.3	T cell force-responsive release of a fluorescent model drug.....	108
4.4.4	T cell force-responsive release of an anti-cancer drug in vitro and in vivo	110
4.4.5	Design of a bispecific DNA nanomachine for T cell force-responsive release upon recognition of cancer cells	111
4.5	Conclusion	113
4.6	Supplementary materials	114
4.6.1	Experimental methods.....	114
4.6.2	Supplementary figures and tables	121
4.7	Acknowledgements	131
Chapter 5	Conclusion	133
5.1	Achieved results	133
5.2	Future development.....	135
5.2.1	Further understanding of mechanobiology of T cell immunity	135
5.2.2	Mechanical immunoengineering of different steps of T cell immune responses	137
5.2.3	Mechanical immunoengineering of other immune cells for cancer immunotherapy.....	138
References	141
Curriculum Vitae.....	159

List of Figures

Figure 1:1 The cancer-immunity cycle.....	19
Figure 1:2 Models of how force may trigger T cell receptor (TCR) signaling.	24
Figure 1:3 Model of LFA-1 activation at the immunological synapse (IS).	25
Figure 1:4 Cytotoxic T cells use mechanical force to potentiate target cell killing.	26
Figure 1:5 Schematic illustration of mechanical immunoengineering of T cells using passive mechanical cues or active mechanical forces for therapeutic applications. PDMS, polydimethylsiloxane.	27
Figure 1:6 Target cells on stiffer substrate stimulate stronger cytokine productions in CD4 ⁺ T cells.	30
Figure 1:7 Soft hyaluronic acid (HA) hydrogel enhances ex vivo CD8 ⁺ T cell expansion for enhanced adoptive T cell therapy.	31
Figure 1:8 Ellipsoidal topography promotes CD8 ⁺ T cell proliferation for enhanced anti-cancer efficacy.	32
Figure 1:9 Magnetic force clusters T cell receptor (TCR)/CD3 complexes and promotes T cell ex vivo expansion for enhanced adoptive T cell therapy.	36
Figure 1:10 A mechanogenetic circuit for ultrasound-inducible expression of chimeric antigen receptors (CARs) on T cells.	37
Figure 2:1 Schematic of enhancing T cell expansion with anti-CD3/28 antibody-coated spiky TiO ₂ microparticles (aCD3/28@TiO ₂ SMPs).	41
Figure 2:2 Characterization of smooth and spiky TiO ₂ microparticles (TiO ₂ MP and SMP) and their anti-CD3/28 antibody-coated counterparts (aCD3/28@TiO ₂ MP and SMP).	42
Figure 2:3 Ex vivo expansion of T cells in Pmel splenocytes with aCD3/28@TiO ₂ SMPs.	44
Figure 2:4 Ex vivo expansion of Pmel CD8 ⁺ T cells with aCD3/28@TiO ₂ SMPs.	45
Figure 2:5 Ex vivo expansion of polyclonal CD3 ⁺ T cells with aCD3/28@TiO ₂ SMPs.	47
Figure 2:6 Phenotyping of Pmel splenocytes, Pmel CD8 ⁺ T cells, and wild-type (WT) CD3 ⁺ T cells.	51
Figure 3:1 Cholesterol is enriched in the plasma membrane of cancer cells.	56
Figure 3:2 Cancer cell stiffness can be manipulated by supplementation or depletion of membrane cholesterol.	57
Figure 3:3 Cancer cell softness impairs T cell-mediated cytotoxicity in vitro and in vivo.	59
Figure 3:4 Cancer-cell stiffening by Me β CD enhances the efficacy of ACT immunotherapy.	61
Figure 3:5 The chemical nature of Me β CD did not contribute to enhanced T cell-mediated cytotoxicity against stiffened cancer cells.	63
Figure 3:6 Cancer-cell stiffening has negligible influence on biochemical cancer-cell killing pathways mediated by T cells.	65
Figure 3:7 Enhanced cytotoxicity against stiffened cancer cells is mediated by T cell forces.	68
Figure 3:8 Schematic illustration of mechanical immuno-suppression induced by the softness of cancer cells, which could be overcome by stiffening cancer cells for enhanced cancer-cell killing mediated by T cells.	69
Figure 3:9 Cholesterol level is upregulated in various human cancer tissues.	83
Figure 3:10 Treatment of water-soluble cholesterol/methyl- β -cyclodextrin complex (Chol) or methyl- β -cyclodextrin (Me β CD) significantly increases or decreases cholesterol levels in plasma membranes of various cancer cells, respectively.	84
Figure 3:11 Treatment of Chol or Me β CD shows negligible impacts on the viability or apoptosis of various cancer cell lines.	84

Figure 3:12 Treatment of Chol or Me β CD softens or stiffens various cancer cells, respectively, measured by deformability cytometry (DC).	85
Figure 3:13 Syntheses and characterizations of polyacrylamide (PA) hydrogels.....	86
Figure 3:14 Cancer-cell softening by supplementing cholesterol impairs the anti-tumor efficacy of adoptive T cell transfer (ACT) therapy in vivo.	87
Figure 3:15 Regulation of acyl-CoA:cholesterol acyltransferase 1 (ACAT1) level through genetic modification in cancer cells.....	88
Figure 3:16 Kinetics of cholesterol levels in the plasma membrane of B16F10 cancer cells post the treatment of Me β CD and its impact on T cell-mediated cytotoxicity.	88
Figure 3:17 Cancer cell stiffening using a cytoskeleton stiffening reagent, 4-hydroxyacetophenone (4-HAP), enhances T-cell-mediated killing of B16F10 cancer cells.	89
Figure 3:18 Production and characterizations of mouse interleukin-15 super-agonist (IL-15SA).	90
Figure 3:19 Cancer-cell stiffening using Me β CD enhances the anti-tumor efficacy of ACT therapy in mice bearing B16F10 tumors.	91
Figure 3:20 Cancer-cell stiffening using Me β CD enhances the anti-tumor efficacy of ACT therapy in mice bearing EG7-OVA tumors.	92
Figure 3:21 Treatment of Me β CD shows no overt systemic toxicity in mice.....	93
Figure 3:22 Treatment of Me β CD shows negligible effects on proliferation and functions of tumor-infiltrating endogenous (endo) CD8 ⁺ T cells.....	94
Figure 3:23 Treatment of Me β CD shows negligible effects on other tumor-infiltrating immune cells.	95
Figure 3:24 Me β CD shows negligible effects on T cell functions during co-culture with cancer cells.....	96
Figure 3:25 Cancer-cell stiffening using Me β CD shows negligible effects on antigen presentation by cancer cells, T cell proliferation, activation, or other phenotypes.	97
Figure 3:26 Native, ACAT1 KD, and ACAT1 OE B16F10 cancer cells induce similar T cell activation levels.	98
Figure 3:27 Softening or stiffening cancer cells using Chol or Me β CD has no effect on conjugation between T cells and cancer cells.	99
Figure 3:28 Native and stiffened B16F10 cancer cells showed similar susceptibility to membrane tension-assisted perforin-induced lysis.	99
Figure 3:29 T cell force is measured using traction force microscopy (TFM) and can be stably inhibited by cytoskeleton inhibitors.	100
Figure 3:30 Enhanced T cell cytotoxicity against stiffened cancer cells is mediated by T cell forces.	101
Figure 3:31 Treatment of cytoskeleton inhibitors shows negligible impacts on the viability or apoptosis of Pmel CD8 ⁺ T cells.....	101
Figure 4:1 Schematic illustration of T cell force-responsive drug release system based on a mesoporous silica microparticle (M) capped with DNA force sensors (D).	105
Figure 4:2 Evaluation of β -cyclodextrin (β CD)/alkylbenzene complexes as gatekeepers for mesoporous silica microparticles.....	107
Figure 4:3 Characterizations of M , D-M , and AbD-M	108
Figure 4:4 T cell force-responsive release of a fluorescent model drug	109
Figure 4:5 T cell force-responsive release of an anti-cancer drug in vitro and in vivo.....	111
Figure 4:6 T cell force-responsive release upon recognition of cancer cells using a bispecific DNA nanomachine.....	113

Figure 4:7 Schematic of the fabrication of rhodamine B (RB)-loaded mesoporous silica microparticles (Ms) modified with methylbenzene (MB) or tertbutylbenzene (TB) (denoted as MB-M-RB or TB-M-RB , respectively).	121
Figure 4:8 Fourier-transform infrared (FT-IR) spectra of mesoporous silica microparticle (M) and M modified with methylbenzene (MB) or tertbutylbenzene (TB) (denoted as MB-M or TB-M , respectively).....	122
Figure 4:9 Design of a DNA gatekeeper (D) with force sensing function.....	122
Figure 4:10 Schematic of the fabrication of T cell force-responsive mesoporous silica microparticles.	123
Figure 4:11 Characterization of DNA force sensor (D) on mesoporous silica microparticle (M).	124
Figure 4:12 Calibration curves for rhodamine B (RB) (a) and gemcitabine (GEM) (b) in Hank's balanced salt solution (HBSS).	124
Figure 4:13 Release kinetics of rhodamine B (RB) from indicated systems at 37 °C over 1.5 h (n = 3).....	125
Figure 4:14 Release of rhodamine B (RB) from AbD-M-RB depended on T cell activation and internalization of AbD-M-RB by T cells was negligible.....	126
Figure 4:15 Fluorescence imaging of T cell force-responsive release of rhodamine B (RB) from AbD-M-RB	127
Figure 4:16 Schematic of an in vitro release assay of D-M-RB using centrifugal forces.	127
Figure 4:17 AbD-M-RB had a negligible influence on T cell apoptosis.	128
Figure 4:18 Stability of components of DNA nanomachine (NM) in different buffers.	129
Figure 4:19 Self-assembly and stability of DNA nanomachine (NM).	130

List of Tables

Table 4:1 Elemental analysis of bare mesoporous silica microparticle (M) and isocyanate-functionalized M (M-NCO).	130
Table 4:2 Loading capacity of rhodamine B (RB) or gemcitabine (GEM) in M	130

Chapter 1 Introduction

Partially adapted from the published article:

Lei, K., Kurum, A. & Tang, L. Mechanical immunoengineering of T cells for therapeutic applications. ***Accounts of Chemical Research*** 53, 2777-2790 (2020).

T cells, a key component of adaptive immunity, are responsible for cellular responses against pathogens and malignant cells. T cells are identified by T cell receptor (TCR)/cluster of differentiation 3 (CD3) complexes located on the cell surface. TCR triggering by antigen peptide-bound major histocompatibility complex (pMHC) results in intracellular signaling mediated by cytoplasmic portions of CD3 for T cell activation. Given their core role in immunity, T cells lie at the heart of various immunotherapeutic modalities against cancer,¹ infectious disease,² and autoimmune disorders.³ For instance, checkpoint blockades that reactivate exhausted or dysfunctional T cells^{4,5} and adoptive cell therapies (ACT), in particular, chimeric antigen receptor (CAR)-T cells,^{1,6} have been approved recently by the Food and Drug Administration (FDA) for the treatment of a variety of cancers that are non-responsive to traditional forms of cancer therapy (e.g., chemotherapy and radiation therapy). However, only a small fraction of cancer patients respond to current immunotherapies.

Immunoengineering of T cells could improve the potency and/or safety of immunotherapies, potentially benefiting more patients. One such example is ACT adjuvanted by supporting cytokines secreted by genetically-engineered T cells or released from stimuli-responsive biomaterials specifically in the tumor environment.⁷⁻⁹ To date, attempts to improve immunotherapy have focused predominantly on regulating biochemical traits of T cells or their surrounding biochemical microenvironment (we term those strategies biochemical immunoengineering).

On the other hand, biomechanical cues, which represent another major dimension of the relationship between T cells and their environment, have been largely underappreciated. Indeed, across the multiple stages of T cell immunity, T cells experience myriad forces and encounter environments with diverse mechanical properties. T cells patrol the body through the circulatory system, where they are exposed to shear stress induced by blood flow. The resulting shear forces acting on T cells have been shown to promote transmigration through the endothelial layer via force-induced affinity maturation of integrins on T cells.¹⁰ Following extravasation, T cells encounter tissues and organs with a wide range of mechanical properties. Moreover, tumor and fibrotic tissues typically exhibited higher stiffness compared to healthy tissues.¹¹

Accumulating evidence shows that biomechanical cues are essential for T cell functions and enhance T cell sensitivity to biochemical signals.¹²⁻¹⁴ In this regard, integrating biomechanical principles into the design of the next generation of T cell-based immunotherapies may enhance efficacy and lower toxicity by improving specificity. The growing understanding of T cell mechanobiology provides a solid basis to exploit mechanical cues to modulate T cell immunity for therapeutic applications, a new field we term “mechanical immunoengineering”. The following sections introduce the cancer-immunity cycle together with an overview of T cell-based cancer immunotherapy, and representative biochemical immunoengineering approaches for augmenting anti-cancer T cell responses. Next, we review recent progress in T cell mechanobiology and strategies of mechanical immunoengineering of T cells and present them in the context of therapeutic applications. We envision that mechanical immunoengineering will develop into an important methodology that is complementary to biochemical immunoengineering, and ultimately improve the response rate of immunotherapies.

1.1 The cancer-immunity cycle and cancer immunotherapy

Cancer progression accompanies with the accumulation of genetic mutations or alterations, which give rise to the expression of tumor-specific antigens (TSAs) or abnormal expression of tumor-associated antigens (TAAs) that are also expressed by normal cells.¹⁵ The presentation of epitopes from those antigens by MHC distinguishes cancer cells from their normal counterparts and elicits anti-cancer immune responses, especially CD8⁺ T cell response mediating the direct killing of cancer cells. The anti-cancer immune responses proceed in a well-orchestrated and self-propagating manner known as the cancer-immunity cycle (Fig. 1:1).¹⁶

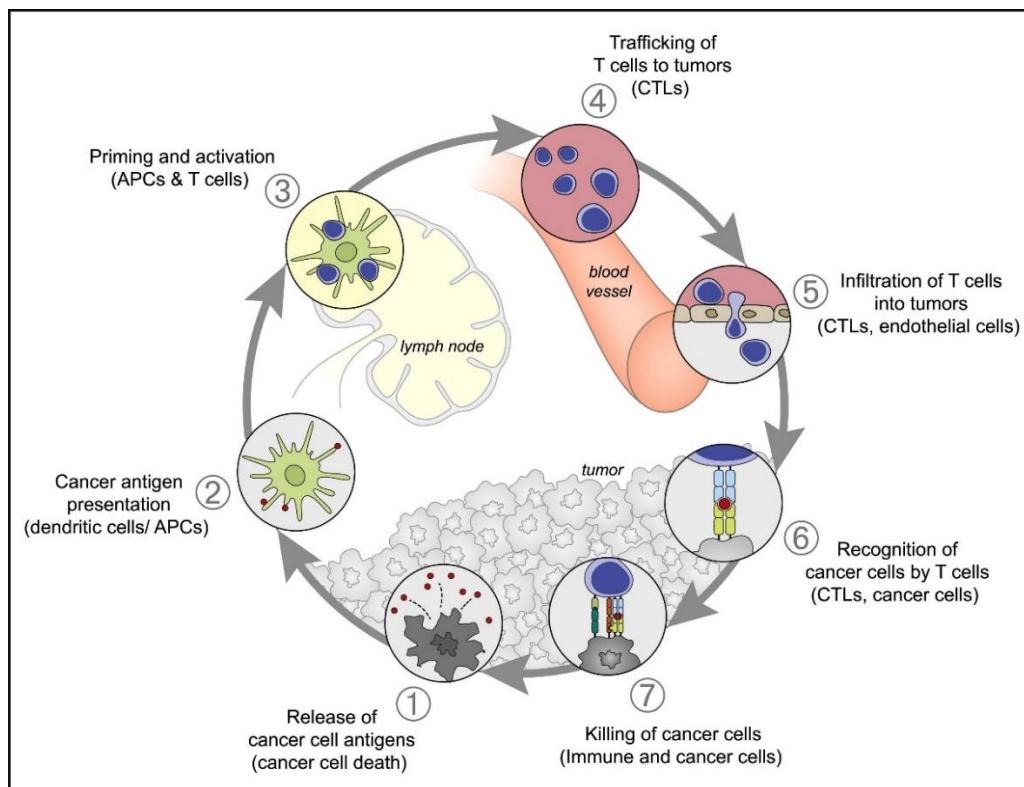


Figure 1:1 The cancer-immunity cycle.

The generation of immunity to cancer is a cyclic process that can be self-propagating, leading to an accumulation of immune-stimulatory factors that, in principle, should amplify and broaden T cell responses. The cycle is also characterized by inhibitory factors that lead to immune regulatory feedback mechanisms, which can halt the development or limit the immunity. This cycle can be divided into seven major steps, starting with the release of antigens from the cancer cell and ending with the killing of cancer cells. Each step is described above, with the primary cell types involved and the anatomic location of the activity listed. Abbreviations are as follows: APCs, antigen-presenting cells; CTLs, cytotoxic T lymphocytes. Adapted from ref. 16.

To initiate the cancer-immunity cycle, antigens should be released from cancer cells and captured and processed by dendritic cells (DCs) for antigen presentation (Fig. 1:1, step 1). During this step, mounting an anti-cancer response rather than tolerance requires immunogenic signals, such as damage-associated molecular patterns (DAMPs) from dying cancer cells, for DC maturation. After migration into adjacent lymph nodes, mature DCs present antigens on MHC-I or MHC-II molecules to CD8⁺ or CD4⁺ T cells, respectively (Fig. 1:1, step 2). Subsequently, the priming and activation of T cells follow with an effector T cell response if TSAs are presented or central tolerance against TAAs has been incomplete (Fig.

1:1, step 3). The activated effector T cells then egress lymph nodes and traffic in the circulating blood before infiltrating into the tumor tissues (Fig. 1:1, step 4). Effector T cells are recruited to the inflamed tumor tissues via transendothelial migration across tumor blood vessels (Fig. 1:1, step 5). After tumor infiltration, effector T cells recognize cognate antigens on cancer cells (Fig. 1:1, step 6) and specifically kill the target cancer cells (Fig. 1:1, step 7). The lysis of cancer cells then releases additional antigens initiating another round of cancer-immunity cycle with possible antigen spreading that is not targeted in the first cycle.

The cancer-immunity cycle is usually defective in one or multiple aspects in cancer patients. For instance, neoantigens released from cancer cells may not be detected, or TAAs overexpressed by cancer cells may generate a tolerance response rather than an effector response. Besides, the tumor microenvironment (TME) is immunosuppressive, and it may impair infiltration of T cells or inhibit T cell effector functions inside the TME.¹⁷ The escape from immunosurveillance by the cancer-immunity cycle typically leads to cancer malignancy. The primary goal of cancer immunotherapy is to reinvigorate the anti-cancer immunity for cancer treatment. As illustrated above, T cell is at the core of the cancer-immunity cycle via direct elimination of cancer cells.¹⁶ However, cancers develop multiple strategies to blunt the anti-cancer T cell responses for progression.¹⁷ A growing understanding of cancer-mediated immunosuppression on T cells has led to the development of immunotherapeutic approaches with unprecedented success in clinics, including immune checkpoint inhibitors and CAR-T cell therapy.¹⁸ Nevertheless, current cancer immunotherapy still faces tremendous challenges such as low response rates and high toxicities. To overcome such challenges, immunoengineering approaches have been developed to assist cancer immunotherapy for optimal outcomes in cancer patients.

In general, immunoengineering is an interdisciplinary field aiming at better understanding and therapeutic manipulation of the immune system with engineering tools and principles.¹⁹ Immunoengineering embraces a broad range of bioengineering techniques, including genetic engineering, protein engineering, tissue engineering, biomechanical engineering, and so on. In particular, biochemical immunoengineering, especially biomaterial-assisted immunoengineering, has been the mainstream of the field.²⁰ In the following sub-sections, we will focus on the two most clinical-relevant T cell-based cancer immunotherapies, immune checkpoint blockade (ICB) and ACT therapies, and their limitations in clinics along with representative biochemical immunoengineering strategies for overcoming those limitations.

1.1.1 Immune checkpoint blockade (ICB) therapy

Immune checkpoints are natural inhibitory pathways in the immune system to avoid aberrant immune activation leading to apoptosis of immune cells or autoimmune disease. In the last decades, various immune checkpoints have been identified, including programmed cell death protein-1 (PD-1)/programmed cell death protein ligand-1 (PD-L1) and cytotoxic T lymphocyte-associated antigen (CTLA-4).⁴ Of particular clinical relevance, cancers utilize those inhibitory pathways to suppress the anti-cancer T cell immunity. This has led to the development of ICB antibodies to block immune checkpoints in cancer to restore anti-cancer immune response. ICB therapy, especially anti-PD-1/PD-L1 and anti-CTLA-4 therapies, has been approved by the FDA to treat a wide range of cancer types, including blood, skin, lung, and kidney cancers.⁵ ICB therapy has witnessed remarkable clinical success with durable responses in some of the cancer patients.

However, the response rate is still low with a range of 10 to 30% in most cancers, which represents a major barrier for substantial clinical benefits.⁵ Besides, severe immune-related adverse effects (irAEs) requiring intervention have been noticed in 15 to 30% of cancer patients receiving treatment of anti-PD-1 or anti-CTLA-4 therapies.²¹ In addition, anti-PD-1 and anti-CTLA-4 combination therapy has remarkably prolonged survival in cancer patients and has been approved by FDA for melanoma and carcinoma treatment. However, the combination therapy induced irAEs in 96% of the cancer patients and was discontinued in 36% of patients due to severe irAEs.²² The low response rate and high toxicities, amongst other challenges, pose an urgent need for innovative immunoengineering approaches to improve the therapeutic outcome and safety profile of ICB therapy.

As blockade of immune checkpoints in normal tissues is unwanted, increasing retention or targeting of ICB antibodies in the tumor could potentially decrease the toxicity of ICB therapy. One recent advance is to engineer ICB antibodies with tumor-targeting moieties such as tumor extracellular matrix (ECM)-binding domains, which shows potential to increase the therapeutic efficacy and safety profile of ICB therapy in cancer treatment.^{23,24} Biomaterial-assisted local delivery is another promising engineering approach to avoid the systemic toxicity of ICB therapy. Local delivery can potentially circumvent systemic dissemination of ICB antibodies which may induce systemic inflammatory responses and thus irAEs. For example, injectable hydrogels have been utilized to achieve local delivery of ICB antibodies in tumors.^{25–28} Injectable hydrogels possess various advantages, including high biocompatibility, high flexibility in composition/drug loading, and ease of administration.^{29,30} After injection into the target location, it can form a depot in situ for sustained release of loaded therapeutics. Microneedle patch is another representative minimally-invasive drug delivery platform and is of particular interest in transdermal delivery of ICB antibodies for skin cancer treatment.^{31–34} Microneedles can readily penetrate the stratum corneum, the primary barrier for permeation of macromolecular drugs, and provide direct access to the transdermal compartment in a painless manner.^{35,36} Thus, microneedle patches have great potential to avoid systemic dissemination of therapeutics and increase treatment compliance. In general, local delivery platforms hold great promise to reduce systemic toxicity of ICB therapy and enable co-delivery of other therapeutics (e.g., chemotherapy) for effective combination cancer immunotherapy.

Besides synthetic biomaterials, living cell (e.g., platelet and bacteria)-assisted delivery is an emerging engineering technique for targeting ICB antibodies to tumor niches.^{37–41} The living cells feature their unique homing ability to specific tissues depending on their surface ligand specificity. Platelet is one elegant example for targeting anti-PD-L1 antibodies to the surgical bed of primary tumor resection.³⁷ Platelets are terminally differentiated cells derived from megakaryocytes and participate in hemostasis to prevent bleeding from injured vessels.⁴² Of particular interest, transfused platelets preferentially migrate to the surgical wound,⁴³ which provides an avenue to target post-surgical cancer recurrence. Conjugation of hematopoietic stem cells (HSCs) to platelets could further confer the specificity targeting the bone marrow.³⁹ It has shown potential to enhance the efficacy of ICB therapy in the treatment of acute myeloid leukemia that is refractory to conventional cancer therapies (e.g., chemotherapy and HSC transplantation), which is usually located in the bone marrow.^{44,45} Although cell-assisted delivery is still in its infancy, it has great potential to increase tissue specificity and the therapeutic efficacy of ICB therapy.

1.1.2 Adoptive T cell (ACT) therapy

Typically, ICB therapy relies on pre-existing tumor-reactive T cells in the TME to elicit an anti-cancer response. In some patients, the number of tumor-infiltrating lymphocytes (TILs) may not be sufficient to mount an effective anti-cancer response. Ex vivo expansion of TILs isolated from tumor biopsy has been developed to improve anti-tumor immune response after infusion back into cancer patients.^{46–49} Particularly, infusion of interleukin-2 (IL-2)-expanded TILs together with IL-2 into the cancer patients preconditioning by lymphodepletion led to complete tumor regression in 22% of the patients with metastatic melanoma.⁴⁸

Although TIL-based ACT therapy has demonstrated dramatic clinical benefits in patients with metastatic melanoma, tumor-reactive effector T cells are usually scarce or absent in many cancer types.⁵⁰ In the past decades, one of the most important advancements in ACT therapy is the development of genetically modified autologous T cells, especially CAR-T cells approved by the FDA for the treatment of hematologic malignancies.¹ CARs are synthetic receptors that redirect T cell effector functions against surface antigens of tumor cells independent of MHC recognition. In a typical clinical manufacturing procedure for CAR-T cell therapy, leukocytes are first isolated from the patient's peripheral blood through leukapheresis. The purified T cells are then enriched from leukapheresis product through centrifugal elutriation followed by activation with anti-CD3/CD28 antibody-coated magnetic beads (Dynabead®) plus IL-2 supplementation. The activation process is usually performed in a bioreactor culture system such as the WAVE Bioreactor (GE Healthcare) with a rocking base to guarantee optimal gas exchange and mixing. During the activation phase, viral vectors encoding the specific CAR ligands are added into the incubation and washed out by medium exchange after several days. The generated CAR-T cells are then further expanded, separated from magnetic beads, and concentrated to a certain volume for infusion back into the cancer patient.⁵¹ Collectively, the whole manufacturing process takes several weeks or months to complete. Such a lengthy manufacturing process represents one of the critical challenges for autologous CAR-T cell therapy as the disease often progresses rapidly in some cancer patients.⁵² In particular, ex vivo expansion of T cells is one of the time limiting steps in the manufacturing as a large amount of CAR-T cells must be expanded from limited T cell resources from the patient for an effective therapeutic dosage.⁵³

To minimize the gap between patient identification and treatment, biomaterial-assisted strategies have been developed for efficient and consistent ex vivo expansion of functional T cells.^{54–58} Among them, anti-CD3 and anti-CD28 antibody-coated magnetic bead (Dynabead®) is a clinical-applicable synthetic system standardized for ex vivo expansion of CAR-T cells. However, the Dynabead® system is non-degradable and requires separation from the final CAR-T cell product, which incurs additional cost and manufacturing challenges.⁵¹ To provide a better solution for rapid expansion of functional T cells, a biodegradable antigen-presenting cell (APC)-mimetic scaffold (denoted as APC-ms) was developed by incorporating supported lipid bilayers (SLBs) on mesoporous silica micro-rods (MSRs).⁵⁸ The degradation of APC-ms was complete before the infusion, which obviated an extra isolation step necessary for the Dynabead® system. In addition, a five-fold greater expansion of CAR-T cells was achieved with APC-ms as compared to Dynabead®.⁵⁸

As abovementioned, CAR-T cell therapy has achieved unprecedented success in the treatment of hematologic cancers. However, its clinical outcomes have been limited in solid tumors, representing about 90% of human cancers.⁵⁹ Solid tumors possess multiple intrinsic factors that hurdle an efficacious CAR-T cell therapy, including lack of tumor-specific

antigens, impaired lymphocyte infiltration, and highly immunosuppressive TME.¹⁷ Over the past decades, various biochemical strategies have evolved to surmount those intrinsic barriers for effective CAR-T cell therapy in solid tumors.⁶⁰ One exquisite example is the development of armored CAR-T cells by incorporating additional genetic circuits encoding supporting cytokines or ligands.^{61–66} A recent advance is the creation of an interleukin-7 (IL-7) and chemokine (C-C motif) ligand 19 (CCL19) co-expressing CAR-T cell (denoted as 7 × 19 CAR-T) to improve the efficacy of CAR-T cell therapy against solid tumors. IL-7 and CCL19 have been shown to be essential to forming T cell zones in lymphoid tissues through recruiting T cells and DCs and maintaining their functions.⁶⁷ The 7 × 19 CAR-T cell therapy induced significant tumor regression and prolonged survival in preclinical murine mastocytoma, lung carcinoma, or pancreatic cancer models compared to conventional CAR-T cells.

Modification of T cells with additional genetic circuits is usually costly, laborious, and varying from batch to batch. Nanoparticle-based drug delivery systems provide a feasible and modular approach to deliver supporting factors to CAR-T cells in a highly standardized and specific manner.^{8,9,68,69} In one elegant study, a redox-responsive nanogel backpack was exploited to achieve a specific release of interleukin-15 (IL-15), a potent T cell expansion cytokine, on CAR-T cells that infiltrate tumors.⁸ This system allowed delivery of a large dose of IL-15 to support T cell functions specifically in the TME which otherwise could be lethal when administrated systemically. This approach substantially widened the therapeutic index of T cell-supporting cytokines and enhanced the *in vivo* expansion and anti-tumor efficacy of CAR-T cell therapy in preclinical human xenograft solid tumor models.⁸

Beyond suboptimal efficacy, high toxicity is another critical bottleneck for improving the clinical benefits of CAR-T cell therapy in cancer patients. Cytokine release syndrome (CRS) is one of the major adverse events associated with the clinical application of CAR-T cell therapy.⁶⁰ CRS reflects robust CAR-T cell/target cell interactions that initiate a systemic release of inflammatory cytokines such as interleukin-6 (IL-6) and tumor necrosis factor- α (TNF- α), which cross-activate endogenous immune cells to release more cytokines in a self-amplifying manner, causing irAEs including fever and organ dysfunctions. In patients with relapsed or refractory B-cell acute leukemia, severe CRS occurred in 19 to 43% of cancer patients treated with CD19-targeted CAR-T cells.⁷⁰ At present, blocking IL-6 receptors with tocilizumab is the standard-of-care treatment to mediate moderate or severe CRS.⁷¹ To better ameliorate CRS in the very first place, various biochemical genetic control systems have been developed and integrated into CAR-T cells to increase their safety profiles.⁶⁰ For example, CAR-T cells with on/off-switches or suicide genes have been engineered to curb activation of CAR-T cells when CRS develops.^{72–75} Among them, small molecule-induced conditional dimerization is of particular interest as it enables refined control over the location, duration, and intensity by simply adjusting injection route, regimen, and dosage, respectively.⁷⁴

Despite that significant effort has been devoted to modulating biochemical signals to enhance T cell-based cancer immunotherapy, challenges such as low response rate and severe toxicity remain unresolved to a great extent. Exploring biomechanical signals, another major dimension of cancer-immune system interactions, in immunoengineering of T cells is thus gaining more and more attention in recent years.^{76–78} Throughout their lifecycle, T cells constantly survey a multitude of organs and tissues and experience diverse biomechanical environments, such as shear force in the blood flow and a broad range of tissue stiffness.⁷⁹ Furthermore, biomechanical properties of tissues or cells may be altered in

disease and inflammation.¹¹ Biomechanical cues, including both passive mechanical cues and active mechanical forces, have been shown to govern T cell development, activation, migration, differentiation, and effector functions.^{12,14,77,80,81} In other words, biomechanical cues provide an additional dimension, complementary to traditional modulation of biochemical cues (e.g., antigen density and co-stimulatory signals), to tailor T cell immune responses and enhance therapeutic outcomes of T cell-based cancer immunotherapy. In the following sections, recent advances in T cell mechanobiology and mechanical immunoengineering of T cells will be elaborated in the context of therapeutic applications.

1.2 T cell mechanobiology

T cell activation requires three elements: 1) antigen-specific stimulation signal through the TCR/CD3 complex; 2) costimulatory signal through CD28; and 3) survival or differentiation signal from autocrine or paracrine cytokines. TCR signaling has been classically viewed as a purely biochemical process initiated upon recognition of pMHC. In recent studies, the TCR, upon binding to agonist pMHC, has been shown to exhibit a “catch bond” behavior under mechanical tension. Catch bond is a specific type of non-covalent receptor-ligand interaction displaying prolonged bond lifetime upon the tensile force applied to the receptor-ligand axis.^{82–84} Catch bond formation between TCR and pMHC enables T cells to discriminate between agonist and antagonist pMHCs.⁸⁵ A recent study further showed that catch bond formation is important for the negative selection of T cells in the thymus.⁸⁰ Moreover, mechanical force directly acting on the TCR or CD3 can trigger TCR signaling likely due to force-induced allosteric changes in the TCR/CD3 complex,^{86,87} showing evidence that the TCR/CD3 complex itself is a mechano-sensor (Fig. 1:2).⁸⁸

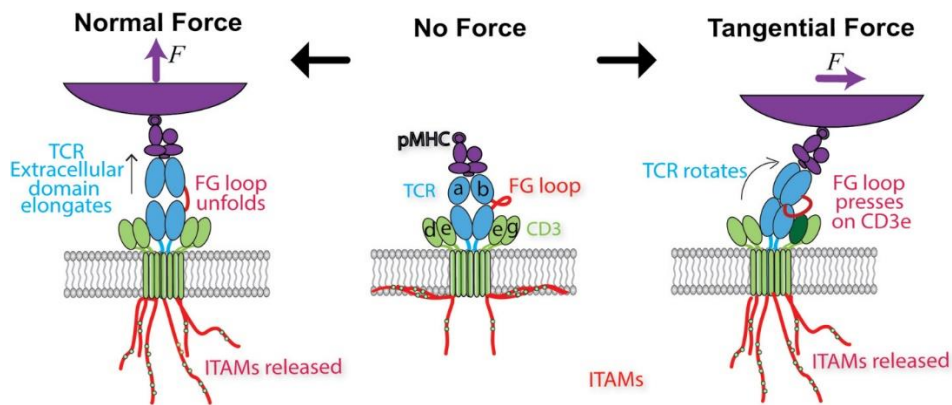


Figure 1:2 Models of how force may trigger T cell receptor (TCR) signaling.

Middle, schematic of the ligated, unloaded, and untriggered TCR. Soluble peptide-major histocompatibility complex (pMHC) binds to the TCR V domains, while the cytoplasmic domains of the TCR-associated CD3 chains remain buried in the lower leaflet of the cell membrane, preventing immunoreceptor tyrosine-based activation motif (ITAM) phosphorylation. Left, a force normal to the cell membrane pulls on the TCR, extending the length of the complex by ~ 10 nm. While the structural region responsible for such conformational change has not been identified, here the FG loop connecting the C β and V β domains is assumed to unfold to result in an extended conformer and in catch-bond formation. Force propagated across the TCR-CD3 connection is assumed to release the CD3 cytoplasmic domains for phosphorylation of the ITAMs. Right, when a force tangential to the cell surface is applied to the ligand-binding site of the TCR that also experiences a lateral reaction force from its membrane anchor, a torque is generated to rotate the complex, which is assumed to allow the FG loop to press down on the CD3 ϵ ectodomain to expose the cytoplasmic ITAMs in a piston-like manner. Adapted from ref. ⁸⁸.

TCR binding to pMHC upon contact with a cognate APC induces a large-scale spatial reorganization of receptor-ligand complexes into a specialized cell-cell junction called immunological synapse (IS), which orchestrates sustained TCR engagement and subsequent T cell functions such as cytokine production and clonal expansion.^{89,90} A canonical IS features a “bull’s eye” pattern with central supramolecular activation cluster (cSMAC) mainly containing TCR/pMHC clusters surrounded by a ring of lymphocyte function-associated antigen 1 (LFA-1)/intercellular cell adhesion molecule-1 (ICAM-1) complexes termed peripheral supramolecular activation cluster (pSMAC).⁹¹ LFA-1, a member of the integrin family exclusively expressed on leukocytes, is of particular interest to T cell mechanobiology as recent evidence shows that LFA-1 is a mechano-sensor and a key regulator of IS formation.⁹² During T cell activation, LFA-1 matures from an inactive, bent conformation with very low affinity to its cognate ligand ICAM-1 on APCs to an intermediate state with higher affinity. Mechanical tension on the LFA-1/ICAM-1 pair arising from F-actin centripetal flow at the IS further transforms LFA-1 into an active, extended conformation with high ligand affinity promoting T cell adhesion and priming (Fig. 1:3).⁹²

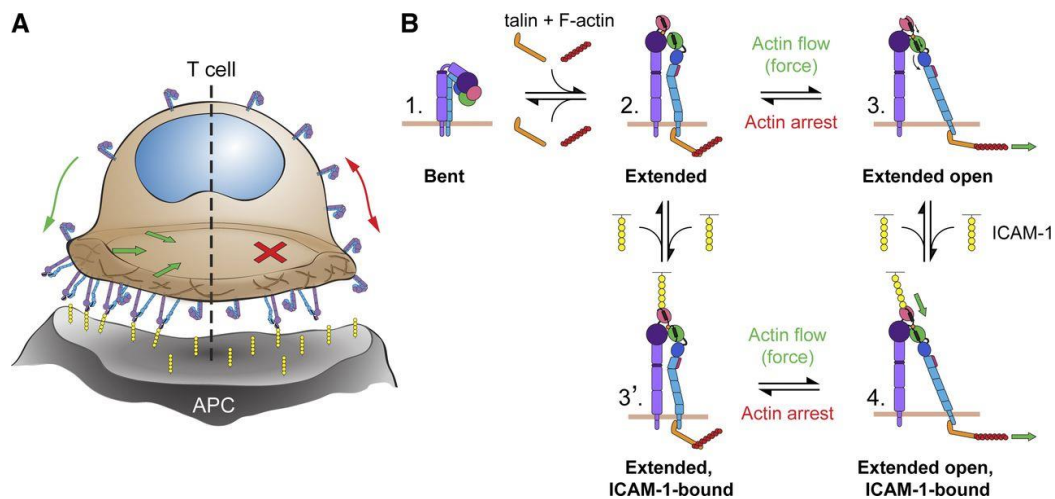


Figure 1:3 Model of LFA-1 activation at the immunological synapse (IS).

(A) Actin-dependent regulation of LFA-1 valency. Ongoing F-actin flow (left) in T cells responding to a polarized T cell receptor (TCR) stimulus drives activation of LFA-1 at the IS. Activated LFA-1 then binds ICAM-1, leading to synaptic enrichment. Arrested F-actin dynamics (right) abrogates activation of LFA-1, allowing passive diffusion of unligated LFA-1 away from the IS. (B) Actin-dependent regulation of LFA-1 affinity. (1) Inactive LFA-1 exists in a bent conformation on the T cell surface. (2) Inside-out signaling events downstream of TCR engagement lead to recruitment of talin and F-actin to the integrin β tail. This allows for the segregation of the α and β tails and the unbending of LFA-1 to yield the extended conformation. (3) F-actin flow generates tensile forces on the LFA-1 β tail (green arrow), facilitating further tail separation and resulting in swingout of the hybrid domain and induction of the open (high affinity) form of LFA-1. (4) The open α domain primes the molecule for binding of ICAM-1, which through induced fit and tension-based mechanisms (green arrows) stabilizes LFA-1 in the high affinity, ligand-bound conformation. Alternatively, LFA-1 affinity maturation can proceed through an ICAM-1-bound, extended conformation (3') in which ICAM-1 weakly interacts with LFA-1 and induces the open head domain before application of force; force then stabilizes this interaction. After the loss of force on the β chain, ligand unbinding may preferentially occur through the 3' step, in which there is no stabilization of the open I domain and therefore much lower affinity for ICAM-1. Alternatively, in the absence of force, LFA-1 does not undergo the priming step to the unligated, open conformation. Regular turnover of LFA-1/ICAM-1 complexes would then lead to loss of bound ICAM-1. Adapted from ref. ⁹².

T cells also actively exert mechanical forces.^{12,93–96} Both TCR and LFA-1 are coupled to the T cell cytoskeleton, effectively connecting the cell intracellular domain to external surfaces and relaying cytoskeletal forces to the surface of the APC or target cell. Lowering these cytoskeletal forces via cytoskeleton inhibition is associated with a substantial reduction in T cell activation events such as calcium influx and IL-2 production.^{12,97} Calcium influx can be partly rescued by external cyclical forces applied to the TCR.¹² These observations suggest that T cells are a major contributor to the mechanical

forces required for TCR triggering. Mechanical forces exerted by cytotoxic T lymphocytes (CTLs) at the IS interface with target cells, such as cancer cells, enhance perforin-based pore formation on the membrane of target cells and potentiate killing of target cells (Fig. 1:4).¹⁴ A recent study further demonstrated that F-actin-rich protrusions of CTLs were required for this synaptic force exertion and cytotoxicity against target cells.⁹⁸

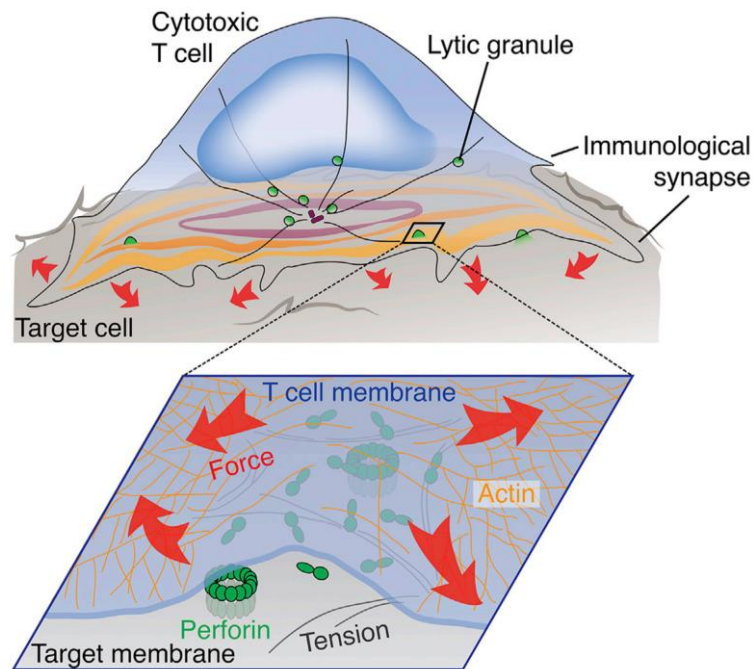


Figure 1:4 Cytotoxic T cells use mechanical force to potentiate target cell killing.

The immunological synapse formed between a cytotoxic T lymphocyte (CTL) and an infected or transformed target cell is a physically active structure capable of exerting mechanical force. CTLs coordinate perforin release and force exertion in space and time. Force potentiates cytotoxicity by increasing target cell tension, which augments pore formation by perforin and thus killing by CTLs. Adapted from ref. ¹⁴.

1.3 Mechanical immunoengineering of T cells

The fundamental studies discussed above provide a brief insight into the mechanical life of T cells. Bioengineering strategies derived from these findings and aimed at modulating T cell immunity can be broadly classified according to their physical nature into two fields: passive mechanical cue-oriented and active force-oriented mechanical immunoengineering of T cells (Fig. 1:5). In general, the same mechanosensitive receptors (e.g., TCR and LFA-1) are involved in both passive and active mechanical stimulations of T cells. In the following sections, recent advances in both fields will be discussed in detail with a focus on therapeutic applications.

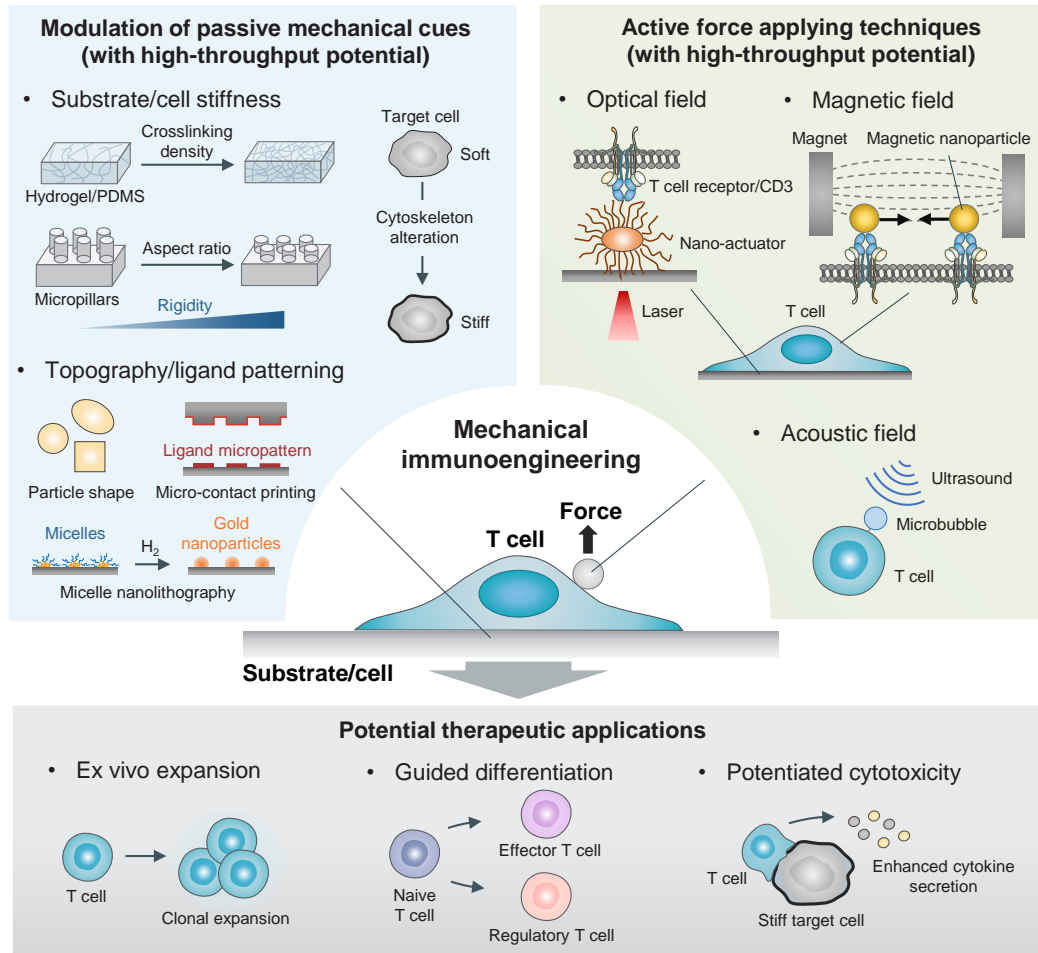


Figure 1:5 Schematic illustration of mechanical immunoengineering of T cells using passive mechanical cues or active mechanical forces for therapeutic applications. PDMS, polydimethylsiloxane.

1.3.1 Passive mechanical cues for mechanical immunoengineering of T cells

Passive mechanical cues refer to mechanical properties of the microenvironment encountered by cells, such as ECM stiffness and spatial organization of its networks, including fibronectin and collagen fibers. These cues exist throughout the body and are indispensable for guiding the cellular responses (e.g., migration and differentiation) of various cell types, such as fibroblasts and stem cells.^{99,100} However, less is known about their effects on T cells.

For example, inflamed and tumor tissues display distinct ECM mechanical properties compared to healthy tissues. Over the course of inflammation, sentinel lymph nodes become up to 10 times stiffer than normal lymph nodes (~4 kPa).¹⁰¹ In tumor tissues, collagen crosslinking contributes to ECM stiffening and promotes tumor progression.¹⁰² At the cellular level, maturation of DCs, the most potent professional APC, results in a rise of their cell stiffness through cytoskeleton remodeling.¹³ At the same time, they undergo drastic morphological changes and exhibit a stellate shape optimal for T cell stimulation.¹⁰³ In this section, we discuss the role of the substrate and cell stiffness as well as topography and ligand patterning, two intensively-studied categories of passive mechanical cues, in regulating T cell responses and their potential use in mechanical immunoengineering of T cells.

1.3.1.1 Substrate/cell stiffness

Stiffness is an inherent mechanical property of materials representing their resistance to deflection or deformation. Substrate stiffness is defined by its Young's modulus or elastic modulus (E). Polydimethylsiloxane (PDMS) elastomer and polyacrylamide (PA) hydrogel are two widely-used substrates to control stiffness experienced by cells in vitro, predominantly due to their non-degradable and bio-inert features that enable the presentation of specific ligands with minimal non-specific biochemical interactions.¹⁰⁰

Early studies identified that PDMS substrates with stiffness values of approximately $E \sim 100$ kPa induced the strongest activation of human or murine naïve T cells.^{97,104} This stiffness-dependent activation was partly attributed to the myosin-mediated cell contractility. Interestingly, a recent study demonstrated that the spreading area of T cells exhibits maximal spreading on PDMS substrates with stiffness of ~ 5 kPa.¹⁰⁵ These results suggest that, within the range of 0-5 kPa, the enhanced T cell activation observed on stiffer PDMS substrates may be partially attributed to the increased amount of stimulatory ligands accessed by the cell due to its larger spreading area. However, why T cells prefer certain stiffness of PDMS substrate (~ 100 kPa) for optimal activation still requires further investigation.

In light of the stiffness-dependent activation of T cells, this mechanical parameter may be incorporated in the design of engineering strategies to improve T cell manufacturing for cell therapies. The current ex vivo expansion of T cells for clinical applications mainly relies on a synthetic microbead system (Dynabead®) modified with anti-CD3 and anti-CD28 antibodies on its surface. However, this system is made of polystyrene (PS), an extremely stiff material with E in the GPa range, several orders of magnitude higher than physiological stiffness. Using PDMS microbeads ($E \sim 8$ MPa) to present stimulatory signals to human primary T cells resulted in an enhanced expansion of functional T cells compared to Dynabead®.⁷⁶ It is worth noting that this PDMS microbead system may be further improved by using lower stiffness values as optimal T cell activation was achieved on a PDMS substrate with stiffness of 100 kPa.

Despite these promising results, the stiffness of PDMS typically ranges from 100 kPa to 10 MPa, which is substantially higher than physiological stiffness that T cells encounter in vivo, typically within 100 Pa to 100 kPa (except bone). Over the past years, in-depth studies of T cell responses to stiffness in a physiologically-relevant range (0.1-100 kPa) have been performed, generally using hydrogel substrates. In an elegant study, Hivroz's group designed an artificial antigen-presenting surface using PA hydrogels with stiffness values ranging from 0.5 to 100 kPa.⁸¹ Within this range of stiffness, re-stimulated human CD4⁺ T cells displayed increasing cell proliferation and inflammatory cytokine production with increasing stiffness. In another study, an alginate hydrogel-based system mimicking the stiffness changes of lymph nodes during inflammation (from 4 to 40 kPa) was developed.¹⁰⁶ This study demonstrated that priming of naïve murine CD4⁺ T cells depends on the mechanical microenvironment in both 2D and 3D culture systems.

The intracellular mechanisms underlying the stiffness dependence of T cell activation are an active field of research. For example, gene expression profiling revealed an upregulation of hypoxia-inducible factor-1 α (HIF1A), a transcriptional factor stimulating glycolytic metabolism, in T cells simulated on a substrate of 100 kPa.⁸¹ Furthermore, the respiratory

electron transport pathway involved in adenosine triphosphate (ATP) production was highly induced, suggesting a potential role of cellular metabolism in regulating T cell responses to stiffness.

Mechanosensing in T cells requires Yes-associated protein (YAP), a well-known transcriptional regulator in mechanotransduction.¹⁰¹ In general, cells recognize increased stiffness via enhanced translocation of YAP from the cytosol into the nucleus. YAP knock-out T cells failed to recognize stiffness changes and displayed enhanced activation on a soft substrate ($E \sim 4$ kPa) compared to wild-type T cells.¹⁰¹ Interestingly, YAP was upregulated upon activation but acted as a negative regulator of T cell activation. This finding is contrary to the usual role of YAP in adherent cells, where YAP promotes proliferation. YAP dampens T cell proliferation by restricting trafficking of Nuclear Factor of Activated T cells (NFAT), a known promoter of IL-2 expression, into the nucleus.¹⁰¹ However, whether YAP itself contributes to T cell proliferation requires further investigation. This finding may provide a novel target to engineer optimal T cell responses by fine-tuning the mechanosensing properties of T cells.

While artificial antigen-presenting surfaces provide convenient tools to study T cell activation, they hardly recapitulate all aspects of a natural APC. To date, there has been a limited volume of research on how the stiffness of APCs or target cells shapes T cell responses. Cancer cells cultured on stiff surfaces adapt to their environment and show increased cellular stiffness as a result.¹⁰⁷ Recently, cancer cells on stiff substrates were shown to be more vulnerable to CTL-mediated cytotoxicity, suggesting that stiffness of target cells may play a role in the T cell responses.¹⁴ Similarly, effector CD4⁺ T cells produced more cytokines when stimulated by target cells cultured on a stiffer substrate (Fig. 1:6).⁸¹ However, mechanistic studies are required to determine the extent to which stiffness of target cells influences T cell effector functions. More recently, Tello-Lafoz et al. discovered that increased cellular stiffness resulting from enhanced expression of myocardin-related transcription factor (MRTF) in metastatic cancer cells enhanced their susceptibility to CTL-mediated killing.¹⁰⁸ Sensing of this biomechanical vulnerability by T cells, a process termed “mechanical immunosurveillance”, offers a novel perspective on the biomechanical nature of T cell immunity, as well as a possible target for mechanical immunengineering of T cells.

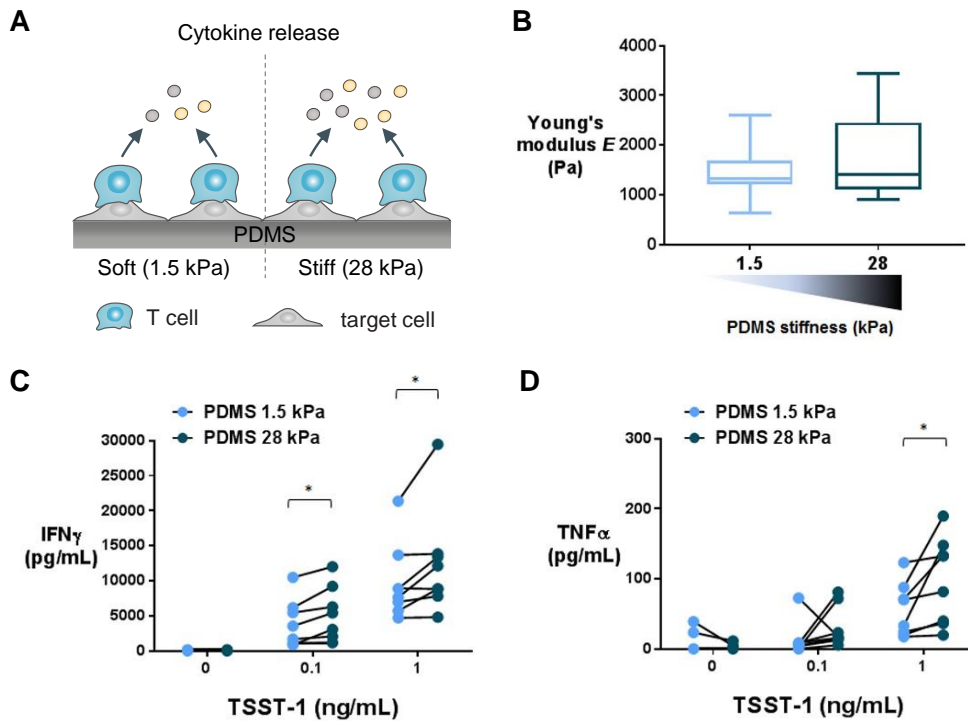


Figure 1:6 Target cells on stiffer substrate stimulate stronger cytokine productions in CD4⁺ T cells.

(A) Schematic of enhanced T cell polyfunctionality toward target cells on a stiffer substrate. (B) Young's modulus of HeLa-CIITA cells (HeLa cancer cells expressing MHC class II molecules) cultured on PDMS substrates of different stiffness. (C, D) Production of IFN γ (C) and TNF α (D) by human CD4⁺ T cells interacting with HeLa-CIITA cells on PDMS of varying stiffness in the presence of TSST-1 superantigen of different concentrations. PDMS, polydimethylsiloxane.

Besides activation of effector T cells, there is scarce information about the role of stiffness in the induction of regulatory T cells (Tregs). Induction of murine Tregs was enhanced on a PDMS substrate with stiffness of ~ 100 kPa compared to a non-physiological stiffness (~ 3 MPa). In contrast to effector T cell activation, interruption of myosin-mediated contractility using a Rho-associated kinase (ROCK) inhibitor increased Treg induction.¹⁰⁹ The mechanism underlying this surprising observation requires further in-depth investigation. The results suggest that stiffness may be an essential parameter to optimize ex vivo induction of Tregs for ACT against autoimmune diseases.¹¹⁰

Recently, attempts have been made to use the stiffness dependence of T cells to enhance cancer immunotherapy. Hickey et al. improved ex vivo expansion of antigen-specific murine CD8⁺ T cells by leveraging a soft hyaluronic acid (HA) hydrogel (~ 0.5 kPa) presenting stimulatory signals. T cells expanded on the HA hydrogel showed improved tumor control and prolonged survival rate in mice compared to T cells expanded on a conventional tissue culture plastic (TCP). This effect is likely due to the enhanced proliferation of antigen-specific T cells (Fig. 1:7).⁷⁷ Of note, T cell activation was reduced on HA hydrogels of higher stiffness, ~ 3 kPa (Fig. 1:7B), which stands in opposition to previous studies. Although the authors did not give an explanation, this singular result may be caused by specific interactions between CD44 of T cells and HA as CD44-mediated signaling is mechanosensitive.¹¹¹

Despite considerable progress on understanding how stiffness affects T cell responses, it is still challenging to study this effect *in vivo*, especially at the cellular level. Lysyl oxidase (LOX) may be an interesting tool to modify tissue stiffness *in vivo*.¹¹² However, to the best of our knowledge, no approach is available to control cell stiffness *in vivo*. In the future, efforts should be dedicated to *in vivo* modulation of cell stiffness, which is critical to study mechanical regulation of T cell responses *in vivo*.

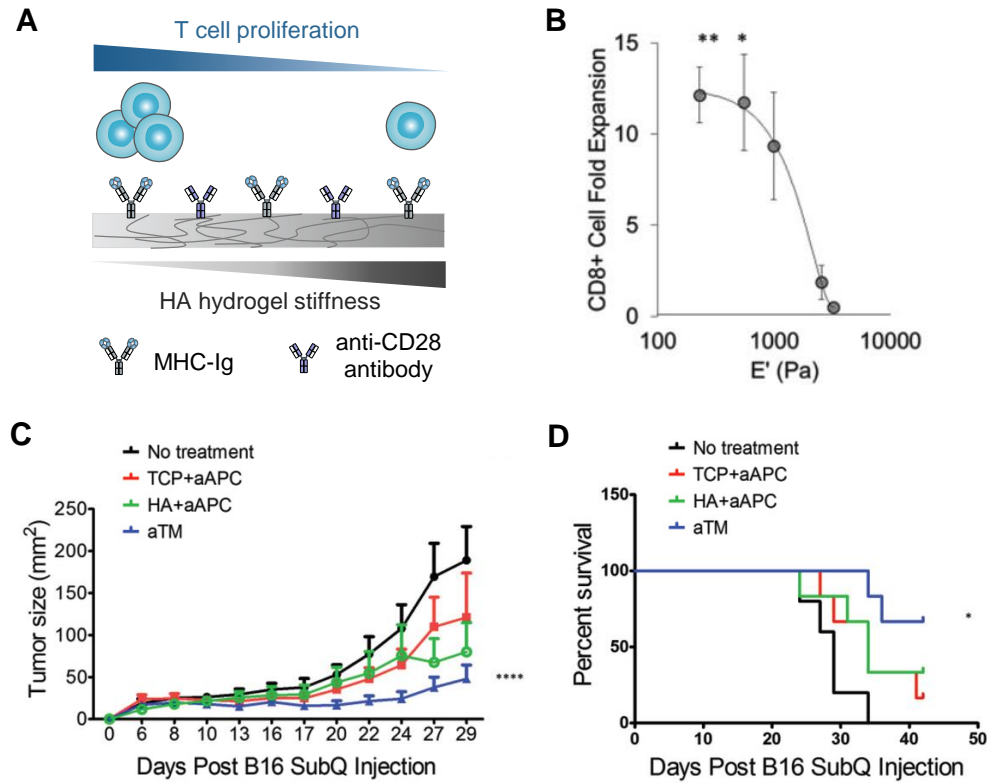


Figure 1:7 Soft hyaluronic acid (HA) hydrogel enhances ex vivo CD8⁺ T cell expansion for enhanced adoptive T cell therapy.

(A) Schematic of stiffness-dependent T cell expansion on an artificial T cell-stimulating matrix (aTM) made from conjugating T cell stimulation signals to a hyaluronic acid (HA) hydrogel. (B) Fold expansion of naïve CD8⁺ T cells on aTMs with the varying elastic modulus (E'). (C, D) B16 tumor growth (C) and survival rate of mice (D) receiving adoptively transferred T cells expanded by different methods. MHC-Ig, major histocompatibility complex-immunoglobulin dimer; aAPC, artificial antigen-presenting cell; TCP, traditional tissue culture plate; SubQ, subcutaneous.

1.3.1.2 Topography and ligand patterning

Upon maturation, DCs exhibit morphological changes characterized by dendrite structures, which are important for migration to lymph nodes and the subsequent priming of T cells.^{113,114} This realization, along with an improved understanding of the biological effects of topography,⁹⁹ has stimulated research on topography as a novel parameter to design artificial APCs. For example, Sunshine et al. evaluated T cell activation by pMHC/anti-CD28-conjugated ellipsoidal microparticles compared to spherical microparticles.¹¹⁵ The topography of microparticles was controlled using a film-stretching method that enables constant particle volume across various topographies. At similar antigen density, the ellipsoidal artificial APC generated higher expansion of antigen-specific murine CD8⁺ T cells *in vitro* and *in vivo* compared to its spherical counterpart and resulted in enhanced therapeutic efficacy (Fig. 1:8). This result is attributed mainly to increased contact frequency and area between the T cell and ellipsoidal artificial APC. In a follow-up study, a similar

trend was observed using nano-sized ellipsoidal particles, which may have additional advantages, such as improved pharmacokinetics upon intravenous injection and easier access to draining lymph nodes, compared to ellipsoidal micro-particles.¹¹⁶

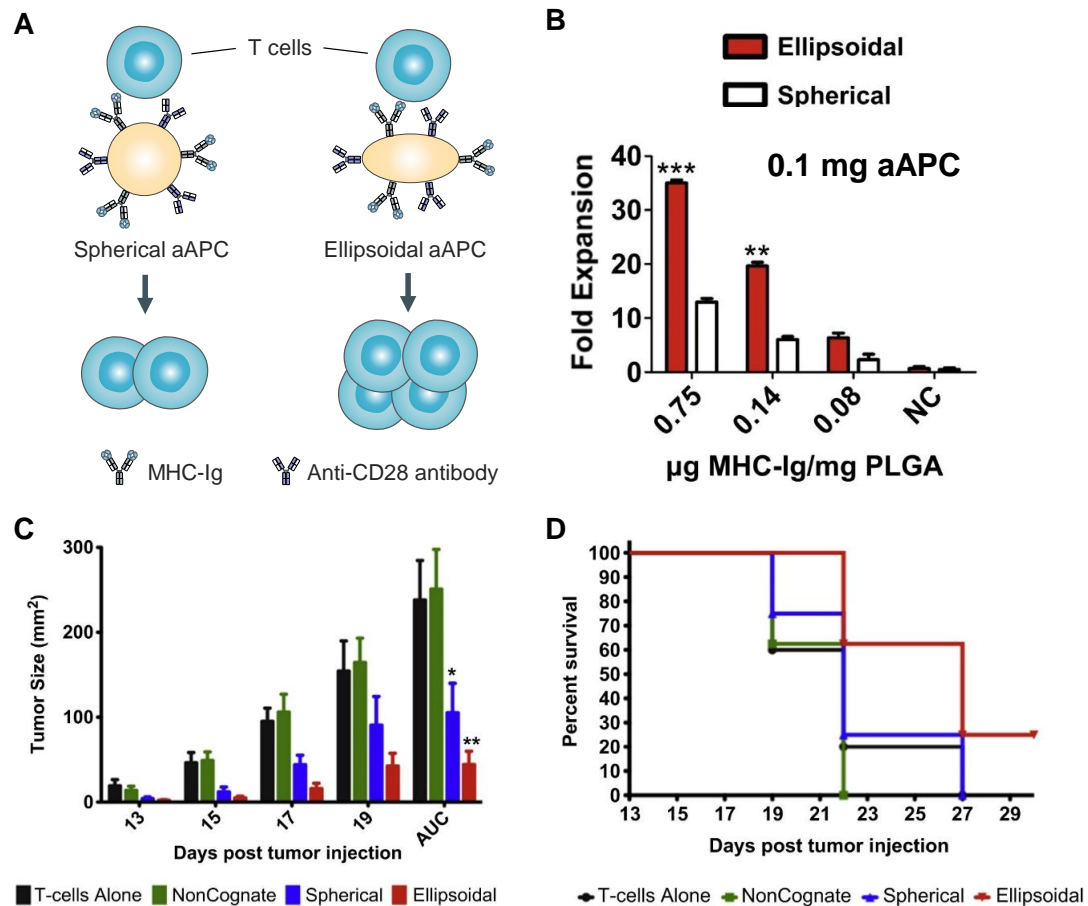


Figure 1:8 Ellipsoidal topography promotes CD8⁺ T cell proliferation for enhanced anti-cancer efficacy.

(A) Schematic of the enhanced proliferation of T cells stimulated by an ellipsoidal artificial antigen-presenting cell (aAPC) compared to its spherical counterpart of similar volume (volume-weighted diameter $\sim 6.7 \mu\text{m}$). (B) Fold expansion of CD8⁺ T cells. (C, D) Tumor size (C) and survival rate (D) of B16 melanoma-bearing mice treated with naïve Pmel CD8⁺ T cells alone or combined with non-cognate ellipsoidal (NonCognate), cognate spherical, and cognate ellipsoidal aAPC. MHC-Ig, major histocompatibility complex-immunoglobulin dimer; PLGA, poly(lactic-co-glycolic acid); AUC, area under the curve.

The spatial proximity of TCR complexes is essential to TCR triggering.¹¹⁷ Ligand nanopatterning techniques have been widely used in the past decade to study the role of lateral ligand spacing on T cell activation.^{118,119} Multiple studies from Spatz's group showed that anti-CD3 antibody lateral spacing should be below 60 nm for optimal activation. Above this threshold, TCR signaling was abrogated, even if sufficient anti-CD3 molecules for T cell activation were present in the contact area.^{118,120,121} It is worth noting that these studies did not decouple the effect of ligand spacing from ligand density. Intriguingly, the threshold for pMHC lateral spacing was as large as $\sim 150 \text{ nm}$,¹²² suggesting other spatial requirements during TCR triggering in addition to CD3/ligand interactions.

In an elegant study reported by Cai et al. recently, lateral ligand spacing was set independently from the number of ligands accessible per cell.¹¹⁹ A threshold of ~50 nm in the lateral spacing of anti-CD3 was revealed in TCR triggering. This finding is consistent with the distance required for auto-phosphorylation of zeta-chain-associated protein kinase 70 (ZAP70) recruited to the TCR intracellular domain, a key step for TCR downstream signaling.¹¹⁹ Knowledge gained in fundamental research can be leveraged to improve the expansion of pre-stimulated human CD4⁺ T cells. Nanopatterned anti-CD3 antibody-coated surfaces with optimized lateral spacing outperformed conventional Dynabead[®],¹²¹ suggesting that ligand nanopatterning may aid in designing more potent artificial APCs for ex vivo T cell expansion.

The spatial organization of the IS varies dramatically between different subtypes of T cells.¹²³ Motivated by these variations, efforts have been made to fabricate artificial ligand micropatterns and study their effects on T cell responses. Using microarrays, Dustin's and Groves' groups showed that TCR clusters mechanically confined in the IS periphery showed longer-lasting TCR signaling than those in the center of an IS with a typical "bull's eye" structure.¹²⁴ As cSMAC has been shown to facilitate TCR degradation via endocytosis,¹²⁵ the peripheral confinement of TCR may augment TCR signaling by preventing TCR degradation. Irvine's group employed polymer-assisted photo-lithography to construct different anti-CD3-immobilized micropatterns which direct the spatial distribution of TCR signaling proteins at the IS.¹²⁶ Production of interferon- γ (IFN- γ), a pro-inflammatory cytokine, by murine CD4⁺ T cells was specifically attenuated on annular micropatterns, while IL-2 secretion was at similar levels on both focal and annular micropatterns.¹²⁶ These observations suggest that TCR micropatterning plays a decisive role in guiding T cell functions, providing a possible mechanical cue to direct T cell responses.

The spatial organization of costimulatory ligand CD28 is another feature of IS formation, which is important in regulating T cell activation.¹²⁷ Typically, CD28 ligands form a ring-like structure surrounding the cSMAC region containing TCR/CD3 complexes. The CD28 pattern is important to retain the spatial proximity between TCR/CD3 and protein kinase C θ (PKC θ), a TCR downstream signaling molecule recruited by CD28.¹²⁷ To study the effects of CD28 patterning, Kam's group utilized microcontact printing to fabricate an anti-CD3/anti-CD28-colocalized central focal (COL) micropattern, as well as a segregation (SEG) layout with a central focal anti-CD3 domain surrounded by four anti-CD28 dots that mimics the native pattern of an IS.^{128,129} While murine CD4⁺ T cells produced more IL-2 on SEG pattern than COL pattern,¹²⁸ human CD4⁺ T cells showed a reversed trend.¹²⁹ These findings not only provide insight into the design principle of ligand spatial organization for engineering T cell responses but also emphasize the potential dissimilarity in mechanosensing between human and murine T cells. Interestingly, dissimilarities between murine Tregs and effector CD4⁺ T cells in adhesion to micropatterns were also noticed.¹³⁰ This preference for distinct spatial ligand organization holds promise for selective activation of Tregs.

To date, investigations of the role of ligand patterning in the regulation of T cell responses are still limited to in vitro studies. As a next step, it is crucial to validate these in vitro findings in animals. Tools for introducing ligand patterning in animals have been reported in investigations of stem cell adhesion¹³¹ and could potentially be applied to study the mechanical modulation of T cells.

1.3.2 Active forces for mechanical immunoengineering of T cells

Immunoreceptors, which connect the intracellular domain to the extracellular environment, experience a variety of mechanical forces as T cells patrol the body and affect their functions. The resulting tension on these receptors (e.g., TCR and LFA-1) is essential for effective outside-in signaling, which notably promotes T cell effector functions and inside-out signaling.¹³² This tension originates, among others, from T cell motion, membrane undulations, and active cytoskeletal rearrangements. T cells continuously remodel their cytoskeleton and actively probe their environment using actin-rich protrusions, which deform target cells and substrates.^{98,133} They exert cytoskeletal forces on their environment when they sense matrix stiffness¹³⁴ and during migration,¹³⁵ activation,^{93,94} and killing.¹⁴ Forces acting on immunoreceptors can also originate from external sources such as hydrodynamic forces and target cell cytoskeleton remodeling. These examples and those discussed earlier in the introduction highlight the key role of active mechanical forces at every step of the T cell response. It is also apparent that strategies aiming to leverage or modulate T cell endogenous forces or apply external forces on immunoreceptors may be used to optimize T cell-based therapies.

1.3.2.1 Forces exerted by T cells

T cell mechanical force and its underlying actin remodeling during motility, activation,¹² and effector functions¹⁴ have been documented. In particular, mechanical forces at the interface between T cells and stimulatory surfaces have been extensively characterized.^{12,93,94} Abrogation of these forces using cytoskeleton inhibitors such as Latrunculin A resulted in a loss of activation or effector functions.^{12,14} Moreover, increased force exertion of phosphatase and tensin homolog (PTEN)-deficient CTLs was shown to significantly enhance tumor cell killing in vitro.¹⁴ Huse's group demonstrated, through a series of in vitro studies, that while T cell force was enhanced in PTEN-deficient T cells, other key biochemical aspects of their cytotoxicity, such as granule polarization and release, were unaffected by PTEN suppression. A direct link between increased force exertion and enhanced killing is still lacking due to technical difficulties. Still, these results suggest that engineering T cells to exert higher forces may be a viable strategy to enhance killing. One main limitation of this strategy lies in its target, PTEN, which is involved in various cellular processes, including cellular proliferation, survival, growth, and motility.¹³⁶ Data from the Huse's group showed that PTEN-deficient CTLs had reduced ability to control tumor size in vivo compared to wild type CTLs, owing to reduced migration and homeostatic proliferation.¹³⁷

Another force-enhancement strategy may be targeting cytoskeletal proteins. For example, microtubules (MT) destabilization using nocodazole was shown to increase traction stresses of Jurkat T cells.¹³⁸ However, the wide-ranging role of MT in T cells means that the disruption of MT is likely to affect T cell functions. Indeed, nocodazole-treated human CD4⁺ T cells exhibited a shift towards an amoeboid phenotype and enhanced migration through complex 3D environments in vitro, which may benefit T cell infiltration in dense tumor tissues.¹³⁹ On the other hand, nocodazole-treated T cells exhibited strongly reduced killing of target cells.¹⁴⁰ Each specific cytoskeletal target should be thoroughly analyzed, and its potential evaluated according to the desired outcome, e.g., enhanced therapeutic efficacy.

1.3.2.2 External forces applied on T cells

It is well established that the TCR is mechanosensitive.^{86,87} Tension on the TCR-pMHC ligand pairs induces catch bonds, exhibiting maximal bond lifetime under forces of approximately 10 piconewton (pN).⁸⁵ This long-lived interaction is essential to trigger strong T cell activation. Using DNA linkers with defined breakage forces, Salaita's group showed that T cells transmit forces of 12-19 pN per TCR to initiate activation.⁹⁶ However, there is no consensus yet on the nature (constant vs. cyclic; normal vs. shear) and magnitude of the force required for optimal T cell activation. Interestingly, several studies showed that external forces on TCR could induce calcium influx in T cells.^{12,85-87} Moreover, force applied on the TCR of LatA-treated cells could rescue calcium flux, suggesting that the cytoskeleton could be bypassed.¹²

The evidence presented here suggests that active mechanical forces may be used to recapitulate the mechanical conditions at the immune synapse during activation and engineer T cell responses. Therapeutic applications require a large number of cells that can be analyzed in vitro and subsequently tested in disease models. The majority of the elegant tools used in mechanobiology, such as magnetic tweezers, atomic force microscopy, and biomembrane force probe, are intrinsically limited to single-cell studies and not suitable for large-scale experiments. We refer readers to several excellent articles on this topic.^{132,141,142} Hence, we highlight key studies using external mechanical forces to engineer T cells for therapeutic purposes in this section.

Formation of the IS following TCR ligation results in intense ligand reorganization, including TCR clustering.⁹¹ This aspect is often overlooked in many artificial T cell activation systems, where anti-CD3 antibodies or pMHCs are immobilized and cannot be reorganized by T cells. Magnetic forces acting on superparamagnetic nanoparticles bound to TCRs were used to drive the receptors laterally towards one another, thus resulting in TCR clustering (Fig. 1:9A).¹⁴³ TCR clusters in the presence of magnetic field were significantly larger than those in the absence of magnetic field, resulting in greater ex vivo T cell expansion and better tumor control and mouse survival in vivo following adoptive transfer of expanded T cells (Fig. 1:9B-D). Recently, magnetic forces were also used to gently stir (250 rpm) T cells attached to magnetic micro-particles displaying anti-CD3 and anti-CD28 antibodies on their surface.⁷⁸ Impressively, T cells expanded up to 12 times more under dynamic conditions compared to static conditions. However, it is unclear whether this enhanced proliferation results from forces acting on TCR and CD28 receptors or other factors, such as increased contact frequency between T cells and beads. In vivo, T cell activation occurs in secondary lymphoid organs (SLO), where fluid flow and changing tissue mechanics create a dynamic mechanical environment. The fluid movement generated during stirring may mimic this aspect of SLO and enhance T cell activation and proliferation. Interestingly, a commercially-available platform for manufacturing clinical-grade CAR-T cells (WAVE Bioreactor[®]) is performed on rocking bioreactors to induce optimal mixing and gas transfer.⁶

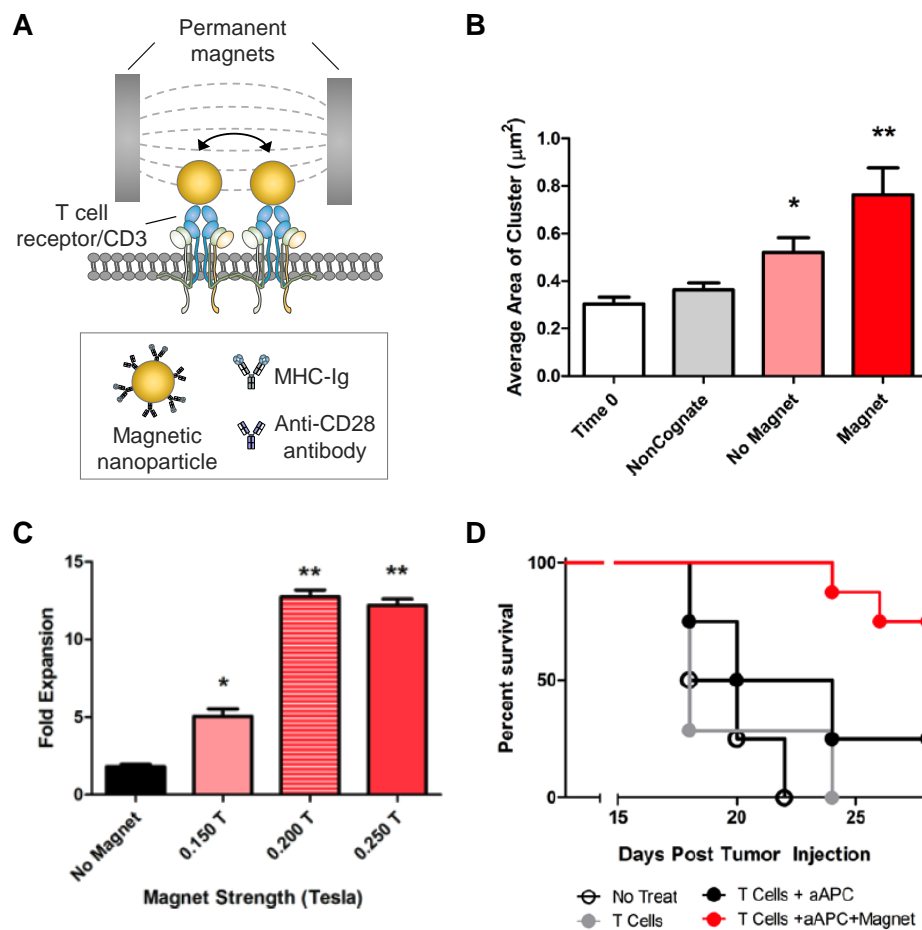


Figure 1:9 Magnetic force clusters T cell receptor (TCR)/CD3 complexes and promotes T cell ex vivo expansion for enhanced adoptive T cell therapy.

(A) Schematic of a magnetic nanoparticle-based system as an artificial antigen-presenting cell (aAPC) through induced TCR/CD3 clustering. (B, C) Average area of TCR/CD3 clusters (B) and fold expansion of T cells (C) in the presence of magnetic field. (D) Survival rate of mice bearing subcutaneous B16 tumors and receiving adoptive transfer of T cells activated by aAPC ex vivo in the presence of a magnetic field. MHC-Ig, major histocompatibility complex-immunoglobulin dimer.

Overall, these studies demonstrate that systems applying forces onto T cell populations globally can be leveraged to optimize T cell activation and expansion, a key step in manufacturing cell-based therapies.

An alternative strategy for stimulating T cells using mechanical force relies on optomechanical actuators,¹⁴⁴ which comprise nanoparticles that can absorb infrared light and shrink upon illumination. The swift particle contraction can generate pN-range forces transmitted through pMHC molecules to activate T cells. While the cell throughput is relatively low, mainly due to the limited illumination area (micrometer range), this technique provides a broad actuation frequency range along with high spatial resolution in a contactless manner.

Despite their promise for precise control of mechanical stimulation of T cells, optical systems are limited in vivo due to the limited penetration of light through tissues (micrometers to millimeters).¹⁴⁵ Ultrasound offers an interesting alternative as it can safely reach tissues at depth up to several centimeters, and ultrasound-based systems have been widely used in the clinic.¹⁴⁶ In addition, microbubbles attached to the cell surface via receptors can be stimulated with low-

frequency ultrasounds of 1-2 MHz at depths up to 5 centimeters.¹⁴⁷ Acoustic stimulation of integrin-bound microbubbles on T cells successfully induced calcium influx through Piezo1 channels in T cells in vitro followed by translocation of NFAT transcription factor to the nucleus (Fig. 1:10A, B). T cells were engineered to express CD19-targeted CARs regulated by NFAT, thus creating T cells genetically engineered to be specifically activated upon ultrasound stimulation, i.e., a mechanogenetic system (Fig. 1:10C, D). Therefore, spatiotemporal control of CAR-T cell activation could be potentially achieved using external mechanical signals. Despite the novelty of this approach, the use of microbubbles coupled to T cells limits its application in vivo, as shear forces are likely to damage or burst the bubbles during T cell migration and extravasation.

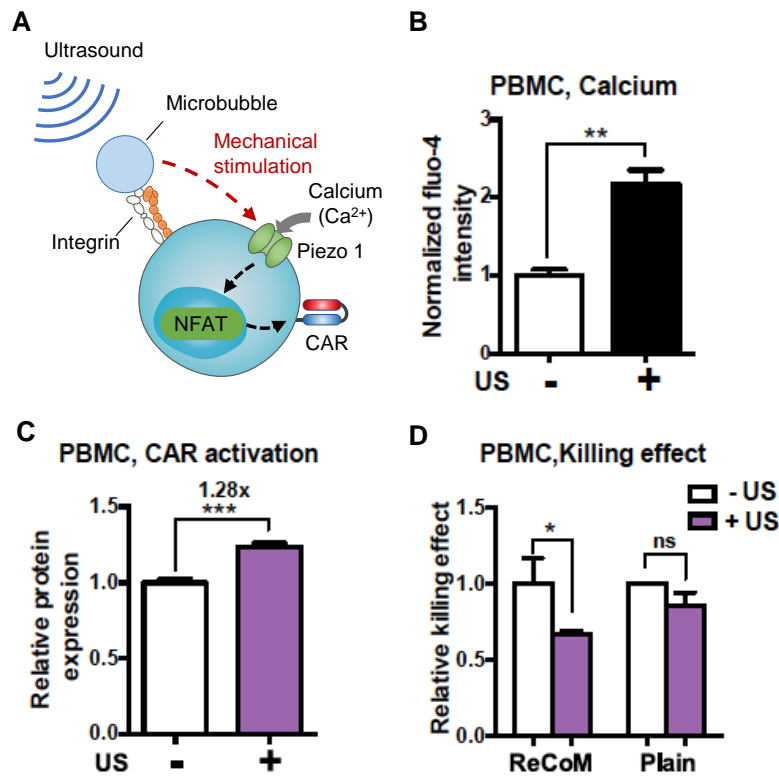


Figure 1:10 A mechanogenetic circuit for ultrasound-inducible expression of chimeric antigen receptors (CARs) on T cells.

(A) Schematic of a remotely-controlled mechanogenetic (ReCoM) system for ultrasound (US)-responsive activation of chimeric antigen receptor (CAR)-T cells. (B, C) Calcium influx (B) and CAR expression (C) of engineered human CAR-T cells from human PBMCs with or without US stimulation. (D) Relative viability of target tumor cells (Nalm6) following co-incubation with CAR-T cells engineered with ReCoM system or native CAR-T cells (plain). PBMCs, peripheral blood mononuclear cells.

Despite increasing efforts on applying T cell mechanobiology to engineer T cell immunity, mechanical immunoengineering is still an emerging field with great potential to improve current biochemical-based cancer immunotherapy modalities. In the following chapters, I will illustrate three new mechanical immunoengineering approaches developed during my Ph.D. study for enhanced cancer immunotherapy: 1) develop a spiky artificial APC mimicking the dendritic shape of DC cells for enhanced ex vivo expansion of functional T cells; 2) identify and overcome a mechanical immune checkpoint for enhanced anti-cancer efficacy of adoptive T cell therapy; and 3) exploit T cell force as a trigger to deliver T cell-supporting drugs specifically in cancer.

Chapter 2 Spiky microparticles provide mechanical stimulation for enhanced T cell expansion

Adapted from the article:

Lei, K., & Tang, L. Mechanical stimulation by spiky microparticles enhances T cell activation and proliferation (2021), in preparation.

2.1 Abstract

Adoptive T cell transfer (ACT) therapy has witnessed remarkable clinical success in achieving complete durable responses in some cancer patients. ACT therapy is a highly personalized therapy requiring the manipulation of autologous T cells from each cancer patient. At present, one of the critical challenges in the clinical manufacturing of ACT therapy is the rapid and consistent expansion of effector T cells into an effective therapeutic dose for cancer treatment. To overcome such challenge, various artificial antigen-presenting cell (aAPC) systems have been developed by mimicking the biochemical aspects of the most potent natural APC—dendritic cell (DC). However, biomechanical aspects of DCs have been underexplored, and it is unclear whether the unique dendritic shape of DCs plays a role in T cell activation. In this study, I fabricated a spiky TiO₂ microparticle (TiO₂ SMP) to recapitulate the dendritic morphology of DCs. TiO₂ SMP presenting stimulatory ligands substantially promoted CD8⁺ T cell activation and expansion compared to its smooth counterpart. TiO₂ SMPs outperformed Dynabead®, a standard aAPC in clinical manufacturing of ACT therapy, in activating and proliferating CD8⁺ T cells into effector phenotype. The enhanced CD8⁺ T cell activation and expansion by TiO₂ SMPs was mediated by T cell forces generated from F-actin polymerization. This study reveals the critical role of shape in designing an effective artificial APC system and may advance the ex vivo T cell manufacturing for ACT therapy.

2.2 Introduction

Adoptive T cell transfer (ACT) is one of the most important advances in cancer immunotherapy, leading to complete and durable tumor regressions in some of cancer patients.^{48,148} ACT therapy nowadays relies on either tumor-infiltrating lymphocytes (TILs) or genetically modified T cells such as chimeric antigen receptor (CAR)-modified T cells. They both require expanding a limited number of autologous T cells from patients into an efficacious therapeutic dosage for cancer treatment.¹⁴⁹ Ex vivo expansion of effector T cells thus becomes a critical step to ensure sufficient functional T cells infused back to cancer patients within the treatment window. Especially in clinical manufacturing of CAR-T cell therapy, activation and expansion of T cells take weeks to complete before infusion back into the same cancer patients.⁵³ Such lengthy manufacturing procedure represents one of the demanding challenges for improving overall clinical outcomes as cancers progress rapidly in some of the patients.⁵²

Antigen-presenting cells (APCs) such as dendritic cells (DCs), the most potent natural APC, have been exploited to activate and expand T cells.¹⁵⁰ However, purifying DCs from patients poses additional manufacturing difficulties. Nevertheless, a reliable T cell expansion by DCs is problematic as DCs' function or potency varies from patient to patient.¹⁵⁰ To achieve an efficient and consistent ex vivo expansion of T cells, various artificial APC (aAPC) systems have been developed by mimicking the biochemical characteristics of natural APCs.^{54–58} One such system is magnetic microbeads (Dynabead®) coated with T cell stimulatory ligands—anti-CD3 and anti-CD28 antibodies (aCD3/28 Abs), which are now used as a standard T cell activation platform for clinical manufacturing of CAR-T cells.¹⁵⁰ However, the Dynabead® system is still far from a natural APC, and efforts have been focused on integrating more physiological features in aAPC systems. For example, instead of endogenous supplementation in the culture medium, interleukin-2 (IL-2) has been loaded into biodegradable artificial APCs to mimic the autocrine secretion of T cell growth factor from DCs during priming of T cells.⁵⁸

Besides biochemical features, DCs possess unique biomechanical characteristics^{151,152} and establish intensive mechanical interactions with T cells for activation of T cells.^{13,153,154} Along with a growing understanding of DCs' biomechanics, biomechanical cues are gaining more and more attention in designing an effective aAPC system.^{76,115,116,121} For example, elliptical microparticles induced substantially higher expansion of functional T cells than spherical counterparts presenting the same amount of stimulatory ligands.¹¹⁵ A recent report also demonstrated that stimulatory ligand-coated nanowires on the flat substrate could stimulate stronger T cell expansion than a smooth surface.¹⁵⁵ Interestingly, when DCs undergo maturation, their cell morphology changes to a dendritic shape with multiple protrusions reaching out for interactions with T cells.¹⁰³ Although this transformation in cell morphology of DCs has been observed for decades, it is still unclear if such dendritic morphology contributes to T cell activation and proliferation.

Here, we fabricated a spiky titanium dioxide (TiO₂) microparticle system coated with aCD3/28 Abs to mimick the dendritic structure of DCs for activation and expansion of T cells (Fig. 2:1). The aCD3/28-coated spiky microparticle significantly expanded more functional CD8⁺ T cells skewed to effector phenotype (CD62L⁻CD44⁺) than its smooth counterpart. F-actin polymerization in T cells contributed to enhanced T cell expansion upon spiky microparticle stimulation (Fig. 2:1), indicating that cellular forces are involved in such enhancement. Our study thus offers a new biomechanical parameter, spiky structure, to optimize current aAPC systems for ex vivo expansion of functional T cells and has the potential to improve clinical manufacturing of ACT therapy (e.g., CAR-T cell therapy) for cancer patients.

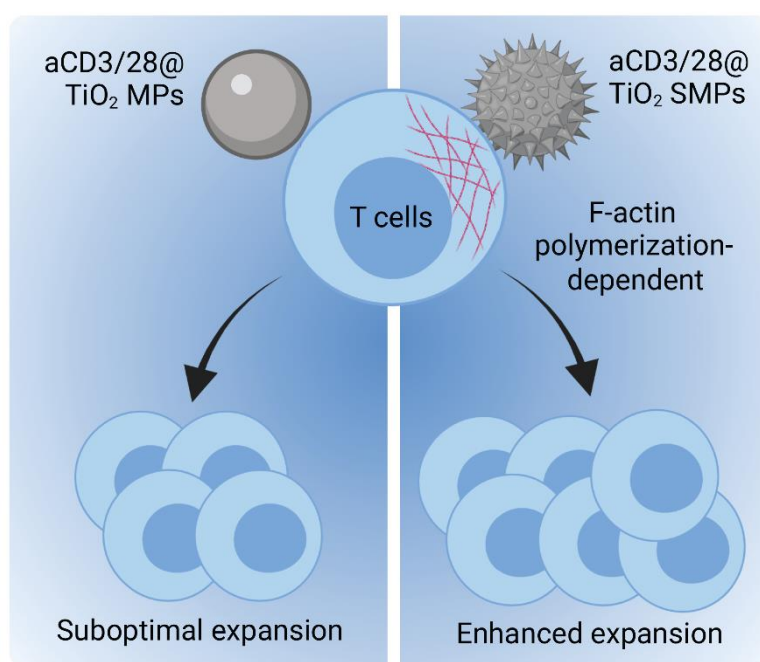


Figure 2:1 Schematic of enhancing T cell expansion with anti-CD3/28 antibody-coated spiky TiO₂ microparticles (aCD3/28@TiO₂ SMPs).

aCD3/28@TiO₂ SMPs promote T cell expansion through F-actin polymerization compared to its smooth counterpart (aCD3/28@TiO₂ MPs).

2.3 Results

2.3.1 Fabrication and characterization of aCD3/28-coated spiky TiO₂ microparticles

TiO₂ is biologically inert so that it provides a good platform to study the effect from morphology independently.¹⁵⁶ We first synthesized spiky TiO₂ microparticles (TiO₂ SMPs) using a well-established wet chemical method.¹⁵⁷ The spiky structure was formed by hydrolysis and oxidation of TiCl₃ at 90 °C. The obtained TiO₂ SMPs were examined with transmission electron microscopy (TEM) to display a dendritic shape with multiple nanospikes on the particle surface (Fig. 2:2a, b). The hydrodynamic diameter and zeta-potential of TiO₂ SMPs were $2.45 \pm 0.04 \mu\text{m}$ and $-20.1 \pm 1.3 \text{ mV}$, respectively (Fig. 2:2c). To generate smooth microparticles (TiO₂ MPs) for comparison, spiky microparticles were sonicated for 15 h to remove nanospikes on the surface. The surface morphology of smooth microparticles was confirmed with TEM imaging (Fig. 2:2c). The hydrodynamic diameter and zeta-potential of TiO₂ MPs were $2.10 \pm 0.03 \mu\text{m}$ and $-24.0 \pm 1.5 \text{ mV}$ (Fig. 2:2c), respectively, which were comparable to TiO₂ SMPs.

To provide stimulatory signals for T cell activation, aCD3/28 antibodies at a molar ratio of 1:1 were physically adsorbed on the surfaces of TiO₂ SMPs and MPs through hydrophobic interactions (denoted as aCD3/28@TiO₂ SMPs and MPs, respectively). The adsorption efficiency was evaluated by measuring aCD3/28 antibody concentration left in the solution. A similar surface density of aCD3/28 antibodies was achieved on aCD3/28@TiO₂ SMPs and MPs (100 and 110 $\mu\text{g}/\text{mg}$, respectively) (Fig. 2:2c). In addition, aCD3/28@TiO₂ SMPs and MPs displayed similar hydrodynamic diameter and zeta-potential values (Fig. 2:2c).

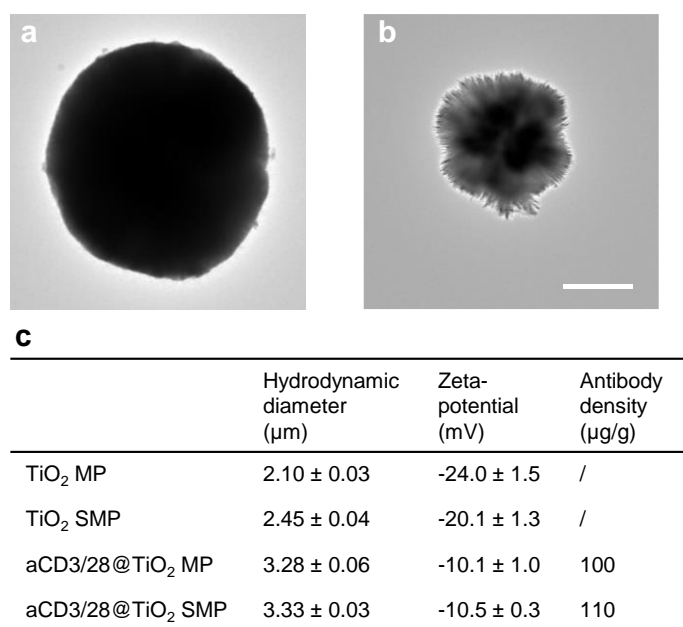


Figure 2:2 Characterization of smooth and spiky TiO₂ microparticles (TiO₂ MP and SMP) and their anti-CD3/28 antibody-coated counterparts (aCD3/28@TiO₂ MP and SMP).

(a, b) Transmission electron microscopy (TEM) images of TiO₂ MP (a) and SMP (b). Scale bar, 500 nm. (c) Summarized physicochemical properties of TiO₂ MP and SMP, and aCD3/28@TiO₂ MP and SMP. Data are mean \pm s.d.

2.3.2 Ex vivo expansion of Pmel splenocytes with aCD3/28-coated spiky microparticles

We first used aCD3/28@TiO₂ SMPs to stimulate splenocytes from Pmel mice, a transgenic mouse strain with rearranged TCRs on CD8⁺ T cells specific to human gp100₂₅₋₃₃ epitopes (hgp100). Splenocytes consist of different cell populations, including T lymphocytes, B lymphocytes, DCs, and macrophages. To compare aCD3/28@TiO₂ SMPs with natural APCs such as DCs and macrophages, we pulsed splenocytes with various concentrations of hgp100 peptide (0.01, 0.1, and 1 μ M) to stimulate hgp100-specific CD8⁺ T cells within the splenocytes for 4 days. As shown in Fig. 2:3, pulsing splenocytes with hgp100 promoted CD8⁺ T cell activation and expansion (Fig. 2:3a). The expansion efficiency depended on hgp100 pulsing concentration, where a negative correlation was observed possibly due to overactivation of T cells at high pulsing concentration evidenced by highly upregulated PD-1 expression on T cells (Fig. 2:3b). Specifically, pulsing splenocytes with 0.01 μ M hgp100 induced optimal CD8⁺ T cell expansion (~7.6-fold compared to day 0). We next co-cultured splenocytes with aCD3/28@TiO₂ SMPs. After stimulation with aCD3/28@TiO₂ SMPs in the presence of IL-2 for 4 days, CD8⁺ T cells in Pmel splenocytes were preferentially expanded (~90% at day 4), and around 6.7-fold CD8⁺ T cell expansion was achieved (Fig. 2:3c and Fig 2:6a). These results suggest that aCD3/28@TiO₂ SMPs show potential to reach similar potency as natural APCs in activation and expansion of T cells.

We next compared aCD3/28@TiO₂ SMPs with the standard aAPC system-aCD3/28-coated Dynabead[®]. Interestingly, aCD3/28@TiO₂ SMPs outperformed aCD3/28-coated Dynabead[®], which just achieved around 5.6-fold CD8⁺ T cell expansion using the manufacturer's recommended procedure (Fig. 2:3a). On the other hand, the smooth counterpart-aCD3/28@TiO₂ MPs induced around 5.9-fold CD8⁺ T cell expansion in the same experiment (Fig. 2:3a), which was similar to aCD3/28-coated Dynabead[®]. In addition, PD-1 level, an T cell activation marker, was highly upregulated in CD8⁺ T cells stimulated by aCD3/28@TiO₂ SMPs versus aCD3/28@TiO₂ MPs (Fig. 2:3b). Moreover, aCD3/28@TiO₂ SMP-expanded CD8⁺ T cells displayed lower percentage of naive phenotype (CD62L⁺CD44⁻) and were skewed to effector phenotype (CD62L⁻CD44⁺) rather than effector memory phenotype (CD62L⁺CD44⁺) as compared to CD8⁺ T cells expanded by aCD3/28@TiO₂ MPs (Fig. 2:3d). It is worth noting that no expansion and PD-1 upregulation of CD8⁺ T cells was observed in TiO₂ SMP or MP only groups (Fig. 2:3a, b), suggesting that TiO₂ SMP or MP itself was biologically inert and did not stimulate T cell activation. Taken together, the results indicate that spiky structure provides additional stimulatory signals to promote T cell activation and expansion and preferentially expand effector CD8⁺ T cells.

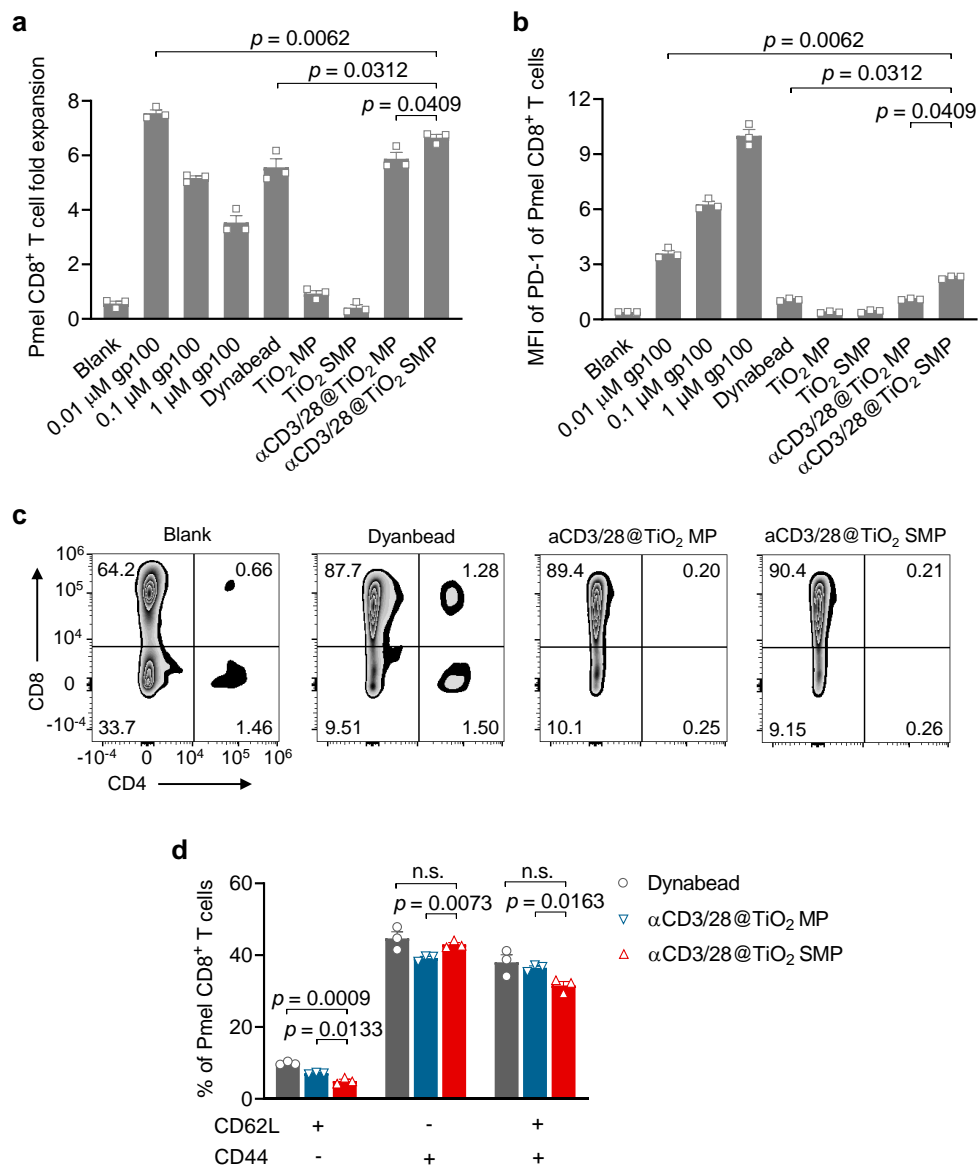


Figure 2:3 Ex vivo expansion of T cells in Pmel splenocytes with aCD3/28@TiO₂ SMPs.

(a-d) Pmel splenocytes were cultured in the indicated conditions for 4 days. Fold expansion (a), PD-1 level (b), and CD62L/CD44 phenotype (d) of Pmel CD8⁺ T cells at day 4. (b) Representative flow cytometry plots presenting populations of CD4⁺ and CD8⁺ T cells at day 4. Numbers within the plots represent the percentages of each fraction. *P* values were determined by unpaired Student's *t* test. Error bars represent standard error of the mean (SEM). MFI, mean fluorescence intensity; n.s., not significant.

2.3.3 Ex vivo expansion of Pmel CD8⁺ T cells with aCD3/28-coated spiky microparticles

As abovementioned, splenocytes have a complex composition that may indirectly contribute to the activation and expansion of T cells. To specifically study the CD8⁺ T cell activation and expansion, we isolated CD8⁺ T cells from Pmel splenocytes to perform the experiments. The isolated Pmel CD8⁺ T cells had a high purity of ~93% (Fig. 2:6b). To track the cell division, we stained Pmel CD8⁺ T cells with CFSE before co-culture with corresponding systems (Fig. 2:4a). Soluble aCD3/28 antibodies provided marginal stimulation, which is consistent with previous results. The stimulation with aCD3/28@TiO₂ SMPs for 3 days promoted higher CD8⁺ T cell expansion (~2.6-fold) and PD-1 expression of CD8⁺ T cells

as compared to its smooth counterpart (~2-fold) or aCD3/28-coated Dynabead® (~1.5-fold) (Fig. 2:4b, c). In the meantime, Pmel CD8⁺ T cells stimulated by aCD3/28@TiO₂ SMPs demonstrated a faster rate of cell division, evidenced by a higher proliferation index derived from the CFSE dilution plot (Fig. 2:4a, b). Among the expanded T cells, the effector phenotype (CD62L^{low}CD44^{high}) was substantially enriched in the aCD3/28@TiO₂ SMPs group (Fig. 2:3d, e). These results further confirm that aCD3/28@TiO₂ SMPs present stronger stimulation to specifically expand effector CD8⁺ T cells compared to its smooth counterpart.

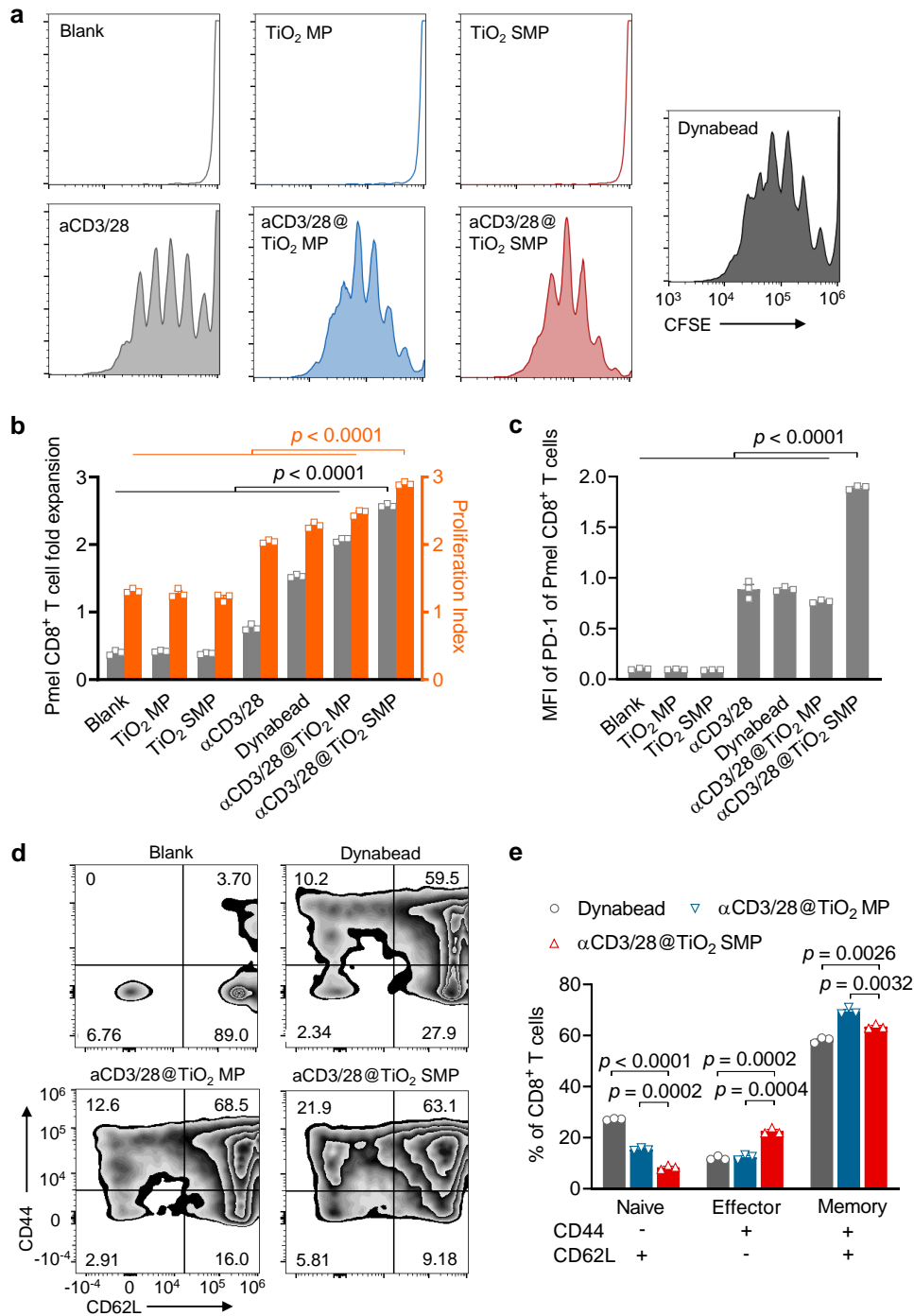


Figure 2:4 Ex vivo expansion of Pmel CD8⁺ T cells with aCD3/28@TiO₂ SMPs.

(a-e) Pmel CD8⁺ T cells were cultured in the indicated conditions for 3 days. (a) Representative flow cytometry histograms of CFSE dilution of CD8⁺ T cells at day 3. Numbers within the plots represent the percentages of each fraction. (b, c, e) The fold expansion (b), PD-1 level (c), and CD62L/CD44 phenotype (e) of Pmel CD8⁺ T cells at day 3. (d) Representative flow cytometry plots presenting CD62L/CD44 phenotypes of CD8⁺ T cells at day 3. Numbers within the plots represent the percentages of each fraction. *P* values were determined by unpaired Student's *t* test. Error bars represent standard error of the mean (SEM). MFI, mean fluorescence intensity; n.s., not significant.

2.3.4 Ex vivo expansion of polyclonal CD3⁺ T cells with aCD3/28-coated spiky microparticles

In the clinical manufacturing of CAR-T cell therapy, the whole polyclonal CD3⁺ T lymphocyte population is isolated from the patient's peripheral blood mononuclear cell (PBMC) for subsequent activation and expansion. To test aCD3/28@TiO₂ SMPs in a similar scenario, we isolated CD3⁺ T cells from spleens of wildtype (WT) C57BL/6J mice for ex vivo expansion experiments. The isolated WT CD3⁺ T cells were composed of ~38% CD8⁺ T cells and ~55% CD4⁺ T cells (Fig. 2:6c). In addition, to better adjust the surface density of stimulatory ligands, we fabricated neutravidin-coated TiO₂ SMPs and MPs (denoted NA@TiO₂ SMPs and MPs) using a similar physical adsorption procedure. The surface density of neutravidin was similar on NA@TiO₂ SMPs and MPs (110 µg/mg and 120 µg/mg, respectively). The biotinylated aCD3/28 antibodies were then anchored on NA@TiO₂ SMPs or MPs via biotin/neutravidin interactions (denoted as aCD3/28-NA@TiO₂ SMPs or MPs, respectively).

aCD3/28-NA@TiO₂ SMPs or MPs with various aCD3/28 antibody densities (0.1, 1, and 10 µg/mL according to final concentrations in co-culture systems) were co-cultured with CD3⁺ T cells in the presence of IL-2 for 3 days. Both aCD3/28-NA@TiO₂ SMPs and MPs preferentially expanded CD8⁺ T cells over CD4⁺ T cells (Fig. 2:5a, b). At low aCD3/28 antibody density (0.1 and 1 µg/mL), the spiky structure did not provide any additional advantage in expanding CD8⁺ or CD4⁺ T cells compared to its smoothness counterpart. However, aCD3/28-NA@TiO₂ SMPs substantially promoted expansion of CD8⁺ and CD4⁺ T cells at high aCD3/28 antibody density (10 µg/mL) (Fig. 2:5a, b). Moreover, at high aCD3/28 antibody density (10 µg/mL), a higher percentage of naïve T cells were activated and showed a trend to develop into effector phenotype (CD62L⁻CD44⁺) in aCD3/28-NA@TiO₂ SMPs group (Fig. 2:5c, d). It suggests that spiky structure promotes T cell activation and expansion only when sufficient stimulatory ligands are provided.

Finally, we tried to figure out possible mechanisms underlying enhanced CD8⁺ T cell activation by spiky structure. According to previous studies, the spiky structure could generate mechanical stress on the plasma membrane of DCs or macrophages, which triggers K⁺ efflux through mechanosensitive channels inducing an inflammatory response. It motivated us to examine biomechanical aspects of T cell/spiky structure interactions. First of all, we treated T cells with a F-actin polymerization inhibitor, Cytochalasin D (CytoD), to inhibit T cell force generation. Indeed, when T cell force was inhibited, the enhanced activation and expansion of CD8⁺ T cells by spiky structure were eliminated (Fig. 2:5e), suggesting that T cell force is essential in such enhancement. In addition, T cell force inhibition showed no influence on T cell expansion stimulated by soluble aCD3/28 antibodies (Fig. 2:5e), which were supposed to activate T cells without creating mechanical stress. Next, we checked if mechanosensitive channels are involved in this process. Piezo 1 and TRPV4 are two important mechanosensitive channels expressed on T lymphocytes^{158,159} and have been shown to be important in mechanical stress-induced Ca²⁺ influx in immune cells.^{159,160} We then co-cultured CD8⁺ T cells with corresponding systems in the presence of a Piezo1 inhibitor (GdCl₃) or a TRPV4 inhibitor (HC-067047). Both inhibitors suppressed CD8⁺

T cell expansion in all the groups (Fig. 2:5e). Interestingly, the spiky structure still promoted CD8⁺ T cell activation and expansion in the presence of GdCl₃ or HC-067047 (Fig. 2:5e), indicating that Piezo1 and TRPV4 were not involved in enhanced CD8⁺ T cell activation by spiky structure.

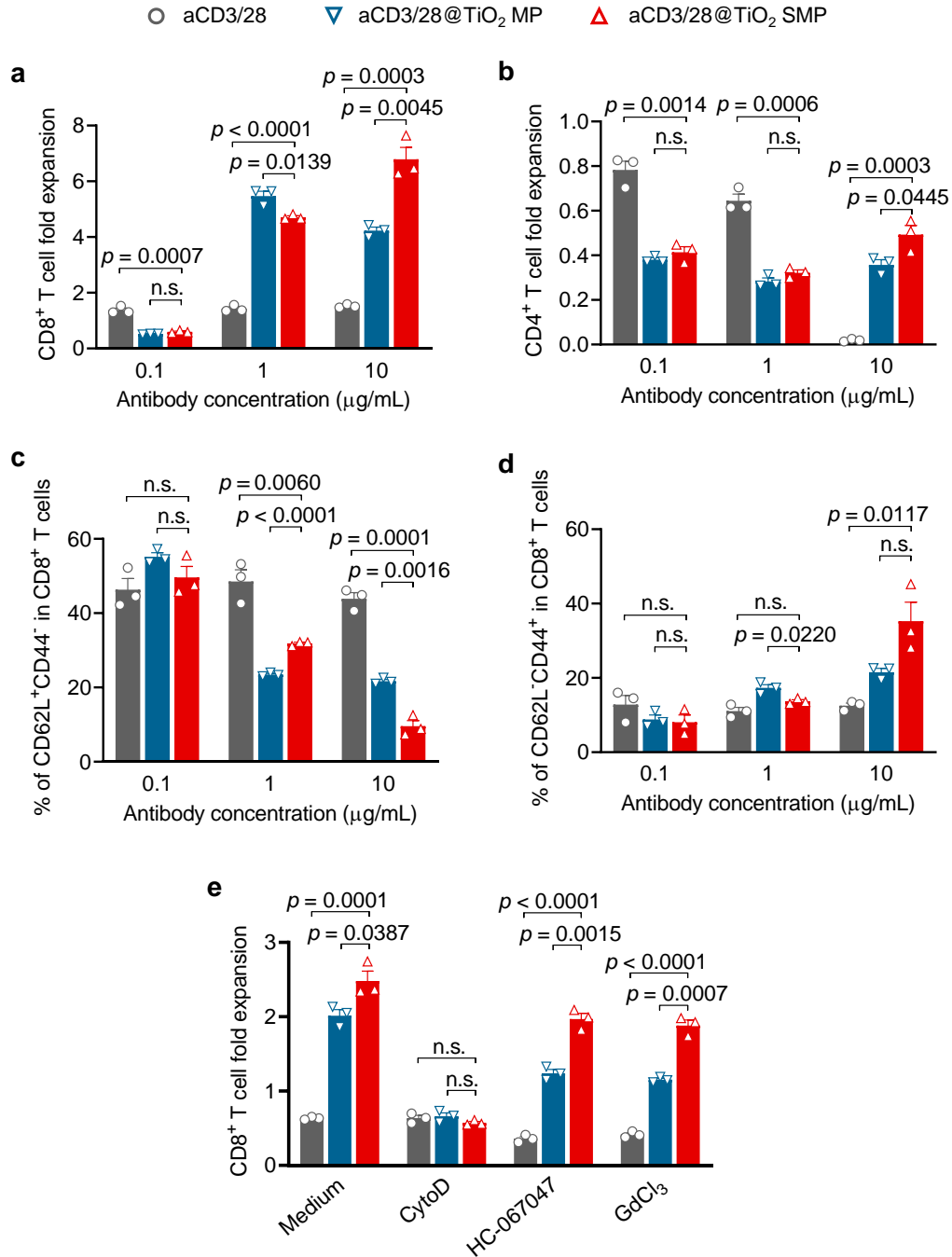


Figure 2:5 Ex vivo expansion of polyclonal CD3⁺ T cells with aCD3/28@TiO₂ SMPs.

(a-d) Polyclonal CD3⁺ T cells were cultured in the indicated conditions for 3 days. Shown are fold expansion (a), CD62L⁺CD44⁻ (naive) percentage (c), and CD62L⁻CD44⁺ (effector) percentage (d) of CD8⁺ T cells and fold expansion of CD4⁺ T cells (b) at day 3. (e) Polyclonal CD3⁺ T cells were co-cultured soluble aCD3/28 antibodies, aCD3/28@TiO₂ SMPs, or aCD3/28@TiO₂ SMPs in the presence of indicated reagents for 3 days. P values were determined by unpaired Student's t test. Error bars represent standard error of the mean (SEM). CytoD, cytochalasin D; n.s., not significant.

2.4 Conclusion

In summary, we synthesized an aCD3/28-coated spiky TiO₂ microparticle resembling the unique dendritic shape of DCs. The spiky structure mimicking dendritic morphology substantially enhanced CD8⁺ T cell activation and expansion of effector phenotype via T cell force-dependent mechanism. The enhanced activation and expansion were achieved in both antigen-specific and polyclonal CD8⁺ T cells. The following studies should evaluate if effector T cells expanded by aCD3/28@TiO₂ SMPs generate a similar or even better anti-cancer response in vivo compared to those stimulated by the standard Dynabead[®] system.

To study the effect of spiky structure independently, here we controlled similar aCD3/28 coating amount per mg particle on spiky (100 µg/mg) and smooth (110 µg/mg) microparticles. Theoretically, the spiky microparticle should have a higher surface area than its smooth counterpart, which results in a lower antibody density per surface area on the spiky microparticle. A lower antibody surface density usually induces less T cell activation.¹³ For this reason, the enhanced T cell proliferation by the spiky structure is unlikely due to the difference in antibody surface densities between spiky and smooth microparticles. It has been shown that the spiky structure on microparticles would enhance electrostatic interactions with the surrounding microenvironment.¹⁶¹ However, similar Zeta-potentials were noticed on aCD3/28-coated spiky (-10.5 ± 0.3 mV) and smooth (-10.1 ± 1.0 mV) microparticles, suggesting no significant difference in surface charges between two microparticles.

We provided evidence to show that F-actin polymerization plays a key role in enhanced T cell activation and expansion by spiky structure. Surprisingly, the important mechanosensitive channels on T cells such as Piezo 1 and TRPV4 did not contribute to such enhancement. In particular, Piezo 1 is critical in optimal T cell activation¹⁵⁸ and has been exploited to control genetic circuits such as CAR expression using ultrasound-induced mechanical forces.¹⁴⁷ It implies that intracellular mechanosensors may be acting an important role here. Recently, one study revealed that T cells sense the mechanical environment via yes-associated protein (YAP),¹⁰¹ a well-known intracellular mechanosensor for environmental mechanics such as ECM stiffness.¹⁶² Intriguingly, YAP is a negative regulator of T cell activation by inhibiting the nuclear translocation of NFAT1, an important transcription factor regulating T cell effector responses such as IL-2 production.¹⁰¹ In addition, it has been shown that F-actin polymerization downregulates YAP phosphorylation and promotes its nuclear translocation for subsequent transcription activity.¹⁶² For future studies, it is interesting to investigate the possible role of YAP in enhanced T cell activation by spiky structure.

Although aCD3/28@TiO₂ SMPs outperformed the standard Dynabead[®] system in activating and expanding T cells, there is still room for optimization to reach similar potency as natural APCs. A possible direction is to optimize the particle size of TiO₂ SMPs. The particle size of aAPC has a positive impact on T cell activation according to a recent study.⁷⁸ Specifically, particles with a diameter of ~4.5 µm induced significantly higher T cell activation and expansion than particles with smaller sizes (0.3 and 0.8 µm).⁷⁸ The standard Dynabead[®] system has an average particle diameter of ~4.5 µm, which fits into the optimal size for T cell activation. It is noted that the particle size of TiO₂ SMPs used in the current study was around 1 µm. Thus, increasing particle size may further enhance the potency of aCD3/28@TiO₂ SMP system. Besides, particle stiffness is another important parameter to optimize aAPCs for activation of T cells. Several studies showed that 100 kPa is an optimal stiffness value to stimulate T cell activation on polydimethylsiloxane (PDMS) substrates.^{97,104} In

contrast, TiO_2 is an extremely stiff material of hundreds of GPa, which is out of range of physiological stiffness. In future studies, fabricating a softer spiky particle system offers opportunities to achieve higher T cell activation and expansion efficiency.

Besides efficient ex vivo expansion, another important aspect in clinical manufacturing of ACT therapy is the separation of effector T cells from aAPCs to avoid any adventitious effects from impurity when infused back into the patients. The standard Dynabead® system is super-paramagnetic, which can be easily removed from the expanded T cells with a magnetic field.¹⁵⁰ In the current study, we focused on investigating the fundamental question if spiky morphology contributes to T cell activation. Therefore, we chose biologically inert TiO_2 SMPs without incorporating magnetic components into the system. Nevertheless, multiple magnetic spiky microparticle systems are available in various reports,^{163–165} and provide possibilities to develop spiky aAPCs that can be easily separated from the expanded T cells using a magnetic field.

Overall, a novel biomechanical cue, spiky structure, is identified to promote T cell activation and expansion. It holds promise to be incorporated into current standard aAPC systems to improve efficiency and consistency in producing ACT products for clinical applications such as cancer treatment.

2.5 Supplementary materials

2.5.1 Experimental methods

Chemicals and reagents. Sodium chloride (NaCl), 4',6-diamidino-2-phenylindole dihydrochloride (DAPI), and bovine serum albumin (BSA) were purchased from Sigma-Aldrich (St. Louis, MO, USA). Titanium trichloride (TiCl_3 , 20 w/v% aqueous solution in 2N hydrochloric acid) and NH_4OH solution (28.0–30.0%) were obtained from Acros Organics (Fisher Scientific, Waltham, MA, USA). Neutravidin, EZ-Link™ NHS-Biotin, and CellTrace™ CFSE cell proliferation kit were purchased from Thermo Fisher Scientific (Waltham, MA, USA). Human gp100_{25–33} (hgp100) peptide was purchased from GenScript (Piscataway, NJ, USA). Recombinant mouse interleukin-2 (IL-2) was purchased from PeproTech (London, UK). Anti-mouse CD3 antibody (clone 17A2) and anti-mouse CD28 antibody (clone 37.51) were purchased from Bioxcell (West Lebanon, NH, USA). Fluorescent-labelled anti-CD8 (YTS156.7.7), anti-CD4 (RM4-5), anti-PD-1 (29F.1A12), anti-CD44 (IM7), and anti-CD62L (MEL-14) antibodies were purchased from Biolegend (San Diego, CA, USA). All products were used as received.

Animals. All the mouse studies were approved by the Swiss authorities (Canton of Vaud, animal protocol ID 3206 and 3533) and performed in accordance with EPFL CPG guidelines. Six- to eight-week-old female C57Bl/6 (C57BL/6J) mice were purchased from Charles River Laboratories (Lyon, France). T cell receptor (TCR)-transgenic pmel-1 (Pmel) mice (B6.Cg-*Thy1*^a/Cy Tg(Tcr α Tcr β)8Rest/J) were purchased from The Jackson Laboratory (Bar Harbor, ME, USA) and maintained in the animal facility at EPFL.

Synthesis of TiO_2 spiky microparticles and their surface modifications. In a typical synthetic procedure, TiCl_3 (10 mL, Acros, 20% aqueous solution) was dissolved in deionized water (200 mL) in a glass bottle (500 mL), and then NaCl (1

mol) was added to the solution under constant stirring. The color of this solution was violet, and the pH was adjusted by adding NH_4OH solution (1.0 mL, ~25%). Afterward, the glass bottle was sealed and maintained at 90 °C for 6 h, after which the system was allowed to cool to room temperature naturally. The obtained precipitates were washed with deionized water and ethanol several times and then dried at 50 °C for 24 h.

To coat microparticle surface with aCD3/CD28 antibodies, the TiO_2 MPs or SMPs (500 μg) were suspended in aCD3/CD28 antibodies (w/w = 1:1) solution in PBS (500 μL , 1 mg/mL). The suspension was gently stirred at room temperature for 1 h, followed by incubation at 4 °C for 4 h. Finally, the aCD3/28-coated TiO_2 MPs or SMPs (denoted as aCD3/28@ TiO_2 MPs or SMPs) were obtained by centrifuging the solution at a rate of 8000 rpm for 2 min. The precipitate was washed with PBS solution twice. The concentration of antibodies in the supernatant was measured with a microvolume spectrophotometer (NanoDrop, Thermo Fisher Scientific) to determine the amount of antibodies coated on the microparticle surface. A similar procedure was performed to coat neutravidin on the surface of TiO_2 MPs or SMPs.

Characterizations of spiky microparticles. The sizes and zeta-potentials of TiO_2 MPs and SMPs, and aCD3/28@ TiO_2 MPs and SMPs were characterized by dynamic light scattering (DLS) with a Zetasizer NanoZS (Malvern, Worcester, UK). For size measurement, experiments were performed at 25 °C using a He-Ne laser (633 nm) and non-invasive backscatter optics. For zeta-potential measurement, the electrophoretic mobility measurements were performed at 25 °C using M3-PALS technology (Malvern). The transmission electron microscope (TEM) images of TiO_2 MPs and SMPs were obtained with the Tecnai Osiris (FEI, Hillsboro, OR, USA).

Biotinylated antibodies. NHS-Biotin (3 μL , 10 mM) solution in DMSO was added to anti-CD3, anti-CD28, or isotype antibody solution (2 mg/mL) in 100 μL of phosphate-buffered saline (PBS) (Gibco) at a final concentration of 300 μM of NHS-Biotin. After 30-min incubation on a shaker at 25 °C (800 rpm), the biotinylated antibody solution was washed with PBS (500 μL) using Amicon® ultra centrifugal filter with 30-kDa MWCO (Merck) (8,000 g, 5 min, $\times 5$). The final concentration of biotinylated antibodies was determined using a microvolume spectrophotometer (NanoDrop, Thermo Fisher Scientific). The biotinylated antibodies were stored at 4 °C before use.

Activation and expansion of T cells with spiky microparticles. Spleens collected from Pmel or WT C57BL/6J mice were ground through a cell strainer (70 μm , Fisher Scientific, Pittsburgh, PA, USA), and red blood cells were lysed with ACK lysing buffer (Gibco, 2 mL per spleen) at 25 °C for 5 min. After washing twice with PBS, splenocytes were collected and cultured in complete RPMI 1640 medium supplemented with FBS (10 v/v%), HEPES (Gibco, 1 v/v%), penicillin/streptomycin (1 v/v%), β -mercaptoethanol (Gibco, 0.1 v/v%), and recombinant mouse IL-2 (10 ng/mL) in the presence of hgp100 (0.01, 0.1 or 1 μM), aCD3/28@ TiO_2 MPs (50 $\mu\text{g}/\text{mL}$) or aCD3/28@ TiO_2 SMPs (50 $\mu\text{g}/\text{mL}$) for 4 days. For flow cytometry analysis, the expanded T cells were then stained with fluorescently labeled anti-CD8, anti-PD-1, anti-CD44, and anti-CD62L antibodies.

Pmel CD8⁺ or WT CD3⁺ T cells were isolated from Pmel or WT C57BL/6J splenocytes using CD8⁺ T cell or Pan T cell isolation kit (Miltenyi Biotec Inc., Bergisch Gladbach, Germany), respectively, according to the manufacturer's recommended protocol. The isolated Pmel CD8⁺ or WT CD3⁺ T cells were then cultured in complete RPMI 1640 medium supplemented with FBS (10 v/v%), HEPES (Gibco, 1 v/v%), penicillin/streptomycin (1 v/v%), β -mercaptoethanol (Gibco, 0.1

v/v%), and recombinant mouse IL-2 (10 ng/mL) in the presence of aCD3/28@ TiO₂ MPs or SMPs (50 µg/mL) for 3 days. The expanded T cells were then stained with fluorescently labeled anti-CD8, anti-CD4, anti-PD-1, anti-CD44, and anti-CD62L antibodies for flow cytometry analysis.

Statistical analyses. Statistical analyses were performed by using unpair t test in GraphPad Prism 9 software. Shown are mean ± s.e.m unless otherwise indicated. In all cases, two-tailed tests with *p* values of less than 0.05 were considered significant.

2.5.2 Supplementary figures

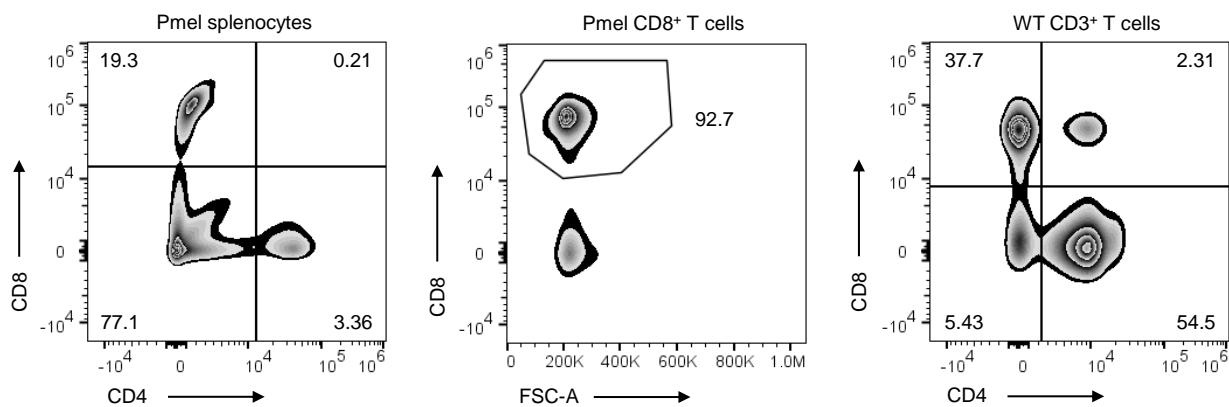


Figure 2:6 Phenotyping of Pmel splenocytes, Pmel CD8⁺ T cells, and wild-type (WT) CD3⁺ T cells.

Representative flow cytometry plots presenting populations of CD4⁺ or CD8⁺ T cells in indicated cell sources. Numbers within the plots represent the percentages of each fraction.

Chapter 3 Stiffening cancer cells enhances T cell mechanical forces and anti-tumor efficacy

Adapted from the article:

Lei, K., Kurum, A., Kaynak, M., Bonati, L., Han, Y., Cencen, V., Gao, M., Xie, Y.-Q., Guo, Y., Hannebelle, M.T.M., Wu, Y., Zhou, G., Guo, M., Fantner, G.E., Sakar, M.S., & Tang, L. Cancer-cell stiffening via cholesterol depletion enhances adoptive T-cell immunotherapy. *Nature Biomedical Engineering* 5, 1411-1425 (2021).

Contributions:

K.L. and L.T. conceived the study and designed the experiments. K.L., A.K., M.K., L.B., Y.H., V.C., M.G., Y.-Q.X., Y.G., M.T.M.H., Y.W., G.Z., M.G., G.E.F., and M.S.S. performed the experiments. K.L., A.K., L.T., M.S.S., M.G., and G.E.F. analyzed the data. L.T. supervised the project. K.L., A.K., and L.T. wrote the manuscript. All authors edited the manuscript.

3.1 Abstract

Malignancy and tumor progression are associated with cancer-cell softening. However, how cancer cell biomechanics affect T cell-mediated cytotoxicity and thus the outcome of adoptive T cell immunotherapies is unknown. Here, we show that T cell-mediated cancer-cell killing is hampered for cortically soft cancer cells, whose plasma membrane is enriched with cholesterol. Cancer-cell stiffening via cholesterol depletion augments T cell cytotoxicity and enhances the efficacy of adoptive T cell therapy against solid tumors in mice. We also show that the enhanced cytotoxicity against stiffened cancer cells is mediated by augmented T cell forces arising from an increased accumulation of filamentous actin at the immunological synapse and that cancer-cell stiffening has a negligible influence on T cell receptor signaling, the production of cytolytic proteins such as granzyme B, the secretion of interferon-gamma and tumor necrosis factor-alpha, and Fas-receptor–Fas-ligand interactions. Our findings reveal a mechanical immune checkpoint that could be targeted therapeutically to improve the effectiveness of cancer immunotherapies.

3.2 Introduction

Tumors employ certain immune inhibitory pathways, termed immune checkpoints, to evade anti-tumor immunity, particularly T cell-mediated cytotoxicity. Blockade of the ligand-receptor-based immune checkpoints using antibodies, such as anti-cytotoxic T lymphocyte-associated protein 4 (anti-CTLA-4) and anti-programmed cell death protein 1 (anti-PD-1) antibodies, can reactivate anti-tumor immunity and has led to remarkable clinical success in cancer immunotherapy.^{5,166} Identifying new checkpoints and blocking them with therapeutic interventions could potentially benefit patients broadly, especially those who fail to respond to current checkpoint blockade immunotherapies. Despite substantial efforts in seeking new checkpoints based on biochemical signals,^{167,168} potential inhibitory pathways involving biomechanical signals, such as target cell stiffness, remain largely unexplored. Although tumors are typically stiffer than the paired normal tissues due to the aberrant production and crosslinking of extracellular matrix proteins,¹⁰² individual cancer cells are generally softer than their non-malignant counterparts.¹⁶⁹ Cellular softness is a biomechanical characteristic correlated with the transformation, malignancy, and metastasis of cancer cells.^{170,171} The decrease in cancer cell stiffness has been shown to arise from softening of both cytoskeletal network¹⁷² and plasma membrane.¹⁷³ T cells directly interact with the target cell surface; thus, the mechanical properties of cell cortical structures, including the plasma membrane and the underlying actin cortex,¹⁷⁴ may impact cancer cell-T cell interactions. Nevertheless, the role of cancer cell stiffness in evading immunosurveillance remains elusive.

T cells not only sense mechanical environments^{77,85,97,101,124,147} but also exert forces at the immunological synapse to potentiate cytotoxicity against target cells.¹⁴ Cytoskeletal forces⁹⁵ and effector cytokine production⁸¹ are substantially reduced when T cells sense a soft substrate surface or soft target cells. Inspired by these observations, we hypothesized that cancer cells utilized cellular softness as a mechanical immune checkpoint to develop resistance toward T cell-mediated cytotoxicity by impairing T cell mechanical forces. Here, we show that cancer cells soften the cortical structure through cholesterol enrichment in the plasma membrane leading to evasion from T cell-mediated cytotoxicity in vitro and in vivo. The cortical stiffness of cancer cells could be augmented by depleting cholesterol in the membrane lipid

bilayer using methyl- β -cyclodextrin (Me β CD). Overcoming this mechanical immune checkpoint (target cell softness/T cell mechano-sensing axis) by stiffening cancer cells markedly improves the anti-tumor efficacy of adoptive T cell transfer (ACT) immunotherapy against solid tumors. We further provide evidence that the enhanced cytotoxicity against stiffened cancer cells is mediated by increased T cell forces but not known cytotoxic pathways based on biochemical signals.

3.3 Results

3.3.1 Cancer cells enrich cholesterol in the plasma membrane

We first explored how cancer cells soften their cortical structure. It has been reported that depleting cholesterol from the plasma membrane in endothelial cells increases cell cortical stiffness.^{175,176} These studies suggest that high membrane cholesterol level correlates with decreased cell stiffness. We, therefore, measured the cholesterol levels in murine and human tumor tissues as well as cells isolated from those tissues using Filipin III staining, a fluorescent dye that binds specifically to cholesterol.¹⁷⁷ Interestingly, in the B16F10 murine melanoma model, histological analysis showed that tumor tissues exhibited a substantially higher cholesterol level than the paired healthy tissues (Fig. 3:1a). In line with the results of histological studies, B16F10 tumors showed a 4.0 and 1.7-fold increase of global cholesterol levels compared to adjacent skin and muscle tissues, respectively, as quantified by an Amplex Red cholesterol assay (Fig. 3:1b). Cholesterol levels were also upregulated in several human tumor biopsies from various cancers, including small cell lung cancer, colon cancer, squamous cell lung cancer, and liver cancer (Fig. 3:9), suggesting a possible common signature of cholesterol dysregulation in diverse cancer types. Further, single-cell analyses by flow cytometry revealed that cancer cells in a 4T1 murine breast tumor (defined by tdTomato⁺) displayed a 2.9-fold greater amount of plasma membrane cholesterol compared to the tumor-infiltrating leukocytes (defined by CD45.2⁺) (Fig. 3:1c). In addition, EG7 cancer cells, a murine T lymphoma cell line, enriched 1.7-fold more cholesterol in the plasma membrane than normal murine T cells (Fig. 3:1d).

Next, we sought to tune the plasma membrane cholesterol level in order to control cell stiffness. Me β CD, a biocompatible compound widely used as a drug solubilizer in the clinic,¹⁷⁸ has been reported to scavenge cholesterol through host-guest interaction.¹⁷⁹ We, therefore, used Me β CD to extract membrane cholesterol from cancer cells. Upon Me β CD treatment at a concentration of 5 mM for 30 min, the membrane cholesterol level of B16F10 cancer cells dropped markedly to only 16.0% of the native state, whereas the intracellular cholesterol level showed much less alteration (Fig. 3:1e). Similarly, the membrane cholesterol level of cancer cells could be lowered down to 44% of the original level in vivo through a single intratumoral (i.t.) injection of Me β CD (Fig. 3:1f). In addition, supplementing the plasma membrane with cholesterol using a water-soluble cholesterol/Me β CD complex increased the membrane cholesterol level by 56% (Fig. 3:1e). Similarly, the plasma membrane cholesterol level was manipulated in various murine cancer cell lines including a murine lymphoma cell line expressing ovalbumin (EG7-OVA) and a murine colon cancer cell line (MC38), and a human melanoma cell line (Me275) (Fig. 3:1e and 3:10). Notably, these treatments showed no direct impact on the viability or apoptosis of the cancer cells (Fig. 3:11).

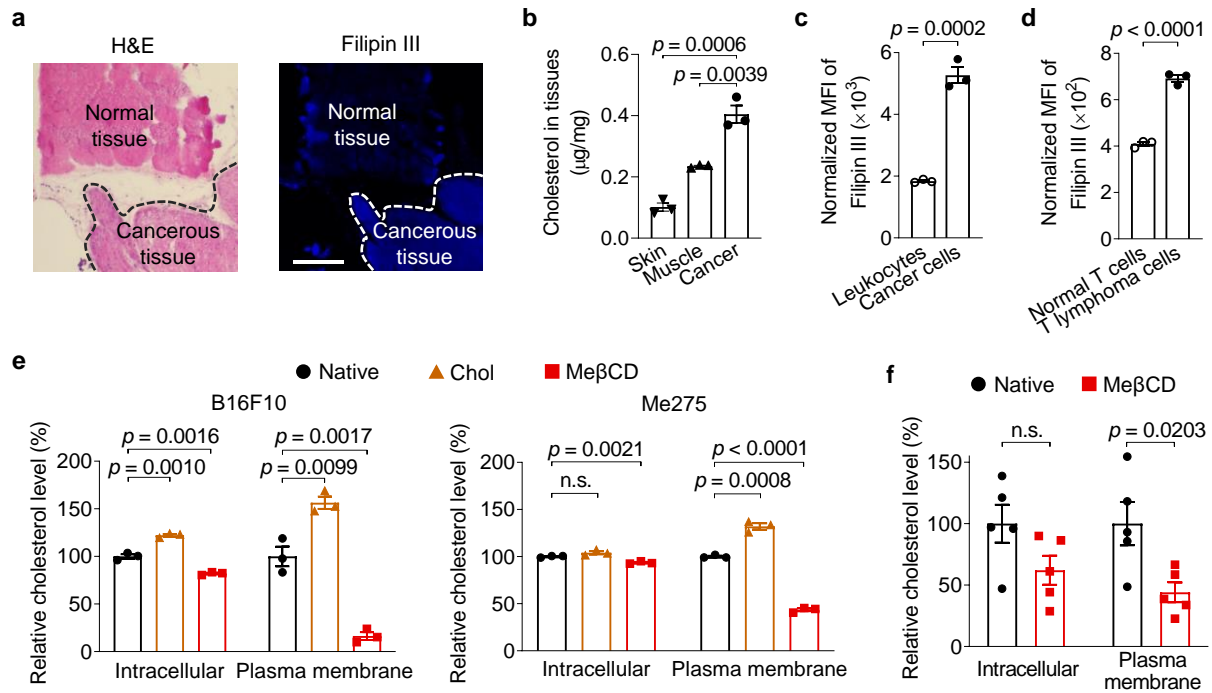


Figure 3:1 Cholesterol is enriched in the plasma membrane of cancer cells.

a, B16F10 tumor tissues (indicated with dash lines) and the adjacent normal tissues were stained with hematoxylin and eosin (H&E) and Filipin III (shown in blue color). Scale bar, 500 μ m. **b**, Cholesterol levels in B16F10 tumor tissues and the adjacent skin and muscle tissues ($n = 3$). **c**, **d**, Membrane cholesterol levels of tumor-infiltrating leukocytes (CD45.2⁺) and cancer cells (tdTomato⁺) in 4T1-Fluc-tdTomato tumor (**c**), and murine T lymphoma cells (EG7-OVA) and normal murine T cells (**d**) determined by Filipin III staining ($n = 3$). The displayed MFI values were normalized by the forward scatter area (FSC-A) of corresponding samples. **e**, **f**, Relative intracellular and plasma membrane levels of cholesterol (normalized to that of native cells) in murine B16F10 and human Me275 cancer cells treated with water-soluble cholesterol/methyl- β -cyclodextrin complex (Chol) or methyl- β -cyclodextrin (Me β CD) in vitro (**e**, $n = 3$) and in vivo (**f**, B16F10, $n = 5$). Data are one representative of at least two independent experiments with biological replicates. P values were determined by unpaired Student's t test. Error bars represent standard error of the mean (SEM). MFI, mean fluorescence intensity; n.s., not significant.

3.3.2 Controlling cancer cell stiffness by manipulating membrane cholesterol levels

To examine whether membrane cholesterol level indeed influences cell mechanical properties, we directly measured single-cell cortical stiffness using an atomic force microscope (AFM) (Fig. 3:2a).¹⁸⁰ We found that cholesterol-supplemented and -depleted B16F10 cancer cells exhibited 40% lower and 2.4-fold higher cortical stiffness, respectively, compared to the untreated cells (Fig. 3:2b). To confirm the results, we used another well-established technique to measure cell mechanics, optical tweezer,¹⁸¹ to probe the cortical stiffness of cancer cells (Fig. 3:2c). In line with AFM measurements, membrane cholesterol supplementation or depletion could markedly decrease or increase cortical stiffness of both murine B16F10 and human Me275 cancer cells (Fig. 3:2d). To investigate whether the results of single-cell measurements could be extrapolated to cell populations, we employed a recently reported high throughput microfluidic technique called deformability cytometry to measure cellular deformation (Fig. 3:12a-c), which is correlated with cellular stiffness (higher deformation correlates with lower stiffness, and vice versa).¹⁸² Murine B16F10 and human Me275 cancer cells showed markedly reduced cellular deformation after Me β CD treatment, suggesting increased cellular stiffness (Fig. 3:2e-g). In contrast, cholesterol supplementation in B16F10 or Me275 cancer cells increased cellular deformation (Fig. 3:2e-g). A similar trend was noted in various cancer cell types (Fig. 3:12d). These results provide evidence

that cholesterol enrichment in the plasma membrane contributes to cancer-cell softening, and cholesterol depletion via Me β CD treatment could increase cancer cell stiffness.

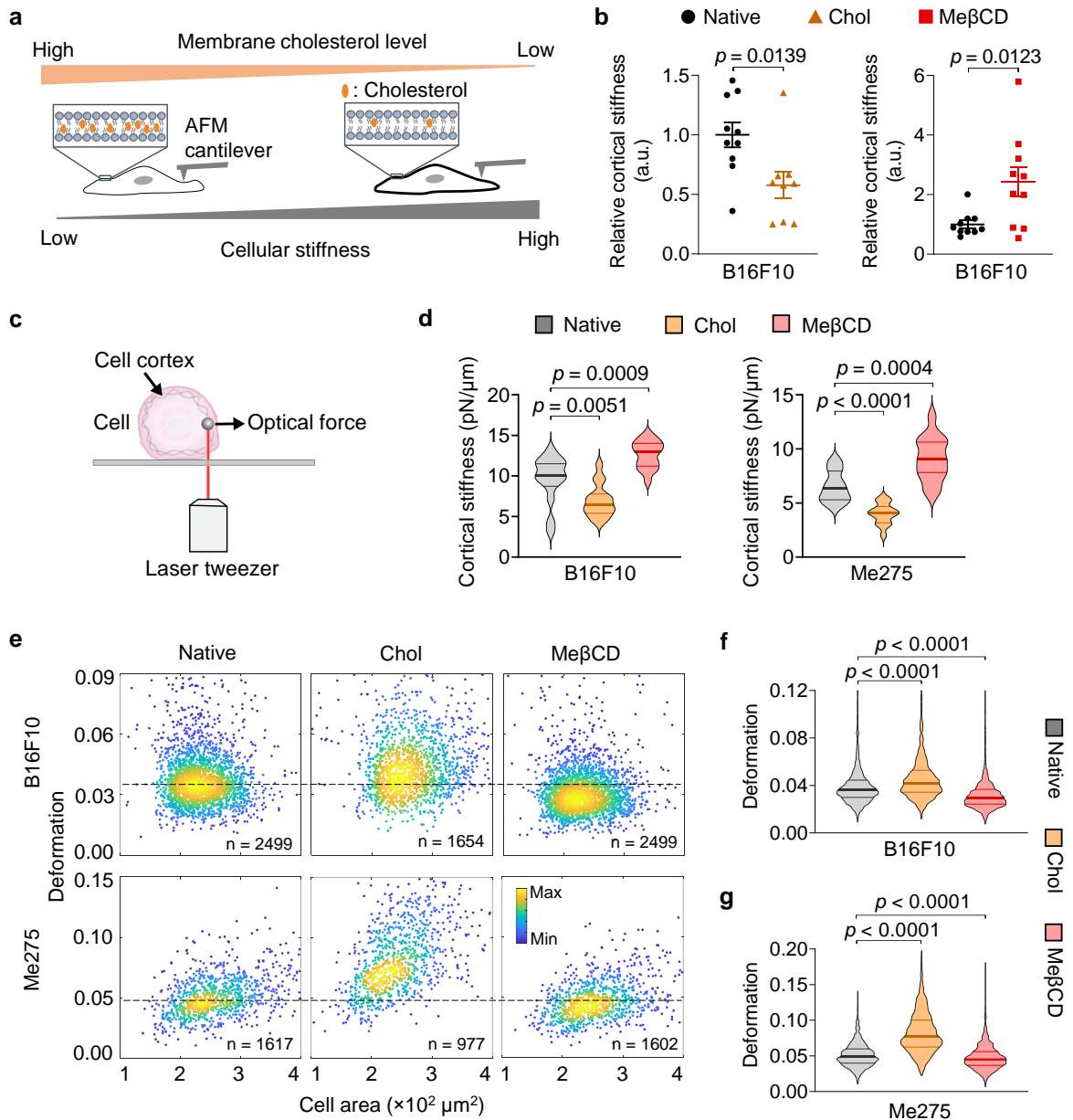


Figure 3:2 Cancer cell stiffness can be manipulated by supplementation or depletion of membrane cholesterol

a, Schematic illustration of the correlation between cellular stiffness and membrane cholesterol level. **b**, Relative cortical stiffness determined by nanoindentation measurements using atomic force microscopy (AFM) for native, Chol- or Me β CD-treated B16F10 cancer cells ($n = 9 \sim 10$ individual cells). Each data point is the average of at least twenty force curve measurements of a single cancer cell. Native B16F10 cancer cells serve as a standard (100%). Error bars represent SEM. **c**, Schematic illustration of the optical tweezer setting for cell cortical stiffness measurement. **d**, Cortical stiffness of native, Chol- or Me β CD-treated murine B16F10 and human Me275 cancer cells measured by the optical tweezer ($n = 14 \sim 17$ individual cells). **e-g**, Cellular deformation was measured using deformability cytometry to compare cellular stiffness in a high throughput manner. Shown are representative scatter plots (**e**; indicated are sample size, outliers not shown) and quantitative deformation of native, Chol- or Me β CD-treated murine B16F10 (**f**) and human Me275 (**g**) cancer cells. In all the violin plots (**d**, **f**, **g**), the middle solid line shows median, and lower and upper dash lines show 25th and 75th percentiles, respectively. P values were determined by unpaired Student's t test. a.u., arbitrary unit; n.s., not significant.

3.3.3 Cancer cell softness as a mechanical immune checkpoint impairs T cell-mediated cytotoxicity

We next investigated whether cellular softness imparted resistance to T cell-mediated cytotoxicity. As culture substrates influence cell biomechanics,¹⁰⁷ we first prepared polyacrylamide (PA) hydrogels of physiologically relevant Young's modulus as substrates mimicking the tumor mechanical microenvironment (Fig. 3:13, PA-1 and 2).¹⁸³ B16F10 cancer cells seeded on hydrogels with varying stiffness were co-cultured with activated Pmel CD8⁺ T cells—T cell receptor (TCR) transgenic T cells that can recognize the gp100 antigen in B16F10 cancer cells. In accordance with a recent report,¹⁴ lysis efficiency increased with higher substrate stiffness (Fig. 3:3a). When supplemented with exogenous cholesterol, B16F10 cancer cells seeded on a hydrogel substrate with stiffness of 143 kPa or a glass substrate (~ 3 GPa¹⁸⁴) survived in higher numbers compared to the native cells suggesting that softened cancer cells were more resistant to T cell-mediated cytotoxicity (Fig. 3:3a). To validate this observation in vivo, C57BL/6J mice bearing subcutaneous (s.c.) B16F10 tumors were administered with exogenous cholesterol through i.t. injections every other day (2 mg \times 8) (Fig. 3:14a). The increased cholesterol level in tumors dampened the anti-tumor efficacy of the adoptive transfer of Pmel CD8⁺ T cells (Fig. 3:14). Notably, cholesterol administration alone showed no effect on tumor growth or the survival rate of treated mice.

In order to achieve cancer cell-specific modulation of cholesterol levels in vivo, we first genetically engineered the B16F10 cancer cells by knocking down acyl-CoA:cholesterol acyltransferase 1 (ACAT1) (denoted as ACAT1 KD B16F10) (Fig. 3:15). ACAT1 is an enzyme specific for cholesterol esterification and has been utilized to control cell membrane cholesterol levels.^{185,186} We found that ACAT1 KD B16F10 cells enriched a 1.5-fold higher level of cholesterol in the plasma membrane as compared to the native B16F10 cells (Fig. 3:3b). Similar to the cholesterol-supplemented cells, ACAT1 KD B16F10 cells displayed lower stiffness (Fig. 3:3c, d) as well as increased resistance toward T cell-mediated killing (Fig. 3:3e) as compared to the native B16F10 cells. When there was no treatment, mice inoculated with ACAT1 KD B16F10 cells showed similar tumor progression as the native B16F10 tumor (Fig. 3:3f, g). However, ACT of Pmel CD8⁺ T cells was less effective in controlling ACAT1 KD B16F10 tumor growth as compared to the native B16F10 tumor (Fig. 3:3g), leading to reduced median survival of ACAT1 KD B16F10 tumor-bearing mice (Fig. 3:3h). Altogether, the results show that cancer cells present decreased cellular stiffness as a mechanically inhibitory pathway to evade T cell-mediated cytotoxicity in vitro and in vivo.

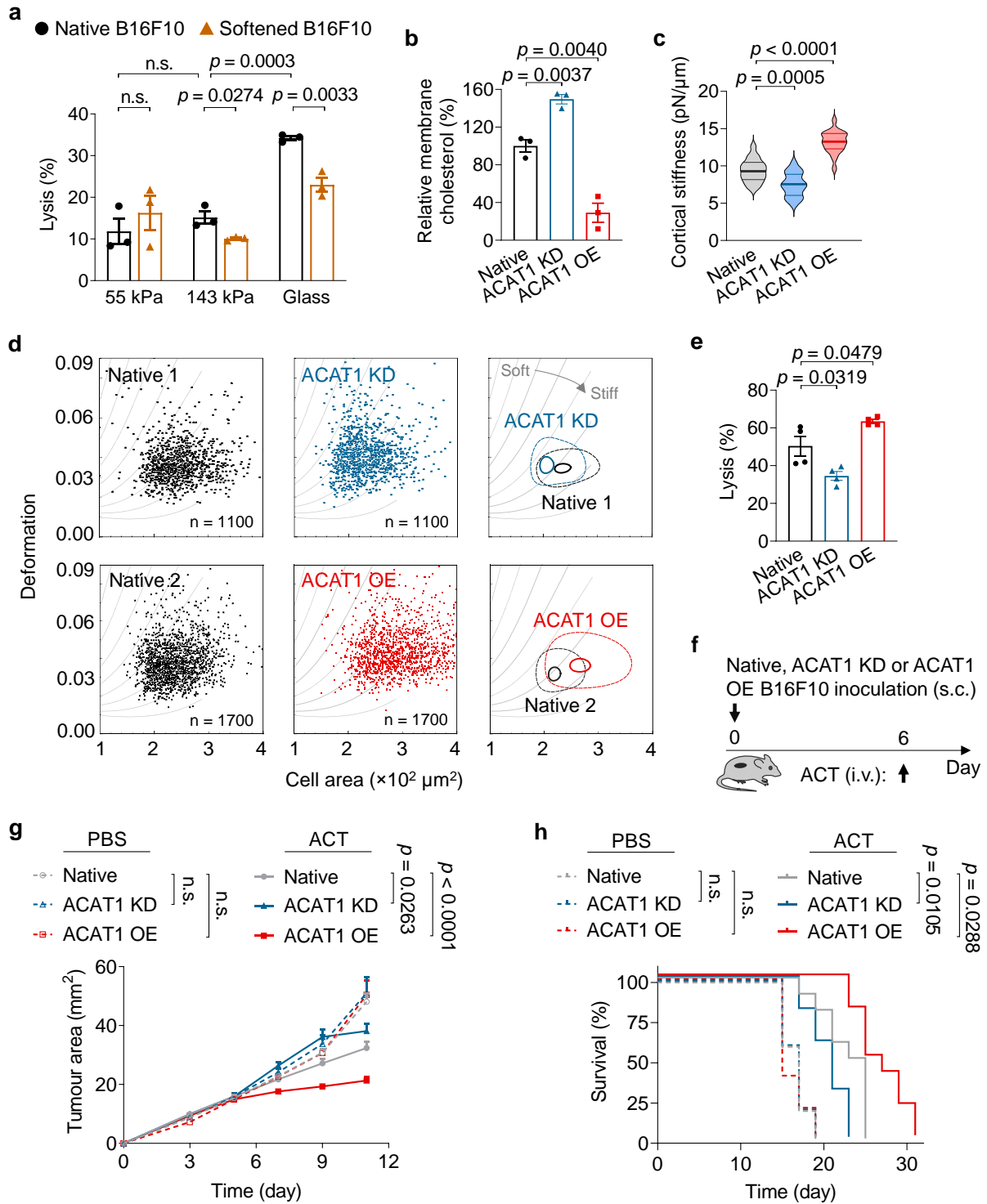


Figure 3:3 Cancer cell softness impairs T cell-mediated cytotoxicity in vitro and in vivo.

a, Lysis percentage of B16F10 cancer cells pre-treated with Chol (softened) or PBS (native) and co-cultured with activated Pmel CD8⁺ T cells at an effector:target (E:T) ratio of 10:1 for 5 h ($n = 3$). **b**, Relative membrane cholesterol levels of B16F10 cancer cells with ACAT1 knock-down (ACAT1 KD) and ACAT1 overexpression (ACAT1 OE) ($n = 3$). Native B16F10 cancer cells serve as a standard (100%). **c**, Cortical stiffness of native, ACAT1 KD, and ACAT1 OE B16F10 cells measured by the optical tweezer ($n = 19 \sim 21$ individual cells). In the violin plots, the middle solid line shows median, and lower and upper dash lines show 25th and 75th percentiles, respectively. **d**, Representative scatter plots for native, ACAT1 KD, and ACAT1 OE B16F10 cells by deformability cytometry analysis, and their 50%-density contour plots (the inner contours correspond to 95% event density) with iso-elasticity lines dividing the diagrams into areas of different stiffness. **e**, Lysis percentage of ACAT1 KD and ACAT1 OE B16F10 cancer cells after 5-h co-culture with Pmel CD8⁺ T cells at an E:T ratio of 10:1 ($n = 4$). Data are one representative of at least two independent experiments with biological replicates

(a, b, e). f-h, Mice bearing native, ACAT1 KD, or ACAT1 OE B16F10 tumors were treated with adoptive transfer of Pmel CD8⁺ T cells (5×10^6 per mouse), as outlined in the experimental scheme (f) (n = 5 and 10 animals for PBS- and ACT-treated groups, respectively). Shown are tumor growth curves (g) and survival curves (h) of pooled data from two independent experiments with biological replicates. *P* values were determined by unpaired Student's *t* test in (a-c, e), two-way ANOVA in (g), or log-rank test in (h). Error bars represent SEM. ACAT1, acyl-CoA:cholesterol acyltransferase 1; PBS, phosphate-buffered saline; ACT, adoptive cell transfer; s.c., subcutaneous; i.v., intravenous; n.s., not significant.

3.3.4 Cancer-cell stiffening enhances the efficacy of ACT therapies

We next investigated whether such a mechanical immune checkpoint can be overcome by stiffening cancer cells. We first prepared the ACAT1-overexpressing B16F10 cancer cells (denoted as ACAT1 OE B16F10) (Fig. 3:15), which showed a 70% lower membrane cholesterol level than that of native B16F10 cells (Fig. 3:3b). As measured by both optical tweezer and deformability cytometry, ACAT1 OE B16F10 cells with reduced membrane cholesterol levels were stiffer than the native B16F10 cells (Fig. 3:3c, d). Indeed, ACAT1 OE B16F10 cells displayed increased susceptibility toward T cell-mediated cytotoxicity compared to the native B16F10 cancer cells (Fig. 3:3e). To further test this hypothesis *in vivo*, we inoculated mice with ACAT1 OE B16F10 tumor, which exhibited a similar growth rate as the native B16F10 tumor. However, ACT of Pmel CD8⁺ T cells better controlled the ACAT1 OE B16F10 tumor compared to the native B16F10 tumor (Fig. 3:3f, g). Treated mice bearing ACAT1 OE B16F10 tumors also showed prolonged survival (Fig. 3:3h). In this proof-of-concept study, tumor cells were specifically stiffened, leading to enhanced susceptibility toward ACT therapy.

Based on these findings, we next sought to develop a potentially applicable therapeutic intervention to stiffen cancer cells for enhanced cancer immunotherapy. We found that B16F10 cancer cells treated with Me β CD maintained a low membrane cholesterol level up to 5 hours post-treatment (Fig. 3:16a). Further, cancer cells that were stiffened by Me β CD pre-treatment displayed considerably increased sensitivity to T cell-mediated killing on all three substrates of different stiffness (55 kPa, 143 kPa, and glass) (Fig. 3:4a). The enhanced lysis of stiffened cancer cells was most prominent on substrates closely mimicking the physiological mechanical environment in tumors (55 and 143 kPa).¹⁸³ Once the cholesterol level in the cancer cell membrane recovered to the native state after 12 hours (Fig. 3:16a), the enhancement of killing was abrogated (Fig. 3:16b). To further confirm the role of cancer cell stiffness, we used a cytoskeleton-based cell stiffening reagent, 4-hydroxyacetophenone (4-HAP),¹⁸⁷ to pretreat B16F10 cancer cells. We found that stiffening cancer cells using 4-HAP also significantly enhanced T cell-mediated killing (Fig. 3:17), confirming that cancer cell stiffness indeed contributes to their sensitivity to T cell-mediated cytotoxicity. Finally, to rule out the potential effects of a synthetic substrate, EG7-OVA, a suspension cancer cell line, was stiffened with Me β CD and found to exhibit similarly enhanced susceptibility to cytotoxicity mediated by OT-I TCR transgenic CD8⁺ T cells that recognize SIINFEKL epitope derived from OVA (Fig. 3:4b).

Next, we extended the stiffening strategy using Me β CD treatment to *in vivo* studies. C57BL/6J mice bearing s.c. B16F10 tumors were treated with an ACT of Pmel CD8⁺ T cells adjuvanted with an interleukin-15 super-agonist (IL-15SA, Fig. 3:18) along with or without daily administration of Me β CD (i.t., 1 mg \times 10) (Fig. 3:4c). ACT therapy supported by IL-15SA delayed the tumor growth but failed to achieve durable control of tumor progression in all treated mice. In contrast, the combination therapy of IL-15SA-supported ACT and cancer-cell stiffening intervention using Me β CD led to the complete eradication of 5 out of 12 tumors and durable cures in 41.7% of treated mice (Fig. 3:4d, e). Similarly, ACT plus

Me β CD treatment without IL-15SA also induced substantial tumor regression and prolonged the survival of treated mice compared to ACT alone (Fig. 3:19). In addition, the stiffening intervention with Me β CD also effectively reduced the tumor burden in mice bearing s.c. EG7-OVA lymphoma tumors when combined with an ACT of OT-I CD8⁺ T cells supported by IL-15SA (Fig. 3:20), suggesting that overcoming the mechanical immune checkpoint may be a versatile therapy for different types of cancers. Notably, the stiffening intervention using Me β CD did not cause any side effects, such as body weight drop, splenomegaly, or increased infiltration and activation of CD8⁺ T cells in the spleens (Fig. 3:21). Me β CD alone as a monotherapy showed no therapeutic efficacy indicating that the presence of antigen-specific cytotoxic T cells was necessary for the enhanced killing of stiffened target cells (Fig. 3:4d, e).

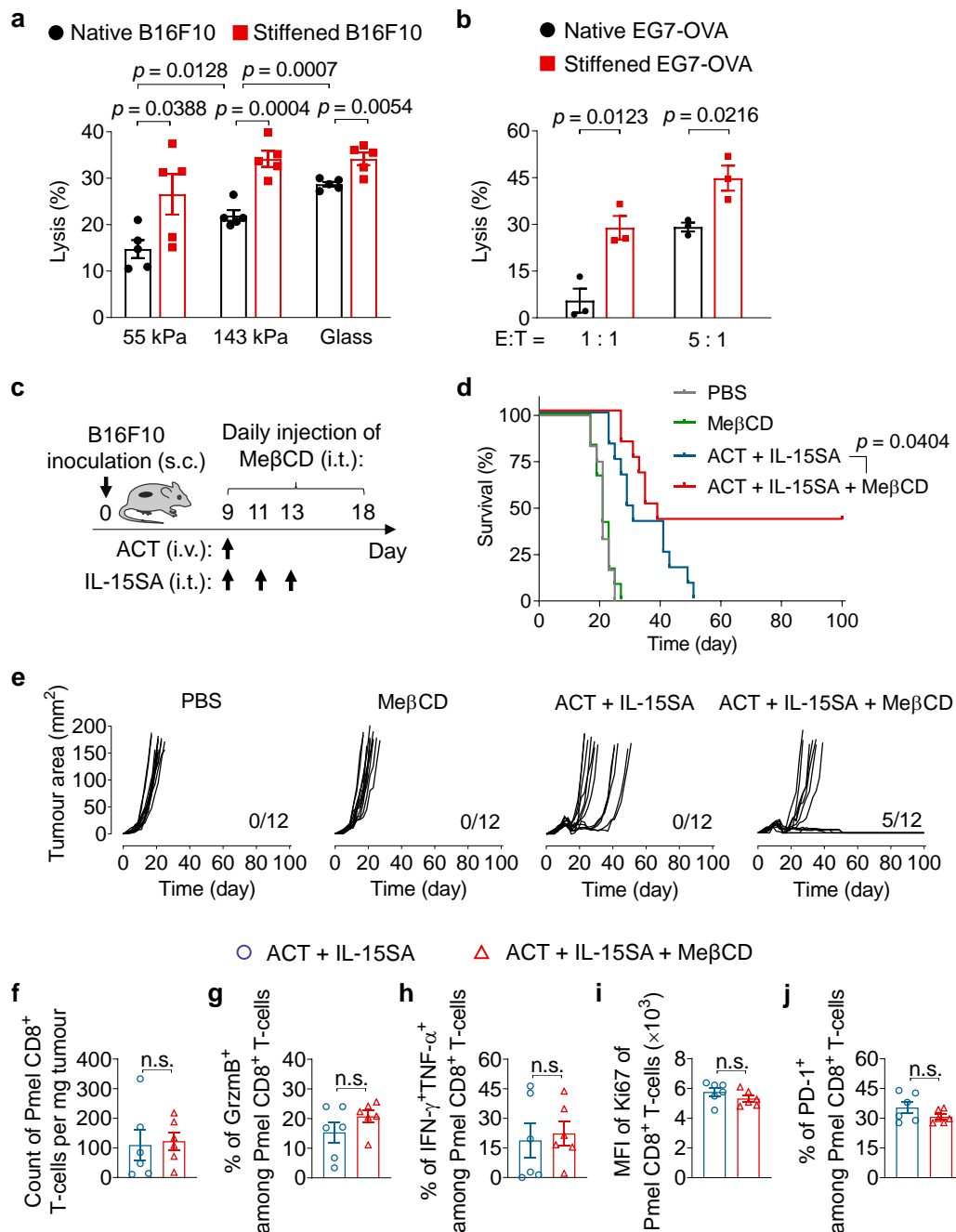


Figure 3:4 Cancer-cell stiffening by Me β CD enhances the efficacy of ACT immunotherapy.

a, Lysis percentage of B16F10 cancer cells pre-treated with Me β CD (stiffened) or PBS (native) and co-cultured with activated Pmel CD8⁺ T cells at an E:T ratio of 10:1 for 5 h (n = 5). **b**, Lysis percentage of EG7-OVA cancer cells pre-treated with Me β CD (stiffened) or PBS (native) and co-cultured with activated OT-I CD8⁺ T cells at indicated E:T ratios for 5 h (n = 3). Data in (**a**, **b**) are one representative of at least three independent experiments with biological replicates. **c-e**, B16F10 tumor-bearing mice were treated with adoptive transfer of Pmel CD8⁺ T cells (5×10^6 per mouse) adjuvanted by interleukin-15 super-agonist (IL-15SA, 10 μ g per injection) with or without daily Me β CD administration (1 mg per injection) as outlined in the experimental scheme (**c**). Mice receiving injections of PBS or Me β CD only serve as controls (n = 12 animals per group). Shown are survival curves (**d**), and individual tumor growth curves (**e**, indicated are the number of mice with durable responses out of all treated mice) of pooled data of two independent experiments with biological replicates. **f-j**, Tumour-infiltrating Pmel CD8⁺ T cells were analyzed by flow cytometry on day 14 (the experimental scheme is shown in Fig. 3:21b). Shown are counts (**f**), frequencies of granzyme B (GrzmB)⁺ (**g**), polyfunctional (**h**), and PD-1⁺ (**j**), and Ki67 expression level (**i**) of tumour-infiltrating Pmel CD8⁺ T cells (n = 6 animals per group). Data are one representative of two independent experiments with biological replicates. *P* values were determined by unpaired Student's *t* test in (**a**, **b**, **f-j**) or log-rank test in (**d**). Error bars represent SEM. PBS, phosphate-buffered saline; ACT, adoptive cell transfer; MFI, mean fluorescence intensity; s.c., subcutaneous; i.v., intravenous; i.t., intratumoral; n.s., not significant.

3.3.5 Biochemical pathways of T cell-mediated cytotoxicity are not affected by cancer-cell stiffening

Surprisingly, comparing IL-15SA-supported ACT therapy with the combination therapy of IL-15SA-supported ACT and Me β CD, we found that the stiffening intervention with Me β CD showed negligible effects on tumor infiltration of adoptively transferred Pmel CD8⁺ T cells, as well as their granzyme B production, polyfunctionality, proliferative capacity, or exhaustion phenotypes (Fig. 3:4f-j and 3:21b). Further flow cytometry analyses revealed that Me β CD treatment had almost no impact on the counts and phenotypes of tumor-infiltrating endogenous CD8⁺ T cells (Fig. 3:22) or other immune cells, including regulatory T cells, B cells, natural killer cells, macrophages, dendritic cells, and myeloid-derived suppressor cells (Fig. 3:23). To further examine the potential effects of Me β CD on T cells, we performed an in vitro experiment by co-culturing Pmel CD8⁺ T cells and B16F10 cancer cells in the presence of Me β CD. While Me β CD enhanced T cell-mediated killing of cancer cells, it had negligible influence on T cell proliferation or degranulation (Fig. 3:24). Altogether, these results suggest that the stiffening intervention with Me β CD markedly enhances the efficacy of ACT immunotherapy against solid tumors, an effect that is not owed to the alteration of immune cell infiltration, proliferation, or effector functions in tumors.

To rule out possible effects from the chemical nature of Me β CD, we looked into Me β CD chemical analogs without cholesterol depletion/cancer cell stiffening capacity. Me β CD is a cyclic methyl-modified oligosaccharide consisting of seven glucose subunits. Based on this, we first screened two candidates, α -cyclodextrin (α CD) and maltodextrin, which are a cyclic oligosaccharides with six glucose subunits and a linear analog of Me β CD, respectively. Using an in vitro cholesterol quantification assay, we found that α CD treatment was less efficient in depleting cholesterol from the plasma membrane of B16F10 cancer cells as compared to Me β CD (Fig. 3:5a). In contrast, maltodextrin treatment could not reduce membrane cholesterol levels (Fig. 3:5a). Consistent with cholesterol quantification results, α CD treatment showed a trend to enhance T cell-mediated killing of cancer cells while maltodextrin treatment did not influence T cell-mediated cytotoxicity against cancer cells (Fig. 3:5b), suggesting that maltodextrin is a chemical analog of Me β CD without cancer cell stiffening effect. We thus selected maltodextrin for in vivo test. C57BL/6J mice bearing s.c. B16F10 tumors were treated with intravenous (i.v.) ACT of Pmel CD8⁺ T cells adjuvanted with IL-15SA along with daily administration of Me β CD or maltodextrin (i.t., 1 mg \times 10) (Fig. 3:5c). Consistent with previous results (Fig. 3:4d, e), ACT therapy supported by both IL-15SA and tumor cell stiffening intervention using Me β CD outperformed IL-15SA-supported ACT in suppressing tumor growth (Fig. 3:5d). In contrast, the maltodextrin treatment did not improve the efficacy of IL-15SA-supported

ACT therapy (Fig. 3:5d). It is worth noting that the maltodextrin treatment itself had no anti-tumor or pro-tumor effects (Fig. 3:5d). Taken together, the chemical nature of Me β CD did not contribute to enhanced T cell-mediated cytotoxicity against stiffened cancer cells.

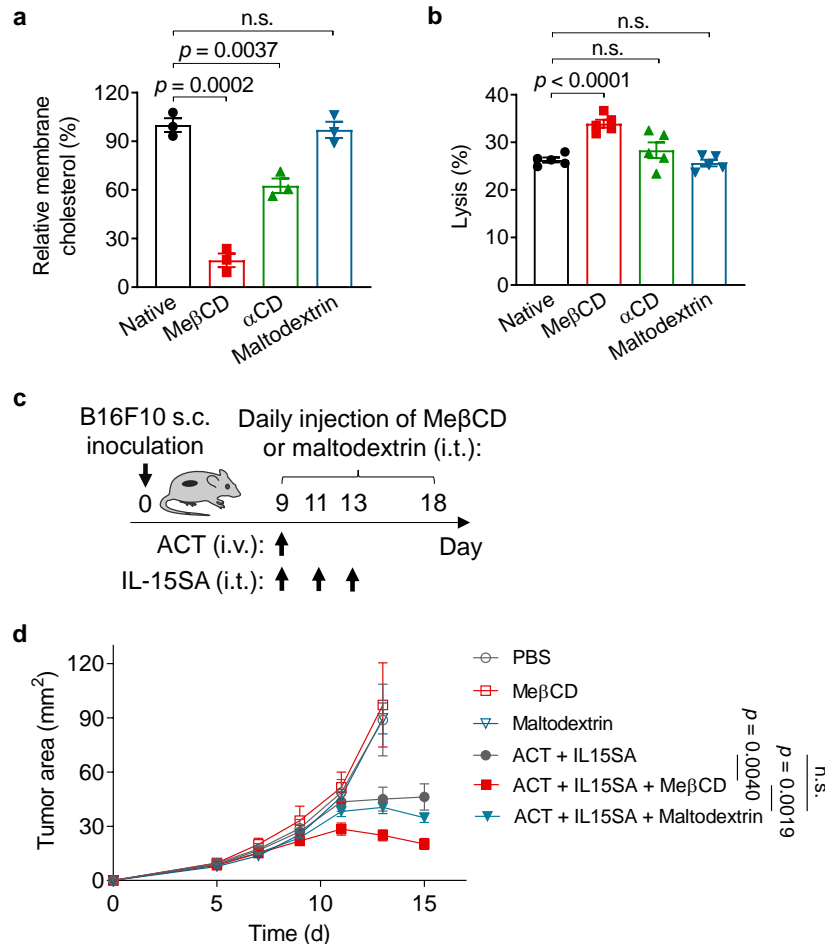


Figure 3:5 The chemical nature of Me β CD did not contribute to enhanced T cell-mediated cytotoxicity against stiffened cancer cells.

a, Relative membrane cholesterol levels of B16F10 cancer cells treated methyl- β -cyclodextrin (Me β CD), α -cyclodextrin (α CD), or maltodextrin ($n = 3$). Membrane cholesterol level of native B16F10 served as 100% standard. **b**, Lysis percentage of Me β CD, α CD, or maltodextrin-treated B16F10 cancer cells co-cultured with activated Pmel CD8⁺ T cells at an E:T ratio of 10:1 for 5 h ($n = 5$). Data are one representative of at least two independent experiments with biological replicates in (**a**, **b**). **c**, **d**, B16F10 tumor-bearing mice were treated with adoptively transferred Pmel CD8⁺ T cells (5×10^6 per mouse) adjuvanted by interleukin-15 super-agonist (IL-15SA, 10 μ g per injection) with daily Me β CD or maltodextrin administration (1 mg per injection) as outlined in the experimental scheme (**c**). Mice receiving injections of PBS, Me β CD, or maltodextrin only served as controls ($n = 10$ animals per group). Shown are tumor growth curves (**e**) of pooled data of two independent experiments with biological replicates. P values were determined by unpaired Student's t test. Error bars represent SEM. PBS, phosphate-buffered saline; ACT, adoptive cell transfer; s.c., subcutaneous; i.v., intravenous; i.t., intratumoral; n.s., not significant.

In order to elucidate the mechanism by which the stiffening intervention with Me β CD enhances tumor control by T cells, we performed mechanistic studies on different pathways that T cells exploit for cancer-cell killing. Those pathways include the Fas protein (also called CD95)—Fas ligand (FasL) interactions, the secretion of effector cytokines, such as interferon- γ (IFN- γ) and tumor necrosis factor- α (TNF- α), and the granule exocytosis of cytolytic proteins (e.g., perforin and granzymes) (Fig. 3:6a).^{188,189} As TCR activation depends on cognate antigen recognition, we first validated that OVA

antigen presentation on B16F10-OVA cancer cells, NFAT activation (as indicated by IL-2 production)¹⁹⁰ and phosphorylation levels of ZAP70, Erk1/2, and NF- κ B (as indicated by p65 phosphorylation)¹⁹¹ as the downstream markers of TCR-signalling were not affected by the Me β CD treatment of cancer cells (Fig. 3:6b, c and 3:25a-c). Next, we co-cultured Me β CD-stiffened B16F10 cancer cells with activated Pmel CD8⁺ T cells to examine whether Me β CD treatment of cancer cells altered any of the abovementioned biochemical cytotoxic pathways. Proliferation, activation, and exhaustion phenotypes were unchanged in T cells co-cultured with stiffened B16F10 cancer cells compared to the native cancer cells (Fig. 3:25d-f). Importantly, Me β CD treatment of cancer cells did not influence the expression levels of Fas on B16F10 cancer cells and FasL on T cells (Fig. 3:6d, e), or the susceptibility of cancer cells to FasL-induced apoptosis (Fig. 3:6j). In addition, IFN- γ and TNF- α secretion were unchanged in T cells co-cultured with native or stiffened B16F10 cancer cells (Fig. 3:6f, g and 3:25g, h). Both native and stiffened B16F10 cancer cells exhibited comparable levels of apoptosis when incubated with TNF- α (Fig. 3:6k). Finally, flow cytometry analyses of degranulation activity and granzyme B production revealed that Me β CD treatment of cancer cells had negligible influence on the granule exocytosis activity of the cytotoxic T cells in the co-culture (Fig. 3:6h, i and 3:25i). To consolidate aboved observations, ACAT1 KD (softer) or ACAT1 OE (stiffer) B16F10 cancer cells induced similar degranulation, NFAT activation, and cytokine release levels as compared to native B16F10 cells (Fig. 3:26). Based on these results, we excluded the known biochemical pathways as the major underlying mechanisms of the enhanced T cell cytotoxicity against stiffened cancer cells.

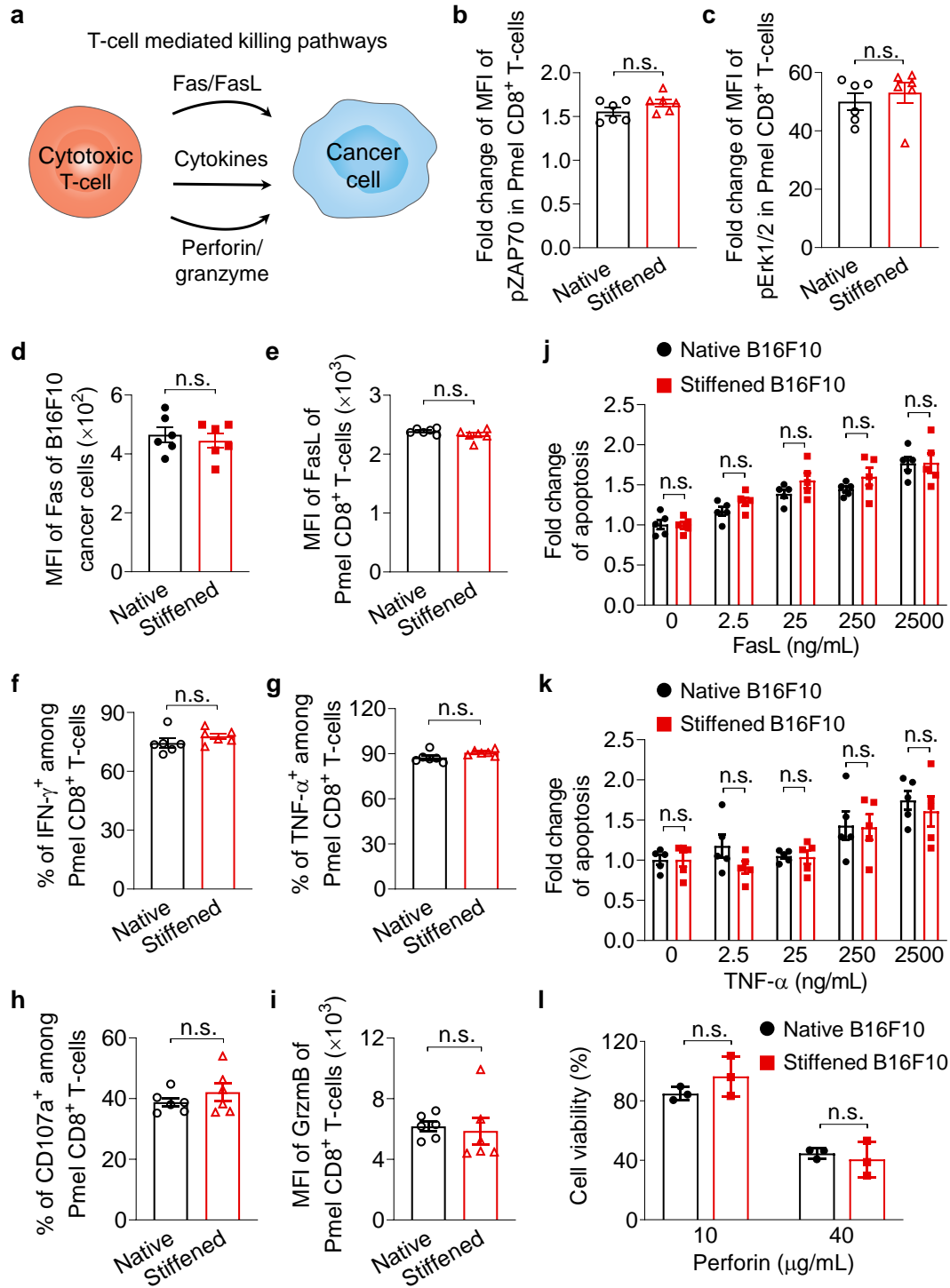


Figure 3:6 Cancer-cell stiffening has negligible influence on biochemical cancer-cell killing pathways mediated by T cells.

a, Schematic illustration of T cell-mediated killing pathways. **b, c**, Fold change of MFI of phosphorylated ZAP70 (pZAP70, **b**) and Erk1/2 (pErk1/2, **c**) in activated Pmel CD8⁺ T cells stimulated by native or MeßCD-treated (stiffened) B16F10 cancer cells at 37 °C for 5 min ($n = 6$). **d**, Expression levels of Fas of native and stiffened B16F10 cancer cells ($n = 6$). **e-i**, Activated Pmel CD8⁺ T cells were co-cultured with native or stiffened B16F10 cancer cells (E:T ratio = 10:1) at 37 °C for 5 h. Shown are expression levels of Fas ligand (FasL) (**e**) and granzyme B (GrzmB) (**i**), and frequencies of IFN- γ ⁺ (**f**), TNF- α ⁺ (**g**), and CD107a⁺ (**h**) of Pmel CD8⁺ T cells ($n = 6$). **j, k**, Fold change of frequencies of apoptotic native and stiffened B16F10 cancer cells after incubation with FasL (**j**) or TNF- α (**k**) at indicated concentrations at 37 °C for 5 h ($n = 5$). **l**, Viability of native and stiffened B16F10 cancer cells after incubation with perforin of indicated concentrations at 37 °C for 20 min ($n = 3$). *P* values were determined by unpaired Student's *t* test. Error bars represent SEM. MFI, mean fluorescence intensity; n.s., not significant. All data are one representative of at least three independent experiments with biological replicates.

3.3.6 Cancer-cell stiffening augments cellular forces and cytotoxicity mediated by T cells

These findings motivated us to investigate whether biomechanical factors contributed to the enhanced T cell-mediated killing. As T cell-mediated killing requires intense physical contact, e.g., immunological synapse formation, with cancer cells, we first validated that cancer cell softening or stiffening B16F10 cancer cells had a negligible effect on the expression levels of important adhesion ligands (LFA-1 and CD49d) on Pmel T cells (Fig. 3:27a, b). In addition, Pmel T cells showed similar conjugation efficiencies with native, softened, and stiffened B16F10 cancer cells (Fig. 3:27c). We first incubated Me β CD-stiffened B16F10 cancer cells with perforin, a pore-forming effector protein, in the absence of T cells, and found that cancer-cell stiffening had no impact on perforin-mediated lysis, suggesting that the enhanced cytotoxicity against stiffened cancer cells is T cell-dependent (Fig. 3:6l).¹⁴ We first tested if stiffening cancer cells enhances their sensitivity to membrane tension-assisted pore formation by perforin. We followed a well-established technique to generate membrane tension on cancer cells by applying a hypotonic solution to increase cell volume. As shown in Fig. 3:28a, increasing membrane tension on B16F10 cancer cells significantly enhanced perforin-induced lysis, which is consistent with reported results. However, stiffened B16F10 cancer cells showed similar susceptibility to membrane tension-assisted perforin-induced lysis compared to native cancer cells (Fig. 3:28a). It is worth noting that Me β CD treatment itself did not change the cell volume of B16F10 cancer cells, evidenced by unaltered cell size (forward scattering area, FSC-A) and granularity (side scattering area, SSC-A) in flow cytometry analysis (Fig. 3:28b).

We thus speculated that stiffening cancer cells enhances T cell forces to augment T cell-mediated cytotoxicity against cancer cells. To provide direct evidence that cytotoxic T cells exert increased forces on stiffer substrates, we used traction force microscopic (TFM)¹⁹² to measure forces exerted by primary T cells on hydrogel substrates of various stiffness. We synthesized PA hydrogels with Young's modulus from 260 to 890 Pa (Fig. 3:13, PA-3-5), a range representative of the physiological stiffness of cancer cells.^{193–195} Upon TCR triggering by anti-CD3 and anti-CD28 antibodies coated on the hydrogel surface, T cell forces were measured by quantifying the displacement of the embedded fluorescent beads in hydrogels (Fig. 3:29a). Pmel CD8⁺ T cells exerted markedly higher cellular forces on stiffer substrates (Fig. 3:7a, b), with average values of 0.5, 1.0, and 1.8 nanonewton per cell on PA hydrogels of 260, 510, and 890 Pa, respectively (Fig. 3:7c). When the coated antibodies were replaced by anti-CD45 antibodies, a non-stimulatory antibody, or T cells were pre-treated with latrunculin A (LatA), a potent inhibitor of actin polymerization, the cellular forces dropped substantially (Fig. 3:29b). Confocal fluorescence imaging of Pmel CD8⁺ T cells on the same PA hydrogels revealed the presence of filamentous actin (F-actin)-rich peripheral structures across the T cell/hydrogel interfaces, which represented the formation of immunological synapses (Fig. 3:7d). F-actin accumulation in this synaptic interface was notably increased on stiff hydrogel substrates (Fig. 3:7e). As F-actin polymerization is essential for cellular force generation,¹⁹⁶ this observation, along with the TFM result, indicates that Pmel CD8⁺ T cells generate higher mechanical stress on stiffer surfaces. It has been reported that phosphorylation of proline-rich tyrosine kinase 2 (Pyk2), a member of the focal adhesion kinase family, positively correlates with cellular forces exerted by primary T cells.⁹⁴ To compare the T cell forces exerted on target cells of different stiffness, we measured the phospho-Pyk2 (pPyk2) levels in Pmel CD8⁺ T cells co-cultured with native, softened, or stiffened B16F10 cancer cells. A higher level of pPyk2 was induced in Pmel CD8⁺ T cells co-cultured with stiffened B16F10 cancer cells as compared to the native or softened cancer cells (Fig. 3:7f), suggesting that T cells

indeed exerted higher cellular forces against stiffened cancer cells. Taken together, these results showed that T cells exert higher forces against a stiffer surface upon TCR triggering.

To determine whether enhanced T cell forces played an important role in augmented cytotoxicity, we pre-treated T cells with LatA to inhibit actin polymerization and thereby T cell forces. T cells pre-treated with LatA exerted greatly reduced cellular forces even 5 hours post the treatment (Fig. 3:29c). As a result, the percentage of cancer cell lysis was substantially reduced on all hydrogel substrates (Fig. 3:7g, compared with results shown in Fig. 3:4a). Importantly, the cytotoxicity enhancement observed following cancer-cell stiffening was completely abrogated on all substrates (Fig. 3:7g). Similarly, pre-treatment of T cells with blebbistatin (Bleb), a myosin II inhibitor that inhibits T cell contractility,¹⁴ or Mycalolide B (MycalB), an irreversible cytoskeleton inhibitor that covalently binds to G-actin for inhibiting actin polymerization and thus cellular forces^{154,197} (Fig. 3:29d), led to the complete abrogation of enhanced lysis of stiffened cancer cells (Fig. 3:7h and 3:30). Of note, these inhibitors showed no direct effect on T cell viability or apoptosis at the concentrations used (Fig. 3:31). These results reveal that cellular forces exerted by T cells mediated the augmented killing efficiency of stiffened target cells.

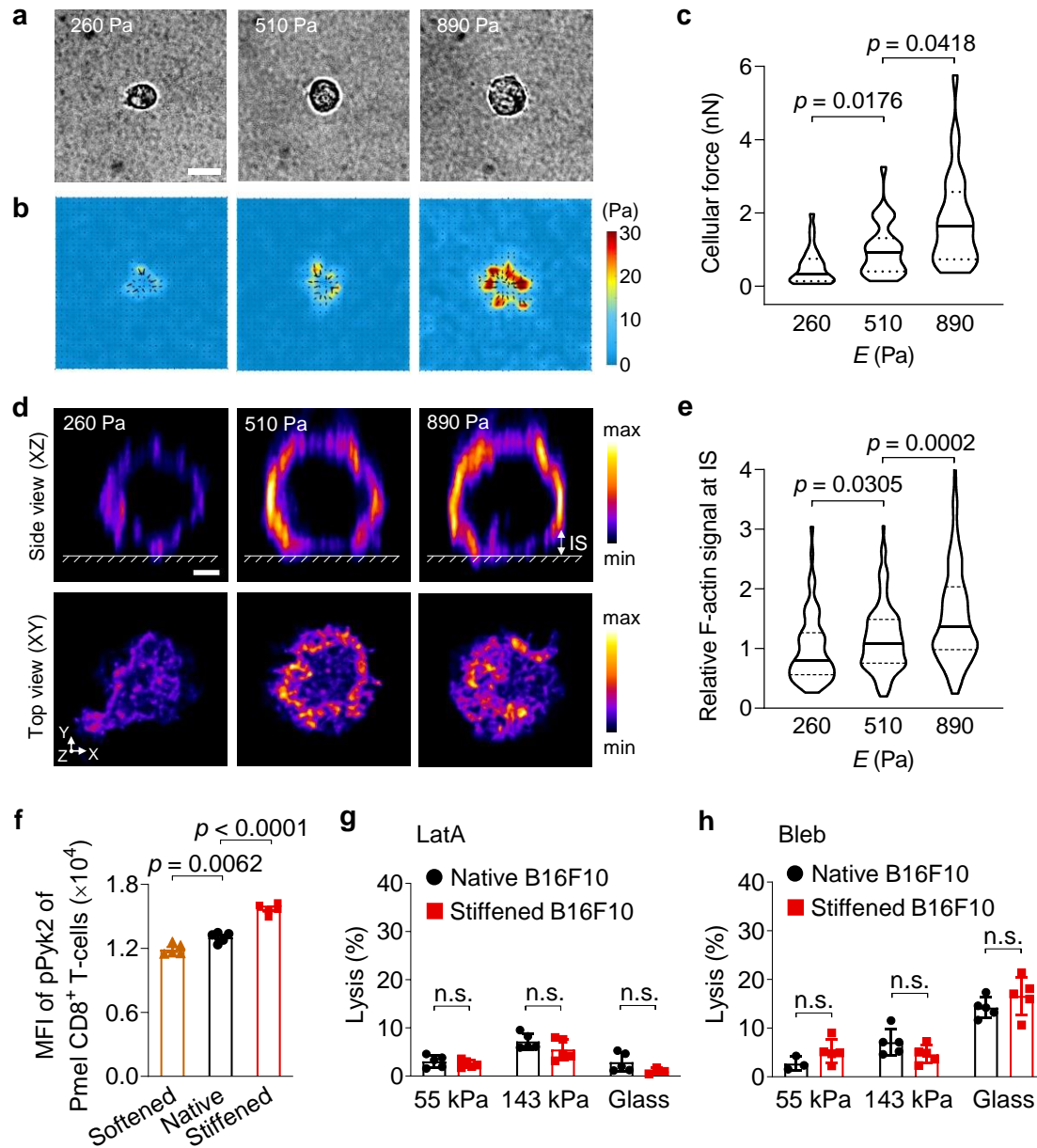


Figure 3:7 Enhanced cytotoxicity against stiffened cancer cells is mediated by T cell forces.

a-c, Forces exerted by activated Pmel CD8⁺ T cells on polyacrylamide (PA) hydrogel substrates of indicated stiffness coated with anti-CD3 and anti-CD28 antibodies were measured using traction force microscopy. Shown are representative bright-field images (**a**) and the corresponding traction stress maps (**b**), and average total force per cell (**c**) ($n = 29$ individual cells). The color bar indicates the magnitude of stress. Scale bar, 5 μ m. **d**, Representative deconvoluted confocal fluorescence images of F-actin of activated Pmel CD8⁺ T cells on PA hydrogel substrates of indicated stiffness coated with anti-CD3 and anti-CD28 antibodies. The upper row shows the side view (XZ plane); the lower row shows the top view (XY plane) of F-actin at the T cell immunological synapse (IS, defined as the structure between the surface of hydrogel and a height of 2 μ m above the surface of the hydrogel). The color bar indicates the intensity of the F-actin fluorescence signal. Scale bar, 2 μ m. **e**, Relative total fluorescence intensity (normalized by the mean value at 260 Pa) of F-actin at the IS in the images from (**d**) ($n = 66, 119$, and 179 individual cells for 260, 510, and 890 Pa, respectively). **f**, MFI of phosphorylated Pyk2 (pPyk2) in activated Pmel CD8⁺ T cells co-cultured with native, Chol-treated (softened) or MeBCD-treated (stiffened) B16F10 cancer cells ($n = 5$). **g, h**, Lysis percentage of native and stiffened B16F10 cancer cells co-cultured with activated Pmel CD8⁺ T cells (E:T ratio = 10:1), which were pre-treated with latrunculin A (LatA, **g**) or blebbistatin (Bleb, **h**) ($n = 5$). P values were determined by Kruskal-Wallis test in (**c, e**) or unpaired Student's t test in (**f-h**). Error bars represent SEM. In the violin plots (**c, e**), the middle solid line shows median, and lower and upper dash lines show 25th and 75th percentiles, respectively. MFI, mean fluorescence intensity; n.s., not significant. All data are one representative of at least two independent experiments with biological replicates.

3.4 Conclusion

Discovering and targeting new immune checkpoints has the potential to improve patients' response rate to cancer immunotherapy. Here we identified an immune checkpoint of biomechanical basis, i.e., cellular softness, which is employed by cancer cells to impair T cell forces at the immunological synapse and therefore evade anti-tumor immunity (Fig. 3:8). By stiffening cancer cells through depletion of the membrane cholesterol, we show that the mechanical immune checkpoint could be overcome to enhance T cell forces and tumor clearance and durable responses in pre-clinical mouse tumor models when combined with ACT therapy (Fig. 3:8).

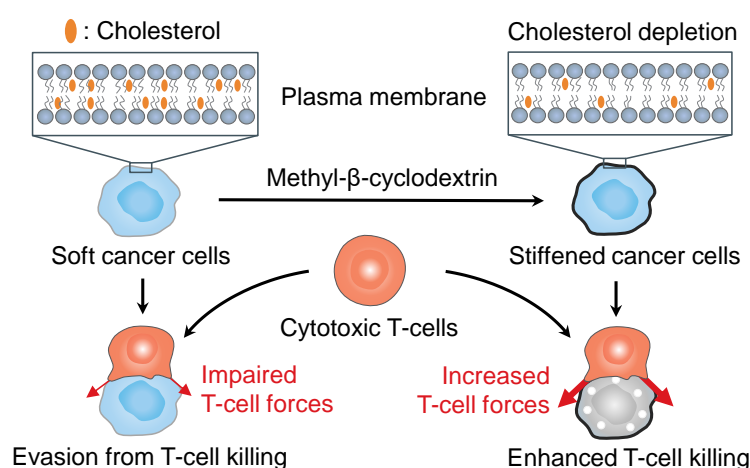


Figure 3:8 Schematic illustration of mechanical immuno-suppression induced by the softness of cancer cells, which could be overcome by stiffening cancer cells for enhanced cancer-cell killing mediated by T cells.

Specifically, modulating cell mechanics *in vivo* is the key to the clinical application but still challenging. As a proof-of-concept, we used an *ex vivo* genetic modification approach to regulate the membrane cholesterol levels specifically in cancer cells without perturbing tumor-infiltrating immune cells such as T cells. Cholesterol in T cells has been reported to be important in enhancing TCR clustering and thus TCR signaling upon antigen stimulation.¹⁸⁶ We employed intratumoral injection of MeβCD to deplete cholesterol from plasma membranes transiently. In those experiments, we found that injected MeβCD had negligible influence on the functions of tumor-infiltrating T cells *in vivo* likely because the depletion of cholesterol by MeβCD was transient and less potent as compared to genetic modification of T cells in previous reports.¹⁸⁶ Future work to target reagents for mechanical modulation, such as MeβCD, specifically to cancer cells using biomaterial-assisted delivery strategies would be necessary to minimize any undesired side effects.¹⁹⁸

Cholesterol accumulates in lipid rafts on the cell membrane, which can recruit specific surface receptors for signal transduction, such as the epidermal growth factor receptor (EGFR), which is involved in tumor survival signaling.¹⁹⁹ However, we did not notice any difference in apoptosis or viability of B16F10 melanoma cells after membrane cholesterol depletion by MeβCD treatment, suggesting negligible influences on signal transduction through lipid rafts. In addition, we also confirmed that membrane cholesterol depletion using MeβCD treatment had negligible effects on Fas/FasL-induced apoptosis in B16F10 melanoma cells. Fas protein is known to associate with lipid rafts to induce cell death signals.²⁰⁰

This result further supports that Me β CD treatment does not significantly influence lipid raft-assisted signal transduction in cancer cells.

We found that T cell forces were critical for the enhanced vulnerability of stiffened cancer cells toward T cell-mediated cytotoxicity as inhibition of T cells forces completely abrogated such effects. In addition, TFM measurement showed that T cells exerted higher cellular forces against flat substrates with increased stiffness (from 260 to 890 Pa), which mimicked the stimulatory surface of target cells. To closely recapitulate the spatial features of the target cell surface, including the curvature, a recently developed TFM technique based on spherical microparticles may better map the dynamic forces at the T cell immunological synapse in the future.²⁰¹ Interestingly, it seems that the enhanced T cell force on the stiffer surface did not depend on TCR signaling (Fig. 3:6b, c and 3:25a-c) but may on integrin signaling (Fig. 3:7f). As LFA-1 is an essential integrin in T cell immunological synapse formation,⁹² future work should be dedicated to studying how LFA-1 mechanosensing contributes to the enhanced T cell cytotoxicity against stiffened target cells.

Degranulation and cytokine production of CD8⁺ T cells is less stiffness-dependent than CD4⁺ T cells, particularly on substrates of low stiffness (<8 kPa).^{13,81} Consistent with previous reports, we found that cancer-cell stiffening via membrane cholesterol depletion had a negligible effect on degranulation or cytokine production of CD8⁺ T cells. Recently, overexpression of myocardin-related transcription factors (MRTFs) was shown to increase cancer cell stiffness by inducing rigidification of filamentous actin and promote degranulation and cytokine production in cytotoxic CD8⁺ T cells.¹⁰⁸ These results suggest that different target cell stiffening methods (membrane cholesterol depletion vs. intracellular cytoskeleton rigidification) may result in different T cell responses, for which the underlying mechanism is still unknown. One possibility is that MRTF overexpression enhances F-actin polymerization and hence increases the cellular force generation of cancer cells,¹⁰⁸ whereas Me β CD treatment has negligible influences on F-actin polymerization.¹⁷⁵ Based on these observations, it is likely that the discrepancy in T cell response derives from the difference in cellular force generation in cancer cells. Nevertheless, as cellular stiffness is contributed jointly by both cell membrane and cytoskeleton,²⁰² modulations of both components are promising to overcome the mechanical immune checkpoint for enhanced cancer immunotherapy. Recently, a subset of CD4⁺ T cells with cytotoxic functions has been identified in vivo contributing to anti-tumor immunity.^{203,204} It is of great interest to investigate whether cancer cell softening also contributes to evasion from CD4⁺ T cell-mediated cytotoxicity.

Overall, our studies provide a novel insight into the multidimensional mechanisms of immune suppression in tumors. Leveraging cellular mechanical properties and T cell forces provide new therapeutic strategies in addition to conventional biochemical modulation. Therapeutically targeting both biochemical and mechanical immune checkpoints has the potential to further improve patients' responses to cancer immunotherapies. Despite tremendous efforts in searching and investigating immune checkpoints based on biochemical signals, much less is known about how biomechanical cues and interactions could potentially regulate immune responses against diseases such as cancer. Cancer—immunity interactions are multidimensional, involving not only biochemical but also substantial biophysical signals.^{16,205} Our studies provide an insight into the multidimensional mechanisms of immune suppression in tumors. The growing knowledge

in fundamental mechano-immunology provides the basis for developing new engineering approaches to modulate bio-mechanical cues for enhanced anti-tumor immunity.^{132,206} Leveraging cancer cell mechanics and T cell forces, as demonstrated in this study, provide new therapeutic strategies in addition to conventional biochemical modulation. Therapeutically targeting both biochemical and mechanical immune checkpoints could potentially benefit patients more broadly with cancer immunotherapies.

3.5 Supplementary materials

3.5.1 Supplementary methods

Animals, cell lines, and reagents. All the mouse studies were approved by the Swiss authorities (Canton of Vaud, animal protocol ID 3206 and 3533) and performed in accordance with guidelines from the Center of PhenoGenomics (CPG) in EPFL. Six- to eight-week-old female Thy1.2⁺ C57BL/6 (C57BL/6J) mice and BALB/cByJ (BALB/c) mice were purchased from Charles River Laboratories (Lyon, France). T cell receptor (TCR)-transgenic Thy1.1⁺ pmel-1 (Pmel) mice (B6.Cg-Thy1²/Cy Tg(Tcr α Tcr β)8Rest/J) and TCR-transgenic OT-I mice (C57BL/6-Tg(Tcr α Tcr β)1100Mjb/J) were purchased from The Jackson Laboratory (Bar Harbor, ME, USA) and maintained in the animal facility in the CPG in EPFL. B16F10 murine melanoma cells and EL4 murine lymphoma cells expressing ovalbumin (EG7-OVA) were originally acquired from the American Type Culture Collection (ATCC; Manassas, VA, USA). MC38 murine colon cancer cells expressing human epidermal growth factor receptor 2 (MC38-HER2) and Me275 human melanoma cells expressing HER2 (Me275-HER2) were kindly provided by Pedro Romero Lab (UNIL, Switzerland). B16F10 murine melanoma cells expressing ovalbumin (B16F10-OVA) and 4T1 murine breast cancer cells expressing luciferase and tdTomato fluorescent protein (4T1-Fluc-tdTomato) were kindly provided by Darrell Irvine Lab (MIT, USA). HEK293T cells and pLKO.1 vector were kindly provided by Didier Trono Lab (EPFL, Switzerland). B16F10, B16F10-OVA, MC38-HER2, and HEK293T cells were cultured in Dulbecco's modified Eagle's medium (DMEM) (Gibco, Thermo Fisher Scientific, Waltham, MA, USA) supplemented with fetal bovine serum (FBS) (10 v/v%, Gibco) and penicillin/streptomycin (1 v/v%, Gibco). EG7-OVA and Me275-HER2 cells were cultured in Roswell Park Memorial Institute (RPMI) 1640 medium (Gibco) supplemented with FBS (10 v/v%), HEPES (1 v/v%, Gibco), penicillin/streptomycin (1 v/v%), and β -mercaptoethanol (0.1 v/v%, Gibco). For culturing EG7-OVA cells, G418 (Geneticin) (0.4 mg/mL, Gibco) was supplemented to maintain OVA expression. 4T1-Fluc-tdTomato cells were cultured in Iscove's Modified Dulbecco's Medium (IMDM) (Gibco) supplemented with FBS (10 v/v%) and penicillin/streptomycin (1 v/v%).

Filipin III (from *Streptomyces filipinensis*), methyl- β -cyclodextrin (Me β CD), water-soluble cholesterol/Me β CD complex (Chol), α -cyclodextrin (α CD), maltodextrin, 4-hydroxyacetophenone (4-HAP), blebbistatin (Bleb), glutaraldehyde solution (25 wt% in H₂O), Triton X-100, 4',6-diamidino-2-phenylindole dihydrochloride (DAPI), propidium iodide (PI) solution (1 mg/mL in H₂O), Hoechst 33342, acrylamide, *N,N'*-methylenebisacrylamide, ammonium persulfate, tetramethylethylenediamine (TEMED), N-sulfosuccinimidyl-6-(4'-azido-2'-nitrophenylamino) hexanoate (Sulfo-SANPAH), deoxyribonuclease I (DNase I, from bovine pancreas), dispase II, hyaluronidase, cholesterol oxidase (from microorganisms), protamine sulfate, bovine serum albumin (BSA), sodium dodecyl sulfate (SDS), calcium chloride dihydrate and polystyrene (PS) bead (carboxylate-modified, 500 nm, orange fluorescence) were purchased from Sigma-Aldrich (St. Louis, MO,

USA). 3-aminopropyl-trimethoxysilane (APTMS) was purchased from ACROS Organics (Thermo Fisher Scientific). Methyl-cellulose (4000 cPs) was purchased from Alfa Aesar (Thermo Fisher Scientific). Phalloidin-iFluor™ 488 conjugate was purchased from AAT Bioquest (Sunnyvale, CA, USA). Latrunculin A (LatA) (1 mM in DMSO) was purchased from Calbiochem (Merck, Darmstadt, Germany). Mycalolide B (MycaB) was purchased from Enzo Life Science (Farmingdale, NY, USA). EZ-Link™ NHS-Biotin, collagenase IV, puromycin dihydrochloride, and anti-phospho (Ser536)-NF-κB p65 antibody (clone T.849.2) were purchased from Thermo Fisher Scientific. Streptavidin acrylamide, fluorescent PS bead (carboxylate-modified, 200 nm, red fluorescence), and CellTrace™ CFSE Cell Proliferation Kit were purchased from Invitrogen (Thermo Fisher Scientific). Active Perforin-1 was purchased from Cloud-Clone (Houston, TX, USA). Recombinant human fibronectin fragment (RetroNectin®) was purchased from Takara (Nojihigashi, Shiga, Japan). OVA₂₅₇₋₂₆₄ (SIINFEKL) and human gp100₂₅₋₃₃ (hgp100) peptides were purchased from GenScript (Piscataway, NJ, USA). Recombinant mouse interleukin-2 (IL-2) and interleukin-7 (IL-7), and tumor necrosis factor-α (TNF-α) were purchased from PeproTech (London, UK). Anti-mouse CD3 antibody (clone 17A2) and anti-mouse CD28 antibody (clone 37.51) were purchased from Bioxcell (West Lebanon, NH, USA). Anti-phospho (Tyr402)-Pyk2 antibody (R402) was purchased from EnoGene (New York, NY, USA). Anti-ACAT1 polyclonal antibody was purchased from Cayman Chemical (Ann Arbor, MI, USA). Brefeldin A solution (1000×), Monensin solution (1000×), 7-amino-actinomycin D (7-AAD), and anti-His Tag (J099B12) antibody were purchased from Biolegend (San Diego, CA, USA). Recombinant mouse Fas ligand (FasL) (TNFSF6) was purchased from R&D Systems (Minneapolis, MN, USA).

For flow cytometry analyses, fluorescently-labelled anti-phospho (Tyr319/Tyr352)-ZAP70/Syk antibody (n3kobu5), and goat anti-rabbit IgG (H+L) secondary antibody (polyclonal) were purchased from Invitrogen. Fluorescently-labeled Annexin V, and antibodies including anti-mCD4 (RM4-5), anti-mCD8 (YTS156.7.7), anti-mCD3ε (17A2), anti-IFN-γ (XMG1.2), anti-TNF-α (MP6-XT22), anti-IL-2 (JES6-5H4), anti-granzyme B (GB11), anti-CD107a (1D4B), anti-CD69 (H1.2F3), anti-PD-1 (29F.1A12), anti-LFA-1 (H155-78), anti-CD49d (R1-2), anti-Ki67 (16A8), anti-Foxp3 (MF-14), anti-NK1.1 (PK136), anti-I-A/I-E (M5/114.15.2), anti-F4/80 (BM8), anti-CD19 (6D5), anti-Gr-1 (RB6-8C5), anti-CD11b (M1/70), anti-CD11c (N418), anti-Siglec-F (S17007L), anti-Thy1.1 (OX-7), anti-CD45.2 (104), anti-phospho (Thr202/Tyr204)-Erk1/2 (4B11B69), anti-FasL (MFL3), anti-H-2K^b-SIINFEKL (25-D1.16), anti-Fas (SA367H8) and anti-PD-L1 (10F.9G2) were purchased from Biolegend.

Histological analyses. Mouse samples including tumor tissues and adjacent tissues (skin and muscle) were harvested from C57BL/6J mice 10 days after subcutaneous inoculation with B16F10 cancer cells (5×10^5). The collected tissues were embedded in O.C.T. compound (Tissue-Tek®, Sakura Finetek, Tokyo, Japan) and frozen with liquid nitrogen for cryosection with Leica CM3050S cryostat (Leica Microsystems, Milton Keynes, UK). Cryosections collected on slides were thawed and hydrated in phosphate-buffered saline (PBS; Gibco) for 15 min at room temperature. The section slides were then stained with Filipin III (100 µg/mL in PBS) for 1 h followed by rinsing with PBS twice. The corresponding adjacent section slides were sent to the Histology Core Facility at EPFL for hematoxylin and eosin (H&E) staining. The slide images were acquired using a confocal microscope (LSM700, Zeiss, Oberkochen, Germany) and processed using ImageJ.

All human biopsy samples were obtained from West China Hospital (Chengdu, China) following the approved protocol (No.120, 2016). Informed consent was obtained from West China Hospital ethics committee. Briefly, the collected cancer samples from human patients were embedded in O.C.T. compound (Tissue-Tek®) and frozen with liquid nitrogen for cryosection with Leica CM3050S cryostat. Filipin III and H&E staining were performed on the section slides for observing the cholesterol level and tissue structure, respectively. The slide images were acquired using an inverted microscope (Eclipse Ti-U, Nikon, Kyoto, Japan) and processed by ImageJ.

Quantification of global cholesterol levels in tumor, skin, and muscle tissues. B16F10 tumor, skin, or muscle tissues adjacent to tumor was harvested separately from tumor-inoculated mice and digested with tissue digestion buffer (0.1 mg/mL DNase I, dispase II and hyaluronidase, and 1 mg/mL collagenase IV in RPMI 1640 medium) on a shaker at 37 °C for 1 h. The tissue fluid passing through a cell strainer (70 µm, Fisher Scientific, Pittsburgh, PA, USA) was added with methanol/chloroform (1:2, v/v) for cholesterol extraction and shaken at room temperature for 2 h. Afterward, the organic phase containing cholesterol was collected, and the solvent was evaporated under a vacuum. Finally, the cholesterol in each sample was quantified using the Amplex Red cholesterol assay kit (Invitrogen) according to the manufacturer's recommended protocol.

Filipin staining of cholesterol for flow cytometry analyses. Tumour tissue was harvested from BALB/c mice 12 days after subcutaneous inoculation with 4T1-Fluc-tdTomato cancer cells (5×10^5) and digested with tissue digestion buffer on a shaker at 37 °C for 45 min. After passing through a cell strainer (70 µm), the red blood cells were lysed with ACK lysing buffer (Gibco) at room temperature for 5 min. The collected cells were then stained with Filipin (10 µg/mL in PBS) at 4 °C for 30 min. After washing with PBS (0.2 w/v% BSA), the cells were resuspended in PI solution (10 µg/mL in PBS) for flow cytometry analyses. Similar Filipin staining was performed with EG7-OVA cancer cells and activated CD8⁺ T cells to compare membrane cholesterol levels.

Modulation of cholesterol levels in plasma membrane of cancer cells. To deplete cholesterol from plasma membrane, B16F10 (or EG7-OVA, MC38-HER2, and Me275-HER2) cancer cells were incubated with DMEM medium supplemented with Me β CD (5 mM) at 37 °C for 30 min, and then washed with PBS twice. To supplement cell plasma membrane with cholesterol, B16F10 (or EG7-OVA, MC38-HER2, and Me275-HER2) cancer cells were treated with Chol (5 mM) in the DMEM medium at 37 °C for 30 min, and then washed with PBS twice.¹⁸⁶

Generation of acyl-CoA:cholesterol acyltransferase-1 (ACAT1) knock-down and overexpressing B16F10 cancer cell lines. Lentiviral plasmids containing the ACAT1 knock-down and overexpression constructs were generated by standard molecular cloning methods. To generate ACAT1 knock-down cells, the shRNA target sequence (5'-CCAACCAGAGACTAAACATAT-3') was cloned into the pLKO.1 vector with the AgeI/EcoRI sites.²⁰⁷ To generate ACAT1 overexpressing cells, codon-optimized cDNA encoding ACAT1 (NM_009230.3) was synthesized by Twist Biosciences (South San Francisco, CA, USA) and cloned into the lentiviral expression vector S002 by Gibson assembly cloning.

Lentivirus was produced by transient transfection of HEK293T cells with the S002 or pLKO.1 transgene expression vectors, the pDelta8.9 packaging plasmid, and the VSV-G envelope plasmid. In brief, HEK293T cells were transfected with

a mixture of plasmid DNA [VSV-G: pDelta8.9: S002 (or pLKO.1) with a weight ratio of 1:2:3] assembled in calcium-phosphate particles. After overnight incubation, the medium was replaced with a normal culture medium. Supernatants containing viral particles were collected 48 and 72 hours after transfection and filtered through a 0.45- μ m filter. Untitrated viral supernatant supplemented with protamine (10 μ g/mL) was added to B16F10 cells, and the contact of viral particles with cells was ensured by centrifugation (2000 rpm, 1 h). One day after transduction, stably transduced B16F10 cells were subjected to puromycin selection (0.5 μ g/mL) for two weeks.

Quantification of intracellular and plasma membrane cholesterol levels. The total cellular cholesterol level was first quantified using the Amplex Red cholesterol assay kit. In brief, B16F10 (or EG7-OVA, MC38-HER2, and Me275-HER2) cancer cells were fixed with glutaraldehyde (0.1 wt% in PBS), and the total cholesterol was extracted with methanol/chloroform (1:2, v/v) under sonication. After removal of organic solvent under vacuum, the cholesterol level was quantified using the Amplex Red cholesterol assay kit as described above. To quantify the intracellular cholesterol, the fixed cancer cells were treated with cholesterol oxidase (2 U/mL in PBS) to oxidize the plasma membrane cholesterol before extraction. The plasma membrane cholesterol level was calculated by subtracting the intracellular cholesterol level from the total cellular cholesterol level.¹⁸⁶ The cholesterol levels of cancer cells were measured immediately post the Me β CD-, Chol-, α CD-, or maltodextrin-treatment. Additionally, a kinetic study was performed to follow the cholesterol levels of B16F10 cancer cells at 0, 1, 3, 5, and 12 h post Me β CD-treatment.

To measure the cellular cholesterol level of cancer cells in B16F10 tumors, tumor tissues were harvested 30 min after a single intratumoral injection of PBS (100 μ L) or Me β CD solution (100 μ L, 20 mg/mL in PBS) in tumor-bearing mice. Tumour tissues were digested with tissue digestion buffer on a shaker at 37 °C for 1 h. Afterward, the cells were collected after passing through a cell strainer (70 μ m) and centrifugation (2000 rpm, 5 min). The cells were resuspended in 40 v/v% Percoll (GE Healthcare, Chicago, IL, USA), followed by the addition of 55 v/v% Percoll at the bottom. The concentrated cancer cells were collected at the interface after centrifugation (2000 rpm, 20 min). The intracellular and plasma cholesterol levels were measured using the abovementioned procedures.

Viability and apoptosis assays of cancer cells. The viability and apoptosis of Me β CD or Chol-treated cancer cells were evaluated using Annexin V and 7-AAD (or DAPI) staining. Briefly, B16F10 (or EG7-OVA, MC38-HER2, and Me275-HER2) cancer cells were incubated with DMEM medium supplied with Me β CD or Chol (5 mM) at 37 °C for 30 min, and washed with PBS twice. The treated cancer cells were then stained with fluorescently-labeled Annexin V and 7-AAD (0.5 μ g/mL in PBS, or DAPI, 0.1 μ g/mL in PBS) for flow cytometry analysis.

In another assay, B16F10 cancer cells were treated with Me β CD (5 mM in DMEM medium) at 37 °C for 30 min. After washing with PBS twice, the cancer cells were resuspended in DMEM medium (10 v/v% FBS and 10 mM HEPES) followed by the addition of various concentrations of recombinant mouse FasL plus anti-His Tag antibody (5 μ g/mL) for multimerization²⁰⁸ or TNF- α in DMEM medium (10 v/v% FBS and 10 mM HEPES) and incubation at 37 °C for 5 h. After washing with PBS (0.2 w/v% BSA), the cancer cells were stained with fluorescently-labeled Annexin V and DAPI for flow cytometry analysis. Similarly, various concentrations of active perforin-1 in PBS were added to cancer cells resuspended in Hank's Balanced Salt Solution (HBSS, Gibco) supplemented with BSA (0.4 w/v%), HEPES (10 mM), and CaCl₂ (5 mM), of which

the viability was determined by DAPI staining and flow cytometry analysis. To generate membrane tension on cancer cells, a hypotonic (H₂O instead of PBS) buffer was used to dilute perforin.

Measurement of cell cortical stiffness by atomic force microscope (AFM). The measurement of cell cortical stiffness using AFM followed a well-established protocol.¹⁸⁰ In brief, AFM force curves were recorded using a customized Dimension Icon AFM (Bruker, Billerica, MA, USA) mounted on an IX81 inverted optical microscope (Olympus, Tokyo, Japan) equipped with a 20× objective and a heating stage for live-cell imaging. The samples were mobilized using an XY stage until the cell of interest was placed under the AFM tip as visualized through the optical microscope. Force curves on the cell were recorded at a ~5 µm/s rate in relative trigger mode (15 nm trigger threshold) using a PNP-TR-B cantilever (Nanoworld, Neuchâtel, Switzerland). The cantilever spring constant was 0.08 N/m, measured using the deflection sensitivity (170 nm/V) and a thermal tune. Measurement was performed on single cells at 37 °C before and after treatment with Chol or MeßCD (5 mM, 15 min at 37 °C). Nanoscope Analysis software (Bruker) was used to process the force curves and calculate the sample Young's Modulus by doing a fit of the approach curve less than 500 nm indentation (to take into account only the cortical stiffness), assuming a cortex Poisson's ratio of 0.3.

Measurement of cell cortical stiffness by optical tweezer. The measurement of cell cortical stiffness by optical tweezer was adapted from a well-established method in the literature¹⁸¹. The laser beam (10 W, 1064 nm) was tightly focused through a series of Keplerian beam expanders and a high numerical aperture objective (100×/1.45, oil immersion, Nikon). A high-resolution quadrant detector (PDQ80A, Thorlabs, Newton, NJ, USA) was used for force measurement. To measure the mechanical properties of the cell cortex, polystyrene particles (500 nm in diameter, orange fluorescence) were added to the culture medium and endocytosed by the cells. The particle was then dragged by optical tweezers toward the cell membrane to deform the cell cortex with a speed of 1 µm/s. The displacement of the particle and the resistant force were recorded by the quadrant photodetectors. The stiffness of the cell cortical structure, including plasma membrane and cell cortex, was defined by the slope of the force-displacement curve. The data collection and post-processing were performed using MATLAB (Mathworks, Natick, MA, USA).

Deformability cytometry (DC). DC setup was built following a published report¹⁸². A 4-inch silicon wafer was selectively etched using photolithography and deep reactive ion etching to fabricate the microfluidic device. The height, width, and length of the constriction area were measured using a mechanical profiler (Dektak[®] XT, Bruker) as 30 µm, 30 µm, and 300 µm, respectively. The chosen geometry ensured that the cells were correctly deformed. The projected areas of cells were 90% to 50% of the cross-sectional area of the constriction zone. Devices were cast using a 10:1 mixture of polydimethylsiloxane (PDMS) (Sylgard 184, Dow Corning, Midland, MI, USA) from the microfabricated molds by curing the prepolymer overnight at 65 °C. Glass coverslips (No.1, VWR, Radnor, PA, USA) were cleaned thoroughly by soaking them in acetone, isopropyl alcohol, ethanol, and distilled water, and subsequently dried at 65 °C to avoid any possible leakage in the microfluidic device due to the high viscosity of the solutions and high flow rate. The surfaces of the coverslips and PDMS devices were treated with a plasma cleaner (PDC-002-HPCE, Plasma Harrick, Ithaca, NY, USA) at 29 Watt for 45 seconds prior to bonding. They were subsequently compressed using a 1-kg weight overnight at 100 °C to ensure firm and robust attachment.

In a typical DC measurement, cells were flowed through a microfluidic chamber at a rate of 4 $\mu\text{L}/\text{min}$ (Me275-HER2) or 5.34 $\mu\text{L}/\text{min}$ (B16F10, EG7-OVA, and MC38-HER2). The cells were centered in the microfluidic channel using a sheath flow (Fig. 12a). The sheath flow rate was set at 3 \times the cell flow rates, i.e., 12 $\mu\text{L}/\text{min}$ or 16 $\mu\text{L}/\text{min}$, respectively. The flow rates were controlled with a programmable syringe pump (neMESYS 290N, Cetoni, Korbußen, Germany). Prior to the measurement, the cells were treated with Me β CD or Chol as mentioned above or kept in PBS without treatment. The cells were then suspended in a methyl-cellulose solution (0.6 w/v% in HBSS) at a concentration of 2×10^6 cells/mL. The cells were passed through the narrow constriction zone of 30 $\mu\text{m} \times 30 \mu\text{m} \times 300 \mu\text{m}$ (height \times width \times length) and visualized using an inverted microscope (Nikon) equipped with a 20 \times objective and a high-speed camera (VEO640L, Phantom, Wayne, NJ, USA). To ensure that cell deformation was measured at the equilibrium state, a region of interest (ROI) of 128 \times 256 pixels was imaged at the end of the channel where the laminar flow was fully developed. The cell imaging was performed using the following camera parameters: exposure time, 1 μs ; frame rate, 7000 or 10,000 frames per second (fps). Time-lapse movies containing several thousands of cells were analyzed using a custom ImageJ macro (Bioimaging and Optics Platform, EPFL). Briefly, the cell contour was first identified based on greyscale value. Subsequently, a convex hull (Convex Hull, ImageJ) was fitted on the cells to avoid a large increase in cell perimeter. The measured projected cellular area and perimeter were used to calculate the deformation (D) defined as:

$$D = 1 - \frac{2\sqrt{\pi A}}{l}$$

where A is the projected cell surface area and l is the cell perimeter.

Further post-processing was performed using MATLAB. In particular, cells with irregular shapes or poor contour identification were eliminated as proposed in published literature²⁰⁹. Briefly, the ratio R of the projected area was calculated using the hull approximation A_{hull} and the greyscale values A_{contour} as:

$$R = \frac{A_{\text{contour}}}{A_{\text{hull}}}$$

Cells with $R \geq 1.07$ were eliminated in the final analysis.

Deformations of cell populations with different cell areas were compared using iso-elasticity lines plotted using Shape-Out (Paul Müller and others, version 2.7.4). In order to input the data in Shape-Out, the above post-processed data in xlsx format were converted into the H5 format using MATLAB.

Fabrication and rheological analysis of polyacrylamide (PA) hydrogel substrates. PA hydrogel substrates were prepared using a protocol adapted from reported literature.²¹⁰ Briefly, a 96-well glass-bottom plate (Falcon, Corning, NY, USA) was treated with a NaOH solution (0.1 M in H₂O, 50 μL per well) for 5 min at room temperature (Fig. 3:13a). Upon removing NaOH solution, APTMS (20 μL per well) was applied for 3 min at room temperature. The well plate was then thoroughly rinsed with de-ionized (DI) water to remove any remaining APTMS followed by adding a glutaraldehyde

solution (0.5 wt% in H₂O, 50 μ L per well) and incubation at room temperature for 20 min. The well plate was subsequently rinsed with DI water and dried in the air for 30 min. To prepare PA hydrogels of different stiffness (PA-1 and 2 as shown in Fig. 3:13b), we made the PA hydrogel precursor solutions (30 μ L per well) with various concentrations of acrylamide monomer and bis-acrylamide cross-linker. Ammonium persulfate (0.1 w/v% in final concentration) and TEMED (0.1 v/v% in final concentration) were then added to initiate the polymerization, followed by brief vortexing and incubation at room temperature for 1 h. The hydrogel substrates were then washed with PBS (200 μ L per well \times 2) to remove any unreacted acrylamide. To facilitate cell attachment, fibronectin was conjugated to the hydrogel surface using the heterobifunctional linker Sulfo-SANPAH. In brief, a Sulfo-SANPAH solution (1 mg/mL in milli-Q H₂O, 20 μ L per well) was pipetted onto the hydrogel surface followed by UV irradiation (365 nm, 0.8 mW, 20 mA) for 10 min and washing with HEPES buffer (50 mM in PBS) twice. After incubation with fibronectin solution (50 μ g/mL in PBS, 50 μ L per well) at 4 °C overnight and washing for three times with PBS, the coated PA hydrogels were stored in PBS at 4 °C before use.

DHR3 shear rheometer (TA Instruments, New Castle, DE, USA) with a parallel plate (8 mm in diameter) was used for the rheological test. The shear storage modulus G' was measured using the following parameters: strain, 5%; frequency, 5 rad/s. PA hydrogel sample of a typical thickness of 1.5 mm and a diameter of 14 mm was measured at a constant axial force of 0.5 N and a constant temperature of 37 °C. The tensile elastic modulus E (Young's modulus) was retrieved using: $E = 2 \times (1+n) \times G'$, where $n = 0.45$ for the Poisson's ratio of polyacrylamide.

Activation of Pmel and OT-I CD8⁺ T cells. Spleens collected from Pmel Thy1.1⁺ mice were ground through a cell strainer (70 μ m) at day 0. Red blood cells were lysed with ACK lysing buffer (2 mL per spleen) at room temperature for 5 min. After washing twice with PBS, splenocytes were cultured in complete RPMI 1640 medium supplemented with FBS (10 v/v%), HEPES (1 v/v%), penicillin/streptomycin (1 v/v%), and β -mercaptoethanol (0.1 v/v%) in the presence of hgp100 peptide (1 μ M), recombinant mouse IL-2 (10 ng/mL) and recombinant mouse IL-7 (2 ng/mL) for 3 days. After Ficoll-Paque Plus (GE Healthcare) gradient separation to eliminate dead cells, the activated Pmel CD8⁺ T cells (purity > 95%) were maintained in the medium containing recombinant mouse IL-2 (10 ng/mL) and IL-7 (10 ng/mL) and used between day 4 to 8 post splenocyte collection for in vitro or in vivo studies. Activated OT-I CD8⁺ T cells were obtained from the spleens of OT-I mice using a similar protocol by replacing hgp100 peptide with SIINFEKL peptide.

In vitro killing assays of cancer cells by T cells. B16F10 cancer cells were seeded on fibronectin-coated hydrogel substrates and incubated overnight. Afterward, B16F10 cancer cells were pulsed with hgp100 peptide (2 μ M in complete RPMI 1640 medium) for 30 min and then treated with Me β CD, Chol, α CD, or maltodextrin (5 mM in DMEM medium) at 37 °C for another 30 min followed by washing with PBS twice. In another group, after hgp100 peptide pulsing, the cancer cells were treated with various concentrations of 4-HAP in PBS for 30 min followed by washing with PBS twice. The cancer cells were immediately added with a suspension of activated Pmel CD8⁺ T cell in complete RPMI 1640 medium at an effector:target (E:T) ratio of 10:1 and co-cultured at 37 °C for 5 h. In a control sample, a Triton X-100 solution (0.1 wt%) was added to determine the 100% cell lysis. To quantify target cell death, supernatant from each well was retrieved for lactate dehydrogenase (LDH) cytotoxicity assay using a CytoTox 96[®] Non-Radioactive Cytotoxicity Assay kit (Promega, Madison, WI, USA) according to the manufacturer's recommended protocol. In another experiment, Me β CD-

treated B16F10 cancer cells were further cultured in DMEM medium (10 v/v% FBS) at 37 °C for an additional 12 h, and pulsed with hgp100 peptide (2 μ M in complete RPMI 1640 medium) for 30 min followed by the addition of Pmel CD8⁺ T cells for the killing assay. In mechanism experiments, T cells were pre-treated with various cytoskeleton inhibitors (2 μ M LatA for 10 min, 100 μ M Bleb for 10 min, or 1 μ M MycaB for 15 min) at 37 °C to inhibit T cell forces before adding to the co-culture.

In the killing assay for EG7-OVA cancer cells, the cancer cells were first pulsed with SIINFEKL (5 μ M in complete RPMI 1640 medium) for 30 min and then treated with Me β CD (5 mM in DMEM medium) at 37 °C for another 30 min followed by washing with PBS twice. Next, a suspension of activated OT-I CD8⁺ T cell (pre-labeled with 2 μ M CFSE at 37 °C for 5 min) in complete RPMI 1640 medium was added at E:T ratios of 1:1 or 5:1. After a co-culture at 37 °C for 5 h, the cell death of EG7-OVA cancer cells was quantified by DAPI staining and flow cytometry analysis. Pmel CD8⁺ T cell-mediated killing of B16F10 (or ACAT1 KD and ACAT1 OE B16F10) cancer cells were analyzed at an E:T ratio of 10:1 using a similar killing assay (without Me β CD treatment) by pulsing cancer cells with hgp100 peptide (2 μ M).

Production of mouse interleukin-15 super-agonist (IL-15SA). The engineered IL-15SA construct (gWIZ-mIL-15SA) was a generous gift from Prof. Darrell J. Irvine (MIT, USA). As shown in Fig. 3:18a, the IL-15SA contains a mouse IL-15 fused at the C-terminal of Sushi domain of a mouse IL-15 receptor α (IL-15R α), which is next fused at the C-terminal with a mouse IgG2 Fc. IL-15SA was expressed by HEK293-E cells (Gibco) in Freestyle medium at the EPFL Protein Production and Structure Core Facility (PTPSP). The supernatant of the culture medium containing IL-15SA was harvested by centrifugation after a 7-day culture and was filtered through a filter membrane (0.22 μ m) to obtain a clear solution. The IL-15SA was first captured with a HiTrap Protein A affinity chromatography column on the AKTA pure 25 system (GE Healthcare) and eluted with an elution buffer (0.05 M sodium citrate, 0.3 M sodium chloride, pH = 3.0). The eluted protein was next collected immediately in a neutralization buffer (1 M Tris-HCl, pH = 10.0) followed by concentration with membrane ultrafiltration (molecular weight cut-off 10 kDa) in a Vivaspinn (GE Healthcare). The concentrated protein solution was further purified with a Superdex 200 increase size exclusion column (GE Healthcare) at a flow rate of 1.0 mL/min with PBS buffer on the AKTA pure 25 system. The purity and activity of IL-15SA were confirmed with sodium dodecyl sulfate-polyacrylamide gel electrophoresis (SDS-PAGE) (Fig. 3:18b) and T cell proliferation assay (Supplementary Fig. 3:18c), respectively. The purified protein was aliquoted and stored at -80 °C before use.

Adoptive T cell transfer (ACT) therapy in solid tumor models. In an experiment with cholesterol supplementation in tumour (Fig. 3:14), B16F10 melanoma cells (0.5×10^6) in PBS (100 μ L) were inoculated subcutaneously in the right flanks of Thy1.2⁺ C57BL/6J mice at day 0. Recipient mice were randomized before ACT. Activated Pmel Thy1.1⁺CD8⁺ T cells (5×10^6) were intravenously infused via the tail vein into recipient mice at day 7. In another group, post-T cell transfer mice received the intratumoral injections of Chol every other day (2 mg/dose in 100 μ L PBS \times 8; day 7 to 21). Tumour area (product of measured orthogonal length and width) and body weight were monitored every 2 days. Mice were euthanized when the body weight loss was higher than 20% of the pre-dosing weight or the tumor area reached 150 mm².

In the experiments with ACAT1 KD or ACAT1 OE B16F10 tumors, native, ACAT1 KD, or ACAT1 OE B16F10 cells (0.5×10^6) in PBS (100 μ L) were inoculated subcutaneously in the right flanks of Thy1.2⁺ C57BL/6J mice at day 0. Tumor-bearing mice were randomized and treated similarly with PBS or activated Pmel Thy1.1⁺CD8⁺ T cells (5×10^6) through intravenous injection at day 6. Mice were then monitored as described above.

In an experiment for cancer-cell stiffening with Me β CD, B16F10 melanoma cells (0.5×10^6) were inoculated similarly in Thy1.2⁺ C57BL/6J mice at day 0. At day 9, activated Pmel Thy1.1⁺CD8⁺ T cells (5×10^6) were intravenously infused via the tail vein into recipient mice followed by intratumoral injections of IL-15SA (10 μ g/dose in 50 μ L PBS) on day 9, 11, and 13, and daily intratumoral injections of Me β CD (1 mg/dose in 50 μ L PBS) from day 9 to 18. Mice receiving PBS, Me β CD only, maltodextrin only, ACT + IL-15SA, or ACT + IL-15SA + maltodextrin served as controls. In another therapeutic experiment (Fig. 3:19), B16F10 tumor-bearing mice received three adoptive transfers of activated Pmel Thy1.1⁺CD8⁺ T cells (5×10^6 per injection) on day 5, 11, and 22 without IL-15SA adjuvant. A similar therapeutic experiment was conducted with Thy1.2⁺ C57BL/6J mice bearing subcutaneous EG7-OVA lymphoma tumors (0.5×10^6 cancer cells inoculated per mouse at day 0; Fig. 3:20), which received two intravenous infusions of activated OT-I CD8⁺ T cells (5×10^6 per injection) on day 11 and 15 followed by intratumoral injections of IL-15SA (5 μ g/dose in 50 μ L PBS \times 5; every other day from day 11 to 19) and Me β CD (1 mg/dose in 50 μ L PBS \times 10; daily from day 11 to 20). Mice were monitored as described above.

Characterizations of tumor-infiltrating leukocytes by flow cytometry analyses. B16F10 melanoma cells (1×10^6) were inoculated subcutaneously in the right flanks of Thy1.2⁺ C57BL/6J mice at day 0. At day 9, activated Pmel Thy1.1⁺CD8⁺ T cells (5×10^6 per injection) were intravenously infused via the tail vein into tumor-bearing mice followed by intratumoral injections of IL-15SA (10 μ g/dose in 50 μ L PBS \times 2; day 9 and 11) and Me β CD (1 mg/dose in 50 μ L PBS \times 5; daily from day 9 to 13). Mice receiving PBS, Me β CD only, or ACT + IL-15SA served as controls. Mice were euthanized at day 14, and tumor tissues were collected and ground through a cell strainer (70 μ m). Red blood cells were lysed with ACK lysis buffer at room temperature for 5 min. All cells were stained with Aqua live/dead stain (Invitrogen) followed by surface marker staining in buffer (PBS, 0.2 w/v% BSA) with the corresponding antibodies at 4 °C for 20 min. For transcription factor staining, cells were stained for surface markers first followed by fixation and permeabilization with Foxp3/Transcription Factor Staining Buffer Set (eBioscience, San Diego, CA, USA) and addition of fluorescent antibodies against intracellular transcription factors. For intracellular cytokine staining, cells were first stimulated in a complete RPMI 1640 medium containing 1 \times Cell Activation Cocktail with Brefeldin A (Biolegend) at 37 °C for 4 h. Following surface staining, cells were fixed and permeabilized with Cyto-Fast Fix/Perm Buffer Set (Biolegend) and stained with the fluorescent antibodies against cytokines. Flow cytometry analysis was performed with Attune NxT flow cytometer (Invitrogen), and data analysis was performed using FlowJo software (Tree Star, BD Biosciences, Franklin Lakes, NJ, USA).

Flow cytometry analyses of cancer cells and T cells from in vitro co-culture assays. For analysis of B16F10 (or B16F10-OVA) cancer cells only, cells were treated with Me β CD (5 mM in DMEM medium) at 37 °C for 30 min, and then stained with fluorescently labeled anti-H-2K^b-SIINFEKL, anti-Fas, and anti-PD-L1 antibodies for flow cytometry analysis.

In a typical co-culture assay, B16F10 cancer cells were seeded on a 96-well plate and incubated overnight for cell attachment. Afterward, B16F10 cancer cells were pulsed with hgp100 peptide (2 μ M in complete RPMI 1640 medium) for 30 min and then treated with Me β CD (5 mM in DMEM medium) for another 30 min followed by washing with PBS twice. Next, a suspension of activated Pmel CD8⁺ T cell in complete RPMI medium supplemented with FBS (10 v/v%) was added to each well at an E:T ratio of 10:1. In a similar co-culture assay, B16F10 cancer cells were pulsed with various concentrations of SIINFEKL peptide and then added with a suspension of activated OT-I CD8⁺ T cells at an E:T ratio of 10:1. For T cell function and cytokine secretion analyses, Brefeldin A (5 μ g/mL) and Monensin (2 μ M) were added to the co-culture. After 5-h co-incubation at 37 °C, T cells were stained with fluorescently-labeled anti-PD-1, anti-CD69, anti-FasL, anti-CD107a, anti-LFA-1, anti-CD49d, anti-granzyme B, anti-TNF- α , anti-IFN- γ , and anti-IL-2 antibodies for flow cytometry analysis.

To determine the protein phosphorylation in T cells, the plate for co-culture was centrifuged at 1500 rpm for 2 min followed by a brief co-incubation for 5 min. To detect phosphorylation of TCR signalling proteins ZAP70, Erk1/2 and NF- κ B, T cells were fixed with a paraaldehyde solution (1.5 w/v% in PBS) and then permeabilized by resuspending in ice-cold MeOH at 4 °C for 10 min followed by washing with PBS (0.2 w/v% BSA). Next, T cells were stained with fluorescently-labeled anti-phospho-ZAP70, anti-phospho-Erk1/2, or anti-phospho-NF- κ B p65 antibodies for flow cytometry analysis. The MFI of phospho-ZAP70, Erk1/2, and NF- κ B p65 were normalized by the corresponding levels in unstimulated Pmel CD8⁺ T cells. To detect phosphorylation of Pyk2, T cells were fixed with paraaldehyde solution (1.5 w/v% in PBS) and then permeabilized by resuspending in Triton X-100 solution (0.1 w/v% in PBS) at 25 °C for 5 min. After washing with PBS (0.2 w/v% BSA), T cells were stained with anti-phospho-Pyk2 antibody and then fluorescently-labeled secondary antibody for flow cytometry analysis.

In another assay, B16F10 cancer cells were seeded on a 48-well plate and incubated overnight for cell attachment. A suspension of activated Pmel CD8⁺ T cell in complete RPMI medium supplemented with FBS (10 v/v%), recombinant mouse IL-2 (10 ng/mL), and Me β CD (0.05 mM) was then added to each well at an E:T ratio of 1:1. After 48-h co-incubation at 37 °C, T cells and B16F10 cells were collected for flow cytometry analysis.

In conjugation assay, B16F10 cancer cells were first labeled with CFSE (2 μ M in PBS, 5 min) and then mixed with activated Pmel CD8⁺ T cells at an E:T ratio of 1:1. The mixture was centrifuged to facilitate cell-cell contact and then incubated in the presence of PE-anti-CD45.2 antibodies at 37 °C for 10 min. Afterward, the cells were resuspended in PFA solution (1 w/v% in PBS) for fixation and analyzed by flow cytometry. The conjugation efficiency was calculated as $(CFSE^+PE^+)/((CFSE^+) \times 100\%)$.

Preparation of fluorescent bead-embedded PA hydrogel substrates for traction force microscopy (TFM). To prepare biotinylated anti-CD3 and anti-CD28 antibodies for hydrogel surface coating, a NHS-Biotin (10 mM) solution in DMSO was added to a solution of anti-CD3 or anti-CD28 antibodies (2 mg/mL in PBS) at a final concentration of 300 μ M of NHS-Biotin. After 30 min incubation on a shaker at room temperature, the biotinylated antibody solution was washed with PBS (500 μ L \times 5) using an ultra-centrifugal filter with 30-kDa cutoff (Amicon®, Merck), and the final protein concentration

was determined with a microvolume UV-Vis spectrophotometer (NanoDrop One, Thermo Fisher Scientific). The biotinylated antibodies were stored at 4 °C before use.

The antibody-coated hydrogel substrates for TFM were prepared according to a protocol adapted from the published literature.⁸¹ Briefly, NaOH solution (1 mL, 0.1 M in H₂O) was added on top of a coverslip (Carl Roth, thickness 0.17 mm, diameter 25 mm) and heated at 70 °C until a film of dried NaOH was formed. APTMS was then added on the coverslip surface and incubated at room temperature for 5 min. After rinsing the coverslips with DI water, glutaraldehyde (0.5 wt% in H₂O) was added for 30 min. The amino-silanated coverslip was rinsed with DI water. Next, the hydrogel precursor solution (PA-3, 4, and 5 as shown in Fig. 3:13b) containing fluorescent PS beads (0.6 w/v%, 200 nm), streptavidin acrylamide (0.2 mg/mL), ammonium persulfate (0.1 wt%), and TEMED (0.1 v/v%) was pipetted onto a methyl-silanated glass slide. The amino-silanated coverslip with the treated side facing down was placed on top of the solution to create a sandwich structure. After polymerization for 1 h, the coverslip-hydrogel composite was immersed in PBS for 5 min twice to remove any unpolymerized acrylamide. Afterwards, a PBS solution of biotinylated anti-CD3 (10 µg/mL) and biotinylated anti-CD28 (10 µg/mL) or biotinylated anti-mouse CD45 (20 µg/mL, Clone 30F-11, Biolegend) was added onto the hydrogel surface and incubated at 37 °C for 1 h. Finally, the coverslip-hydrogel composite was immersed in PBS for 5 min to remove free antibodies. The fluorescent bead-embedded, antibody-coated hydrogel substrates were stored in PBS at 4 °C before use.

TFM measurement of T cell forces. The experiment was performed using an inverted microscope (IX83, Olympus) equipped with a spinning disk confocal scanner (CSU-W1, Visitron, Puchheim, Germany), a 60×/1.42 UPLSAPO objective (Olympus), and a sCMOS camera (Orca Flash 4.0, Hamamatsu, Shizuoka, Japan). The experiment was performed at 37 °C with 5% CO₂. The microscope was pre-heated to 37 °C for at least 2 h prior to the experiment. The gels and all reagents were kept at 37 °C during the experiment. At the start of the experiment, activated Pmel T cells (1×10^5) were added onto the gel in RPMI 1640 medium without phenol red (Gibco) supplemented with FBS (10 v/v%), HEPES (1 v/v%), penicillin/streptomycin (1 v/v%), and β-mercaptoethanol (0.1 v/v%). After a 20-min incubation at 37 °C, unbound or weakly bound cells were removed by aspirating the medium and replacing it with a fresh medium. Z-stack imaging of the cells (Brightfield) and the gel (RFP channel) were captured 30 min after the addition of the cells to the gel. Afterward, SDS (50 µL, 0.5 w/v%) was added to the medium to lyse the cells, and the unstressed gel was imaged 5 min later. The same procedure was repeated on hydrogels of various stiffness (PA-3, 4, and 5 as shown in Fig. 13b). As a control group, activated Pmel T cells were treated with LatA (2 µM in PBS) at 37 °C for 10 min before TFM measurement. To measure T cell forces post pre-treatment with LatA (2 µM at 37 °C for 10 min) or MycaB (1 µM at 37 °C for 15 min), pre-treated T cells were incubated in the complete RPMI medium supplemented with FBS (10 v/v%) at 37 °C for 0 h or 5 h followed by the measurement procedure described above.

The cellular forces were measured using an automated ImageJ macro (Bioimaging and Optics Platform, EPFL). The top layer of the PA gel was automatically found in both stressed and unstressed gels, combined into an image pair, and the drift was corrected using the “Linear stack alignment with SIFT” plugin in ImageJ. The particle displacement and force maps were generated using freely-available particle image velocimetry (PIV) analysis and Fourier transform traction

cytometry (FTTC) plugins.²¹¹ The PIV plugin was run with the cross-correlation iteration option (piv1=128 sw1=128 vs1=64 piv2=64 sw2=64 vs2=32 piv3=32 sw3=32 vs3=16). The FTTC analysis was performed using the following parameters: Poisson ratio, 0.5; Young's modulus, 210/560/890 Pa. The cell contour was automatically identified from the brightfield Z-stacks. The force field and cell contour were exported and post-processed using MATLAB. Briefly, the stress under the cell was multiplied by the area of the final interrogation window (vector spacing vs3) to yield the cellular force (F_{cell}). The background noise of each gel was calculated by averaging the stress values of the gel away from the cell. The cellular force was corrected ($F_{corrected}$) by subtracting the noise of an area equivalent to the cell area (F_{noise}) from F_{cell} :

$$F_{corrected} = F_{cell} - F_{noise}$$

F-actin imaging of T cells on PA hydrogel substrates with varying stiffness. PA hydrogel substrates with varying stiffness were fabricated on glass-bottom dishes (35 mm, glass-bottom diameter 20 mm, ibidi, Gräfelfing, Germany) and coated with anti-CD3 and anti-CD28 antibodies as described above. Activated Pmel CD8⁺ T cell suspension in complete RPMI medium supplemented with FBS (10 v/v%) was added on hydrogels on glass-bottom dishes and centrifuged at low speed (1500 rpm) for 2 min to bring the T cells into contact with the hydrogel surface. After incubation for 10 min, T cells were fixed with a formaldehyde solution in PBS (4 w/v%) at room temperature for 20 min followed by washing with PBS twice. T cells were next permeabilized using Triton X-100 in PBS (0.1 w/v%) at room temperature for 5 min. After washing with PBS twice, T cells were stained with phalloidin-iFluor™ 488 (1/1000 dilution according to the manufacturer's recommended protocol) and Hoechst 33342 (5 µg/mL) in PBS (1 wt% BSA) at room temperature in the dark for 30 min. After washing with PBS three times, Fluoromount-G mounting medium (300 µL, Invitrogen) was added on the hydrogel surface, and a coverslip (thickness 0.17 mm, diameter 25 mm) was placed on top to seal the glass bottom. The confocal images were acquired using an inverted microscope (IX83, Olympus) equipped with a spinning disk confocal scanner (CSU-W1, Visitron) and a 100×/1.40 UPLSAPO objective (Olympus). T cells in Fig. 3:7d were imaged at high resolution (Z-stack step size, 150 nm) and deconvoluted using Huygens Remote Manager (Scientific Volume Imaging, Hilversum, Netherlands). The F-actin fluorescence images in the XZ plane (side view) were obtained by summing 20 slices in the XZ plane in the middle of the cells (*Z project* plugin). The intensity display settings are identical for each side view image (1500-25000). The F-actin fluorescence images at the immunological synapse (IS, defined as the structure between the surface of hydrogel and a height of 2 µm above the surface of the hydrogel) of T cell were obtained by overlaying Z-stack slices located within the IS. The intensity display settings are identical for each IS image (0-18000).

The total F-actin fluorescence intensity at the IS of T cell was measured using a semi-automated ImageJ macro (Bioimaging and Optics Platform, EPFL). Briefly, Z-stack slices located within the IS were summed (*Z project* plugin). The resulting image was thresholded (*Threshold* plugin) and holes filled (*Fill Holes* plugin). Cell contours were automatically identified (*Analyze Particles* plugin). Further post-processing was performed using MATLAB. The corrected F-actin fluorescence intensity per pixel at the IS was obtained by subtracting the average background value from the average F-actin fluorescence intensity per pixel at the IS. Finally, to calculate the total F-actin fluorescence intensity at the IS, the corrected F-actin fluorescence intensity per pixel was multiplied by the cell area.

Statistical analyses. Data are presented as mean \pm standard error of the mean (SEM) unless otherwise noted. Violin plots show frequency distribution curves created by kernel density method in which the middle solid line shows median, and lower and upper dash lines show 25th and 75th percentiles, respectively. Statistical analysis for each experiment is specified in the corresponding figure legend. Statistical analyses were performed using GraphPad Prism 8 software. In all cases, two-tailed tests with *P* values of less than 0.05 were considered significant.

3.5.2 Supplementary figures

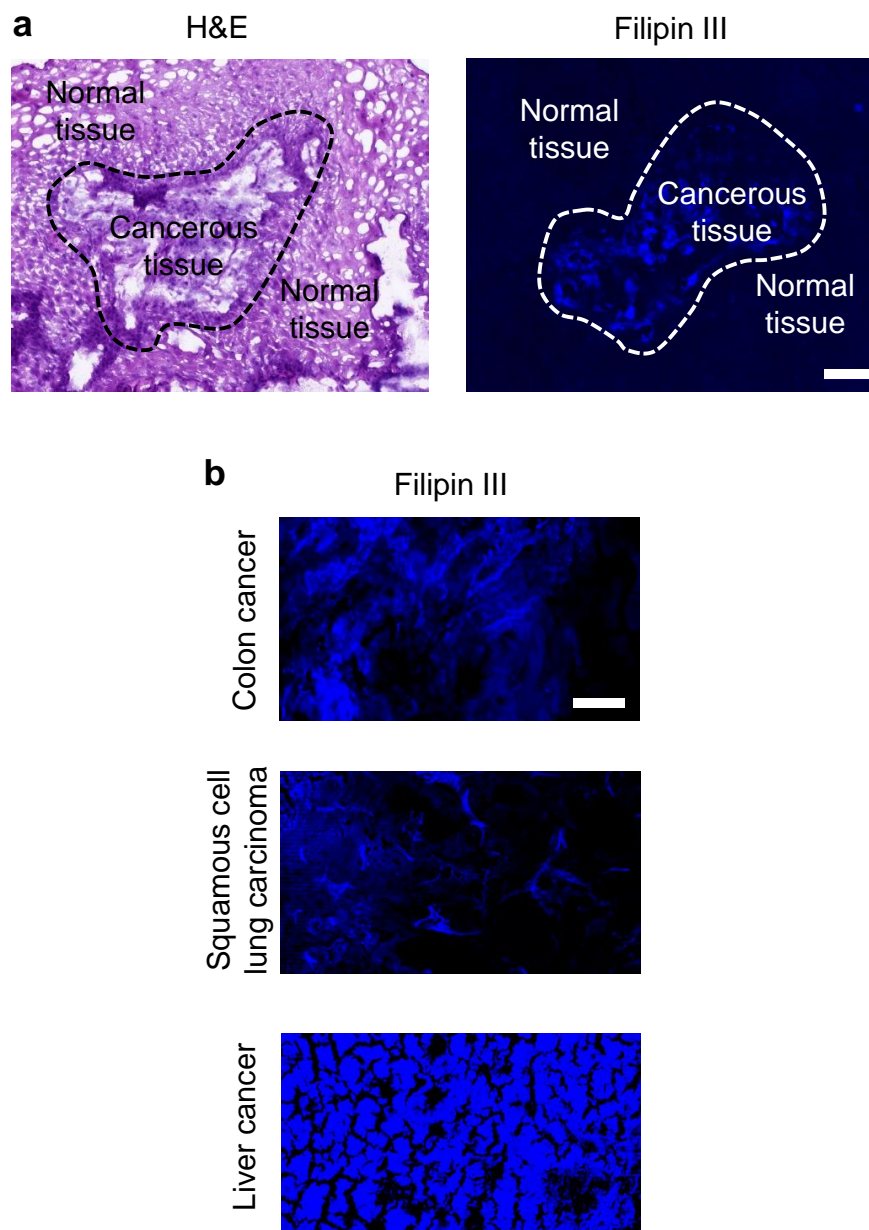


Figure 3:9 Cholesterol level is upregulated in various human cancer tissues.

a, Human small cell lung cancer tissue (indicated within the dashed line) and its adjacent normal tissue from a patient were stained with hematoxylin and eosin (H&E) and Filipin III (shown in blue color). Scale bar, 100 μ m. **b**, Filipin III staining (shown in blue color) of human colon cancer, squamous cell lung carcinoma, and liver cancer biopsies from patients. Scale bar, 100 μ m.

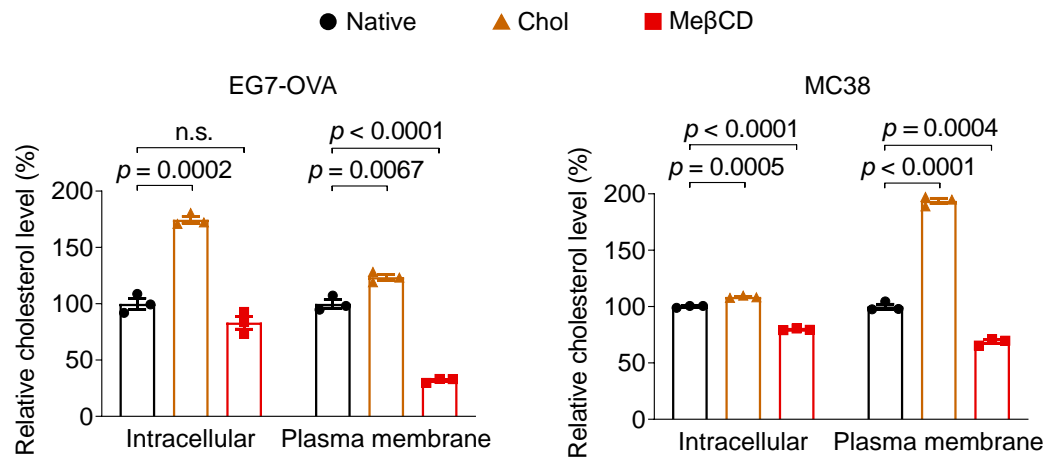


Figure 3:10 Treatment of water-soluble cholesterol/methyl- β -cyclodextrin complex (Chol) or methyl- β -cyclodextrin (Me β CD) significantly increases or decreases cholesterol levels in plasma membranes of various cancer cells, respectively.

Relative intracellular and plasma membrane cholesterol levels of native, Chol (5 mM), and Me β CD (5 mM)-treated cancer cells at 37 °C for 30 min ($n = 3$). Native cancer cells serve as a standard (100%). Data are one representative of two independent experiments with biological replicates. P values were determined by unpaired Student's t test. Error bars represent standard error of the mean (SEM). n.s., not significant.

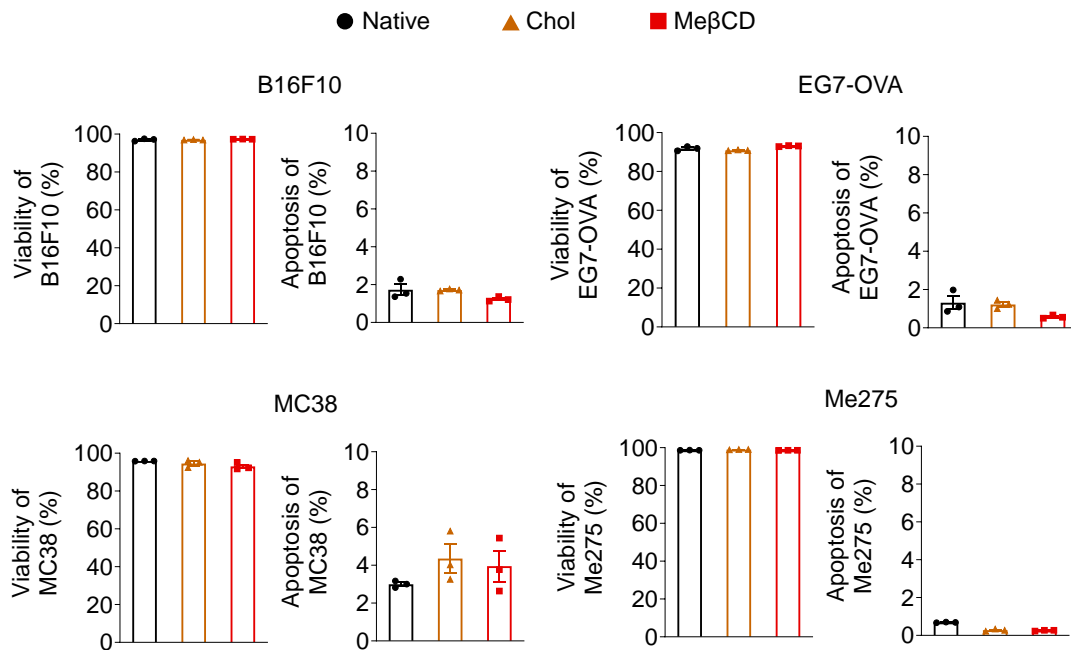


Figure 3:11 Treatment of Chol or Me β CD shows negligible impacts on the viability or apoptosis of various cancer cell lines.

Viability and apoptosis percentage of indicated cancer cell lines after treatment with Chol (5 mM) or Me β CD (5 mM) at 37 °C for 30 min ($n = 3$). Data are one representative of at least two independent experiments with biological replicates. Error bars represent SEM.

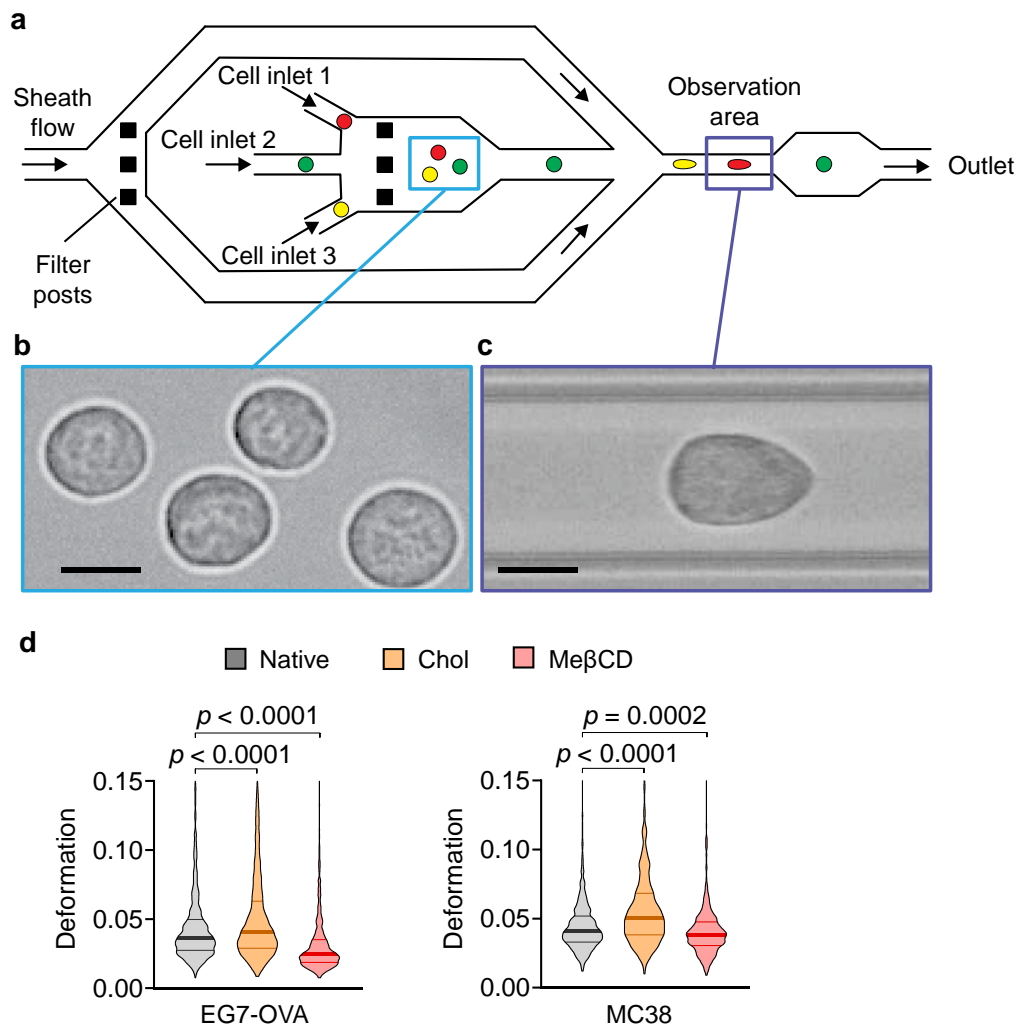


Figure 3:12 Treatment of Chol or Me β CD softens or stiffens various cancer cells, respectively, measured by deformability cytometry (DC).

a, Schematic illustration of the microfluidic device for DC. The deformations of native, Chol-, and Me β CD-treated cancer cells were measured using the same microfluidic device that has three inlets dedicated for different groups. Cells from different groups were introduced through the designated inlets in sequence, and the cell deformation generated by the sheath flow was recorded in the observation area. Microfabricated posts serve as size-selective filters to remove cell aggregates. **b**, A representative image of the cells before they were introduced to the constriction showing that the majority of cells had round shapes. Scale bars, 15 μm . **c**, A representative image of a deformed cell that is passing through the observation area. The cells display a characteristic bullet shape because they were deformed by shear stresses and pressure gradients. Scale bars, 15 μm . **d**, Quantitative cell deformation of native, Chol-, and Me β CD-treated EG7-OVA ($n = 2026, 1947, \text{ and } 1947$, respectively) or MC38 ($n = 999$ for each group) cancer cells (outliers not shown). In the violin plots, the middle solid line shows median, and lower and upper dash lines show 25th and 75th percentiles, respectively. P values were determined by unpaired Student's t test.



Sample	Acrylamide (w/v %)	Bis-acrylamide (w/v %)	Young's Modulus (kPa)
PA-1	10	0.35	55 ± 3
PA-2	18	0.38	143 ± 5
PA-3	4	0.10	0.26 ± 0.01
PA-4	4	0.11	0.51 ± 0.07
PA-5	4	0.13	0.89 ± 0.02

a, Schematic illustration of the fabrication process of PA hydrogels on a glass-bottom well plate. **b**, Summary of the compositions and Young's modulus of PA hydrogel substrates (n = 3 independent samples).

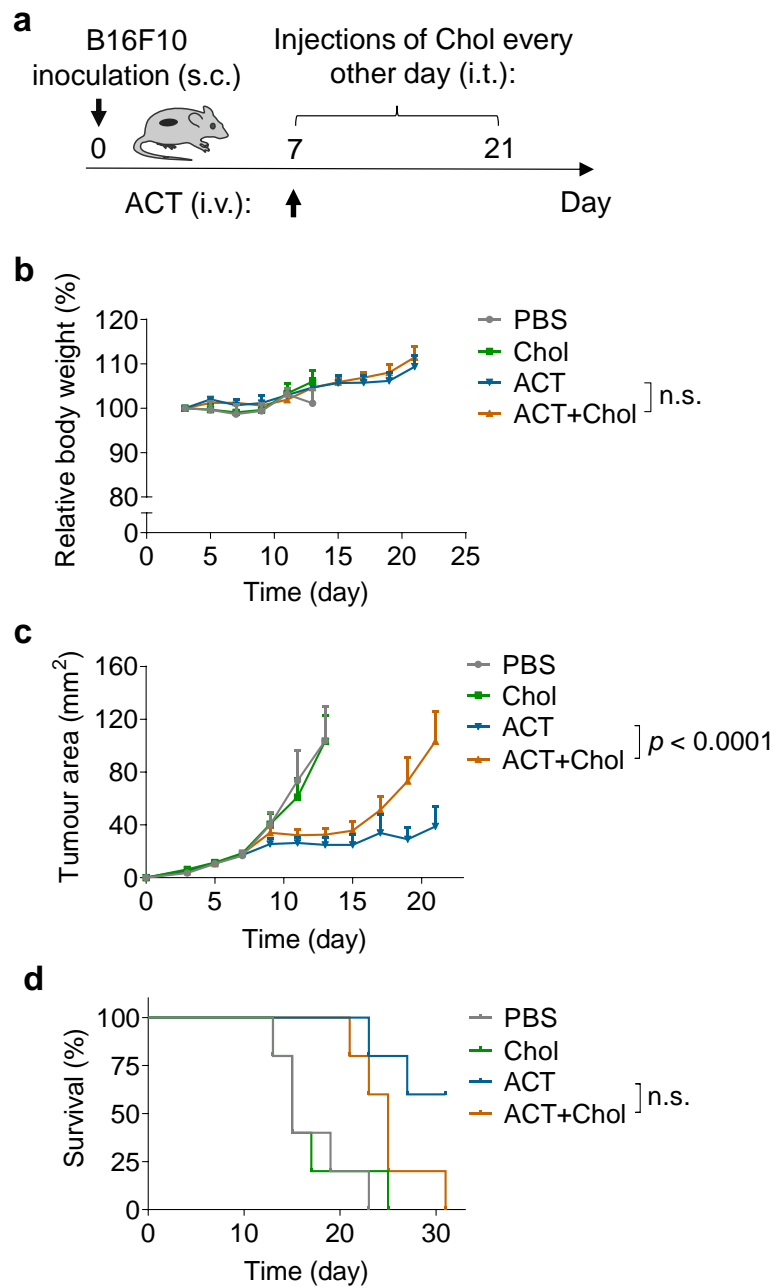


Figure 3:14 Cancer-cell softening by supplementing cholesterol impairs the anti-tumor efficacy of adoptive T cell transfer (ACT) therapy in vivo.

a-d, C57BL/6 mice were inoculated subcutaneously (s.c.) with B16F10 cancer cells (0.5×10^6 per mouse) at day 0, and received intravenous (i.v.) adoptive transfer of activated Pmel CD8⁺ T cells (5×10^6 per mouse) at day 7 followed by intratumoral (i.t.) administration of Chol (2 mg per injection) or PBS every other day from day 7 to 21. B16F10 tumor-bearing mice receiving i.t. administration of PBS or Chol only (2 mg per injection) every other day from day 7 to 21 serve as controls. Experimental scheme (**a**). Shown are relative body weights (**b**), tumor growth curves (**c**), and survival curves (**d**) ($n = 5$ animals per group). Data are one representative of two independent experiments. P values were determined by two-way ANOVA in (**b**, **c**) or log-rank test in (**d**). Error bars represent SEM. PBS, phosphate-buffered saline; n.s., not significant.

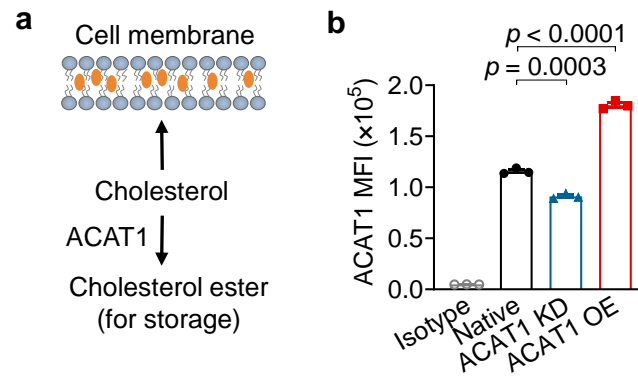


Figure 3:15 Regulation of acyl-CoA:cholesterol acyltransferase 1 (ACAT1) level through genetic modification in cancer cells.

a, Schematic illustration of regulating membrane cholesterol levels through ACAT1. **b**, ACAT1 expression levels in native, ACAT1 knock-down (ACAT1 KD), and ACAT1 overexpressing (ACAT1 OE) B16F10 cancer cells detected by antibody staining and flow cytometry analysis ($n = 3$). Data are one representative of two independent experiments with biological replicates. P values were determined by unpaired Student's t test in (**b**). Error bars represent SEM. MFI, mean fluorescence intensity.

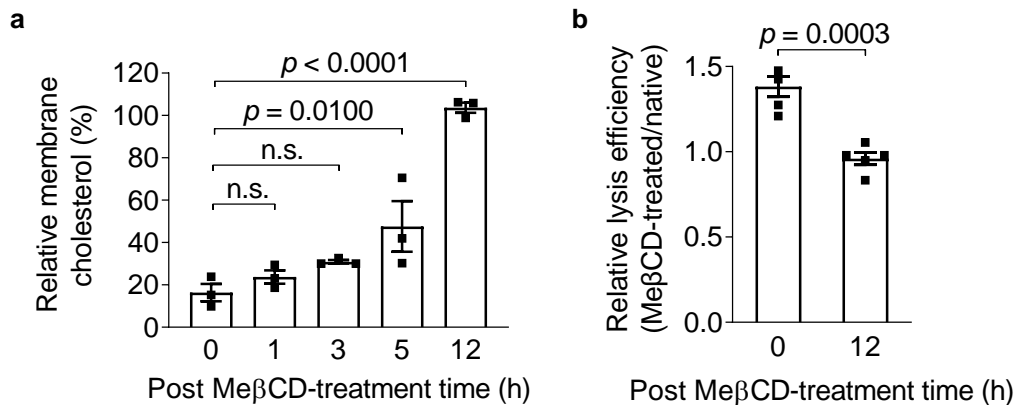


Figure 3:16 Kinetics of cholesterol levels in the plasma membrane of B16F10 cancer cells post the treatment of Me β CD and its impact on T cell-mediated cytotoxicity.

a, Relative membrane cholesterol levels of Me β CD-treated B16F10 cancer cells at indicated time points post-treatment ($n = 3$). Membrane cholesterol level of native B16F10 serves as a standard (100%). **b**, Relative lysis efficiency of Me β CD-treated B16F10 cancer cells (0 or 12 h post-treatment) co-cultured with activated Pmel CD8⁺ T cells at an effector:target ratio of 10:1 for 5 h ($n = 5$). Relative lysis efficiency was calculated by normalizing the lysis percentages by the mean value of native B16F10 cancer cells. Data are one representative of two independent experiments with biological replicates. P values were determined by unpaired Student's t test. Error bars represent SEM. n.s., not significant.

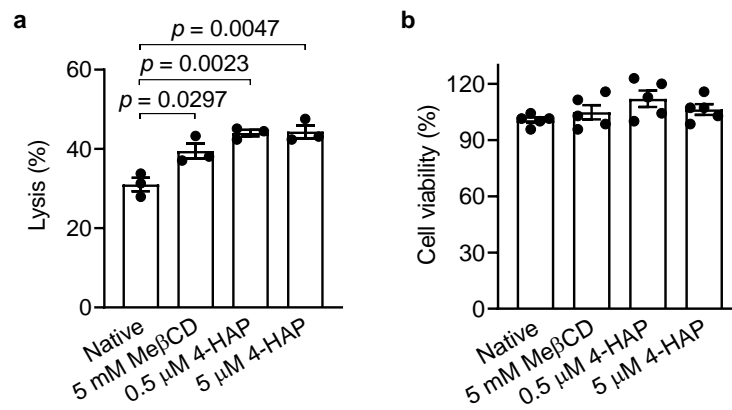


Figure 3:17 Cancer cell stiffening using a cytoskeleton stiffening reagent, 4-hydroxyacetophenone (4-HAP), enhances T cell-mediated killing of B16F10 cancer cells.

a, Lysis percentage of B16F10 cancer cells pre-treated with indicated concentrations of 4-HAP or MeβCD and co-cultured with activated Pmel CD8+ T cells at an effector:target (E:T) ratio of 10:1 for 5 h ($n = 3$). **b**, Viability percentage of B16F10 cancer cells after treatment with indicated concentrations of 4-HAP or MeβCD at 37 °C for 30 min ($n = 5$). Data are one representative of at least two independent experiments with biological replicates. Error bars represent SEM.

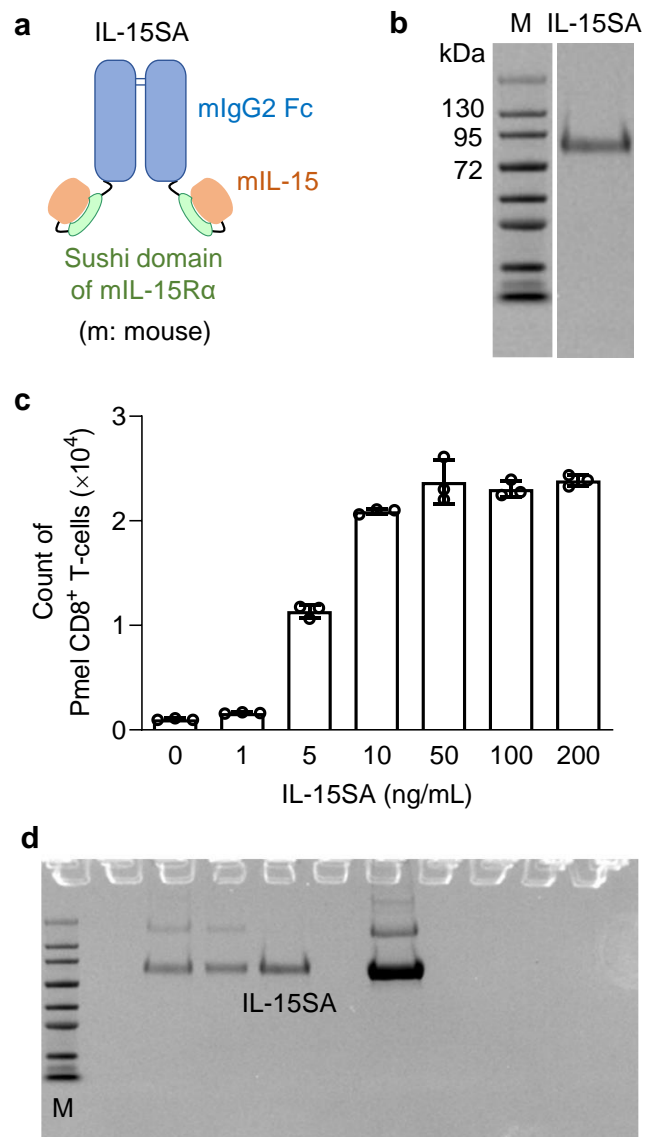


Figure 3:18 Production and characterizations of mouse interleukin-15 super-agonist (IL-15SA).

a, Schematic diagram of the protein structure of IL-15SA. **b**, Representative sodium dodecyl sulfate-polyacrylamide gel electrophoresis (SDS-PAGE) analysis of the purified IL-15SA. **c**, Activated Pmel CD8⁺ T cells (5×10^3) were cultured in complete RPMI 1640 medium supplemented with IL-15SA at the indicated concentrations for 2 days ($n = 3$). Counts of T cells were determined with flow cytometry. Data are one representative of two independent experiments with biological replicates. Error bars represent SEM. **d**, Unprocessed SDS-PAGE gel image for (**b**). M, prestained protein marker; kDa, kilodalton.

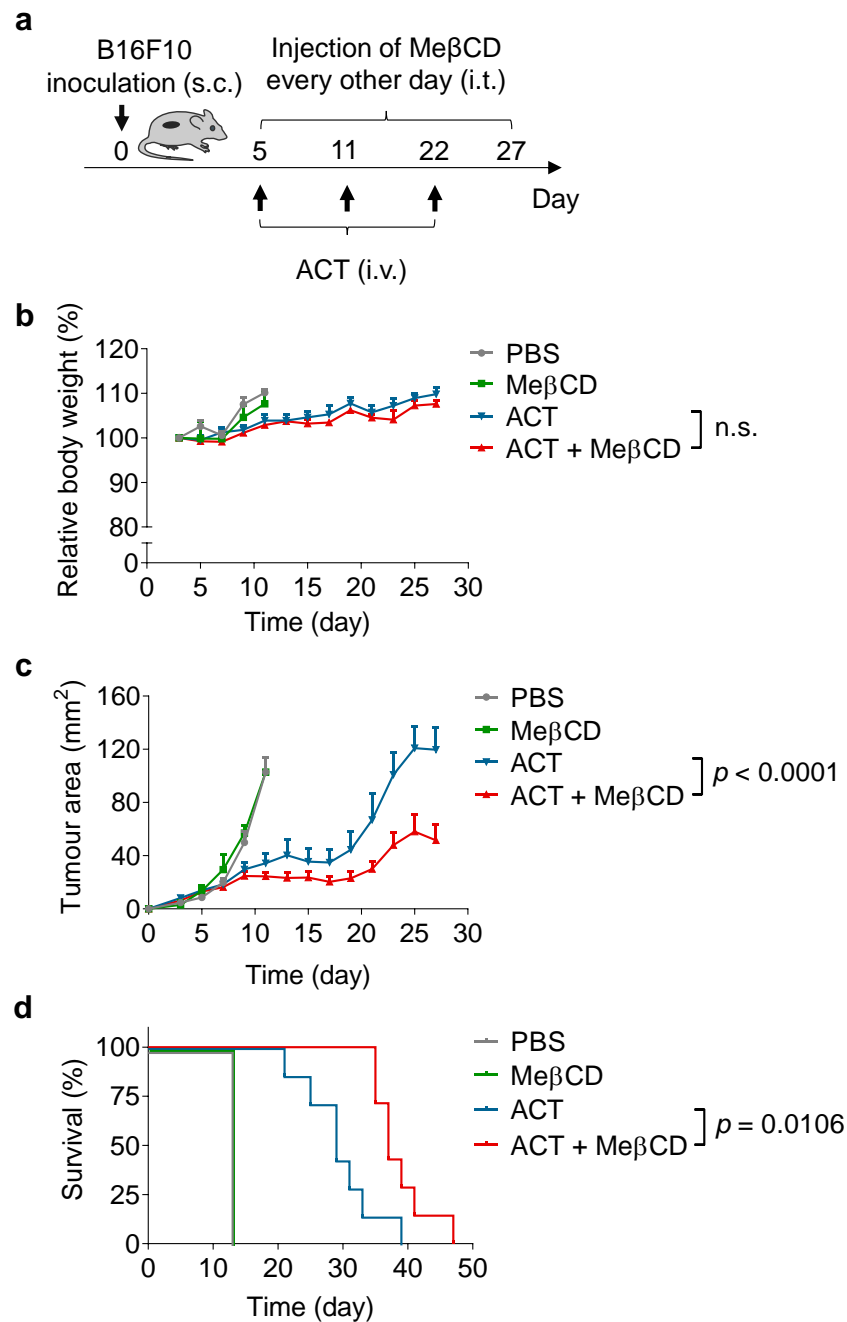


Figure 3:19 Cancer-cell stiffening using Me β CD enhances the anti-tumor efficacy of ACT therapy in mice bearing B16F10 tumors.

a-d, C57BL/6 mice were inoculated subcutaneously (s.c.) with B16F10 tumor cells (0.5×10^6 per mouse) at day 0, and received intravenous (i.v.) adoptive transfer of activated Pmel CD8⁺ T cells (5×10^6 per injection) at day 5, 11, and 22 followed by intratumoral (i.t.) administration of Me β CD (2 mg per injection) or PBS every other day from day 5 to 27. B16F10 tumor-bearing mice receiving i.t. administration of PBS or Me β CD only (2 mg per injection) every other day from day 5 to 27 serve as controls. Experimental scheme (**a**). Shown are relative body weights (**b**), tumor growths (**c**), and survival curves (**d**) ($n = 3$ mice for PBS and Me β CD groups, and 7 mice for ACT and ACT + Me β CD groups). Data are one representative of two independent experiments with biological replicates. P values were determined by two-way ANOVA in (**b**, **c**), or log-rank test in (**d**). Error bars represent SEM. PBS, phosphate-buffered saline; n.s., not significant.

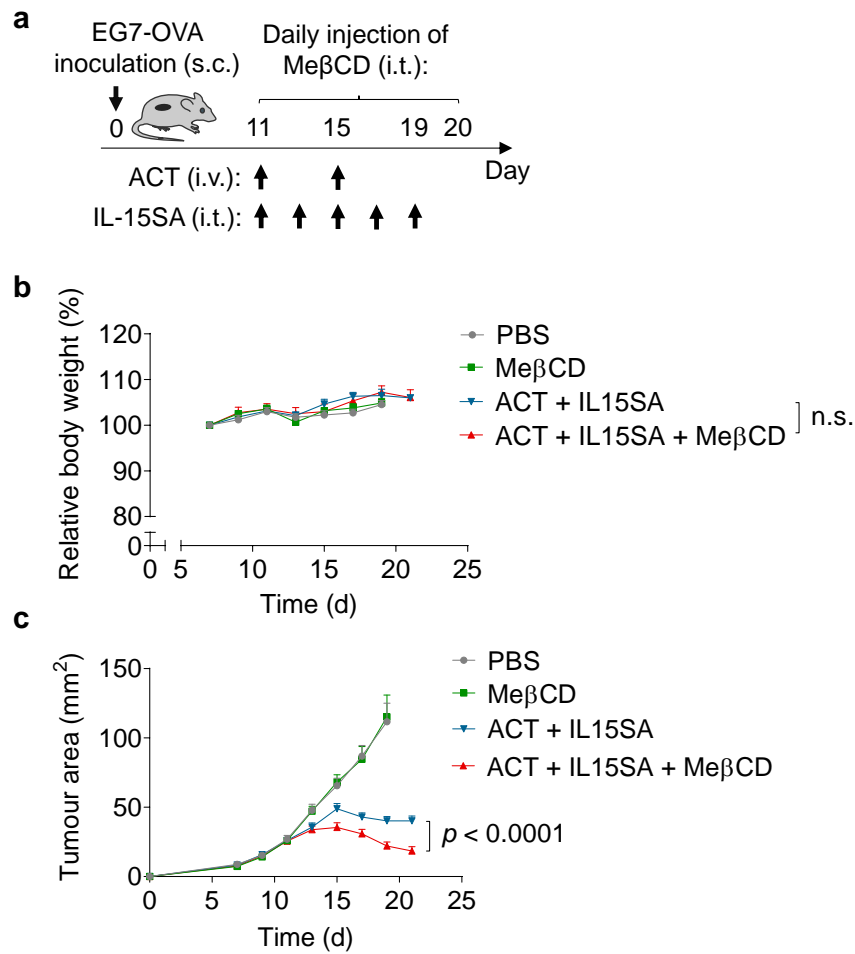


Figure 3:20 Cancer-cell stiffening using Me β CD enhances the anti-tumor efficacy of ACT therapy in mice bearing EG7-OVA tumors.

a-c, C57BL/6 mice were inoculated subcutaneously (s.c.) with EG7-OVA tumor cells (0.5×10^6 per mouse) at day 0, and received intravenous (i.v.) adoptive transfer of activated OT-I CD8⁺ T cells (5×10^6 per injection) at day 11 and 15, followed by intratumoral (i.t.) administration of IL-15SA ($5 \mu\text{g}$ per injection) every other day from day 11 to 19, and daily i.t. administration of Me β CD (1 mg per injection) or PBS from day 11 to 20. EG7-OVA tumor-bearing mice receiving daily i.t. administration of PBS or Me β CD (1 mg per injection) only from day 11 to 20 serve as controls. Experimental scheme (**a**). Shown are relative body weights (**b**) and tumor growths (**c**) ($n = 10$ animals per group). Shown are pooled data of two independent experiments with biological replicates. P values were determined by two-way ANOVA. Error bars represent SEM. PBS, phosphate-buffered saline; n.s., not significant.

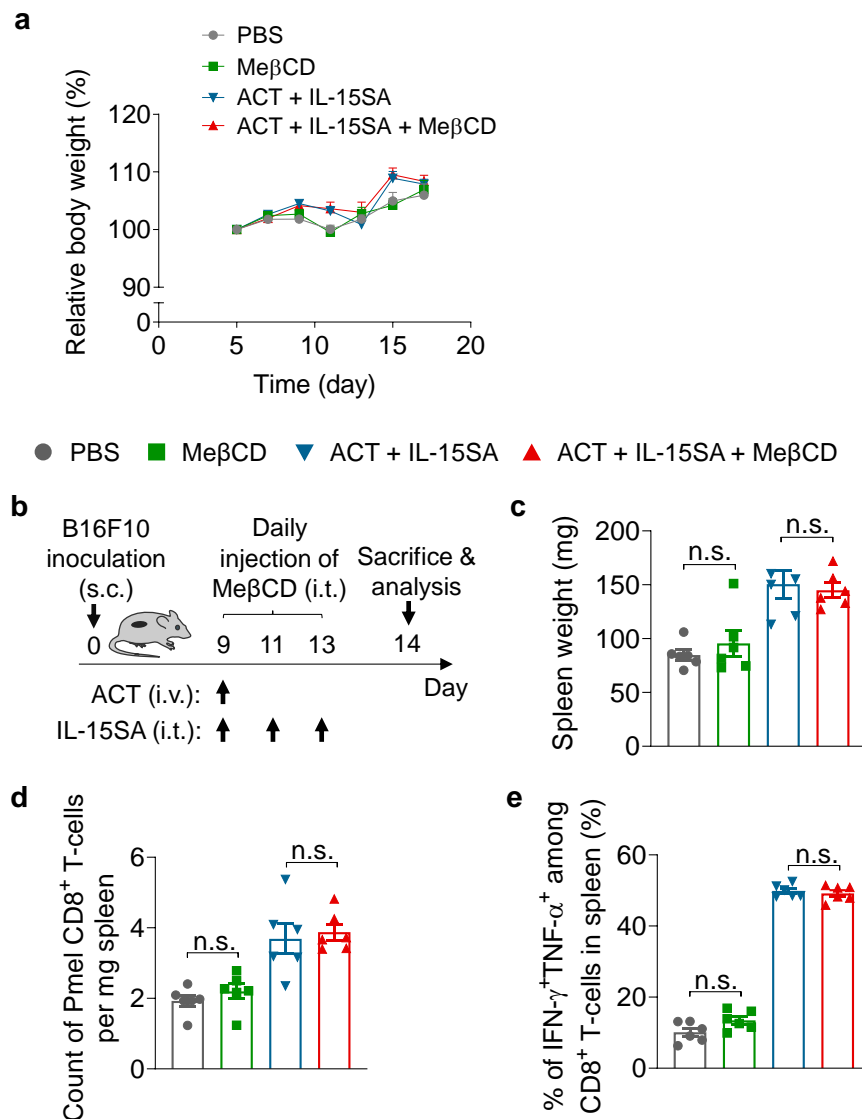


Figure 3:21 Treatment of MeβCD shows no overt systemic toxicity in mice.

a, B16F10 tumor-bearing mice received the same treatment as shown in Fig. 3:4c. Shown are relative body weights ($n = 12$ animals per group). Shown are pooled data of two independent experiments. **b-e**, C57BL/6 mice were inoculated subcutaneously (s.c.) with B16F10 tumor cells (0.5×10^6 per mouse) at day 0 and received intravenous (i.v.) adoptive transfer of activated Pmel CD8⁺ T cells (5×10^6 per mouse) at day 9, followed by intratumoral (i.t.) administration of IL-15SA ($5 \mu\text{g}$ per injection) at day 9, 11, and 13, and daily i.t. administration of MeβCD (1 mg per injection) or PBS from day 9 to 13. B16F10 tumor-bearing mice receiving daily i.t. administration of PBS or MeβCD (1 mg per injection) only from day 9 to 13 serve as controls. At day 14, all mice were sacrificed, and spleens harvested from the mice were weighed and processed for flow cytometry analyses. Experimental scheme (**b**). Shown are spleen weight (**c**), counts of Pmel CD8⁺ T cells (**d**), frequency of polyfunctional CD8⁺ T cells (**e**) in spleens ($n = 6$ animals per group). Data are one representative of two independent experiments with biological replicates. P values were determined by one-way ANOVA. Error bars represent SEM. PBS, phosphate-buffered saline; n.s., not significant.

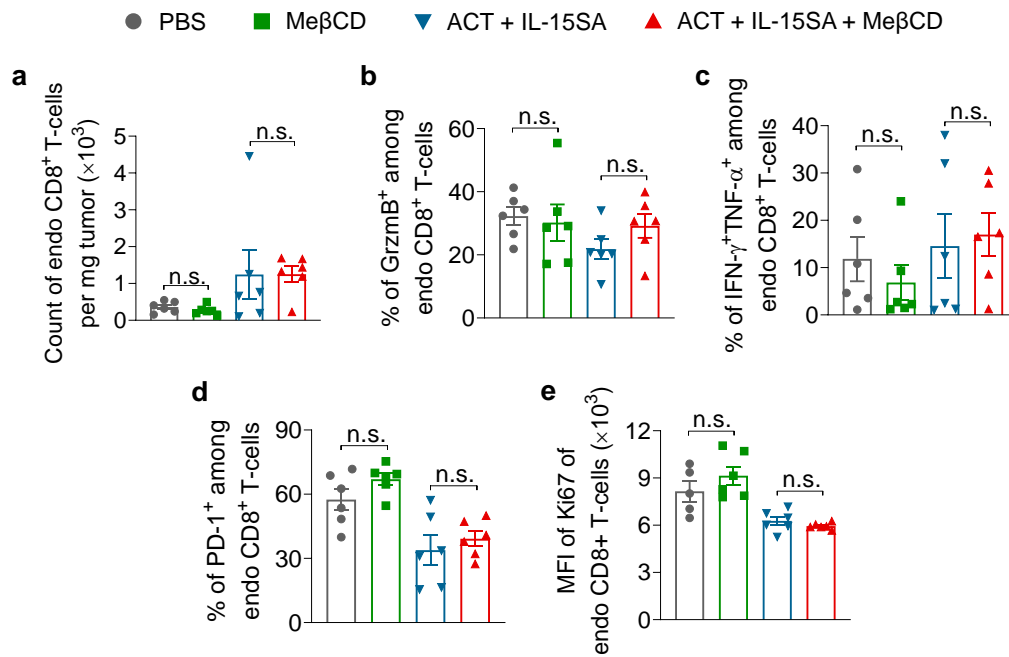


Figure 3:22 Treatment of MeβCD shows negligible effects on proliferation and functions of tumor-infiltrating endogenous (endo) CD8⁺ T cells.

a-e, B16F10 tumor-bearing mice received the same treatment as shown in Fig. 3:21b. At day 14, mice were sacrificed, and tumors harvested from the mice were processed for flow cytometry analyses. Shown are counts of endo CD8⁺ T cells (**a**), frequencies of granzyme B (GrzmB)⁺ (**b**), polyfunctional (**c**), and PD-1⁺ (**d**), and mean fluorescence intensity (MFI) of Ki67 (**e**) of endo CD8⁺ T cells ($n = 6$ animals per group). Data are one representative of two independent experiments with biological replicates. *P* values were determined by one-way ANOVA. Error bars represent SEM. PBS, phosphate-buffered saline; n.s., not significant.

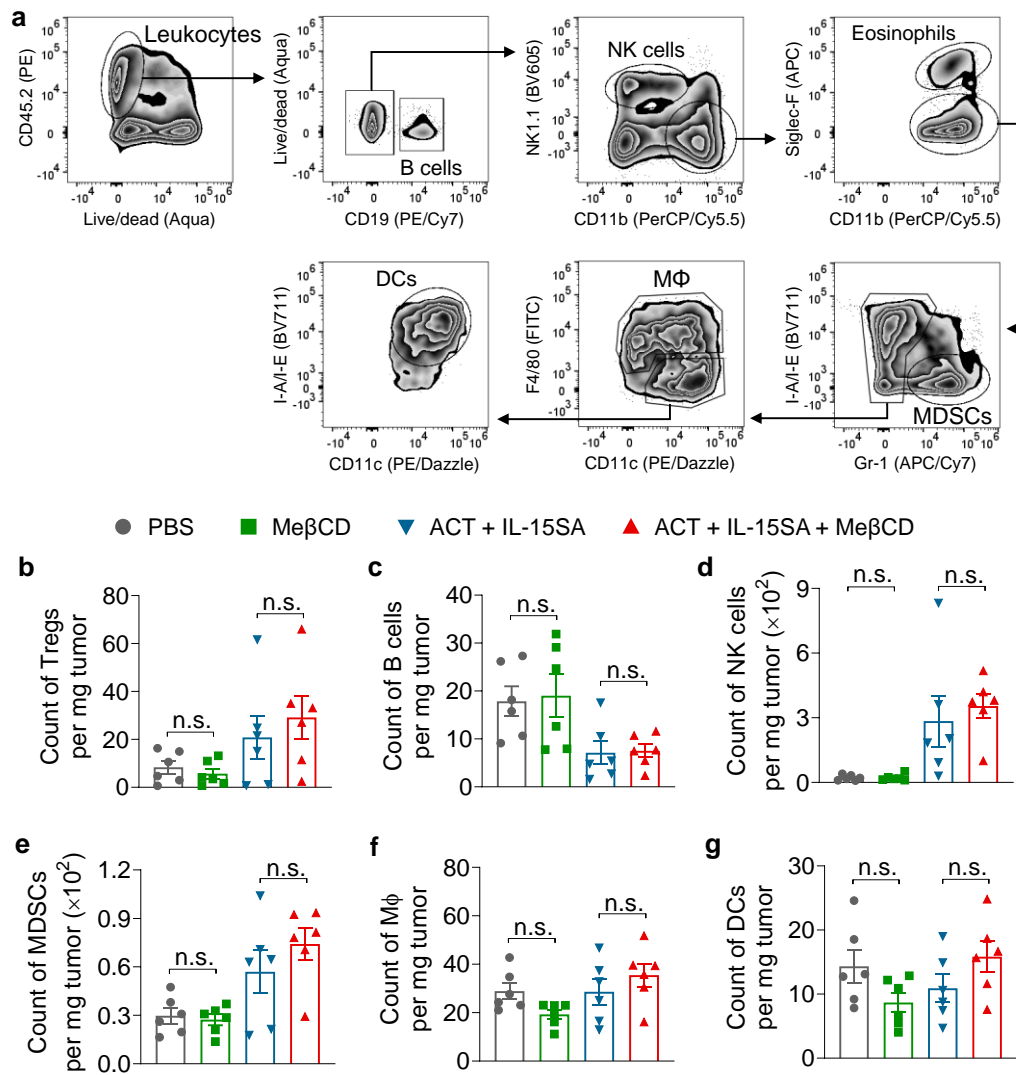


Figure 3:23 Treatment of MeβCD shows negligible effects on other tumor-infiltrating immune cells.

a-g, B16F10 tumor-bearing mice received the same treatment as shown in Fig. 3:21b. At day 14, mice were sacrificed, and tumors harvested from the mice were processed for flow cytometry analyses. **a**, Shown are the gating strategies for B cells, natural killer (NK) cells, eosinophils, myeloid-derived suppressor cells (MDSCs), macrophages (MΦ), and dendritic cells (DCs) in tumors. **b-g**, Shown are counts of regulatory T cells (Tregs; Foxp3⁺CD4⁺ T cells) (**b**), B cells (**c**), NK cells (**d**), MDSCs (**e**), MΦ (**f**), and DCs (**g**) infiltrating in tumours (n = 6 animals per group). Data are one representative of two independent experiments with biological replicates. *P* values were determined by one-way ANOVA. Error bars represent SEM. PBS, phosphate-buffered saline; n.s., not significant.

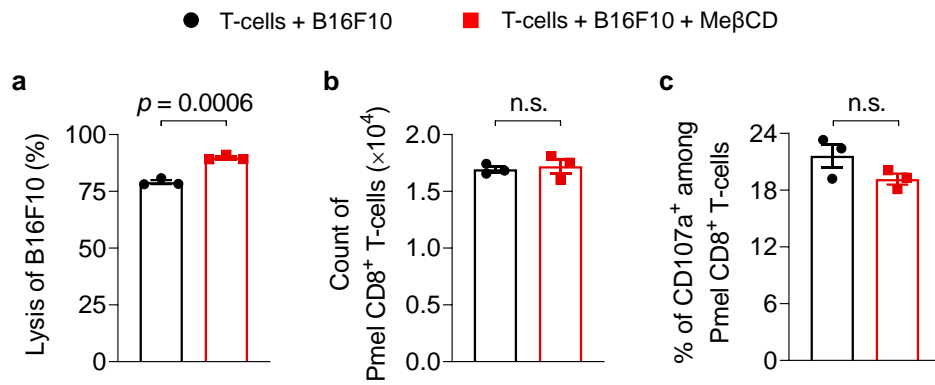


Figure 3:24 MeβCD shows negligible effects on T cell functions during co-culture with cancer cells.

a, Lysing percentage of B16F10 cancer cells after 48-h co-culture with Pmel CD8⁺ T cells at an effector:target ratio of 1:1 in the presence of MeβCD ($n = 3$). **b**, **c**, Cell counts (**b**) and frequency of CD107a⁺ (**c**) of Pmel CD8⁺ T cells were analyzed by flow cytometry. Data are one representative of two independent experiments with biological replicates. P values were determined by unpaired Student's t test. Error bars represent SEM. n.s., not significant.

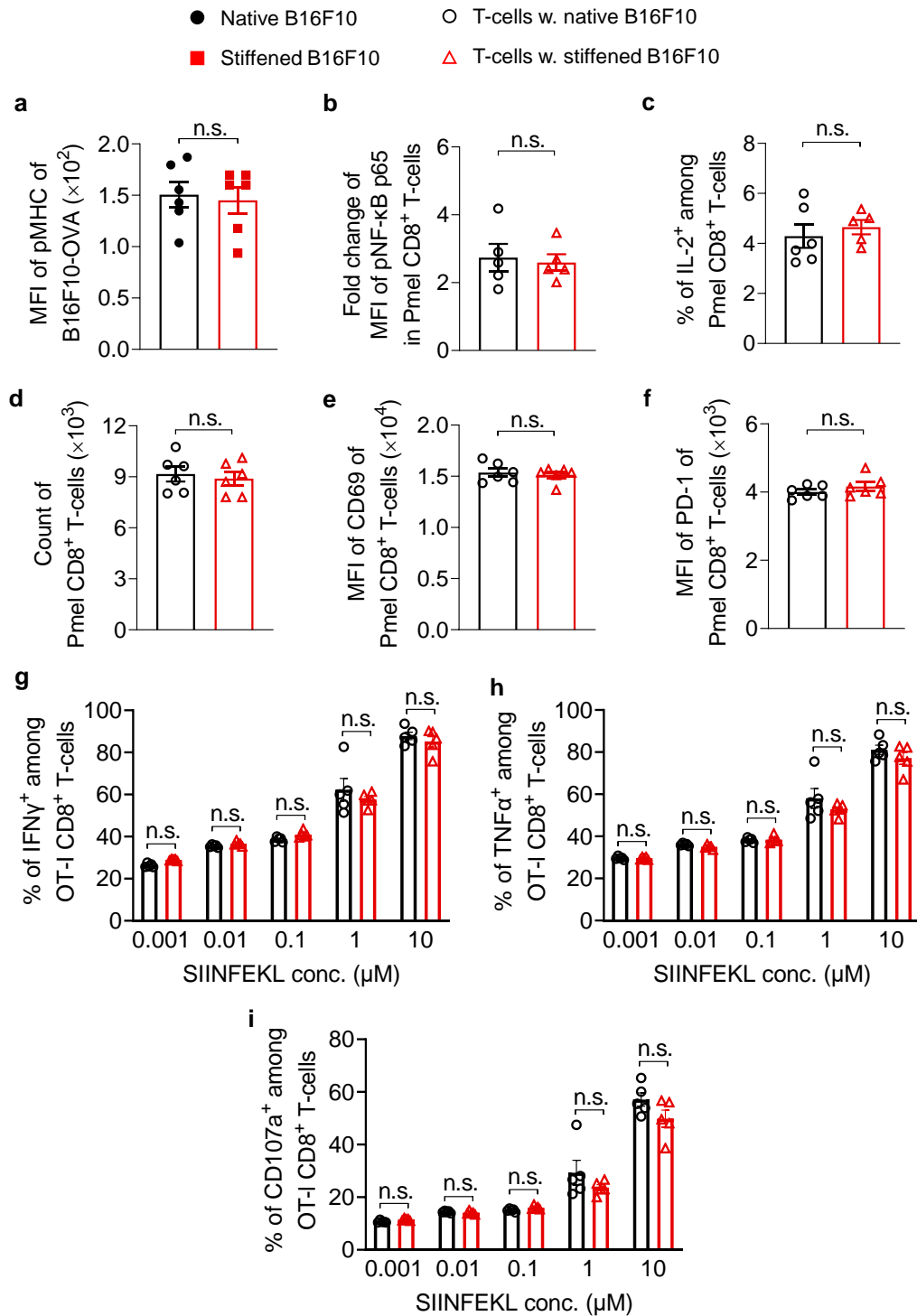


Figure 3:25 Cancer-cell stiffening using Me β CD shows negligible effects on antigen presentation by cancer cells, T cell proliferation, activation, or other phenotypes.

a, SIINFEKL-MHC-I complex (pMHC) expression level on B16F10-OVA cancer cells after treatment with Me β CD (5 mM) at 37 °C for 30 min ($n = 6$). **b**, Fold change of mean fluorescence intensity (MFI) of phosphorylated NF- κ B subunit p65 (pNF- κ B p65) in activated Pmel CD8 $^+$ T cells stimulated by Me β CD-treated (stiffened) B16F10 cancer cells at 37 °C for 5 min ($n = 5$). **c-f**, Activated Pmel CD8 $^+$ T cells were co-cultured with stiffened B16F10 cancer cells at an effector:target (E:T) ratio of 10:1 for 5 h. Shown are IL-2 $^+$ percentage (**c**), count (**d**), and MFI of CD69 (**e**) and PD-1 (**f**) of Pmel CD8 $^+$ T cells ($n = 6$). **g-i**, Activated OT-I CD8 $^+$ T cells were co-cultured with stiffened B16F10 cancer cells (E:T ratio = 10:1) pulsed with various concentrations of SIINFEKL peptide at 37 °C for 5 h. Shown are frequencies of IFN- γ $^+$ (**g**), TNF- α $^+$ (**h**), and CD107a $^+$ (**i**) of OT-I CD8 $^+$ T cells ($n = 6$). Data are one representative of three independent experiments with biological replicates. P values were determined by unpaired Student's t test. Error bars represent SEM. conc., concentration; n.s., not significant.

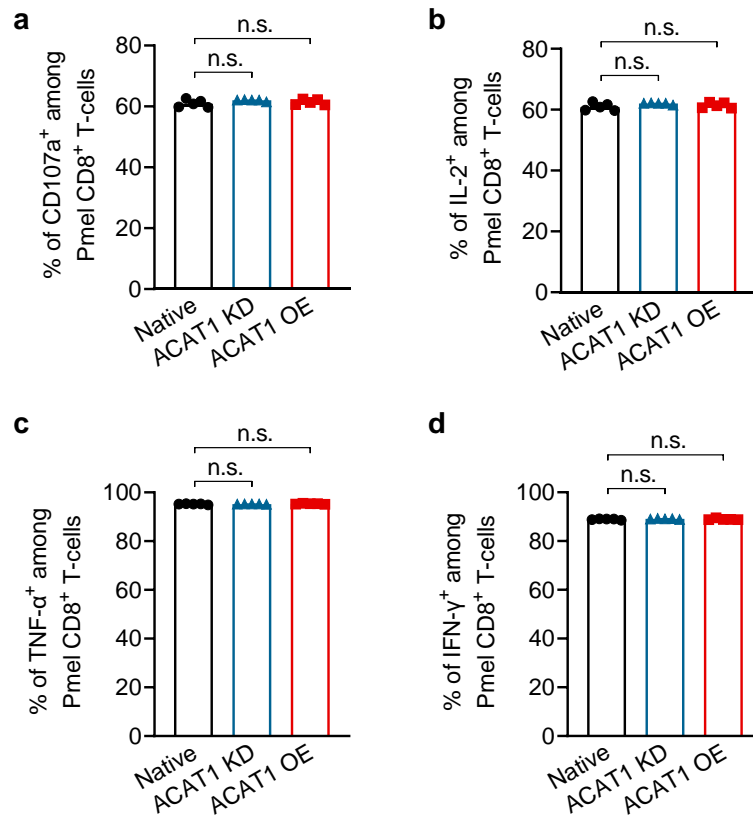


Figure 3:26 Native, ACAT1 KD, and ACAT1 OE B16F10 cancer cells induce similar T cell activation levels.

a-d, Activated Pmel CD8⁺ T cells were co-cultured with native, ACAT1 KD or ACAT1 OE B16F10 cancer cells at an effector:target (E:T) ratio of 10:1 for 5 h. Shown are frequencies of CD107a⁺ (**a**), IL-2⁺ (**b**), TNF-α⁺ (**c**) and IFN-γ⁺ (**d**) of Pmel CD8⁺ T cells (n = 6). *P* values were determined by unpaired Student's *t* test. Error bars represent standard error of the mean (SEM). n.s., not significant. Data are one representative of at least two independent experiments.

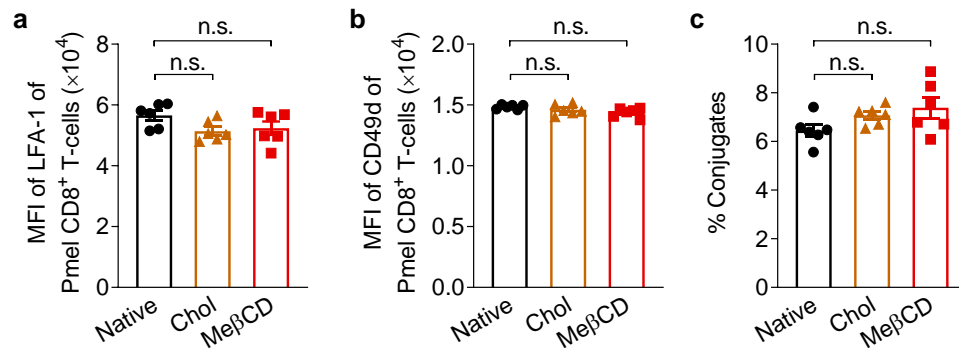


Figure 3:27 Softening or stiffening cancer cells using Chol or MeβCD has negligible effects on conjugation between T cells and cancer cells.

a, b, Activated Pmel CD8⁺ T cells were co-cultured with softened or stiffened B16F10 cancer cells at an effector:target (E:T) ratio of 10:1 for 5 h. Shown are mean fluorescence intensity (MFI) of LFA-1 (**a**) and CD49d (**b**) of Pmel CD8⁺ T cells ($n = 6$). **c**, Activated Pmel CD8⁺ T cells were co-cultured with softened or stiffened B16F10 cancer cells at an E:T ratio of 1:1 at 37 °C for 10 min. Shown is the percentage of conjugates between Pmel CD8⁺ T cells and B16F10 cancer cells ($n = 6$). P values were determined by unpaired Student's t test. Error bars represent SEM. n.s., not significant. Data are one representative of three independent experiments with biological replicates.

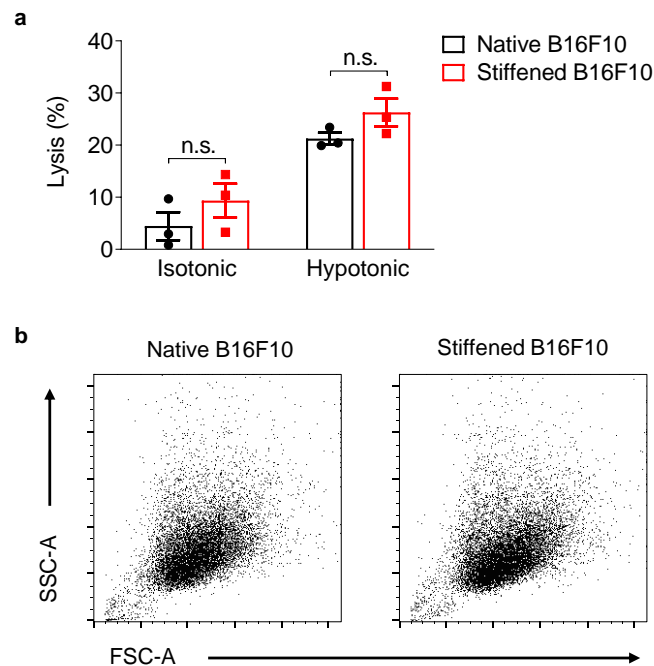


Figure 3:28 Native and stiffened B16F10 cancer cells showed similar susceptibility to membrane tension-assisted perforin-induced lysis.

a, Lysing percentage (the percentage of target cell death) of native and MeβCD-treated (stiffened) B16F10 cancer cells after incubation with 10 μg/mL perforin for 20 min at 37 °C. In isotonic and hypotonic conditions, perforin was diluted in PBS buffer and H₂O, respectively. **b**, Representative flow cytometry plots showing similar cell size (forward scattering area, FSC-A) and granularity (side scattering area, SSC-A) between native and methyl-β-cyclodextrin (MeβCD)-treated (stiffened) B16F10 cancer cells. P values were determined by unpaired Student's t test. Error bars represent standard error of the mean (SEM). n.s., not significant. Data are one representative of two independent experiments with biological replicates.

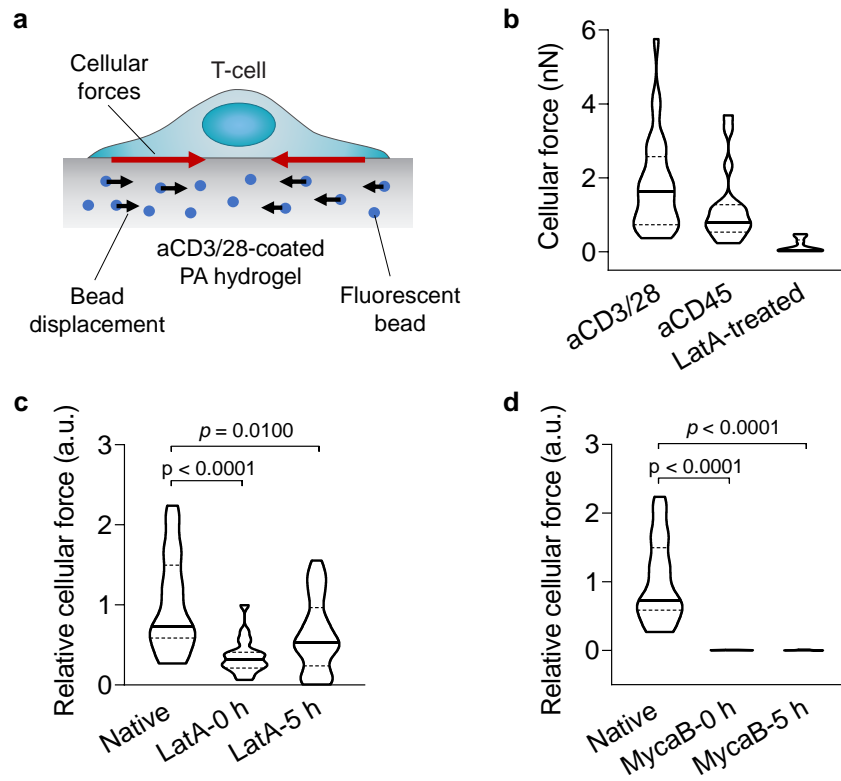


Figure 3:29 T cell force is measured using traction force microscopy (TFM) and can be stably inhibited by cytoskeleton inhibitors.

a, Schematic illustration of TFM measurement of T cell forces on a PA hydrogel coated with anti-CD3/anti-CD28 antibodies (aCD3/28) and embedded with fluorescent beads. **b**, Average total forces per cell exerted by activated Pmel CD8⁺ T cells on a hydrogel substrate ($E = 890$ Pa) coated with aCD3/28 ($n = 29$) or non-stimulatory anti-CD45 antibody (aCD45) ($n = 17$), or by T cells pre-treated with Latrunculin A (LatA) on an aCD3/28-coated hydrogel substrate ($E = 890$ Pa; $n = 10$). **c**, **d**, Relative total forces per cell exerted by T cells on hydrogel substrate ($E = 890$ Pa) coated with aCD3/28 ($n = 27$), or T cells pre-treated with LatA (**c**) or mycalolide B (MycaB; **d**) at 0 h ($n = 20$ and 10 for LatA and MycaB, respectively) and 5 h ($n = 29$ and 8 for LatA and MycaB, respectively) post pre-treatment on the same substrate. In the violin plots, the middle solid line shows median, and lower and upper dash lines show 25th and 75th percentiles, respectively. Data are one representative of two independent experiments with biological replicates. P values were determined by unpaired Student's t test. Error bars represent SEM. a.u., arbitrary unit.

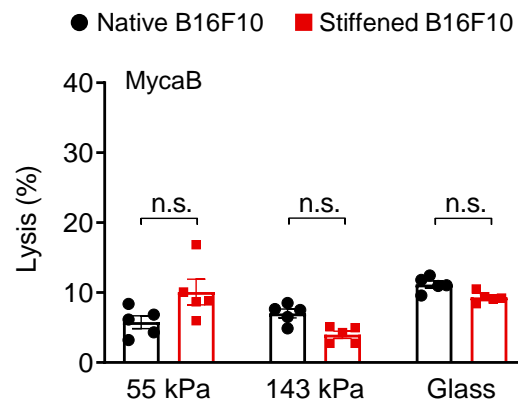


Figure 3:30 Enhanced T cell cytotoxicity against stiffened cancer cells is mediated by T cell forces.

Lysis percentage of native and Me β CD-treated (stiffened) B16F10 cancer cells co-cultured with activated Pmel CD8⁺ T cells (effector:target ratio = 10:1), which were pre-treated with mycalolide B (MycaB) ($n = 5$). Data are one representative of two independent experiments with biological replicates. P values were determined by unpaired Student's t test. Error bars represent SEM. n.s., not significant.

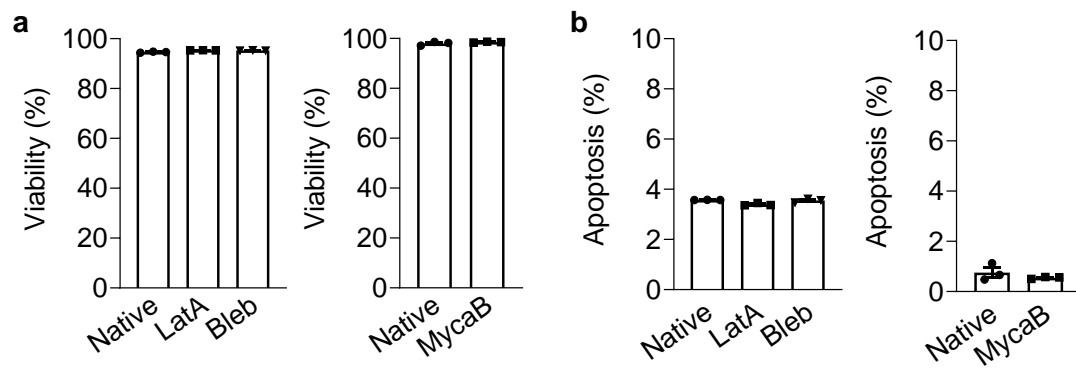


Figure 3:31 Treatment of cytoskeleton inhibitors shows negligible impacts on the viability or apoptosis of Pmel CD8⁺ T cells.

a, b, Percentages of viable (**a**) and apoptotic (**b**) Pmel CD8⁺ T cells after the treatment with different cytoskeleton inhibitors ($n = 3$). Lata, latrunculin A; Bleb, blebbistatin; MycaB, mycalolide B. Data are one representative of two independent experiments with biological replicates. Error bars represent SEM.

3.6 Acknowledgements

We thank R. Guet (EPFL) for assistance with image analysis. We acknowledge the assistance of W. Li (West China Hospital) for histological analyses of human biopsies. We are grateful to EPFL Bioimaging and Optics Platform, Center of PhenoGenomics, Flow Cytometry Core Facility, Protein Production, Structure Core Facility, and Histology Core Facility for technical support. We thank S. M. Leitão and B. Ghadiani (EPFL) for technical assistance on AFM measurement; P. Müller (Max Planck Institute) for assistance in analyzing deformability cytometry data; D. J. Irvine (MIT) for providing IL-15SA construct, B16F10-OVA, and 4T1-Fluc-tdTomato cell lines; P. Romero (UNIL) for providing MC38-HER2 and Me275-HER2 cell lines; D. Trono (EPFL) for providing HEK293T cells and pLKO.1 vector; E. Amstad (EPFL) for providing access to a rheometer. We are grateful for the discussions with F. Stellacci, M. De Palma, A. Cont, and A. Persat (EPFL). This work was supported in part by the European Research under the ERC grant agreements MechanoIMM (805337) and ROBOCHIP (714609), Swiss National Science Foundation (Project grant 315230_173243), Swiss Cancer Research Foundation (No. KFS-4600-08-2018), Kristian Gerhard Jebsen Foundation, Anna Fuller Fund Grant, and École Polytechnique Fédérale de Lausanne (EPFL). A.K. acknowledges funding from the European Union's Horizon 2020 research and innovation program under the Marie Skłodowska-Curie grant agreement No. 754354. M.G. was supported by the Chinese Scholarship Council (CSC) (No. 201808320453).

Chapter 4 T cell force-responsive delivery of anti-cancer drugs

Adapted from the published article:

Lei, K. & Tang, L. T cell force-responsive delivery of anticancer drugs using mesoporous silica microparticles. *Materials Horizons* 7, 3196-3200 (2020).

Contributions:

K.L. and L.T. conceived the study and designed the experiments. K.L. performed the experiments and analyzed the data. L.T. supervised the project. K.L. and L.T. wrote the manuscript.

4.1 Abstract

T cell-based cancer immunotherapy has achieved great success in the clinic; however, only a small fraction of patients respond to this therapy. Strategies to specifically and safely augment anticancer activity through controlled delivery of T cell supporting factors or drugs for combination therapy remain of high interest. Here, we devised a T cell force-responsive system for selective delivery of anticancer drugs using a mesoporous silica microparticle capped with a DNA force sensor. Upon T cell receptor (TCR) triggering, T cells exerted synaptic forces, a unique biophysical stimulus, to rupture the force-sensitive DNA gatekeepers on the mesopores leading to rapid drug release. Our results demonstrated that this cellular force-responsive system specifically released anticancer drugs in a T cell force-dependent manner and significantly enhanced cancer cell killing *in vitro* and *in vivo*. This work opens a new horizon toward designing next-generation drug delivery systems in response to signaling-specific cellular forces.

4.2 New concepts

Most physiological stimulus-responsive drug delivery systems rely on altered biochemical signals in specific tissues or cells, such as pH, redox potential, and enzymes. However, biophysical signals, such as mechanical forces, are much less exploited. Biomechanical forces ubiquitously exist in the human body and have been reported to be associated with many specific biological processes or pathologies. Efforts that explore mechanical forces as triggers for responsive drug delivery so far have been exclusively focused on forces from tissues (e.g., shear stress in the circulation) or external sources (e.g., ultrasound). It remains challenging to develop a cellular force-triggered drug delivery system. Here, we demonstrated, for the first time, a T cell force-responsive delivery system for anticancer drugs. Specifically, the drug release was controlled by cellular forces exerted by T cells upon cognate antigen encounter and T cell receptor (TCR) activation. Thus, the drug release is restricted to the sites of high antigen concentration, such as the tumor microenvironment. Employing cellular force as a new biophysical stimulus, we achieved highly specific TCR signaling-responsive drug release for enhanced cancer cell killing. This new concept of cellular force-responsive drug delivery based on intelligent material design can be potentially applied to various immune or non-immune cells for therapies with improved efficacy and safety.

4.3 Introduction

Spatiotemporally controlled drug delivery using stimulus-responsive release systems can improve the specificity of various therapeutics, including anticancer drugs.^{212,213} Among the diverse stimuli explored to date, biochemical signals dominate, such as pH,^{214–216} redox potential,^{8,9,217} enzymes,^{218–220} and reactive oxygen species.^{221–223} Nevertheless, biophysical signals, such as mechanical forces, are garnering increasing attention due to their ubiquitous existence in the human body.^{224–226} Exertion or alteration of biomechanical forces has been reported to be associated with specific biological processes or pathologies.^{227,228} For instance, the shear stress in constricted vessels of patients with atherosclerosis increases significantly, providing a potential disease-specific stimulus for targeted drug delivery.²²⁹ In addition to the mechanical forces at the tissue level, cells exert rapid and strong cellular forces. For example, myofibroblasts exert

traction forces for remodeling the extracellular matrix (ECM) during wound healing.²³⁰ Recently, cytotoxic T cells were found to exert significant mechanical forces specifically at the immunological synapse upon antigen recognition/T cell receptor (TCR) activation to potentiate the killing of target cells in addition to secreting cytolytic enzymes.¹⁴

Cytotoxic T cells are among the most important effector cells in cancer immunotherapy.^{231,232} Approaches to safely and effectively supplement T cells with supporting drugs for enhanced immunotherapy or other therapeutics for combination therapy remain of great interest. In previous work, we reported a T cell surface-conjugated nanogel that responded to an increase in the T cell surface reduction potential upon tumor antigen recognition.⁸ The release of cytokines in the nanogel was therefore controlled by TCR activation and restricted to sites of cognate antigen encounter, such as the tumor microenvironment. The TCR signaling-responsive release of cytokines greatly enhanced the efficacy and safety of adoptive T cell therapy. However, this approach relies on a relatively slow-responding biochemical signal as the trigger, i.e., the cell surface reduction potential.

The cellular force exerted by cytotoxic T cells upon TCR activation by cognate antigens is a highly specific and instantaneous mechanical stimulus. We, therefore, exploit the T cell force as a unique biophysical trigger to achieve TCR signaling-responsive drug delivery. However, designing and obtaining a triggered release system in response to cellular forces remains challenging as they are of extremely small magnitude (nanonewton level). Here, we describe a T cell force-responsive delivery platform for anticancer drugs using a drug-loaded mesoporous silica microparticle (**M**) capped with double-stranded DNA (**D**) as a force-sensitive gatekeeper (Fig. 4:1). One of the DNA strands was linked to anti-CD3 and anti-CD28 antibodies (**Ab**), which bound to the T cell surface receptors and triggered TCR signaling. Upon TCR triggering by the stimulatory antibodies, T cells exerted cellular forces that disrupted the DNA gatekeepers, leading to rapid drug release from uncapped mesopores. Using rhodamine B (**RB**) as a model drug, we demonstrated that the drug release was controlled by T cell forces. When loaded with an anticancer drug, gemcitabine (**GEM**), T cell force-responsive drug release enhanced the killing efficiency of cancer cells *in vitro* and *in vivo*.

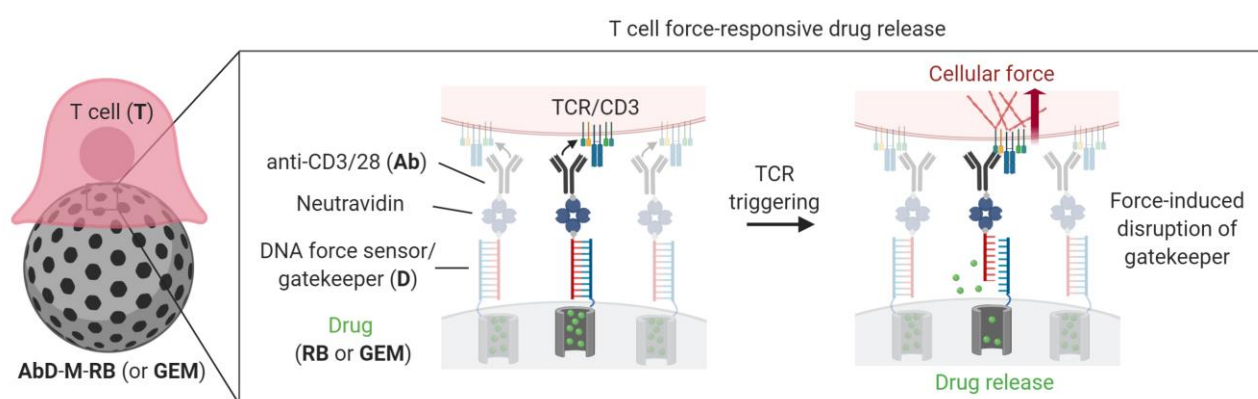


Figure 4:1 Schematic illustration of T cell force-responsive drug release system based on a mesoporous silica microparticle (**M**) capped with DNA force sensors (**D**).

TCR, T cell receptor; **Ab**, anti-CD3 and anti-CD28 antibodies; **RB**, rhodamine B; **GEM**, gemcitabine.

4.4 Results

4.4.1 Screening of force-sensitive gatekeepers for mesoporous silica microparticle system

We first looked into the possible interactions that can be potentially broken down by cellular forces estimated to be dozens of piconewton (pN) per receptor.²³³ After reviewing the literature, we focused on two promising candidates: host-guest interaction and DNA double-strand interaction. Their rupture forces are in the range of dozens of pN,^{234,235} which potentially match the scale of cellular forces. We first evaluated a well-studied host-guest complex, i.e., β -cyclodextrin/alkylbenzene, as a potential force-sensitive gatekeeper for the mesoporous silica microparticle system. According to the magnitude of cellular forces, we selected β -cyclodextrin (β CD)/methylbenzene (**MB**) and β CD/tertbutylbenzene (**TB**) complexes, which have average rupture forces of 45 and 89 pN, respectively.²³⁴

The mesoporous silica microparticles were first modified with amino groups and then conjugated with **MB** or **TB** groups through the amidation reaction (Fig. 4:7). The successful conjugation of **MB** or **TB** groups was confirmed with Fourier-transform infrared spectroscopy (FT-IR) analysis showing a characteristic carbon-carbon stretching vibration bands of aromatic structure (1700 to 1500 cm^{-1}) (Fig. 4:8). Afterward, **MB** or **TB**-modified mesoporous silica microparticles were loaded with **RB** (denoted as **MB-M-RB** or **TB-M-RB**, respectively) for tracing the release from mesopores (Fig. 4:2a). The **MB-M-RB** or **TB-M-RB** were then capped with β CD serving as a gatekeeper for mesopore release (Fig. 4:2a). Surprisingly, the uncapped **MB-M-RB** or **TB-M-RB** showed notably decreased release of **RB** compared to the **M-RB** without modification (Fig. 4:2b, c). It suggests that **MB** or **TB** modification itself blocked the release of **RB** from mesopores, possibly due to π - π interactions between **RB** and **MB** (or **TB**).²³⁶ In the control group, the **M-RB** displayed similar release kinetics of **RB** without or with the presence of β CD (Fig. 4:2b, c), indicating that β CD did not interfere with the release of **RB** from mesopores. Unfortunately, capping the **MB-M-RB** or **TB-M-RB** with β CD did not slow down the release of **RB** from the **MB-M-RB** or **TB-M-RB** (Fig. 4:2b, c). The possible reasons may be that **MB** or **TB** blocking itself becomes the limiting step of **RB** release from mesopores, or β CD/**MB** (or **TB**) interactions are not efficient enough to block the release of **RB** from mesopores.

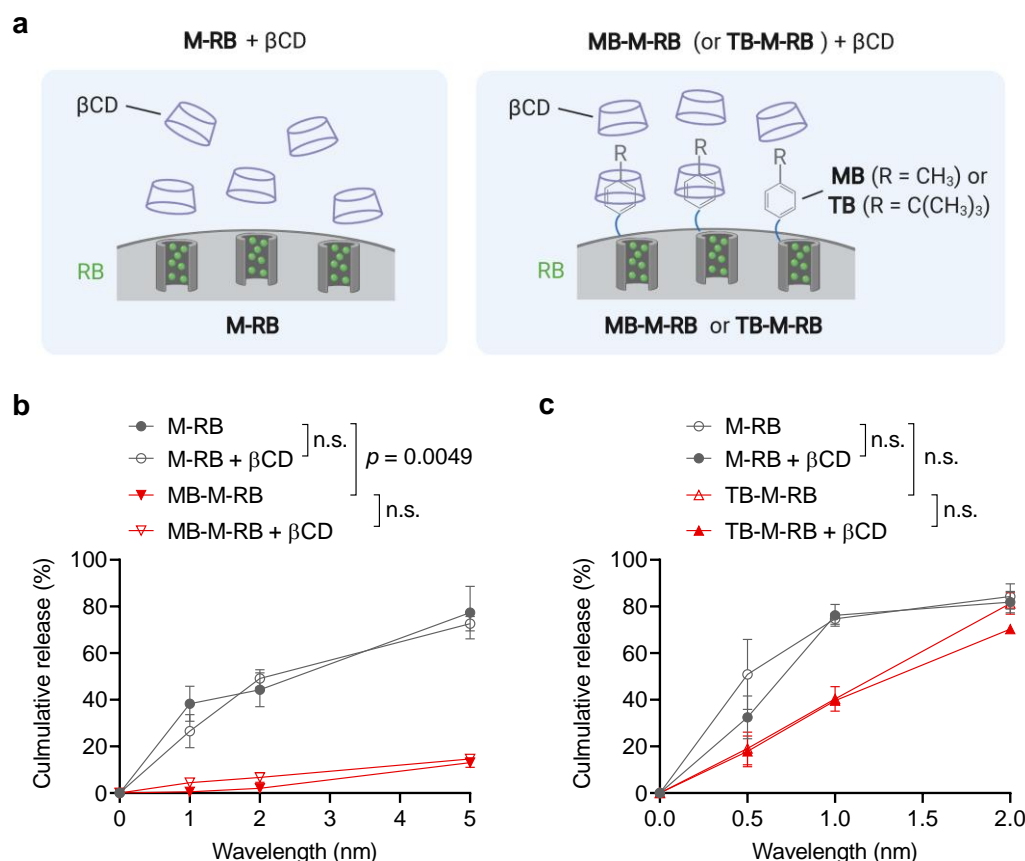


Figure 4:2 Evaluation of β -cyclodextrin (β CD)/alkylbenzene complexes as gatekeepers for mesoporous silica microparticles.

(a) Schematic of a rhodamine B (RB)-loaded mesoporous silica microparticle (M) without capping (denoted as M-RB) or capped with β CD/methylbenzene (MB) or tertbutylbenzene (TB) complexes (denoted as MB-M-RB or TB-M-RB, respectively). (b) Release kinetics of rhodamine B (RB) from indicated systems at 37 °C over time (n = 3).

4.4.2 Fabrication and characterization of T cell force-responsive drug release system using DNA-based force-sensitive gatekeepers

We then paid attention to DNA double strands as gatekeepers, which have a large molecular diameter (2.2 to 2.6 nm) that can potentially block mesopores (~ 3 nm) on silica microparticles.²³⁷ In addition, the rupture forces of DNA double strands can be fine-tuned by adjusting nucleotide pair numbers.²³⁵ We then designed a DNA force sensor sensitive to cellular forces estimated to be dozens of pN per receptor (Fig. 4:9a).²³³ According to a previous report, the double-strand DNA structure with a sequence of 15 base pairs could be ruptured by a force of ~ 50 pN,^{235,238} which is within the range of force per TCR generated by T cells.⁹⁶ The sensor is the self-assembly of two complementary DNA strands, an anchor strand bearing an amino group for conjugation to the surface of microparticles and a capper strand bearing a biotin molecule for coupling to antibodies through the biotin/neutralavidin interaction. The assembly structure was confirmed by gel electrophoresis showing resistance to a single-strand nucleic acid-specific nuclease (Fig. 4:9b, c).

Next, commercially purchased **M**s with a pore size of around 3 nm were functionalized with isocyanate groups using (3-isocyanatopropyl)triethoxysilane (Fig. 4:10).²³⁹ The amount of isocyanate groups on the surface was measured by elemental analysis and determined to be 9.86 mmol/g (Table 4:1). The DNA force sensor was next immobilized on the surface of **M** through the amidation reaction between amino and isocyanate groups to afford DNA-functionalized silica microparticles (denoted as **D-M**, Fig. 4:10). Successful conjugation of DNA to **M** was confirmed by UV-vis spectrum (Fig. 4:11a), and the amount of **D** was quantified by UV absorbance at 260 nm (10.9 ± 0.3 nmol/g, Fig. 4:3a and 4:11b). To further functionalize **D-M** with antibodies, **D-M** was incubated in an aqueous solution of neutravidin followed by the addition of biotinylated anti-CD3 and anti-CD28 antibodies (Fig. 4:10). The total amount of conjugated **Ab** on **Ab**-functionalized **D-M** (denoted as **AbD-M**, Fig. 4:10) was determined to be 4.26 ± 0.1 nmol/g using a bicinchoninic acid protein assay (Fig. 4:3a). The **AbD-M** has an average hydrodynamic diameter of 4.27 ± 0.2 μm and zeta potential of -14.1 ± 3.4 mV (Fig. 4:3a). The **AbD-M** maintained a spherical morphology similar to that of **M** as imaged by scanning electron microscopy (Fig. 4:3b, c).

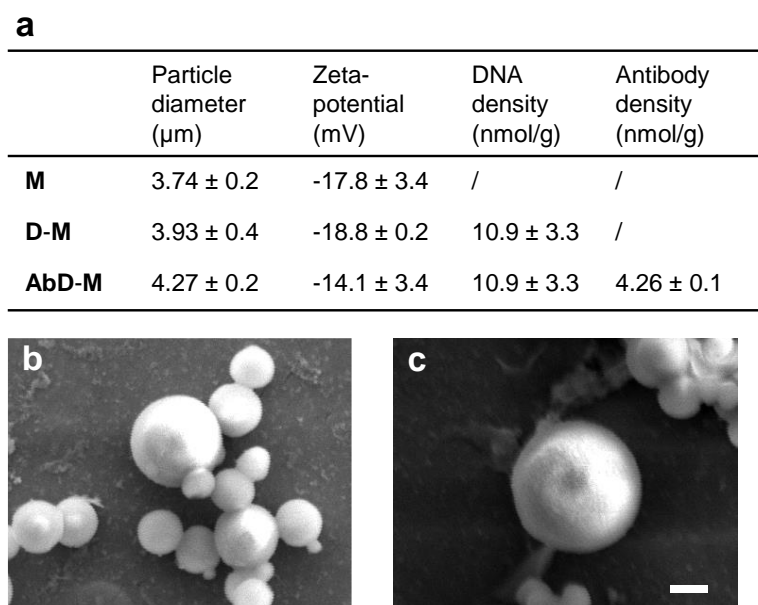


Figure 4:3 Characterizations of **M**, **D-M**, and **AbD-M**.

(a) Summarized physicochemical properties of **M**, **D-M**, and **AbD-M**. Data are mean \pm s.d. (b, c) Scanning electron microscopy (SEM) images of **M** (b) and **AbD-M** (c). Scale bar, 500 nm.

4.4.3 T cell force-responsive release of a fluorescent model drug

To investigate the T cell force-responsive release of the designed system, we pre-loaded **M** with **RB**, a fluorescent model drug, to prepare **RB**-loaded **AbD-M** (denoted as **AbD-M-RB**, Fig. 4:10). The loading amount of **RB** was 157.7 $\mu\text{mol/g}$ according to the fluorescence intensity measurement (Table 4:2 and Fig. 4:12a). By subtracting the background release from **AbD-M-RB** due to nonspecific leakage,²⁴⁰ we showed that uncapped **M-RB** (Fig. 4:10) exhibited a relative release of 46.8% (Fig. 4:4a and 4:13). Upon treatment of DNase I, a DNA degradation enzyme, the relative release of **RB** from **AbD-M-RB** was complete and comparable with that from uncapped **M-RB** (Fig. 4:4a), suggesting the successful capping of the mesopores by the DNA force sensors. We next co-cultured **AbD-M-RB** with activated Pmel CD8⁺ T cells (**T** + **AbD-**

M-RB), which, as expected, triggered a rapid release of loaded **RB** (35.5%, Fig. 4:4a and Fig. 4:13). The triggered release was TCR signaling-dependent as replacing the stimulatory antibodies with an isotype antibody control resulted in a minimum release of **RB** (Fig. 4:14a). Confocal imaging analysis of T cells co-cultured with fluorescently labeled **AbD-M** revealed a negligible level of internalization of the microparticles (Fig. 4:14b), suggesting that the observed drug release was not due to particle internalization by T cells or DNA gatekeeper digestion intracellularly. This observation is consistent with the previous reports that T cells are less phagocytotic, particularly toward large particles.^{69,78}

To validate that the **Ab**-mediated physical rupture of the DNA gatekeeper contributed to the **RB** release, we next replaced the conjugated **Ab** with soluble antibodies for triggering TCR activation of T cells (**T + sol. Ab + D-M-RB**). As the DNA force sensor was not connected to sol. **Ab** and thus did not receive T cell forces, the gatekeepers remained intact, and therefore the release of **RB** was minimal (6.5%, Fig. 4:4a) compared to that from **T + AbD-M-RB**. Next, we performed a time-lapse fluorescence imaging study to monitor the change of the fluorescence intensity of **RB** in **AbD-M-RB** in the presence of activated Pmel CD8⁺ T cells. A rapid decrease of the fluorescence intensity was noticed in **AbD-M-RB** within 30 min as the released **RB** quickly diffused away (Fig. 4:4b and 4:15). By contrast, sol. **Ab + D-M-RB** displayed negligible fluorescence decay even in the presence of activated T cells (Fig. 4:4b and 4:15). Together, soluble stimulatory antibodies failed to trigger the drug release, implying that the physical connection of T cells to the DNA gatekeepers was necessary, and the triggered drug release was not mediated by any soluble biochemical factors secreted by T cells upon TCR activation.

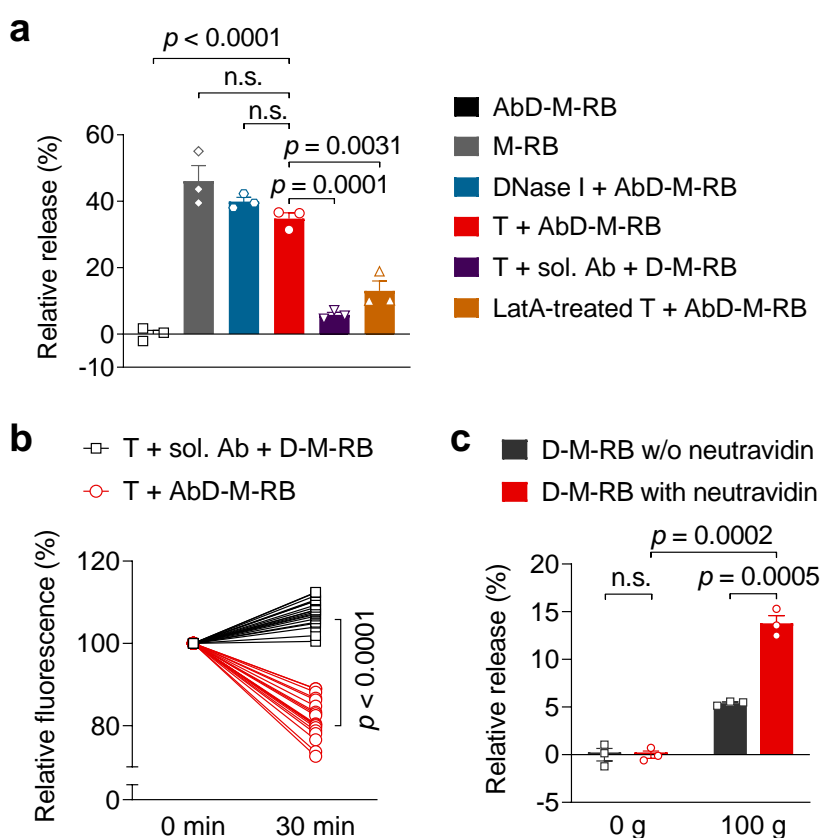


Figure 4:4 T cell force-responsive release of a fluorescent model drug.

(a) Relative release profiles of rhodamine B (**RB**) from the indicated systems after 1.5 h incubation at 37 °C (n = 3). (b) Relative fluorescence intensity of **AbD-M-RB** and **D-M-RB** plus sol. **Ab** after incubation with T cells (**T**) for 30 min (n = 20). (c) Relative release of **RB** from **D-M-RB** upon centrifugal forces with or without neutravidin conjugation (n = 3).

In order to directly examine the role of T cell force, we next co-cultured **AbD-M-RB** with activated Pmel CD8⁺ T cells pretreated with Latrunculin A, a small molecule inhibitor that inhibits actin polymerization and therefore the generation of cellular forces. By inhibiting T cell forces, the release of **RB** was significantly suppressed (13%, Fig. 4:4a). In addition, we applied centrifugal force on **D-M-RB** to mimic the T cell forces in another in vitro release assay (Fig. 4:16). Centrifugation has been widely used to apply controlled forces on cells for cell adherence study.²⁴¹ When **D-M-RB** was conjugated to the well bottom *via* neutravidin, markedly increased release of **RB** was observed under a centrifugal force (100 g, 2 min) as compared to the static condition (0 g) (Fig. 4:4c). These results suggest that the triggered cargo release from **AbD-M-RB** was mediated by T cell forces.

4.4.4 T cell force-responsive release of an anti-cancer drug in vitro and in vivo

Next, we loaded the T cell force-responsive system with **GEM** (denoted as **AbD-M-GEM**, Fig. 4:10) to assess its efficiency in killing cancer cells. The loading capacity of **GEM** in **AbD-M-GEM** was determined by UV absorbance (670 $\mu\text{mol g}^{-1}$, Table 4:2 and 4:12b). In order to evaluate the sole effect of the released anticancer drug and exclude the killing effect mediated by T cells, which requires physical contact between a T cell and a target cell (immunological synapse formation), we performed the cancer cell killing assay in a transwell plate, allowing the transfer of small molecules but not cells from the upper well to the bottom chamber (Fig. 4:5a). **AbD-M-GEM** was co-cultured with activated Pmel CD8⁺ T cells in the upper well, while B16F10 cancer cells, a murine melanoma cell line, were seeded in the bottom chamber. No cancer cell killing was noticed with T cells alone (Fig. 4:5b). However, in the presence of T cells, **AbD-M-GEM** led to a markedly increased efficiency of cancer cell killing (28.8%, Fig. 4:5b) due to the rapid release of **GEM** triggered by T cell forces. Consistently, sol. **Ab** + **D-M-GEM** in the presence of T cells resulted in a significantly lower percentage of cancer cell killing (9.8%, Fig. 4:5b) as the drug release was inefficient. It is worth noting that **AbD-M-GEM** exhibited minimal toxicity against the T cells (3.5% apoptosis induced, as shown in Fig. 4:17a).

To further assess the efficacy in vivo, we next established a tumor prevention model by subcutaneously co-injecting MC38, a murine colon carcinoma cell line, together with activated Pmel CD8⁺ T cells plus **AbD-M-GEM** in mice (Fig. 4:5c). As the antigen recognized by Pmel CD8⁺ T cells (glycoprotein 100) is not expressed in MC38 cancer cells, T cells alone resulted in no influence on the tumor growth (Fig. 4:5d and 4:17b). **AbD-M-GEM** alone failed to control the tumor growth either because anticancer drug release was not triggered. While T cells plus sol. **Ab** + **D-M-GEM** showed a certain effect of tumor growth inhibition, T cells plus **AbD-M-GEM** markedly suppressed the tumor progression in mice with a 3.5-fold decrease of tumor size compared to that of the PBS treatment 7 days post-injection, showing superior anti-cancer efficacy in vivo (Fig. 4:5d).

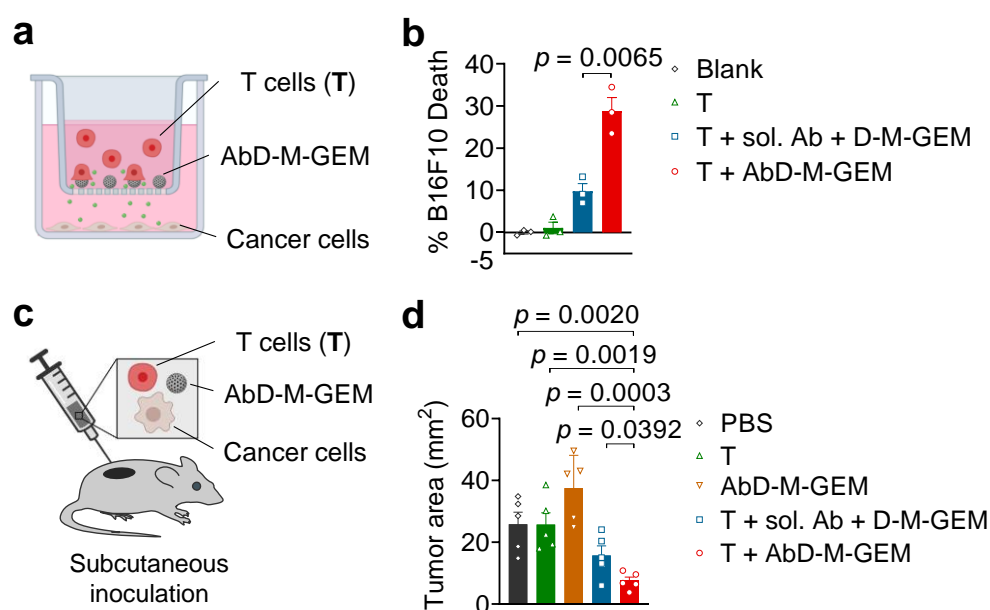


Figure 4:5 T cell force-responsive release of an anti-cancer drug in vitro and in vivo.

(a) Schematic of an in vitro release assay with a transwell plate. (b) Percentage of B16F10 cell death upon the indicated treatment in the upper well ($n = 3$). (c) Schematic of an in vivo cancer prevention assay. (d) Tumor areas at day 7 post-inoculation of MC38 cancer cells mixed with the indicated reagents ($n = 5$ mice per group).

4.4.5 Design of a bispecific DNA nanomachine for T cell force-responsive release upon recognition of cancer cells

As abovementioned, T cells exert mechanical forces at the immunological synapse when recognizing cancer cells presenting cognate antigens. To achieve specific release upon T cell activation on cancer cells, we designed a bispecific DNA nanomachine (**NM**) by adapting a DNA device that can release cargo triggered by antibody-induced conformational force/change.²⁴² The **NM** comprises a backbone DNA single-strand with anti-PTK7 and anti-mIgG-Fc aptamers at two ends, a cargo DNA single-strand with a quencher, and a fluorescent DNA single-strand for indicating the release of cargo strands (Fig. 4:6a). The cargo strand forms a clamp-like triplex structure with the backbone strand through Watson-Crick and Hoogsteen interactions, of which its stability is sensitive to the stretching of the backbone strand.²⁴² The anti-PTK7 and anti-mIgG-Fc aptamers provide anchors to cancer cells and T cells coated with IgG antibodies, respectively. When T cells exert forces on cancer cells, the tension between T cells and cancer cells can then be relayed to stretch the backbone of the **NM** for releasing the cargo strand (Fig. 4:6a). The release of cargo strand leads to the recovery of fluorescence of the fluorescent strand anchored on the backbone, which allows the quantitative measurement of the release events from **NM** (Fig. 4:6a).

We first tested the stability of fluorescent strands in various buffer systems. Intriguingly, the fluorescence of the fluorescent strands slightly decreased over time in phosphate-buffered saline (PBS), a commonly-used buffer in biological studies (Fig. 4:18). Besides, adding free quencher strands induced notable fluorescence loss of the fluorescent strands in PBS buffer (Fig. 4:18). Although adding Mg^{2+} into PBS stabilized the fluorescent strands, it resulted in substantially higher fluorescence loss when adding free quencher strands in the system (Fig. 4:18), which would potentially interfere

with the measurement of the release events from **NM**. As protein has been shown to stabilize DNA strands, we then screened bovine serum albumin (BSA)-supplemented HBSS buffer and FBS-supplemented RPMI medium to stabilize the fluorescent strands. In particular, the fluorescent strands were stable in phenol red-free RPMI medium with 10% FBS (denoted as RPMI buffer) and retained their fluorescence when free quencher strands were added to the system (Fig. 4:18).

To confirm the self-assembly of **NM**, we first constructed **NMs** without quencher strands by assembling backbone and fluorescent strands, which exhibited similar fluorescence signals as free fluorescent strands and were stable in RPMI buffer. After adding quencher strands into the system, fluorescence decreased by ~65% quickly in 15 min and reached an equilibrium state, indicating the successful incorporation of both fluorescent and quencher strands into the **NMs** (Fig. 4:19a). Besides, the **NM** was stable in RPMI buffer over 6 h without considerable fluorescence loss (Fig. 4:19b).

To test the T cell force-responsive release of **NM**, B16F10 cancer cells were first seeded on the well bottom, and a mixture of anti-CD45.2-coated Pmel T cells and **NMs** were then co-cultured with cancer cells for 6 h. The release events were monitored by measuring fluorescence recovery of **NM** as compared to **NM** without quencher strand in the same system. As shown in Fig. 4:6b, the **NM** itself had a minor background release of ~8.2% within 6 h. In addition, B16F10 cancer cells (~1.9%), Pmel T cells (~9.0%), or anti-CD45.2-coated Pmel T cells (~6.0%) alone didn't trigger notable release events from the **NMs** (Fig. 4:6b). In contrast, when co-culturing **NMs** with B16F10 cancer cells and anti-CD45.2-coated Pmel T cells together, considerable release events (~21.8%) were observed in 6 h (Fig. 4:6b). Importantly, removing anti-CD45.2 antibodies, which allow anchoring **NMs** to Pmel T cells, from the co-culture significantly reduced the release of cargos from **NMs** (~15.4%) (Fig. 4:6b). These results suggest that physical interactions between **NMs** and Pmel T cells play an important role in triggering release from **NMs**.

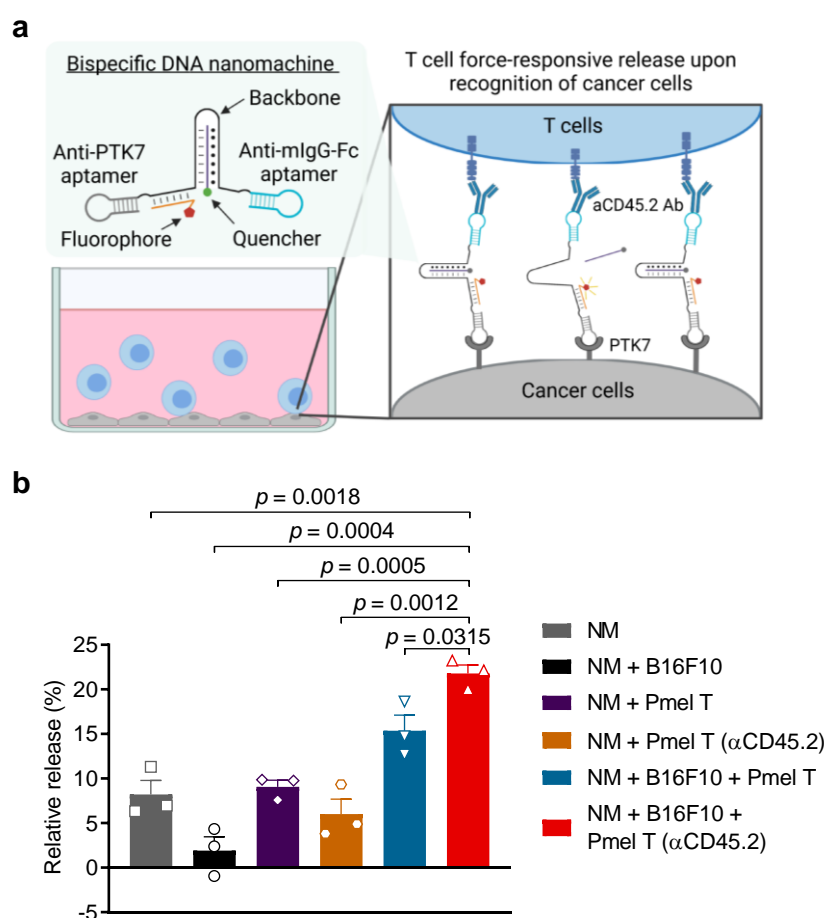


Figure 4:6 T cell force-responsive release upon recognition of cancer cells using a bispecific DNA nanomachine.

(a) Schematic of T cell force-responsive release of cargos from bispecific DNA nanomachines upon recognition of cancer cells. (b) Relative release profiles of cargo (quencher) from the bispecific DNA nanomachine in indicated systems after 6-h incubation at 37 °C (n = 3).

4.5 Conclusion

In summary, we demonstrated, for the first time, a T cell force-responsive delivery system for anticancer drugs. The cellular force-mediated drug release was highly specific and controlled by TCR activation of T cells, leading to the efficient killing of cancer cells in vitro and in vivo. In the meantime, we designed a bispecific DNA nanomachine that could achieve T cell force-responsive release upon recognition of cancer cells. The detailed release mechanism and feasibility of this DNA nanomachine in releasing therapeutics need to be further evaluated in the future.

The DNA mechano-sensor was crucial to respond sensitively to the cellular forces that are on a very small scale.²³³ Integrin binding aptamer has recently been reported as a mechano-sensor to control the release of growth factors in response to random cellular traction forces.²⁴³ By using the functionalized mesoporous silica microparticles, we chemically linked the force-triggered drug delivery to specific cell signaling (i.e., TCR activation of T cells) to achieve cell signaling-controlled drug release and therefore high specificity. In addition, the loading of drugs in mesopores through physical encapsulation allows for high versatility for various therapeutics. A wide range of cargos, including small molecules, peptides, cytokines, and antibodies, could be potentially loaded in this cellular force-responsive delivery system

by adopting mesoporous silica microparticles with suitable pore sizes.^{244,245} Cellular forces controlled by specific cell signaling are widely involved in both innate and adaptive immunity.^{246,247} This cellular force-responsive system has the promise to be coupled with various immune cells for synergistic and enhanced cancer therapies.

Toward potential translational applications, several challenges remain, such as miniaturizing the system down to nano-size for systemic administration and fine-tuning the sensitivity of the force-sensitive gatekeeper to ensure sufficiency as well as specificity of drug release. In addition, instability of DNA in vivo (e.g., nuclease degradation and rapid renal clearance) is another hurdle for therapeutic applications. To this end, chemical modifications of DNA, such as thiol modification of phosphate backbone and PEGylation,²⁴⁸ may stabilize the DNA gatekeepers to facilitate the in vivo applications.

4.6 Supplementary materials

4.6.1 Experimental methods

Chemicals and reagents. (3-isocyanatopropyl)triethoxysilane (ICPTES), mesoporous silica microparticle (MCM-48, particle size < 15 μm , pore size ~ 3 nm, surface area 1400-1600 m^2/g), $\text{MgCl}_2 \cdot 6\text{H}_2\text{O}$, 4',6-diamidino-2-phenylindole dihydrochloride (DAPI), Hoechst 33342, 3,3'-diocetadecyloxycarbocyanine perchlorate (DiO), *N*-(8-Amino-3,6-dioxaoctyl) rhodamine 6G-amide bis(trifluoroacetate) (AmR6G), 4-methylbenzoic chloride, 4-tertbutylbenzoic chloride, triethylamine (NEt_3), β -cyclodextrin (βCD), paraformaldehyde, deoxyribonuclease I (DNase I; from bovine pancreas) and bovine serum albumin (BSA) were purchased from Sigma-Aldrich (St. Louis, MO, USA). S1 nuclease was purchased from Promega (Madison, WI, USA). Rhodamine B (RB), 3-aminopropyl-trimethoxysilane (APTMS), toluene, acetonitrile (CH_3CN), dimethylformamide (DMF), and dimethyl sulfoxide (DMSO) were obtained from Acros Organics (Fisher Scientific, Waltham, MA, USA). Neutravidin, EZ-LinkTM NHS-Biotin, and agarose were purchased from Thermo Fisher Scientific (Waltham, MA, USA). Gemcitabine (GEM) was purchased from MedChemExpress (Sollentuna, Sweden). Latrunculin A (LatA) (1 mM in DMSO) was purchased from Calbiochem (Merck, Darmstadt, Germany). Oligonucleotides 5'-ATC TAA CTG CTG CGC CGC CGG GAA AAT ACT GTA CGG TTA GA-TTTTT-ATG GCA TTA ACC TTG CTT CTC TCC TTT CTC CTG TTT CTC CTC TTT CCT CTC T-TTTTT-TAA TAC GAC TCA CTA TAG CAA TGG TAC GGT ACT TCC AAG CTA ACC CTC ATC TGC GCG CTC CCA AAA GTG CAC GCT ACT TTG CTA A-3', 5'-(Cy3)-AGC AAG GTT AAT GCC AT-3', 5'-AGA AAG GAG AGA (BHQ2)-3', 5'-(NH_2)-ACG GAG GCA CGA CAC-3' and 5'-(Biotin)-GTG TCG TGC CTC CGT-TTTTT-3' were ordered from IDT (Coralville, IA, USA). Human gp100₂₅₋₃₃ (hgp100) peptide was purchased from GenScript (Piscataway, NJ, USA). Recombinant mouse interleukin-2 (IL-2) and interleukin-7 (IL-7) were purchased from PeproTech (London, UK). Anti-mouse CD3 antibody (clone 17A2), anti-mouse CD28 antibody (clone 37.51), and isotype antibody (clone C1.18.4) were purchased from Biorcell (West Lebanon, NH, USA). All products were used as received.

Animals and cell lines. All the mouse studies were approved by the Swiss authorities (Canton of Vaud, animal protocol ID 3206) and performed in accordance with EPFL CPG guidelines. Six- to eight-week-old female Thy1.2⁺ C57BL/6 (C57BL/6J) mice were purchased from Charles River Laboratories (Lyon, France). T cell receptor (TCR)-transgenic Thy1.1⁺ pmel-1 (Pmel) mice (B6.Cg-Thy1^a/Cy Tg(TcrTcrb)8Rest/J) were purchased from The Jackson Laboratory (Bar Harbor, ME, USA) and maintained

in the animal facility at EPFL. B16F10 murine melanoma cells and MC38 murine colon cancer cells were originally acquired from the American Type Culture Collection (ATCC; Manassas, VA, USA) and cultured in Dulbecco's modified Eagle's medium (DMEM) (Gibco, Thermo Fisher Scientific) supplemented with Fetal Bovine Serum (FBS) (Gibco, 10 v/v%) and penicillin/streptomycin (Gibco, 1 v/v%).

Methylbenzoyl (MB) or 4-tertbutylbenzoyl (TB)-functionalized mesoporous silica microparticle (M) loaded with rhodamine B (RB). To synthesize **M** functionalized with amino groups (**M-NH₂**), MSM (400 mg) was suspended in toluene (100 mL), and APTMS (120 μ L) was added into the suspension. The suspension was then refluxed under an N₂ atmosphere for 7 h. After cooling down, the suspension was centrifuged (4000 rpm, 10 min), and the precipitate was washed with deionized water and MeOH. Finally, the **M-NH₂** was obtained by drying at 60 °C for 12 h.

To synthesize methylbenzoyl (MB) or 4-tertbutylbenzoyl (TB)-functionalized **M** (**MB-M** or **TB-M**), **M-NH₂** (200 mg) was suspended in toluene (50 mL). NEt₃ (50 μ L) and 4-methylbenzoic chloride (100 μ L) or 4-tertbutylbenzoic chloride (120 μ L) were then added into the suspension. Afterward, the suspension was stirred under N₂ atmosphere at 25 °C for 24 h. After the reaction, the suspension was centrifuged (4000 rpm, 10 min), and the precipitate was washed with deionized water and MeOH, respectively. Finally, the **MB-M** or **TB-M** was obtained by drying at 60 °C for 12 h and analyzed with an FT-IR spectrometer (Nicolet 6700, Thermo Fisher Scientific).

To load **MB-M** or **TB-M** with **RB** (denoted as **MB-M-RB** or **TB-M-RB**, respectively), **MB-M** or **TB-M** (10 mg) and **RB** (0.5 mg) were suspended in deionized water (1 mL) with sonication. The suspension was shaken at 800 rpm (25 °C) overnight. Finally, the product was collected by centrifugation (6000 g, 2 min) and washed with PBS (pH 7.4) for one time. The obtained **MB-M-RB** or **TB-M-RB** were directly used for the release experiment without delay.

Release of RB from MB-M-RB or TB-M-RB in the presence of β CD. Release buffer (200 μ L/well, HBSS with 0.4 w/v% BSA and 10 mM HEPES) were firstly transferred to a 96-well plate (U bottom) followed by the addition of sample solutions (20 μ L/well) containing **MB-M-RB** (1 mg/mL), **MB-M-RB** (1 mg/mL) + β CD, **TB-M-RB** (1 mg/mL) or **TB-M-RB** (1 mg/mL) + β CD. The plate was then centrifuged at 3000 rpm for 2 min to precipitate the particles and cells at the bottom and incubated at 37 °C. At predetermined time points (0, 1, 2, and 5 h for **MB-M-RB**; 0, 0.5, 1, and 2 h for **TB-M-RB**), supernatant of each well (50 μ L) was retrieved, and release buffer (50 μ L) was replenished in each well. Finally, the fluorescence of the supernatant was measured using a plate reader (Varioskan LUX, Ex 550 nm, Em 580 nm, acquisition time: 100 ms).

Double strand DNA force sensor/gatekeeper (D). To generate double-strand DNA (dsDNA) force sensor/gatekeeper, a mixture of DNA anchor strand (5'-(NH₂)-ACG GAG GCA CGA CAC-3') and DNA capper strand (5'-(Biotin)-GTG TCG TGC CTC CGT-TTTTT-3') in 1:1 mole ratio (total concentration 50 μ M) in hybridization buffer (20 mM Tris-HCl, 37.5 mM MgCl₂) was heated to 95 °C for 3 min and then cooled down to 25 °C slowly in order to achieve DNA hybridization.^{235,238} The formation of dsDNA was validated with agarose gel electrophoresis (Fig. 4:9). In brief, the agarose gel (2 w/v%) with 1 \times SYBR Safe DNA Gel Stain (Invitrogen, Thermo Fisher Scientific) was loaded with DNA samples and run at 25 °C (110 V) for 40 min in Tris-acetate-EDTA (TAE) buffer (pH 6.5). In DNase I-treated groups, samples (20 μ L) were mixed with DNase I solution (10 μ L, 1.5 mg/mL in hybridization buffer) and incubated at 37 °C for 60 min before gel electrophoresis. In S1

nuclease-treated groups, samples (20 μ L) were mixed with S1 nuclease solution (10 μ L, 900 U/mL in hybridization buffer) and incubated at 25 $^{\circ}$ C for 20 min before the gel electrophoresis. After electrophoresis, the gel was scanned with an E-Gel imager (Invitrogen).

Isocyanate-functionalized mesoporous silica microparticle (M) loaded with rhodamine B (RB) or gemcitabine (GEM).

Following a procedure in a previous study,²³⁹ **M** (100 mg) and **RB** (10 mg) were suspended in CH_3CN (5 mL) with sonication. The suspension was shaken at 800 rpm (25 $^{\circ}$ C) overnight. Afterward, ICPTES (125 μ L) was added, and the mixture was shaken at 800 rpm (25 $^{\circ}$ C) for another 24 h. Finally, the product was obtained by washing with CH_3CN by centrifugation (6,000 g, 2 min) and drying at 50 $^{\circ}$ C for 3 h.

For **GEM** loading, **M** (20 mg) was suspended in a solution of GEM (40 mM) in dry DMF (400 μ L), and the mixture was shaken at 800 rpm (25 $^{\circ}$ C) overnight. Afterward, ICPTES (25 μ L) was added and shaken at 800 rpm (25 $^{\circ}$ C) for another 24 h. Finally, the products were obtained by washing with DMF using centrifugation (10,000 g, 3 min) and drying under vacuum at 25 $^{\circ}$ C for 5 h.

Biotinylated antibodies. NHS-Biotin (3 μ L, 10 mM) solution in DMSO was added to anti-CD3, anti-CD28, or isotype antibody solution (2 mg/mL) in 100 μ L of phosphate-buffered saline (PBS) (Gibco) at a final concentration of 300 μ M of NHS-Biotin. After 30-min incubation on a shaker at 25 $^{\circ}$ C (800 rpm), the biotinylated antibody solution was washed with PBS (500 μ L) using Amicon[®] ultra centrifugal filter with 30-kDa MWCO (Merck) (8,000 g, 5 min, \times 5). The final concentration of biotinylated antibodies was determined using a microvolume spectrophotometer (NanoDrop, Thermo Fisher Scientific). The biotinylated antibodies were stored at 4 $^{\circ}$ C before use.

Cellular force responsive M. Isocyanate-functionalized **M** loaded with **RB** or **GEM** were next used for assembly of a T cell force-responsive **Ms** (Fig. 4:10). To cap the surface of drug-loaded **M**, a solution of **D** (100 μ L, 25 μ M) in hybridization buffer (20 mM Tris-HCl, 37.5 mM MgCl_2) was added to a suspension of drug-loaded **M** functionalized with isocyanate groups (1 mg/mL) in 700 μ L of CH_3CN solution with **RB** (1 mM) or **GEM** (saturated) for fabrication of **D-M-RB** or **D-M-GEM**, respectively.²³⁹ The mixture was stirred at 25 $^{\circ}$ C overnight, and the resulting solid was isolated by centrifugation (6,000 g, 2 min) and washed with hybridization buffer to eliminate the residual drugs and the unbounded **D** to afford **D-M-RB** or **D-M-GEM**. Next, the neutravidin solution in PBS (150 μ L, 1 mg/mL) was mixed with a solution of **D-M-RB** or **D-M-GEM** (50 μ L, 14 mg/mL) in hybridization buffer, and the mixture was incubated at 25 $^{\circ}$ C for 5-min. The particles were next washed with hybridization buffer using centrifugation (6,000 g, 2 min, \times 2), resuspended in 100 μ L of hybridization buffer followed by addition of a solution (150 μ L) of biotinylated anti-CD3 (0.5 mg/mL) + biotinylated anti-CD28 (0.05 mg/mL) (**Ab**) or biotinylated isotype antibody (0.55 mg/mL) (**IsoAb**) in hybridization buffer. After incubation at 25 $^{\circ}$ C for 5 min, the **AbD-M-RB**, **IsoAb-M-RB**, or **AbD-M-GEM** was obtained by washing with hybridization buffer (6,000 g, 2 min).

Quantification of D in D-M. For DNA quantification, the amount of DNA in sample solutions (2 μ L) containing **D-M** (1 mg/mL) or **M** (1 mg/mL) was quantified by a microvolume spectrophotometer (NanoDrop). The surface density of **D** on **D-M** was calculated by subtracting the background signal of **M**.

Quantification of Ab in AbD-M. The antibody amount on **AbD-M** was quantified using Pierce™ BCA Protein Assay Kit (Thermo Fisher Scientific) according to the manufacturer's protocol. Briefly, sample solutions (20 µL) containing **AbD-M** (4 mg/mL) before and after antibody conjugation were mixed with working solution (160 µL) in a flat bottom 96-well plate and shaken for 30 seconds followed by a 30-min incubation at 37 °C. After cooling down to 25 °C, the absorbance at 562 nm was measured with a plate reader to quantify the amount of **Ab** (Varioskan LUX, Thermo Fisher Scientific). The surface density of **Ab** on **AbD-M** was calculated by subtracting the background signal of **D-M** (with neutravidin).

Characterizations of M. Isocyanate-functionalized **M** was sent to the Institute of Chemical Sciences and Engineering at EPFL for the elemental analysis to quantify the amount of isocyanate groups. The sizes and Zeta-potential of native **M**, **D-M**, and **AbD-M** were characterized by dynamic light scattering (DLS) with a Zetasizer NanoZS (Malvern, Worcester, UK). For size measurement, experiments were performed at 25 °C using a He-Ne laser (633 nm) and non-invasive backscatter optics. For Zeta-potential measurement, the electrophoretic mobility measurements were performed at 25 °C using M3-PALS technology (Malvern). The scanning electron microscope (SEM) images of native **M** and **AbD-M** were obtained with the GeminiSEM 300 (Zeiss, Oberkochen, Germany).

Activation of Pmel CD8⁺ T cells. Spleens collected from Pmel Thy1.1⁺ mice were ground through a cell strainer (70 µm, Fisher Scientific, Pittsburgh, PA, USA), and red blood cells were lysed with ACK lysing buffer (Gibco, 2 mL per spleen) at 25 °C for 5 min. After washing twice with PBS, splenocytes were collected and cultured in complete RPMI 1640 medium supplemented with FBS (10 v/v%), HEPES (Gibco, 1 v/v%), penicillin/streptomycin (1 v/v%), and β-mercaptoethanol (Gibco, 0.1 v/v%) in the presence of hgp100 (1 µM), recombinant mouse IL-2 (10 ng/mL), and recombinant mouse IL-7 (2 ng/mL) for 3-days followed by Ficoll-Paque Plus (GE Healthcare, Chicago, IL, USA) gradient separation to eliminate dead cells. The activated Pmel CD8⁺ T cells (> 95% purity) were maintained in the medium containing recombinant mouse IL-2 (10 ng/mL) and IL-7 (10 ng/mL) and used between day 4 to 8 for both in vitro and in vivo studies.

T cell force-responsive release of RB. Release buffer (200 µL/well, HBSS with 0.4 w/v% BSA and 10 mM HEPES) or Pmel T cell suspension (5×10⁵/mL) in release buffer (200 µL/well) were firstly transferred to a 96-well plate (U bottom) followed by the addition of sample solutions (20 µL/well) containing **AbD-M-RB** (2.5 mg/mL), **M-RB** (2.5 mg/mL), **D-M-RB** (2.5 mg/mL) + DNase I, **IsoAbD-M-RB** (2.5 mg/mL), or **D-M-RB** (2.5 mg/mL) + sol. **Ab**. The plate was then centrifuged at 3000 rpm for 2 min to precipitate the particles and cells at the bottom and incubated at 37 °C. At predetermined time points (0, 0.5, 1, and 1.5 h), the supernatant of each well (50 µL) was retrieved, and release buffer (50 µL) was replenished in each well. Finally, the fluorescence of the supernatant was measured using a plate reader (Varioskan LUX, Ex 550 nm, Em 580 nm, acquisition time: 100 ms). The relative release was calculated by subtracting the background release of **RB** from **AbD-M-RB** alone. To investigate the role of T cell force in control release, T cells were pre-treated with LatA (2 µM) in PBS at 37 °C for 10 min and washed with PBS before performing the release assay as abovementioned.

Confocal imaging of T cells cultured with M. Isocyanate-functionalized **M** was first covalently labeled with **R6G** during the capping step. In brief, AmR6G (0.3 µL, 10 mg/mL in DMSO) was added to a suspension of isocyanate-functionalized **M** (700 µL, 1 mg/mL in CH₃CN) followed by the addition of a solution of **D** (100 µL, 25 µM) in hybridization buffer. The mixture was stirred at 25 °C overnight, and the resulting solid was isolated by centrifugation (6,000 g, 2 min) and washed

with hybridization buffer to eliminate the residual AmR6G and the unbounded **D** to obtain **D-M-R6G**. Next, the anti-CD3/anti-CD28 antibody was conjugated to the **D-M-R6G** as abovementioned to obtain **AbD-M-R6G**.

To evaluate the potential internalization of **AbD-M** by T cells, a solution (20 μ L) of **AbD-M-R6G** (2.5 mg/mL) was added to a Pmel T cell suspension in release buffer (5×10^5 /mL, 200 μ L). After 2-h incubation at 37 °C, T cells were stained with Hoechst 33342 (5 μ g/mL) and DiO (5 μ M) in PBS (200 μ L) for 15 min at 25 °C. After fixation with paraformaldehyde (2 wt%) in PBS (200 μ L) for 10 min at 25 °C, T cells were transferred on a poly-L-lysine-coated coverslip and centrifuged at 1500 rpm for 2 min to settle down T cells on the coverslip. The coverslip was then inverted on a drop of Fluoromount-G mounting medium (Invitrogen) on a glass slide, and each side of the coverslip was sealed with nail polish. The confocal images were acquired using an inverted microscope (IX83, Olympus, Tokyo, Japan) equipped with a spinning disk confocal scanner (CSU-W1, Visitron, Puchheim, Germany) and a 60 \times /1.42 UPLSAPO objective (Olympus).

Fluorescence imaging of M loaded with RB. A suspension (20 μ L/well) of activated Pmel T cells (0.5×10^6 /mL) in RPMI 1640 medium without Phenol Red (Gibco) was mixed with a suspension (50 μ L/well) of **AbD-M-RB** (1 mg/mL) or **D-M-RB** (1 mg/mL) + sol. **Ab** in RPMI 1640 medium without Phenol Red followed by centrifugation at 3000 rpm for 2 min to settle down T cells and **Ms** at the bottom of a 96-well plate. Time-lapse fluorescence imaging was performed immediately using an EVOS™ M5000 inverted fluorescence microscope equipped with an onstage incubator for live-cell imaging (Thermo Fisher Scientific). Time-lapse sequences were recorded with the integrated Invitrogen™ EVOS™ M5000 Software that allows autofocusing on the **AbD-M-RB** or **D-M-RB** in the RFP channel (Ex 531/40 nm, Em 593/40 nm). Bright-field and RFP channel images were acquired in sequence with a 10 \times 0.3 NA phase objective at 2-min intervals for 30 min. The acquired images were processed using Fiji.

Release of RB from D-M-RB under centrifugal force. To coat the surface with neutravidin, a 96-well plate was first treated with NaOH solution (50 μ L/well, 0.1 M) for 5 min. After NaOH solution was aspirated, and APTMS (20 μ L/well) was applied for 3 min. The well plate was then thoroughly rinsed with de-ionized water. An NHS-Biotin solution in PBS (50 μ L/well, 100 μ M) was added to each well, followed by a 2-h incubation at 25 °C and thorough rinsing with PBS. Next, neutravidin solution in PBS (50 μ L/well, 50 μ g/mL) was applied, followed by overnight incubation at 4 °C. The plate was washed with PBS for 3-times to remove free neutravidin.

The sample solution (50 μ L/well) containing **D-M-RB** (1 mg/mL) was added to 96-well plates with or without neutravidin coating. The plate was centrifuged at 3000 rpm for 2 min to precipitate the particles at the bottom. Afterward, release buffer (370 μ L/well, 20 mM Tris-HCl, 37.5 mM MgCl₂) was carefully added on top of the sample solution. The well plate was then sealed using an adhesive PCR plate seal (Thermo Fisher Scientific) to prevent liquid leakage. The well plate was placed upside down in a centrifuge bucket. After centrifugation (100 g, 2 min), the well plate was unsealed, and supernatant of each well (50 μ L) was retrieved. Finally, the fluorescence of the supernatant was measured using a plate reader (Varioskan LUX). The relative release rate was calculated by subtracting the background release of **RB** without centrifugation (0 g).

Killing assay of B16F10 cancer cells with AbD-M-GEM. B16F10 cells (4×10^4 /well) were seeded at the bottom chamber of a transwell plate overnight. To the upper chamber, a solution (50 μ L/well) of PBS buffer, activated Pmel T cells

(1×10^5 /well) only in RPMI 1640 medium with FBS (10 v/v%), or **AbD-M-GEM** (2 mg/mL) (or **D-M-GEM** [2 mg/mL] + sol. **Ab**) together with Pmel T cells in RPMI 1640 medium with FBS (10 v/v%) was added. After 2-h incubation at 37 °C, the upper chamber was removed, and the bottom chamber containing B16F10 cells was further cultured at 37 °C for 24 h. Afterward, the bottom well was replaced with MTT solution in PBS (100 μ L/well, 0.5 mg/mL) followed by a 4-h incubation at 37 °C. After that, the MTT solution was replaced with 100 μ L of DMSO and shaken at 500-rpm (25 °C) for 10 min. Finally, the absorbance at 490 nm was measured with a plate reader (Varioskan LUX) to quantify the cell viability.

Toxicity of AbD-M-GEM against T cells. To evaluate the potential toxicity of **AbD-M-GEM** against T cells, a solution (50 μ L/well) of **AbD-M-GEM** (2 mg/mL) (or **D-M-GEM** [2 mg/mL] + sol. **Ab**) was added to activated Pmel T cells (100 μ L, 1×10^5 /well) in RPMI 1640 medium with FBS (10 v/v%). After 2-h incubation at 37 °C, T cells were stained with DAPI and Alexa Fluor 488-conjugated Annexin V (Invitrogen) for flow cytometry analyses.

In vivo cancer prevention study. MC38 cancer cells (0.2×10^6) in PBS (100 μ L) were mixed with a solution (100 μ L) of PBS buffer, activated Pmel T cells alone (1×10^6) in PBS, or **AbD-M-GEM** (2 mg/mL) (or **D-M-GEM** [2 mg/mL] + sol. **Ab**) together with Pmel T cells (1×10^6) in PBS. The mixture was inoculated subcutaneously in the right flanks of Thy1.2⁺ C57BL/6J mouse at day 0. Tumor area (product of measured orthogonal length and width) and body weight were measured every 2 days from day 5 after inoculation. Mice were euthanized when the body weight loss was higher than 20% of the pre-dosing weight, or the tumor area reached 150 mm².

Bispecific DNA nanomachine (NM). To fabricate the **NM**, backbone strands (5'-ATC TAA CTG CTG CGC CGC CGG GAA AAT ACT GTA CGG TTA GA-TTTTT-ATG GCA TTA ACC TTG CTT CTC TCC TTT CTC CTG TTT CTC CTC TTT CCT CTC T-TTTTT-TAA TAC GAC TCA CTA TAG CAA TGG TAC GGT ACT TCC AAG CTA ACC CTC ATC TGC GCG CTC CCA AAA GTG CAC GCT ACT TTG CTA A-3') were mixed with fluorescent strands (5'-(Cy3)-AGC AAG GTT AAT GCC AT- 3') and quencher strands (5'-AGA AAG GAG AGA (BHQ2)-3') in 1:1:1 mole ratio (total concentration 100 nM) in the buffer. The formation of nanomachine was validated with quenching of fluorescence upon adding the quencher strand (Fig. 4:19a).

Monitor assembly and stability of NM. To monitor the assembly of **NM**, the backbone strand was first mixed with fluorescence strand, and then quencher strand was added at 30 min post mixing. At predetermined time points (0, 10, 20, 30, 35, 45, 55, and 65 min), the sample's fluorescence was measured using a plate reader (Varioskan LUX, Ex 550 nm, Em 570 nm, acquisition time: 100 ms).

To monitor the stability of components of DNA nanomachine, the single component of DNA nanomachine or its combinations were prepared in various buffers (100 μ L) in a 96-well plate. All the components' concentration was set to 100 nM. At predetermined time points (0, 10, 20, 30, 35, 45, 55, and 65 min), the fluorescence of each sample was measured using a plate reader (Varioskan LUX, Ex 550 nm, Em 570 nm, acquisition time: 100 ms). For monitoring stability of DNA nanomachine with or without quencher strand, fluorescence was measured in RPMI buffer at predetermined time points (0, 30, 60, 120, 240, and 360 min).

Release of cargo from bispecific DNA nanomachine in the presence of B16F10 melanoma cells and Pmel T cells. B16F10 melanoma cells (2×10^4 /well) were first seeded on a 96-well plate overnight. Afterward, **NM** (100 nM) in RPMI buffer

(100 μ L/well, without phenol red, with 10 v/v% FBS and 10 mM HEPES) with or without Pmel T cells (2×10^5 /mL) plus anti-CD45.2 antibodies (100 nM) were then transferred to the 96-well plate seeded with B16F10 melanoma cells and incubated at 37 °C. At predetermined time points (0, 20, 40, 60, 180, and 360 min), the fluorescence of each well (FL) was measured using a plate reader (Varioskan LUX, Ex 550 nm, Em 570 nm, acquisition time: 100 ms). Finally, the relative release (%) was calculated using the following equation.

$$\text{Relative release (\%)} = \frac{[FL_{NM}/FL_{NM \text{ without quencher}}]_t - [FL_{NM}/FL_{NM \text{ without quencher}}]_{t=0}}{1 - [FL_{NM}/FL_{NM \text{ without quencher}}]_{t=0}} \times 100\%$$

Statistical analyses. Statistical analyses were performed by using unpair t test in GraphPad Prism 8 software. Shown are mean \pm s.e.m unless otherwise indicated. In all cases, two-tailed tests with p values of less than 0.05 were considered significant.

4.6.2 Supplementary figures and tables

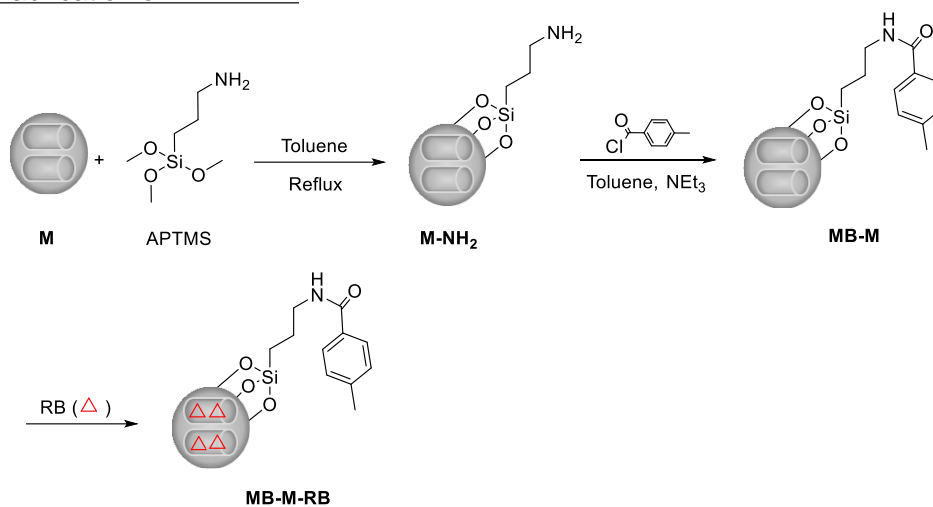
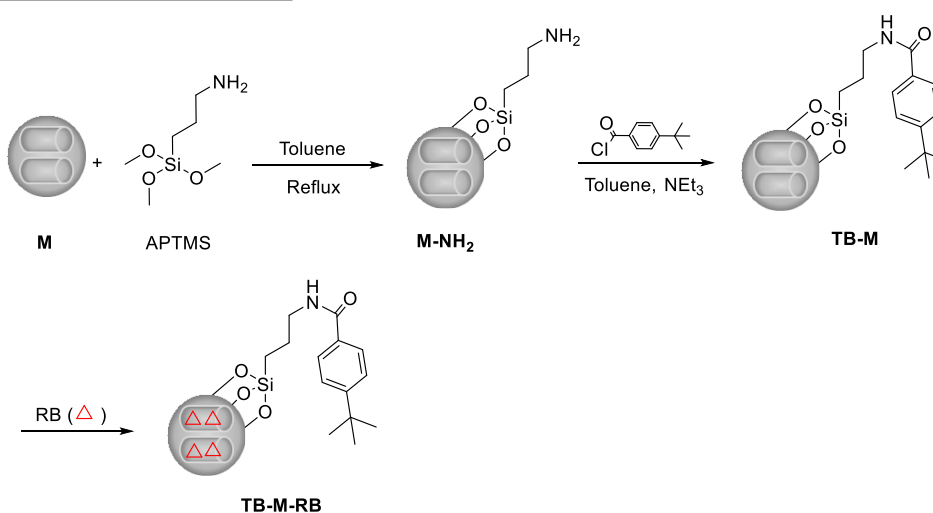
Fabrication of MB-M-RBFabrication of TB-M-RB

Figure 4:7 Schematic of the fabrication of rhodamine B (**RB**)-loaded mesoporous silica microparticles (**Ms**) modified with methylbenzene (**MB**) or tertbutylbenzene (**TB**) (denoted as **MB-M-RB** or **TB-M-RB**, respectively).

APTMS, 3-aminopropyl-trimethoxysilane; NEt₃, triethylamine.

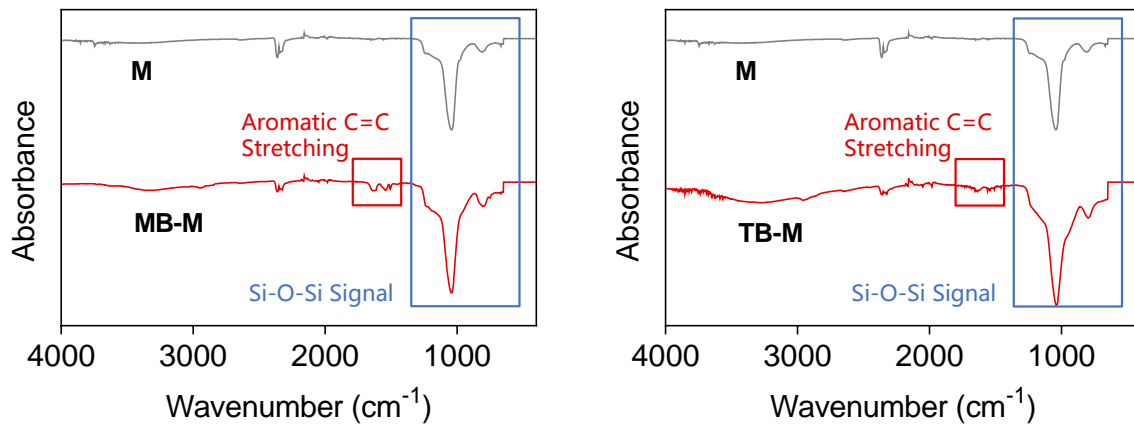


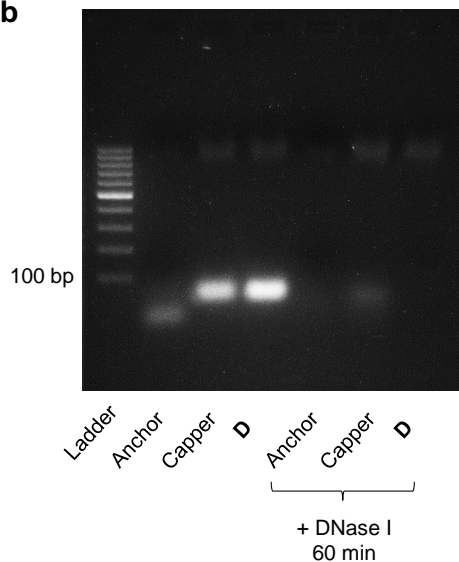
Figure 4:8 Fourier-transform infrared (FT-IR) spectra of mesoporous silica microparticle (**M**) and **M** modified with methylbenzene (**MB**) or tertbutylbenzene (**TB**) (denoted as **MB-M** or **TB-M**, respectively).

a

DNA gatekeeper (**D**) with force sensor function



b



c

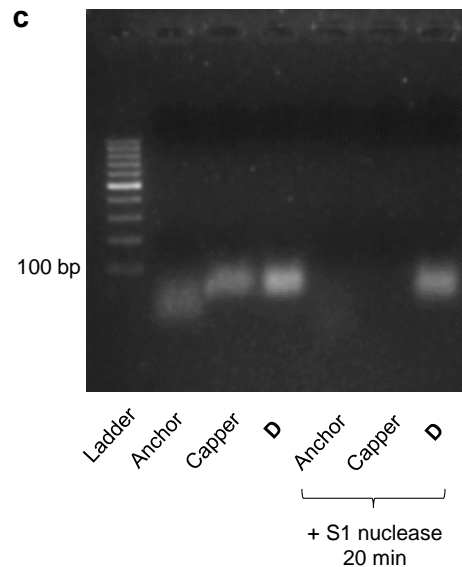
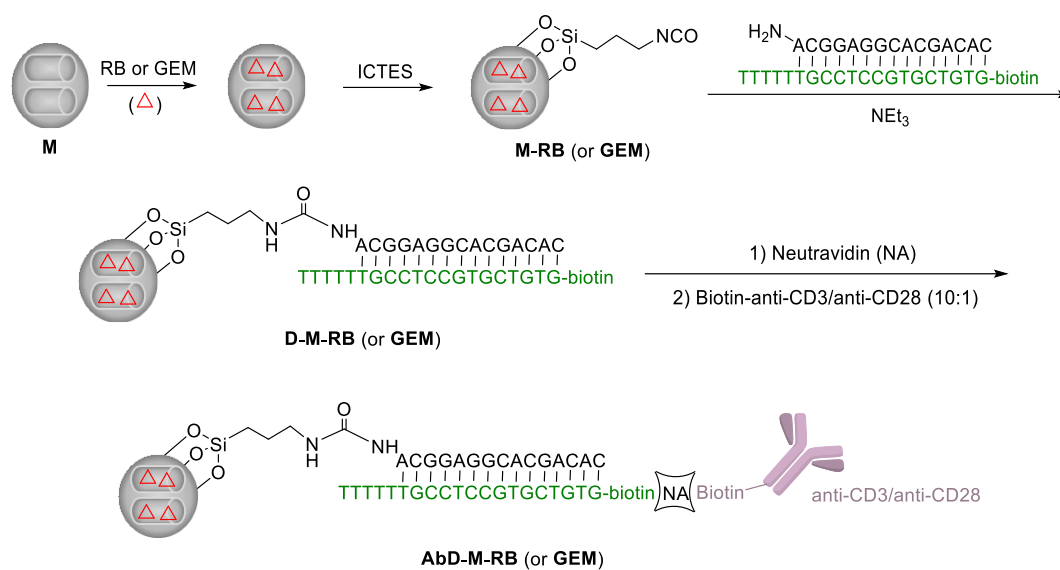


Figure 4:9 Design of a DNA gatekeeper (**D**) with force sensing function.

(a) Sequence of **D** self-assembled from DNA anchor and capper. The 5' end of DNA anchor was modified with an amino group for anchoring on mesoporous silica microparticle surface. For DNA capper, the 5' end was modified with biotin for conjugation with antibodies, and the 3' end was extended with five repeating thymine nucleotides (T) for capping the nanochannels on mesoporous silica microparticle. A, deoxyadenosine; C, deoxycytidine; G, deoxyguanosine. (b, c) Gel electrophoresis of DNA capper, DNA anchor, and their self-assembled double-strand **D** in the absence or presence of DNase I (b) or S1 nuclease (c), an enzyme that specifically degrades single-strand nucleic acids.

Systems with drug loading



Systems without drug loading

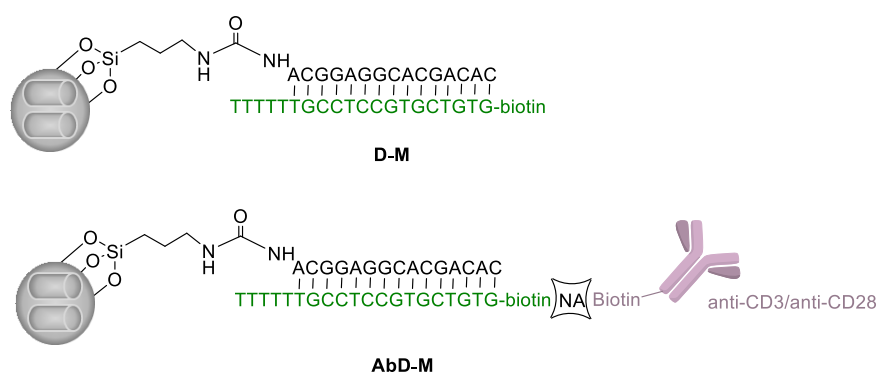


Figure 4:10 Schematic of the fabrication of T cell force-responsive mesoporous silica microparticles.

ICTES, (3-Isocyanatopropyl)triethoxysilane; NEt_3 , triethylamine.

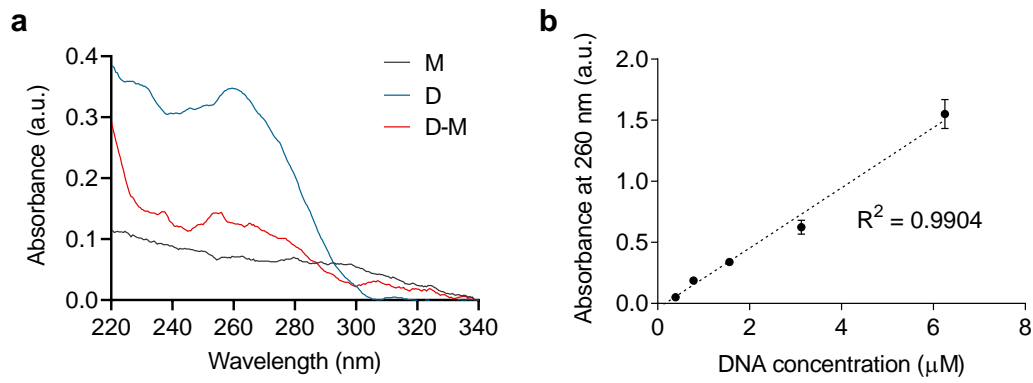


Figure 4:11 Characterization of DNA force sensor (**D**) on mesoporous silica microparticle (**M**).

(a) UV-vis spectra of native **M**, **D**, and DNA-capped mesoporous silica microparticle (**D-M**). (b) A calibration curve for **D** in hybridization buffer (20 mM Tris-HCl, 37.5 mM MgCl_2). Shown are mean \pm s.d. The plot is a simple linear regression of the data points.

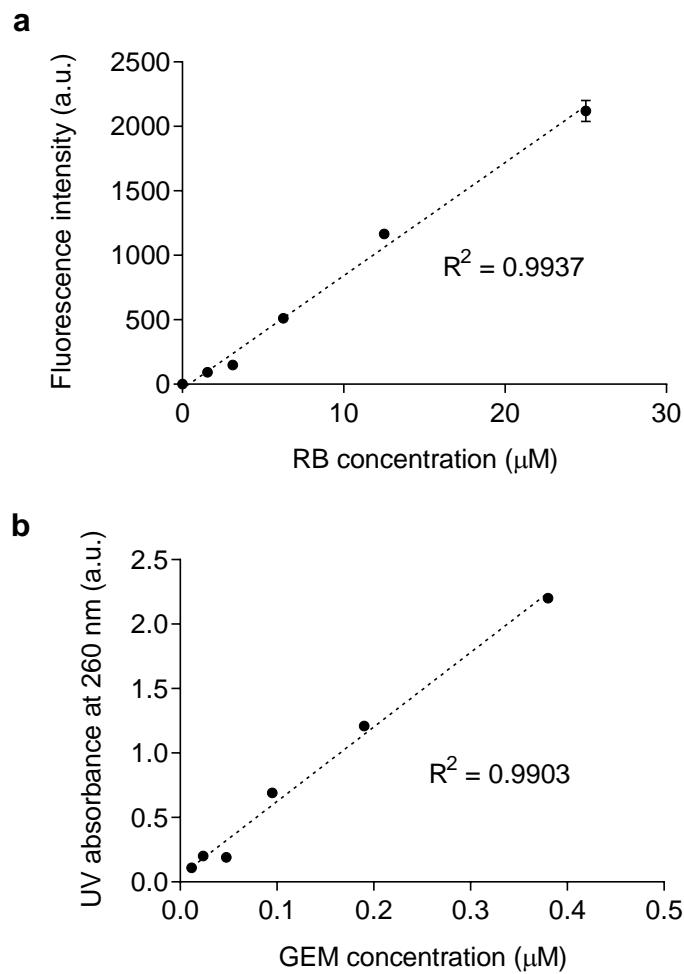


Figure 4:12 Calibration curves for rhodamine B (**RB**) (a) and gemcitabine (**GEM**) (b) in Hank's balanced salt solution (HBSS).

Shown are mean \pm s.d. The plot is a simple linear regression of the data points.

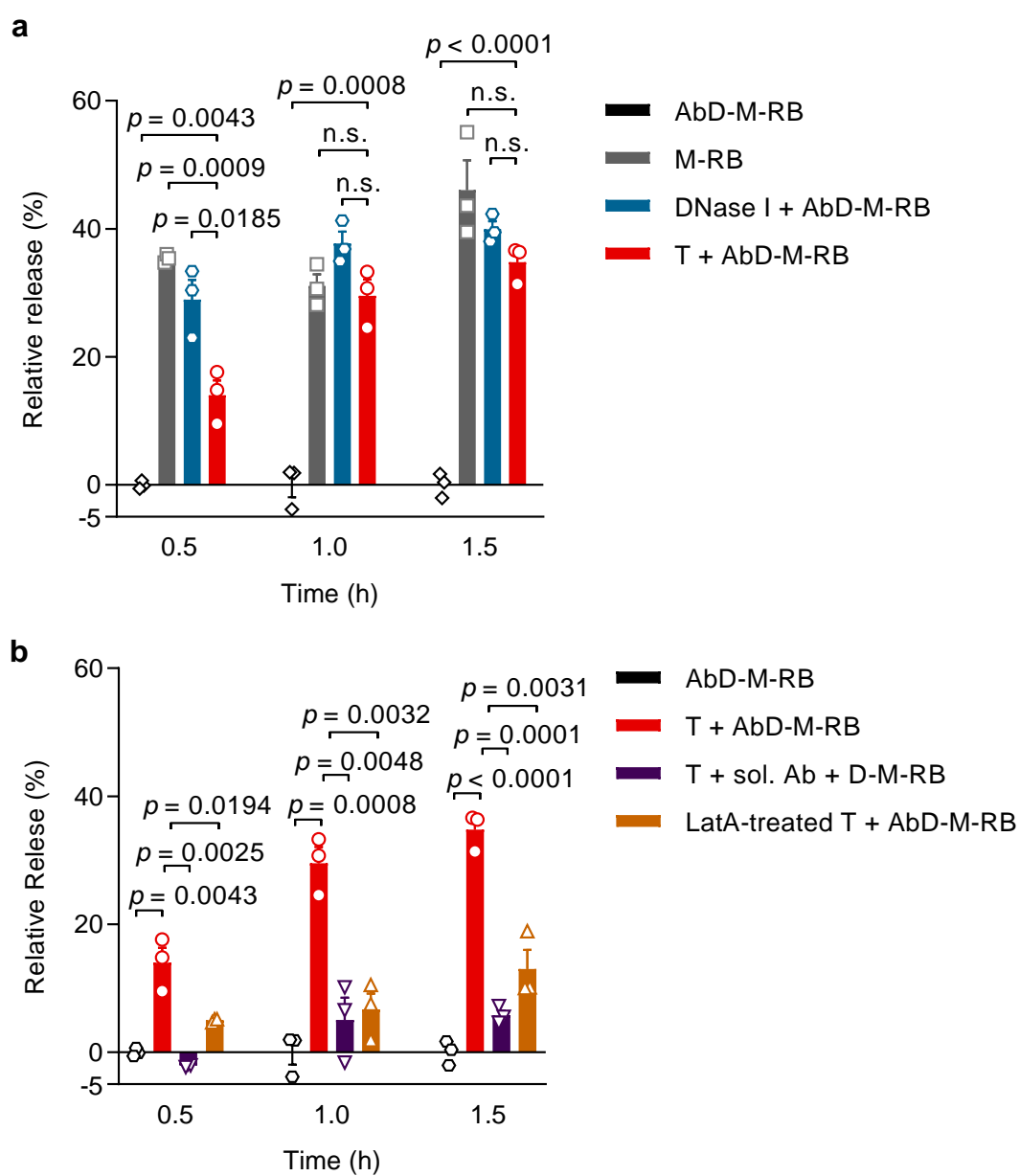


Figure 4:13 Release kinetics of rhodamine B (RB) from indicated systems at 37 °C over 1.5 h (n = 3).

DNase I, deoxyribonuclease I; T, T cells; LatA, latrunculin A.

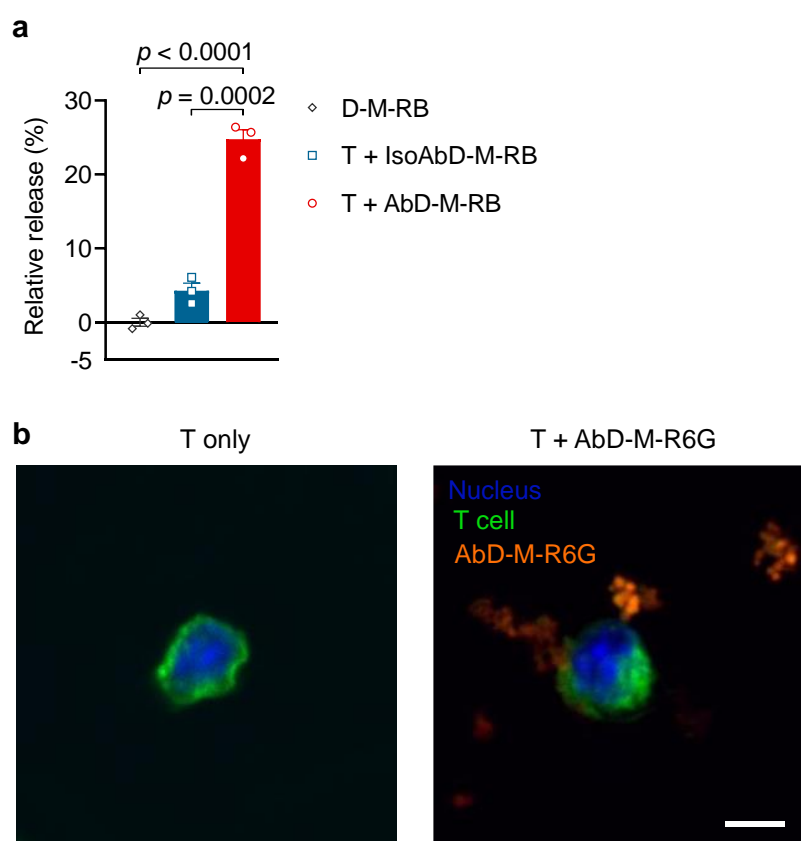


Figure 4:14 Release of rhodamine B (RB) from **AbD-M-RB** depended on T cell activation and internalization of **AbD-M-RB** by T cells was negligible.

(a) Relative release profiles of rhodamine B (RB) from indicated systems after 1.5-h incubation at 37 °C (n = 3). (b) Representative confocal images of T cells (T) only or T after 2-h co-culture with rhodamine 6G (R6G)-labeled **AbD-M** (**AbD-M-R6G**) at 37 °C. The nucleus and plasma membrane of T cells were stained with Hoechst 33342 (blue) and DiO (green), respectively. **AbD-M-R6G** was shown in red. Scale bar, 5 μ m. Statistical analyses were performed by using unpair t test and data are mean \pm s.e.m.

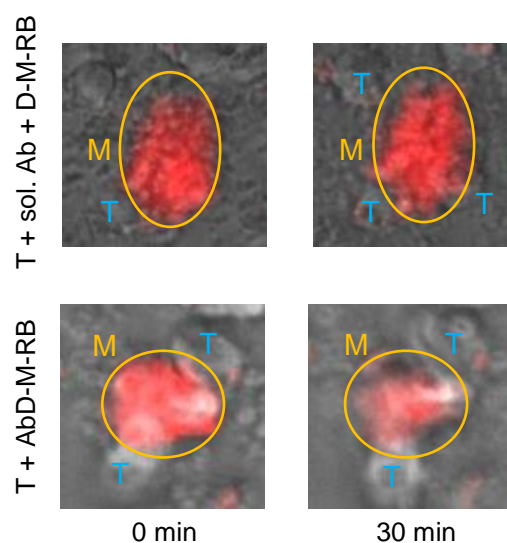


Figure 4:15 Fluorescence imaging of T cell force-responsive release of rhodamine B (RB) from **AbD-M-RB**.

T cells (T) triggered the release of a model drug, **RB**, from the cellular force-responsive mesoporous silica microparticle system upon close contact. The fluorescence images of **AbD-M-RB** and **D-M-RB** (+ sol. **Ab**) in close contact with Pmel CD8⁺ T cells upon 0- or 30-min incubation time. Yellow circles indicate the microparticles (M).

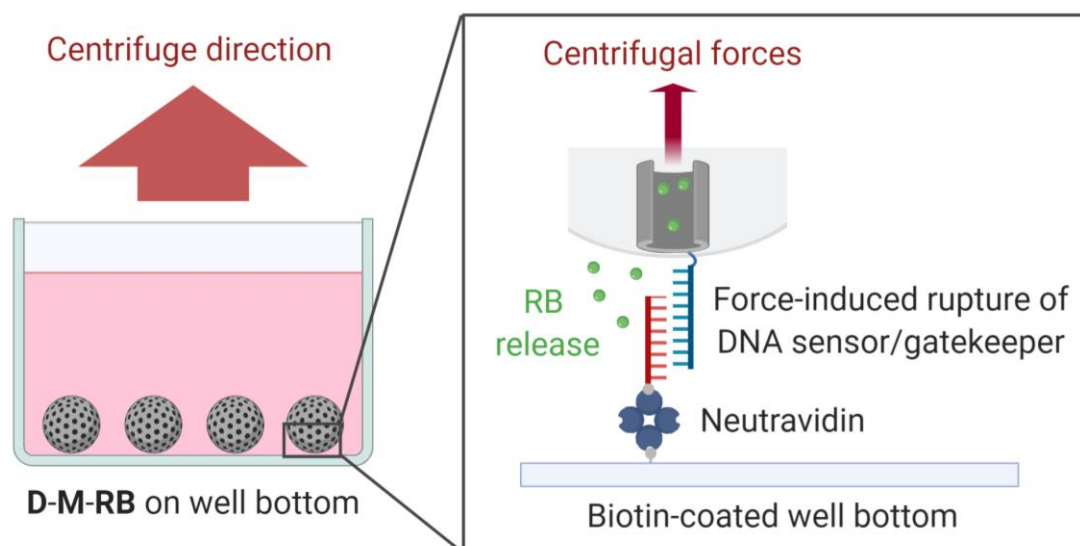


Figure 4:16 Schematic of an in vitro release assay of **D-M-RB** using centrifugal forces.

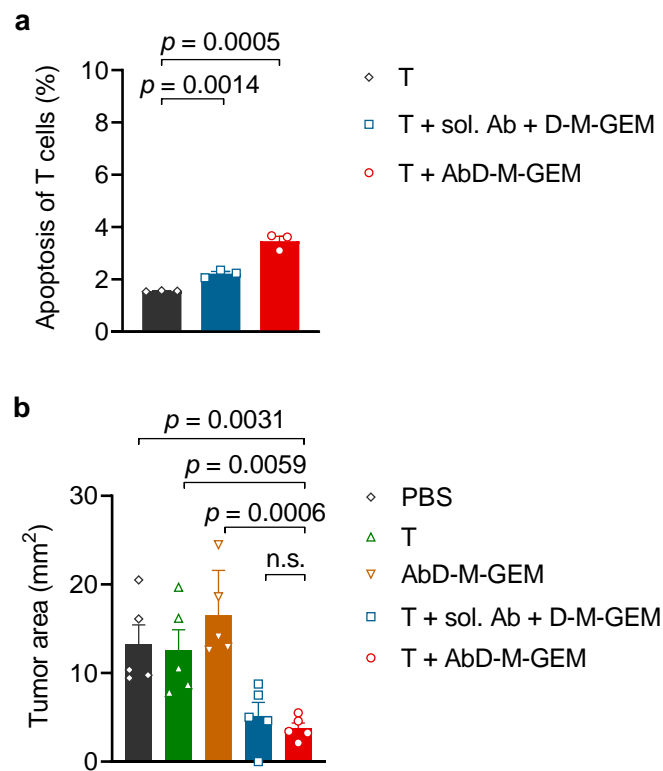


Figure 4:17 **AbD-M-RB** had a negligible influence on T cell apoptosis.

(a) Percentage of apoptotic Pmel T cells after 2-h co-culture with the indicated conditions ($n = 3$). (b) Tumor areas at day 5 post-inoculation of MC38 cancer cells mixed with indicated reagents ($n = 5$ mice per group). Statistical analyses were performed by using unpair t test and data are mean \pm s.e.m.

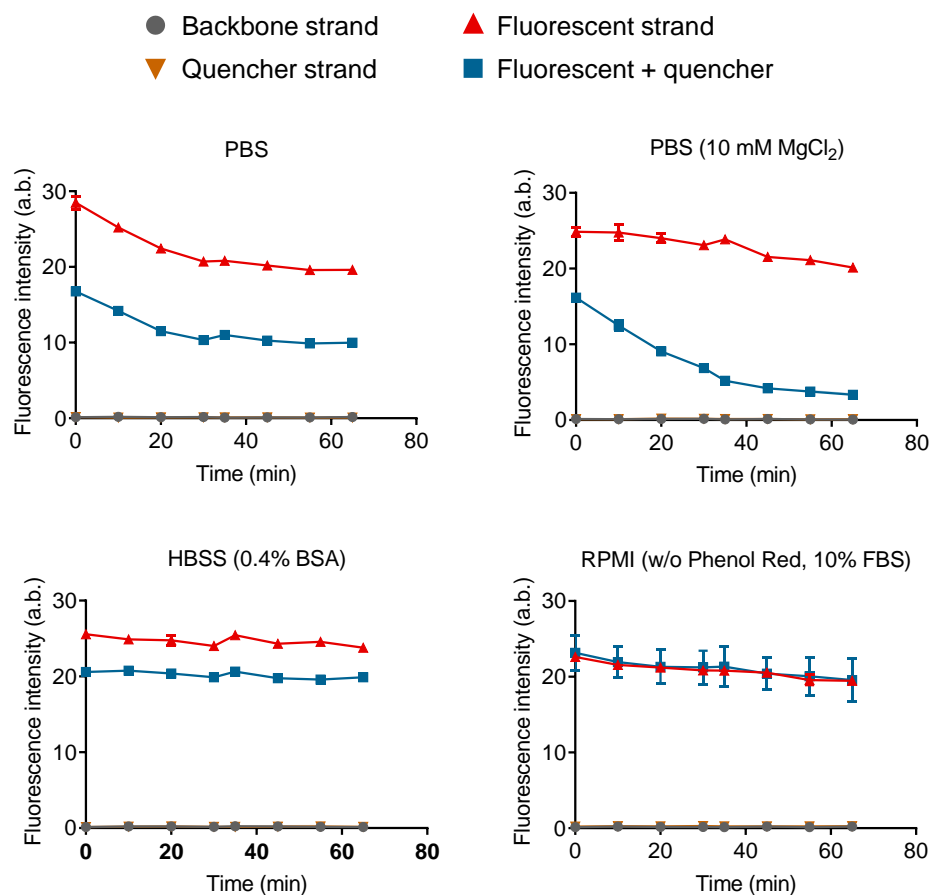


Figure 4:18 Stability of components of DNA nanomachine (**NM**) in different buffers.

The time-course changes of the fluorescence intensity of backbone strands, fluorescent strands, quencher strands, and fluorescent strands plus quencher strands incubated in the indicated buffers at 37 °C ($n = 3$). Data are mean \pm s.e.m.

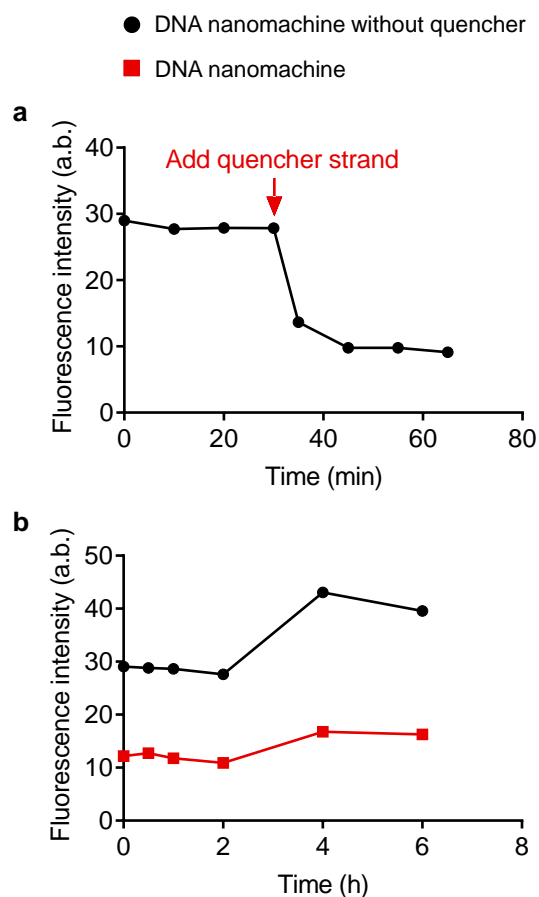


Figure 4:19 Self-assembly and stability of DNA nanomachine (NM).

(a) The fluorescence intensity kinetic profile shows the formation of DNA nanomachine after adding quencher strands ($n = 3$). (b) The time-course changes of the fluorescence intensity of the DNA nanomachines with and without quenchers incubated in the RPMI buffer (w/o phenol red, 10% FBS) at 37 °C ($n = 3$). Data are mean \pm s.e.m.

Table 4:1. Elemental analysis of bare mesoporous silica microparticle (M) and isocyanate-functionalized M (M-NCO). Data are mean \pm s.d.

	N (wt%)	C (wt%)	H (wt%)
M	0	0	0.55 \pm 0.06
M-NCO	1.48 \pm 0.02	7.16 \pm 0.05	1.04 \pm 0.01

Table 4:2. Loading capacity of rhodamine B (RB) or gemcitabine (GEM) in M. Data are mean \pm s.d.

	RB ($\mu\text{mol/g M}$)	GEM ($\mu\text{mol/g M}$)
M-RB	157.7 \pm 0.4	/
M-GEM	/	670 \pm 7.7

4.7 Acknowledgements

We thank Dr. Maartje Bastings (EPFL) for her input on the design of the DNA gatekeeper. L.T. gratefully acknowledges grant support from the Swiss National Science Foundation (Project grant 315230_173243) and European Research Council (ERC starting grant 80533).

Chapter 5 Conclusion

5.1 Achieved results

In this thesis, I developed three different mechanical immunoengineering strategies to enhance T cell-based cancer immunotherapy: 1) efficient ex vivo expansion of effector T cells by controlling the morphology of artificial antigen-presenting cell (aAPC) as a passive mechanical cue; 2) overcoming an immune checkpoint of mechanical basis by modulating cancer cell mechanical properties; and 3) specific delivery of T cell supporting drugs in response to T cell forces. These new strategies provided potential solutions to major challenges in T cell-based cancer immunotherapy, including difficult ex vivo T cell manufacturing for an effective therapeutic dosage, low response rate of current biochemical-based immune checkpoint blockade therapies, and systemic toxicity of T cell supporting drugs. The achieved results are elaborated as below:

- 1) **A spiky aAPC based on titanium dioxide (TiO₂) microparticle presenting T cell stimulatory ligands was fabricated to recapitulate the dendritic morphology of natural dendritic cells (DCs) for augmented T cell expansion.** aAPCs mimicking DCs are an emerging and feasible platform to achieve an efficient and consistent ex vivo expansion of functional T cells for therapeutic purposes. Major efforts have been focused on incorporating biochemical features of DCs into aAPCs. However, there is still a gap between aAPC and DCs in various aspects, such as T cell priming potency. As complementary to biochemical cues, biomechanical characteristics of DCs offer an additional dimension to improve current aAPC systems but have been underexplored in the field. In particular, it remains unclear whether and how the dendritic morphology of DCs, a characteristic of mature DCs, contributes to T cell priming efficiency.

In this thesis, I found that the spiky structure mimicking the dendritic morphology of DCs promoted activation and expansion of effector CD8⁺ T cells through enhancing the F-actin polymerization of T cells. The spiky aAPC could enhance ex vivo expansion of both antigen-specific and polyclonal CD8⁺ T cells and outperformed Dynabead®, a standard aAPC utilized in clinical manufacturing of adoptive T cell transfer (ACT) therapy, in terms of effector T cell expansion. The spiky structure provides a novel biomechanical parameter to improve the ex vivo T cell expansion process in the clinical manufacturing of ACT therapy.

- 2) **Cancer cell softness was identified as a mechanical immune checkpoint and could be therapeutically targeted by a cell-stiffening intervention for enhanced ACT therapy.** The discovery of biochemical immune checkpoints such as programmed cell death protein 1 (PD-1)/ programmed death-ligand 1 (PD-L1) has revolutionized cancer immunotherapy leading to durable tumor regressions in a small fraction of cancer patients. Although recent researches have revealed that biomechanical cues such as stiffness are a key regulator of cytotoxic T cell functions in addition to biochemical cues, it is still unknown whether cancer utilizes biomechanical cues to evade the immunosurveillance by cytotoxic T cells, and if so, how cancer develops such mechanical immune checkpoints and their underlying immuno-evasion mechanisms.

In the thesis, I discovered that membrane cholesterol enrichment contributes to cancer cell softening by decreasing cell cortical stiffness. Such cortically softening of cancer cells conferred their resistance to T cell-mediated cytotoxicity and could be reversed by depleting cholesterol from the cancer cell membrane. Stiffening cancer cells via cholesterol depletion substantially enhanced T cell-mediated cytotoxicity against cancer cells. Applying cancer cell stiffening intervention in vivo significantly augmented the efficacy of ACT therapy in various preclinical tumor models. The enhanced T cell-mediated cytotoxicity against stiffened cancer cells was attributed to increased T cell mechanical force derived from F-actin polymerization but not any known biochemical pathways of T cell-mediated cytotoxicity. Together, an immune checkpoint of mechanical basis, e.g., cancer cell softness, was revealed to suppress T cell-mediated cytotoxicity. Targeting mechanical immune checkpoints is a new concept and may complement current therapies that block biochemical immune checkpoints for improving clinical responses in cancer patients.

- 3) **A T cell force-responsive delivery system was developed using mesoporous silica microparticles capped with DNA force sensors as gatekeepers for reduced systemic toxicity.** Cellular force-responsive drug release has been very challenging due to the extremely small scale of cellular forces at nanonewton (nN) magnitude. However, it has great potential to precisely control drug release at a single-cell level. At present, it remains difficult to develop a versatile cellular force-release system that can respond to specific cell signaling-derived cellular forces and release various types of drugs from small molecules to macromolecular therapeutics.

Here, I developed a cellular force-responsive delivery system that could release payloads in a T cell force-dependent manner and achieve T cell-specific release of an anti-cancer drug-gemcitabine for effective cancer cell killing in vitro and in vivo. For proof of concept, a bispecific DNA nanomachine was also designed to achieve the specific release of cargos upon T cell recognition of cancer cells presenting cognate antigens. The T cell-force delivery system has the potential to target T cell supporting drugs to tumor niches in a T cell-specific manner without causing systemic toxicities.

Throughout the thesis, I performed the majority of experiments and data analyses while some were through collaborations, which are listed below:

Figure caption numbers	Collaborators and their affiliations
Figure 3:2b	Veronika Cencen (EPFL) and Georg E. Fantner (EPFL)
Figure 3:2d and 3:3c	Yulong Han (MIT) and Ming Guo (MIT)
Figure 3:2e-g, 3:3d, and 3:12	Murat Kaynak (EPFL), Armand Kurum (EPFL), and Mahmut S. Sakar (EPFL)
Figure 3:7a-e and 28	Armand Kurum (EPFL)
Figure 3:9	Yangping Wu (West China Hospital) and Guanyu Zhou (West China Hospital)
Figure 3:15	Lucia Bonati (EPFL)
Figure 3:17	Min Gao (EPFL), Yugang Guo (EPFL), and Yuqing Xie (EPFL)

5.2 Future development

5.2.1 Further understanding of mechanobiology of T cell immunity

Our understanding of T cell responses to mechanical stimuli, the basis for developing novel mechanical immunoengineering strategies, is still in its infancy. For instance, peptide-bound major histocompatibility complex (pMHC), a natural T cell receptor (TCR) ligand, generates a more robust stiffness-dependent T cell response compared to anti-CD3 antibody.¹³ However, most stiffness-dependent T cell behaviors were observed on anti-CD3-coated artificial surfaces. Understanding the key differences between pMHC and anti-CD3 may help engineer an APC with well-controlled signal strength. A critical and systematic comparison of the biomechanical behaviors of CD4⁺ and CD8⁺ T cells is still lacking. For example, CD4⁺ and CD8⁺ T cells showed striking differences in mechano-sensitivity when activated on substrates with varying stiffness,¹³ but the underlying mechanism remains elusive. The current thesis also noticed that the degranulation or cytokine release of cytotoxic CD8⁺ T cells showed negligible stiffness-dependency at low stiffness (< 8 kPa), which was consistent with previous results.¹³ However, F-actin polymerization and cellular force generation in cytotoxic CD8⁺ T cells were stiffness-dependent even at low stiffness. This phenomenon provides clues that the mechano-sensing mechanism in CD8⁺ T cells may be more skewed to alter cytoskeleton-related signaling pathways rather than TCR signaling pathways as compared to that in CD4⁺ T cells.

T cell activation is more sensitive to alteration of target cells' stiffness than artificial antigen-presenting substrates. The reason for this distinct difference in sensitivity remains unknown. Besides activation, T cell differentiation is key to initiating and maintaining a desirable T cell response for disease treatments.²⁴⁹ Several recent studies showed that biomechanical cues could regulate T cell differentiation independently of the intensity of biochemical signals.^{77,109} For example, lowering stiffness of hyaluronic acid (HA) hydrogel matrix enhanced induction of central memory-like human CD8⁺ T cells under constant stimulatory ligand density.⁷⁷ However, the pathways or transcription factors involved in mechanical regulations of T cell differentiation are still unknown. Studying these questions may widen our understanding of T cell mechanobiology and improve our control of T cell responses.

Synthetic materials are still the most practical platform so far for studying T cell mechanobiology as their physicochemical properties can be easily adjusted. However, a better understanding and control of the chemistry and materials used for studying T cell mechanical responses is necessary as reports so far show that T cells display different stiffness-dependent behaviors on different materials.^{77,81,106} For example, T cell spreading on a polydimethylsiloxane (PDMS) elastomer substrate is drastically different from that on a polyacrylamide (PA) hydrogel substrate despite exhibiting the same stiffness.¹⁰⁵ Paradoxically, increasing stiffness of HA hydrogel has been reported to suppress T cell activation,⁷⁷ although increased stiffness induces more robust T cell activation on other materials (e.g., PA, PDMS, and alginate). These reports underline the urgent need to dissect key parameters (e.g., chemical structure, hydrophobicity, and porosity) in material design and unify these findings. Furthermore, in most in vitro studies so far, mechanical cues including stiffness and topography are static and lack the dynamic nature of the physiological microenvironment. Incorporating mechanical cues resembling the dynamics of biomechanics in tissues, such as viscoelasticity and stress-stiffening, will provide new insights into T cell mechanobiology.

In vivo mechanical environment is a complex network presenting diverse biomechanical cues. Combining different biomechanical cues defined by previous reports would be critical to recapitulate the intricate biomechanics in the physiological microenvironment. For instance, besides the stiffness of natural APCs,¹³ morphological features of natural APCs is another important biomechanical parameter in T cell priming, as revealed in the current thesis. In this case, engineering a matrix of different stiffness and spiky structure within one material system is essential to investigate the interplay between stiffness and morphology in T cell priming and identify an optimal combination of biomechanical parameters for modulating T cell response.

Biomechanical cues are a key regulator of the biochemical microenvironment. For example, TGF- β 1 is stored on extracellular matrix (ECM) fibers in the form of large latent complexes (LLCs) and released from the LLCs triggered by cell traction forces.²⁵⁰ The force-responsive materials or systems could be a potential platform to recapitulate the coupling of biomechanics and biochemical signals.^{225,226} In particular, the cellular force-responsive release system developed in the current thesis provides a possible tool to mimic the regulation of the biochemical microenvironment by cellular forces. For example, the cellular force-responsive release system can be loaded with cytokines (e.g., IL-2) to mimic the on-demand release of T cell-supporting factors from DCs. In general, any controllable system that can fully recapitulate the physicochemical properties of natural APCs will enhance our understanding of T cell mechanobiology during activation and potentially foster more precisely controlled mechanical immunoengineering strategies.

Measuring and monitoring the spatiotemporal variation of forces applied on or exerted by T cells is essential to better understand T cell mechanobiology. There is a lack of technologies enabling in vivo monitoring of mechanical forces at the cellular level to date. Recently, Vorselen et al. developed a microparticle-based platform for traction force microscopy and applied it to T cell force measurement.²⁰¹ This microparticle-based platform, which can be injected into tissues using needles, shows promise as a method to record the force profile of single T cells in vivo. Directly measuring forces between T cells and target cells remains a significant challenge. To this end, DNA force probes hold particular promise to measure such intercellular forces in vivo as it provides good sensitivity in the pN-range and quantitative readouts.²⁵¹

Applying precise external forces to large-scale T cell populations (thousands to millions and even more) remains challenging due to the complexity and low throughput of the current techniques, therefore curtailing studies on mechano-responses of T cells at a large population scale. Literature in mechanical engineering provides numerous examples of systems that could potentially be applied to T cells, including magnetic particles-based systems,²⁵² 2-dimensional (2D) stretching systems,²⁵³ mechanical compressions,²⁵⁴ and microfluidic systems.¹³⁰ For example, using an optical tweezer, Kim et al. claimed that a shear (tangential) force but not a normal force on CD3 could trigger its downstream signaling.⁸⁷ To further confirm these results in a high-throughput manner, a microfluidic system with a flow chamber could be used to apply shear stress to a large population of T cells. Overall, applying these methods for large-scale studies could potentially enable researchers to decipher the relationship between external forces and cellular phenotypes, metabolism, and effector functions.

5.2.2 Mechanical immunoengineering of different steps of T cell immune responses

The cancer-immunity cycle requires multiple steps to develop anti-cancer T cell responses, including T cell priming, migration, infiltration, recognition, and killing of cancer cells (Section 1.1).¹⁶ Identifying the inhibitory factors in the cancer-immunity cycle has provided therapeutic targets for developing effective cancer immunotherapy.¹⁶ At present, the vast majority of immunosuppressive factors identified in the tumor microenvironment (TME) are based on biochemical pathways¹⁷ despite the fact that biophysics plays an important role in cancer initiation, progression, and metastasis.^{255,256} In the current thesis, a new immunosuppressive factor of mechanical basis, i.e., cancer cell softness, was found to substantially suppress T cell-mediated cytotoxicity. It emphasizes the importance of cancer biomechanics in the development of immunosuppression and opens up new horizons in targeting biomechanically immunosuppressive factors for enhanced cancer immunotherapy. In addition to T cell-mediated cytotoxicity against cancer cells, other steps of the cancer-immunity cycle are also critical to an optimal anti-cancer immune response and involve intensive mechanical interactions between T cells and their surrounding microenvironment. Thus, it provides a vast opportunity for mechanical immunoengineering of different steps of T cell immunity for enhanced cancer immunotherapy.

T cell migration and infiltration are prerequisites for an effective T cell-mediated killing of cancer cells inside tumor tissues.²⁵⁷ At present, few reports are exploring mechanical immunoengineering approaches to modulate T cell migration and infiltration.^{81,139,258–261} Intriguingly, CD4⁺ T cells exhibited substrate stiffness-dependent increase in mobility on intercellular cell adhesion molecule-1 (ICAM-1)-coated substrate but not on vascular cell adhesion molecule-1 (VCAM-1)-coated substrate.^{81,258} Providing that tumor progression is usually associated with increased tissue stiffness, it is interesting to study the ICAM-1/VCAM-1 expression levels in tumor vessels and how they affect the T cell infiltration into tumor tissues. Besides, it has been shown that soluble VCAM-1 could promote CD4⁺ T cell migration on a soft ICAM-1-coated substrate ($E = 1.25$ kPa),²⁵⁸ which may provide a practical target for enhancing T cell infiltration in soft tumors such as brain cancers. Within the 3D collagen matrix or tumor tissue, T cells adopt an amoeboid locomotion mode for rapid migration through the matrix networks, enabling efficient searching for target cells.^{262,263} The amoeboid migration of T cells is, at least partially, attributed to cortical contractility that promotes bleb-to-pseudopod protrusions and can be enhanced by destabilizing microtubules in T cells.¹³⁹ Specifically, destabilization of microtubules using nocodazole substantially increased CD8⁺ T cell migration within tumor tissues,¹³⁹ which offers opportunities to engineer T cell mobility in vivo for enhanced tumor infiltration. It is worth noting that microtubules also play an important role in immunological synapse formation and cytotoxic granule exocytosis.²⁶⁴ Identifying targets downstream microtubule pathways may represent a future direction for modulating T cell migration and infiltration in a more specific manner.

From the perspective of topography, CD4⁺ T cells preferentially migrate along the direction of aligned nanoridges that mimic the aligned fibrillar bundles in ECM. Besides, integrin-mediated adhesion was essential in the directed migration of CD4⁺ T cells on aligned nanoridges.²⁵⁹ Interestingly, the directed migration of CD4⁺ T cells was enhanced and independent of integrin-mediated adhesion under confinement,²⁵⁹ which reflects the limited migration space within the 3D matrix. As tumors possess highly-crosslinked and dense ECM networks,²⁶⁵ it may provide hints for engineering T cell infiltration via regulating density or topography of ECM components in tumor tissues. CD4⁺ T cells also sense the substrate's curvature and prefer migrating towards the concave surface over the convex surface.²⁶¹ Such curvature-directed

migration was significantly reduced by inhibiting lamellipodia formation in T cells through blocking the activity Arp2/3 complex,²⁶¹ a nucleation-promoting factor for branching of F-actin filaments.²⁶⁶ In addition, myosin-driven contractility seems important in the high mobility of T cells for scanning the curved surfaces as myosin inhibition by blebbistatin specifically localized T cells in concaved surfaces.²⁶¹ These observations provide valuable information for designing bio-material-based scaffolds with the ability to precisely control the migration of immune cells of interest.

On the whole, moving this highly interdisciplinary field toward clinical application requires a concerted effort among physicists, chemists, material scientists, immunologists, and clinicians. The experience and know-how gained in conventional biochemical immunoengineering (examples including clinical trials NCT01753089 and NCT03815682 reported in clinicaltrials.gov) could potentially guide these translations. For example, armored CAR-T cells express supporting ligands or cytokines to improve their activity through genetic engineering. Mimicking armored CAR-T cell design, one can genetically modify T cells with a mechano-sensing circuit for mechano-controlled expression of CAR or supporting cytokines. Such a system has the potential to provide additional specificity targeting cancer when combined with biochemical immunoengineering. In addition, key therapeutic targets regarded solely as biochemical receptors, such as PD-1,²⁶⁷ provide a cohort of important subjects for studying the potential role of mechanical cues in regulating their signaling and functions. For example, anti-PD-1 antibodies (aPD-1) have been used to block the PD-1/PD-L1 (or PD-L2) interactions and reverse T cell exhaustion in the tumor. Interestingly, a recent report shows that T cells exert stronger tensile tension along the PD-1/aPD-1 axis than on the PD-1/PD-L2 axis,²⁶⁸ implying that mechanical force may underlie the differential T cell responses upon binding to PD-L1 versus PD-L2. It is fundamentally interesting and therapeutically relevant to determine whether mechanical force plays a role in PD-1 signaling and thus regulates T cell exhaustion.

Besides cancer treatment, mechanical immunoengineering of T cells also has clinical implications in the treatment of other diseases such as infections. For example, some viruses, including human immunodeficiency virus (HIV)²⁶⁹ and severe acute respiratory syndrome coronavirus 2 (SARS-CoV-2),²⁷⁰ upregulate cholesterol biosynthesis in infected cells. It hints that virus-infected cells may exploit the cholesterol-derived cell softening mechanism revealed in the current thesis to evade cytotoxicity mediated by T-cells for disease progression. Mechanical immunoengineering may provide new approaches to immunotherapies against virus infections.

5.2.3 Mechanical immunoengineering of other immune cells for cancer immunotherapy

Tumor immune microenvironment is a highly complex contexture populated with diverse immune cells, including T cells, B cells, macrophages, and so on.²⁷¹ Exploiting other immune cells such as macrophage for cancer immunotherapy is also an intensively-investigated area and has been under clinical investigation for cancer treatments.^{272,273} As other immune cells, such as B cells and macrophages,^{246,274} are also known to sense and respond to mechanical cues, mechanical immunoengineering approaches also provide opportunities to engineer those immune cells for enhanced cancer immunotherapy broadly.

Tumor-infiltrating B cells are abundant in the TME (up to 25% of all cells in some tumors)²⁷⁵ and have been shown to, especially when presenting in tertiary lymphoid structures (TLSs) in tumors, predict a good prognosis and favorable

treatment responses in various cancer types.²⁷⁶ Harnessing B cells for cancer immunotherapy thus has the potential to generate promising clinical benefits and aids in current T cell-based cancer immunotherapy as T cells are another important component in TLS. Like TCR, B cell receptor (BCR) is also a mechanosensor requiring mechanical forces for optimal BCR signaling.²⁷⁷ Acquisition of antigens from APCs by BCR is crucial for B cell antigen presentation to T helper cells and subsequent antibody response.²⁷⁸ Interestingly, B cells utilized mechanical force to discriminate antigen affinity for antigen extraction,²⁴⁶ and the follicular DCs that are stiffer than normal DCs induced a more stringent selection of high-affinity antigens presented on the DC surface.²⁷⁹ It implies that incorporating mechanical components such as stiffness into the design of B cell-based cancer vaccines may facilitate an effective anti-cancer antibody response. Another interesting observation is that B cells exhibit differential stiffness-sensitivity upon activation with different stimulatory ligands.²⁸⁰ Particularly, anti-CD40 antibodies stimulated higher B cell activation on a stiffer substrate while B cell-specific antigen showed an opposite trend. In addition, softer substrate promoted class-switching in B cells upon stimulation by anti-IgM antibodies.²⁸⁰ It indicates that different receptors afford B cells distinct sensitivity to the surrounding mechanical microenvironment, and dissecting the underlying mechanisms may advance our understanding of B cell mechanobiology and motivate mechanical immunoengineering approaches for fine-tuning B cell immunity.

Tumor-associated macrophages (TAMs) are usually associated with a poor prognosis in cancer patients.²⁸¹ In the TME, TAMs are typically polarized to an anti-inflammatory phenotype producing various immunosuppressive signals against anti-cancer immunity, and reprogramming TAMs into a pro-inflammatory phenotype represents a promising strategy to restore anti-cancer innate immunity and augment T cell-based cancer immunotherapy.²⁸² Substrate stiffness is known to modulate macrophage polarization.^{283–286} In the majority of the studies, stiff substrate promotes macrophage polarization into a pro-inflammatory phenotype evidenced by increased production of pro-inflammatory cytokines (e.g., TNF- α and IL-6).^{284–286} Active mechanical forces play an important role in macrophage polarization as well.^{287–290} For example, low constant shear stress induces pro-inflammatory polarization of macrophages while oscillatory shear stress preferentially reprograms macrophages into an anti-inflammatory phenotype.²⁸⁷ There are multiple elegant reviews emphasizing the importance of biophysical signals in the macrophage life cycle, including proliferation, differentiation, aging, etc.^{274,291,292} In general, applying mechanical cues into engineering macrophage responses needs to be prioritized as a complement to current biochemical-based immunoengineering approaches for unleashing the power of innate immunity against cancer.

References

1. June, C. H., O'Connor, R. S., Kawalekar, O. U., Ghassemi, S. & Milone, M. C. CAR T cell immunotherapy for human cancer. *Science* **359**, 1361–1365 (2018).
2. Barber, D. L., Wherry, E. J., Masopust, D., Zhu, B., Allison, J. P., Sharpe, A. H., Freeman, G. J. & Ahmed, R. Restoring function in exhausted CD8 T cells during chronic viral infection. *Nature* **439**, 682–687 (2006).
3. Bluestone, J. A., Buckner, J. H., Fitch, M., Gitelman, S. E., Gupta, S., Hellerstein, M. K., Herold, K. C., Lares, A., Lee, M. R., Li, K., Liu, W., Long, S. A., Masiello, L. M., Nguyen, V., Putnam, A. L., Rieck, M., Sayre, P. H. & Tang, Q. Type 1 diabetes immunotherapy using polyclonal regulatory T cells. *Sci. Transl. Med.* **7**, 315ra189 (2015).
4. Wei, S. C., Duffy, C. R. & Allison, J. P. Fundamental Mechanisms of Immune Checkpoint Blockade Therapy. *Cancer Discov.* **8**, 1069–1086 (2018).
5. Ribas, A. & Wolchok, J. D. Cancer immunotherapy using checkpoint blockade. *Science* **359**, 1350–1355 (2018).
6. Fesnak, A. D., June, C. H. & Levine, B. L. Engineered T cells: the promise and challenges of cancer immunotherapy. *Nat. Rev. Cancer* **16**, 566–581 (2016).
7. Kerkar, S. P., Muranski, P., Kaiser, A., Boni, A., Sanchez-Perez, L., Yu, Z., Palmer, D. C., Reger, R. N., Borman, Z. A., Zhang, L., Morgan, R. A., Gattinoni, L., Rosenberg, S. A., Trinchieri, G. & Restifo, N. P. Tumor-specific CD8+ T cells expressing interleukin-12 eradicate established cancers in lymphodepleted hosts. *Cancer Res.* **70**, 6725–6734 (2010).
8. Tang, L., Zheng, Y., Melo, M. B., Mabardi, L., Castaño, A. P., Xie, Y. Q., Li, N., Kudchodkar, S. B., Wong, H. C., Jeng, E. K., Maus, M. V & Irvine, D. J. Enhancing T cell therapy through TCR-signaling-responsive nanoparticle drug delivery. *Nat. Biotechnol.* **36**, 707–716 (2018).
9. Xie, Y. Q., Arik, H., Wei, L., Zheng, Y., Suh, H., Irvine, D. J. & Tang, L. Redox-responsive interleukin-2 nanogel specifically and safely promotes the proliferation and memory precursor differentiation of tumor-reactive T-cells. *Biomater. Sci.* **7**, 1345–1357 (2019).
10. Walling, B. L. & Kim, M. LFA-1 in T cell migration and differentiation. *Front. Immunol.* **9**, 952 (2018).
11. Guimarães, C. F., Gasperini, L., Marques, A. P. & Reis, R. L. The stiffness of living tissues and its implications for tissue engineering. *Nat. Rev. Mater.* **5**, 351–370 (2020).
12. Hu, K. H. & Butte, M. J. T cell activation requires force generation. *J. Cell Biol.* **213**, 535–542 (2016).
13. Blumenthal, D., Chandra, V., Avery, L. & Burkhardt, J. K. Mouse T cell priming is enhanced by maturation-dependent stiffening of the dendritic cell cortex. *Elife* **9**, e55995 (2020).
14. Basu, R., Whitlock, B. M., Husson, J., Le Floch, A., Jin, W., Oyler-Yaniv, A., Dotiwala, F., Giannone, G., Hivroz, C., Biais, N., Lieberman, J., Kam, L. C. & Huse, M. Cytotoxic T Cells Use Mechanical Force to Potentiate Target Cell Killing. *Cell* **165**, 100–110 (2016).
15. Jhunjhunwala, S., Hammer, C. & Delamarre, L. Antigen presentation in cancer: Insights into tumour immunogenicity and immune evasion. *Nat. Rev. Cancer* **21**, 298–312 (2021).
16. Chen, D. S. & Mellman, I. Oncology meets immunology: The cancer-immunity cycle. *Immunity* **39**, 1–10 (2013).
17. Motz, G. T. & Coukos, G. Deciphering and reversing tumor immune suppression. *Immunity* **39**, 61–73 (2013).
18. Waldman, A. D., Fritz, J. M. & Lenardo, M. J. A guide to cancer immunotherapy: From T cell basic science to clinical practice. *Nat. Rev. Immunol.* **20**, 651–668 (2020).
19. Swartz, M. A., Hirose, S. & Hubbell, J. A. Engineering approaches to immunotherapy. *Sci Transl Med* **4**, 148rv9 (2012).

20. Green, J. J. Immunoengineering has arrived. *J. Biomed. Mater. Res. Part A* **109A**, 397–403 (2021).
21. Michot, J. M., Bigenwald, C., Champiat, S., Collins, M., Carbone, F., Postel-Vinay, S., Berdelou, A., Varga, A., Bahleda, R., Hollebecque, A., Massard, C., Fuerea, A., Ribrag, V., Gazzah, A., Armand, J. P., Amellal, N., Angevin, E., Noel, N., Boutros, C., Mateus, C., Robert, C., Soria, J. C., Marabelle, A. & Lambotte, O. Immune-related adverse events with immune checkpoint blockade: A comprehensive review. *Eur. J. Cancer* **54**, 139–148 (2016).
22. Larkin, J., Chiarion-Sileni, V., Gonzalez, R., Grob, J. J., Cowey, C. L., Lao, C. D., Schadendorf, D., Dummer, R., Smylie, M., Rutkowski, P., Ferrucci, P. F., Hill, A., Wagstaff, J., Carlino, M. S., Haanen, J. B., Maio, M., Marquez-Rodas, I., McArthur, G. A., Ascierto, P. A., Long, G. V., Callahan, M. K., Postow, M. A., Grossmann, K., Sznol, M., Dreno, B., Bastholt, L., Yang, A., Rollin, L. M., Horak, C., Hodi, F. S. & Wolchok, J. D. Combined Nivolumab and Ipilimumab or monotherapy in untreated melanoma. *N. Engl. J. Med.* **373**, 23–34 (2015).
23. Ishihara, J., Fukunaga, K., Ishihara, A., Larsson, H. M., Potin, L., Hosseini, P., Galliverti, G., Swartz, M. A. & Hubbell, J. A. Matrix-binding checkpoint immunotherapies enhance antitumor efficacy and reduce adverse events. *Sci. Transl. Med.* **9**, eaan0401 (2017).
24. Ishihara, J., Ishihara, A., Sasaki, K., Lee, S. S. Y., Williford, J. M., Yasui, M., Abe, H., Potin, L., Hosseini, P., Fukunaga, K., Raczy, M. M., Gray, L. T., Mansurov, A., Katsumata, K., Fukayama, M., Kron, S. J., Swartz, M. A. & Hubbell, J. A. Targeted antibody and cytokine cancer immunotherapies through collagen affinity. *Sci. Transl. Med.* **11**, eaau3259 (2019).
25. Li, Y., Fang, M., Zhang, J., Wang, J., Song, Y., Shi, J., Li, W., Wu, G., Ren, J., Wang, Z., Zou, W. & Wang, L. Hydrogel dual delivered celecoxib and anti-PD-1 synergistically improve antitumor immunity. *Oncoimmunology* **5**, e1074374 (2016).
26. Wang, C., Wang, J., Zhang, X., Yu, S., Wen, D., Hu, Q., Ye, Y., Bomba, H., Hu, X., Liu, Z., Dotti, G. & Gu, Z. In situ formed reactive oxygen species-responsive scaffold with gemcitabine and checkpoint inhibitor for combination therapy. *Sci. Transl. Med.* **10**, eaan3682 (2018).
27. Yu, S., Wang, C., Yu, J., Wang, J., Lu, Y., Zhang, Y., Zhang, X., Hu, Q., Sun, W., He, C., Chen, X. & Gu, Z. Injectable bioresponsive gel depot for enhanced immune checkpoint blockade. *Adv. Mater.* **30**, 1801527 (2018).
28. Ruan, H., Hu, Q., Wen, D., Chen, Q., Chen, G., Lu, Y., Wang, J., Cheng, H., Lu, W. & Gu, Z. A dual-bioresponsive drug-delivery depot for combination of epigenetic modulation and immune checkpoint blockade. *Adv. Mater.* **31**, 1806957 (2019).
29. Yu, L. & Ding, J. Injectable hydrogels as unique biomedical materials. *Chem. Soc. Rev.* **37**, 1473–1481 (2008).
30. Li, Y., Rodrigues, J. & Tomás, H. Injectable and biodegradable hydrogels: Gelation, biodegradation and biomedical applications. *Chem. Soc. Rev.* **41**, 2193–2221 (2012).
31. Wang, C., Ye, Y., Hochu, G. M., Sadeghifar, H. & Gu, Z. Enhanced cancer immunotherapy by microneedle patch-assisted delivery of anti-PD1 antibody. *Nano Lett.* **16**, 2334–2340 (2016).
32. Ye, Y., Wang, J., Hu, Q., Hochu, G. M., Xin, H., Wang, C. & Gu, Z. Synergistic transcutaneous immunotherapy enhances antitumor immune responses through delivery of checkpoint inhibitors. *ACS Nano* **10**, 8956–8963 (2016).
33. Chen, G., Chen, Z., Wen, D., Wang, Z., Li, H., Zeng, Y., Dotti, G., Wirz, R. E. & Gu, Z. Transdermal cold atmospheric plasma-mediated immune checkpoint blockade therapy. *Proc. Natl. Acad. Sci. U. S. A.* **117**, 3687–3692 (2020).
34. Chen, S. X., Ma, M., Xue, F., Shen, S., Chen, Q., Kuang, Y., Liang, K., Wang, X. & Chen, H. Construction of microneedle-assisted co-delivery platform and its combining photodynamic/immunotherapy. *J. Control. Release* **324**, 218–227 (2020).
35. Ochoa, M., Mousoulis, C. & Ziaie, B. Polymeric microdevices for transdermal and subcutaneous drug delivery. *Adv. Drug Deliv. Rev.* **64**, 1603–1616 (2012).

36. Ye, Y., Yu, J., Wen, D., Kahkoska, A. R. & Gu, Z. Polymeric microneedles for transdermal protein delivery. *Adv. Drug Deliv. Rev.* **127**, 106–118 (2018).
37. Wang, C., Sun, W., Ye, Y., Hu, Q., Bomba, H. N. & Gu, Z. In situ activation of platelets with checkpoint inhibitors for post-surgical cancer immunotherapy. *Nat. Biomed. Eng.* **1**, 0011 (2017).
38. Zhang, X., Wang, J., Chen, Z., Hu, Q., Wang, C., Yan, J., Dotti, G., Huang, P. & Gu, Z. Engineering PD-1-Presenting Platelets for Cancer Immunotherapy. *Nano Lett.* **18**, 5716–5725 (2018).
39. Hu, Q., Sun, W., Wang, J., Ruan, H., Zhang, X., Ye, Y., Shen, S., Wang, C., Lu, W., Cheng, K., Dotti, G., Zeidner, J. F., Wang, J. & Gu, Z. Conjugation of haematopoietic stem cells and platelets decorated with anti-PD-1 antibodies augments anti-leukaemia efficacy. *Nat. Biomed. Eng.* **2**, 831–840 (2018).
40. Han, X., Chen, J., Chu, J., Liang, C., Ma, Q., Fan, Q., Liu, Z. & Wang, C. Platelets as platforms for inhibition of tumor recurrence post-physical therapy by delivery of anti-PD-L1 checkpoint antibody. *J. Control. Release* **304**, 233–241 (2019).
41. Gurbatri, C. R., Lia, I., Vincent, R., Coker, C., Castro, S., Treuting, P. M., Hinchliffe, T. E., Arpaia, N. & Danino, T. Engineered probiotics for local tumor delivery of checkpoint blockade nanobodies. *Sci. Transl. Med.* **12**, eaax0876 (2020).
42. Gremmel, T., Frelinger, A. L. & Michelson, A. D. Platelet physiology. *Semin. Thromb. Hemost.* **42**, 191–204 (2016).
43. Nurden, A. T., Nurden, P., Sanchez, M., Andia, I. & Anitua, E. Platelets and wound healing. *Front. Biosci.* **13**, 3525–3548 (2008).
44. Giralt, S. A. & Champlin, R. E. Leukemia relapse after allogeneic bone marrow transplantation: A review. *Blood* **84**, 3602–3612 (1994).
45. Leopold, L. H. & Willemze, R. The treatment of acute myeloid leukemia in first relapse: A comprehensive review of the literature. *Leuk. Lymphoma* **43**, 1715–1727 (2002).
46. Rosenberg, S. A., Packard, B. S., Aebersold, P. M., Solomon, D., Topalian, S. L., Toy, S. T., Simon, P., Lotze, M. T., Yang, J. C., Seipp, C. A., Simpson, C., Carter, C., Bock, S., Schwartzentruber, D., Wei, J. P. & White, D. E. Use of tumor Infiltrating Lymphocytes for the treatment of melanoma. *N. Engl. J. Med.* **319**, 1676–1680 (1988).
47. Rosenberg, S. A., Yannelli, J. R., Yang, J. C., Topalian, S. L., Schwartzentruber, D. J., Weber, J. S., Parkinson, D. R., Seipp, C. A., Einhorn, J. H. & White, D. E. Treatment of patients with metastatic melanoma with autologous tumor-infiltrating lymphocytes and interleukin 2. *J. Natl. Cancer Inst.* **86**, 1159–1166 (1994).
48. Rosenberg, S. A., Yang, J. C., Sherry, R. M., Kammula, U. S., Hughes, M. S., Phan, G. Q., Citrin, D. E., Restifo, N. P., Robbins, P. F., Wunderlich, J. R., Morton, K. E., Laurencot, C. M., Steinberg, S. M., White, D. E. & Dudley, M. E. Durable complete responses in heavily pretreated patients with metastatic melanoma using T-cell transfer immunotherapy. *Clin. Cancer Res.* **17**, 4550–4557 (2011).
49. Zacharakis, N., Chinnasamy, H., Black, M., Xu, H., Lu, Y. C., Zheng, Z., Pasetto, A., Langhan, M., Shelton, T., Prickett, T., Gartner, J., Jia, L., Trebska-McGowan, K., Somerville, R. P., Robbins, P. F., Rosenberg, S. A., Goff, S. L. & Feldman, S. A. Immune recognition of somatic mutations leading to complete durable regression in metastatic breast cancer. *Nat. Med.* **24**, 724–730 (2018).
50. Perica, K., Varela, J. C., Oelke, M. & Schneck, J. Adoptive T cell immunotherapy for cancer. *Rambam Maimonides Med. J.* **6**, e0004 (2015).
51. Wang, X. & Rivière, I. Clinical manufacturing of CAR T cells: Foundation of a promising therapy. *Mol. Ther. - Oncolytics* **3**, 16015 (2016).
52. Tully, S., Feng, Z., Grindrod, K., McFarlane, T., Chan, K. K. W. & Wong, W. W. L. Impact of increasing wait times on overall mortality of chimeric antigen receptor T-Cell therapy in large B-cell lymphoma: A discrete event simulation model. *JCO Clin. Cancer Informatics* 1–9 (2019) doi:10.1200/cci.19.00086.

53. Zhang, D. K. Y., Cheung, A. S. & Mooney, D. J. Activation and expansion of human T cells using artificial antigen-presenting cell scaffolds. *Nat. Protoc.* **15**, 773–798 (2020).
54. Steenblock, E. R. & Fahmy, T. M. A comprehensive platform for ex vivo T-cell expansion based on biodegradable polymeric artificial antigen-presenting cells. *Mol. Ther.* **16**, 765–772 (2008).
55. Fadel, T. R., Sharp, F. A., Vudattu, N., Ragheb, R., Garyu, J., Kim, D., Hong, E., Li, N., Haller, G. L., Pfefferle, L. D., Justesen, S., Harold, K. C. & Fahmy, T. M. A carbon nanotube-polymer composite for T-cell therapy. *Nat. Nanotechnol.* **9**, 639–647 (2014).
56. Mandal, S., Hammink, R., Tel, J., Eksteen-Akeroyd, Z. H., Rowan, A. E., Blank, K. & Figdor, C. G. Polymer-based synthetic dendritic cells for tailoring robust and multifunctional T cell responses. *ACS Chem. Biol.* **10**, 485–492 (2015).
57. Perica, K., Bieler, J. G., Schütz, C., Varela, J. C., Douglass, J., Skora, A., Chiu, Y. L., Oelke, M., Kinzler, K., Zhou, S., Vogelstein, B. & Schneck, J. P. Enrichment and Expansion with Nanoscale Artificial Antigen Presenting Cells for Adoptive Immunotherapy. *ACS Nano* **9**, 6861–6871 (2015).
58. Cheung, A. S., Zhang, D. K. Y., Koshy, S. T. & Mooney, D. J. Scaffolds that mimic antigen-presenting cells enable ex vivo expansion of primary T cells. *Nat. Biotechnol.* **36**, 160–169 (2018).
59. Jo, Y., Ali, L. A., Shim, J. A., Lee, B. H. & Hong, C. Innovative CAR-T cell therapy for solid tumor: Current duel between CAR-T spear and tumor shield. **12**, 2087 (2020).
60. Rafiq, S., Hackett, C. S. & Brentjens, R. J. Engineering strategies to overcome the current roadblocks in CAR T cell therapy. *Nat. Rev. Clin. Oncol.* **17**, 147–167 (2020).
61. Hoyos, V., Savoldo, B., Quintarelli, C., Mahendravada, A., Zhang, M., Vera, J., Heslop, H. E., Rooney, C. M., Brenner, M. K. & Dotti, G. Engineering CD19-specific T lymphocytes with interleukin-15 and a suicide gene to enhance their anti-lymphoma/leukemia effects and safety. *Leukemia* **24**, 1160–1170 (2010).
62. Pegram, H. J., Lee, J. C., Hayman, E. G., Imperato, G. H., Tedder, T. F., Sadelain, M. & Brentjens, R. J. Tumor-targeted T cells modified to secrete IL-12 eradicate systemic tumors without need for prior conditioning. *Blood* **119**, 4133–4141 (2012).
63. Hu, B., Ren, J., Luo, Y., Keith, B., Young, R. M., Scholler, J., Zhao, Y. & June, C. H. Augmentation of antitumor immunity by human and mouse CAR T Cells secreting IL-18. *Cell Rep.* **20**, 3025–3033 (2017).
64. Adachi, K., Kano, Y., Nagai, T., Okuyama, N., Sakoda, Y. & Tamada, K. IL-7 and CCL19 expression in CAR-T cells improves immune cell infiltration and CAR-T cell survival in the tumor. *Nat. Biotechnol.* **36**, 346–351 (2018).
65. Batra, S. A., Rath, P., Guo, L., Courtney, A. N., Fleurence, J., Balzeau, J., Shaik, R. S., Nguyen, T. P., Wu, M. F., Bulsara, S., Mamonkin, M., Metelitsa, L. S. & Heczey, A. Glypican-3-specific CAR T cells coexpressing IL15 and IL21 have superior expansion and antitumor activity against hepatocellular carcinoma. *Cancer Immunol. Res.* **8**, 309–320 (2020).
66. Ma, X., Shou, P., Smith, C., Chen, Y., Du, H., Sun, C., Porterfield Kren, N., Michaud, D., Ahn, S., Vincent, B., Savoldo, B., Pylayeva-Gupta, Y., Zhang, S., Dotti, G. & Xu, Y. Interleukin-23 engineering improves CAR T cell function in solid tumors. *Nat. Biotechnol.* **38**, 448–459 (2020).
67. Link, A., Vogt, T. K., Favre, S., Britschgi, M. R., Acha-Orbea, H., Hinz, B., Cyster, J. G. & Luther, S. A. Fibroblastic reticular cells in lymph nodes regulate the homeostasis of naive T cells. *Nat. Immunol.* **8**, 1255–1265 (2007).
68. Simpson-Abelson, M. R., Purohit, V. S., Pang, W. M., Iyer, V., Odunsi, K., Demmy, T. L., Yokota, S. J., Loyall, J. L., Kelleher, R. J., Balu-Iyer, S. & Bankert, R. B. IL-12 delivered intratumorally by multilamellar liposomes reactivates memory T cells in human tumor microenvironments. *Clin. Immunol.* **132**, 71–82 (2009).
69. Stephan, M. T., Moon, J. J., Um, S. H., Bershteyn, A. & Irvine, D. J. Therapeutic cell engineering with surface-conjugated synthetic nanoparticles. *Nat. Med.* **16**, 1035–1041 (2010).

70. Bonifant, C. L., Jackson, H. J., Brentjens, R. J. & Curran, K. J. Toxicity and management in CAR T-cell therapy. *Mol. Ther. - Oncolytics* **3**, 16011 (2016).
71. Schubert, M. L., Schmitt, M., Wang, L., Ramos, C. A., Jordan, K., Müller-Tidow, C. & Dreger, P. Side-effect management of chimeric antigen receptor (CAR) T-cell therapy. *Ann. Oncol.* **32**, 34–48 (2021).
72. Wang, X., Chang, W. C., Wong, C. L. W., Colcher, D., Sherman, M., Ostberg, J. R., Forman, S. J., Riddell, S. R. & Jensen, M. C. A transgene-encoded cell surface polypeptide for selection, in vivo tracking, and ablation of engineered cells. *Blood* **118**, 1255–1263 (2011).
73. Di Stasi, A., Tey, S.-K., Dotti, G., Fujita, Y., Kennedy-Nasser, A., Martinez, C., Straathof, K., Liu, E., Durett, A. G., Grilley, B., Liu, H., Cruz, C. R., Savoldo, B., Gee, A. P., Schindler, J., Krance, R. A., Heslop, H. E., Spencer, D. M., Rooney, C. M. & Brenner, M. K. Inducible Apoptosis as a Safety Switch for Adoptive Cell Therapy. *N. Engl. J. Med.* **365**, 1673–1683 (2011).
74. Wu, C. Y., Roybal, K. T., Puchner, E. M., Onuffer, J. & Lim, W. A. Remote control of therapeutic T cells through a small molecule-gated chimeric receptor. *Science* **350**, aab4077 (2015).
75. Jan, M., Scarfò, I., Larson, R. C., Walker, A., Schmidts, A., Guirguis, A. A., Gasser, J. A., Słabicki, M., Bouffard, A. A., Castano, A. P., Kann, M. C., Cabral, M. L., Tepper, A., Grinshpun, D. E., Sperling, A. S., Kyung, T., Sievers, Q. L., Birnbaum, M. E., Maus, M. V. & Ebert, B. L. Reversible ON- And OFF-switch chimeric antigen receptors controlled by lenalidomide. *Sci. Transl. Med.* **13**, eabb6295 (2021).
76. Lambert, L. H., Goebrecht, G. K. E., De Leo, S. E., O'Connor, R. S., Nunez-Cruz, S., Li, T. De, Yuan, J., Milone, M. C. & Kam, L. C. Improving T Cell Expansion with a Soft Touch. *Nano Lett.* **17**, 821–826 (2017).
77. Hickey, J. W., Dong, Y., Chung, J. W., Salathe, S. F., Pruitt, H. C., Li, X., Chang, C., Fraser, A. K., Bessell, C. A., Ewald, A. J., Gerecht, S., Mao, H. Q. & Schneck, J. P. Engineering an artificial T-cell stimulating matrix for immunotherapy. *Adv. Mater.* **31**, 1807359 (2019).
78. Majedi, F. S., Hasani-Sadrabadi, M. M., Thauland, T. J., Li, S., Bouchard, L. S. & Butte, M. J. Augmentation of T-Cell Activation by Oscillatory Forces and Engineered Antigen-Presenting Cells. *Nano Lett.* **19**, 6945–6954 (2019).
79. Harrison, D. L., Fang, Y. & Huang, J. T-cell mechanobiology: Force sensation, potentiation, and translation. *Front. Phys.* **7**, 45 (2019).
80. Hong, J., Ge, C., Jothikumar, P., Yuan, Z., Liu, B., Bai, K., Li, K., Rittase, W., Shinzawa, M., Zhang, Y., Palin, A., Love, P., Yu, X., Salaita, K., Evavold, B. D., Singer, A. & Zhu, C. A TCR mechanotransduction signaling loop induces negative selection in the thymus. *Nat. Immunol.* **19**, 1379–1390 (2018).
81. Saitakis, M., Dogniaux, S., Goudot, C., Bufl, N., Asnacios, S., Maurin, M., Randriamampita, C., Asnacios, A. & Hivroz, C. Different TCR-induced T lymphocyte responses are potentiated by stiffness with variable sensitivity. *Elife* **6**, e23190 (2017).
82. Dembo, M., Torney, D. C., Saxman, K. & Hammer, D. The reaction-limited kinetics of membrane-to-surface adhesion and detachment. *Proc. R. Soc. Lond. B* **234**, 55–83 (1988).
83. Thomas, W. E., Trintchina, E., Forero, M., Vogel, V. & Sokurenko, E. V. Bacterial adhesion to target cells enhanced by shear force. *Cell* **109**, 913–923 (2002).
84. Marshall, B. T., Long, M., Piper, J. W., Yago, T., McEver, R. P. & Zhu, C. Direct observation of catch bonds involving cell-adhesion molecules. *Nature* **423**, 190–193 (2003).
85. Liu, B., Chen, W., Evavold, B. D. & Zhu, C. Accumulation of dynamic catch bonds between TCR and agonist peptide-MHC triggers T cell signaling. *Cell* **157**, 357–368 (2014).
86. Li, Y. C., Chen, B. M., Wu, P. C., Cheng, T. L., Kao, L. S., Tao, M. H., Lieber, A. & Roffler, S. R. Mechanical Forces Acting on T Cells Immobilized via the TCR Complex Can Trigger TCR Signaling. *J. Immunol.* **184**, 5959–5963 (2010).

87. Kim, S. T., Takeuchi, K., Sun, Z. Y. J., Touma, M., Castro, C. E., Fahmy, A., Lang, M. J., Wagner, G. & Reinherz, E. L. The $\alpha\beta$ T cell receptor is an anisotropic mechanosensor. *J. Biol. Chem.* **284**, 31028–31037 (2009).
88. Chen, Y., Ju, L., Rushdi, M., Ge, C. & Zhu, C. Receptor-mediated cell mechanosensing. *Mol. Biol. Cell* **28**, 3134–3155 (2017).
89. Monks, C. R. F., Freiberg, B. A., Kupfer, H., Sciaky, N. & Kupfer, A. Three-dimensional segregation of supramolecular activation clusters in T cells. *Nature* **395**, 82–86 (1998).
90. Grakoui, A., Bromley, S. K., Sumen, C., Davis, M. M., Shaw, A. S., Allen, P. M. & Dustin, M. L. The immunological synapse: A molecular machine controlling T cell activation. *Science* **285**, 221–227 (1999).
91. Fritzsche, M. & Dustin, M. L. *Organization of immunological synapses and kinapses. Structural Biology in Immunology: Structure and Function of Novel Molecules of Immunologic Importance* (Elsevier Inc., 2018).
92. Comrie, W. A., Babich, A. & Burkhardt, J. K. F-actin flow drives affinity maturation and spatial organization of LFA-1 at the immunological synapse. *J. Cell Biol.* **208**, 475–491 (2015).
93. Husson, J., Chemin, K., Bohineust, A., Hivroz, C. & Henry, N. Force generation upon T cell receptor engagement. *PLoS One* **6**, e19680 (2011).
94. Bashour, K. T., Gondarenko, A., Chen, H., Shen, K., Liu, X., Huse, M., Hone, J. C. & Kam, L. C. CD28 and CD3 have complementary roles in T-cell traction forces. *Proc. Natl. Acad. Sci. U. S. A.* **111**, 2241–2246 (2014).
95. Hui, K. L., Balagopalan, L., Samelson, L. E. & Upadhyaya, A. Cytoskeletal forces during signaling activation in Jurkat T-cells. *Mol. Biol. Cell* **26**, 685–695 (2015).
96. Liu, Y., Blanchfield, L., Ma, V. P. Y., Andargachew, R., Galior, K., Liu, Z., Evavold, B. & Salaita, K. DNA-based nanoparticle tension sensors reveal that T-cell receptors transmit defined pN forces to their antigens for enhanced fidelity. *Proc. Natl. Acad. Sci. U. S. A.* **113**, 5610–5615 (2016).
97. Judokusumo, E., Tabdanov, E., Kumari, S., Dustin, M. L. & Kam, L. C. Mechanosensing in T lymphocyte activation. *Biophys. J.* **102**, L5–L7 (2012).
98. Tamzalit, F., Wang, M. S., Jin, W., Tello-Lafoz, M., Boyko, V., Heddleston, J. M., Black, C. T., Kam, L. C. & Huse, M. Interfacial actin protrusions mechanically enhance killing by cytotoxic T cells. *Sci. Immunol.* **4**, eaav5445 (2019).
99. Anselme, K. & Biggerelle, M. Role of materials surface topography on mammalian cell response. *Int. Mater. Rev.* **56**, 243–266 (2011).
100. Nemir, S. & West, J. L. Synthetic materials in the study of cell response to substrate rigidity. *Ann. Biomed. Eng.* **38**, 2–20 (2010).
101. Meng, K. P., Majedi, F. S., Thauland, T. J. & Butte, M. J. Mechanosensing through YAP controls T cell activation and metabolism. *J. Exp. Med.* **217**, e20200053 (2020).
102. Levental, K. R., Yu, H., Kass, L., Lakins, J. N., Egeblad, M., Erler, J. T., Fong, S. F. T., Csiszar, K., Giaccia, A., Weninger, W., Yamauchi, M., Gasser, D. L. & Weaver, V. M. Matrix Crosslinking Forces Tumor Progression by Enhancing Integrin Signaling. *Cell* **139**, 891–906 (2009).
103. Schraml, B. U. & Reis e Sousa, C. Defining dendritic cells. *Curr. Opin. Immunol.* **32**, 13–20 (2015).
104. O'Connor, R. S., Hao, X., Shen, K., Bashour, K., Akimova, T., Hancock, W. W., Kam, L. C. & Milone, M. C. Substrate Rigidity Regulates Human T Cell Activation and Proliferation. *J. Immunol.* **189**, 1330–1339 (2012).
105. Wahl, A., Dinet, C., Dillard, P., Nassereddine, A., Puech, P. H., Limozin, L. & Sengupta, K. Biphasic mechanosensitivity of T cell receptor-mediated spreading of lymphocytes. *Proc. Natl. Acad. Sci. U. S. A.* **116**, 5908–5913 (2019).
106. Majedi, F. S., Hasani-Sadrabadi, M. M., Thauland, T. J., Li, S., Bouchard, L. S. & Butte, M. J. T-cell activation is

- modulated by the 3D mechanical microenvironment. *Biomaterials* **252**, 120058 (2020).
107. Azadi, S., Tafazzoli-Shadpour, M., Soleimani, M. & Warkiani, M. E. Modulating cancer cell mechanics and actin cytoskeleton structure by chemical and mechanical stimulations. *J. Biomed. Mater. Res. Part A* **107A**, 1569–1581 (2019).
 108. Tello-Lafoz, M., Sspan, K., Sanchez, E. E., Hu, J., Remsik, J., Romin, Y., Calò, A., Hoen, D., Bhanot, U., Morris, L., Boire, A., Hsu, K. C., Massagué, J., Huse, M. & Er, E. E. Cytotoxic lymphocytes target characteristic biophysical vulnerabilities in cancer. *Immunity* **54**, 1037–1054.e7 (2021).
 109. Nataraj, N. M., Dang, A. P., Kam, L. C. & Lee, J. H. Ex vivo induction of regulatory T cells from conventional CD4+ T cells is sensitive to substrate rigidity. *J. Biomed. Mater. Res. Part A* **106A**, 3001–3008 (2018).
 110. Romano, M., Fanelli, G., Albany, C. J., Giganti, G. & Lombardi, G. Past, present, and future of regulatory T cell therapy in transplantation and autoimmunity. *Front. Immunol.* **10**, 43 (2019).
 111. Kim, Y. & Kumar, S. CD44-mediated adhesion to hyaluronic acid contributes to mechanosensing and invasive motility. *Mol. Cancer Res.* **12**, 1416–1429 (2014).
 112. Panciera, T., Citron, A., Di Biagio, D., Battilana, G., Gandin, A., Giulitti, S., Forcato, M., Bicciato, S., Panzetta, V., Fusco, S., Azzolin, L., Totaro, A., Dei Tos, A. P., Fassan, M., Vindigni, V., Bassetto, F., Rosato, A., Brusatin, G., Cordenonsi, M. & Piccolo, S. Reprogramming normal cells into tumour precursors requires ECM stiffness and oncogene-mediated changes of cell mechanical properties. *Nat. Mater.* **19**, 797–806 (2020).
 113. Yamakita, Y., Matsumura, F., Lipscomb, M. W., Chou, P. C., Werlen, G., Burkhardt, J. K. & Yamashiro, S. Fascin1 Promotes Cell Migration of Mature Dendritic Cells. *J. Immunol.* **186**, 2850–2859 (2011).
 114. Fisher, P. J., Bulur, P. A., Vuk-Pavlovic, S., Prendergast, F. G. & Dietz, A. B. Dendritic cell microvilli: A novel membrane structure associated with the multifocal synapse and T-cell clustering. *Blood* **112**, 5037–5045 (2008).
 115. Sunshine, J. C., Perica, K., Schneck, J. P. & Green, J. J. Particle shape dependence of CD8+ T cell activation by artificial antigen presenting cells. *Biomaterials* **35**, 269–277 (2014).
 116. Meyer, R. A., Sunshine, J. C., Perica, K., Kosmides, A. K., Aje, K., Schneck, J. P. & Green, J. J. Biodegradable Nanoellipsoidal Artificial Antigen Presenting Cells for Antigen Specific T-Cell Activation. *Small* **11**, 1519–1525 (2015).
 117. Cochran, J. R., Cameron, T. O., Stone, J. D., Lubetsky, J. B. & Stern, L. J. Receptor Proximity, Not Intermolecular Orientation, Is Critical for Triggering T-cell Activation. *J. Biol. Chem.* **276**, 28068–28074 (2001).
 118. Delcassian, D., Depoil, D., Rudnicka, D., Liu, M., Davis, D. M., Dustin, M. L. & Dunlop, I. E. Nanoscale ligand spacing influences receptor triggering in T cells and NK cells. *Nano Lett.* **13**, 5608–5614 (2013).
 119. Cai, H., Muller, J., Depoil, D., Mayya, V., Sheetz, M. P., Dustin, M. L. & Wind, S. J. Full control of ligand positioning reveals spatial thresholds for T cell receptor triggering. *Nat. Nanotechnol.* **13**, 610–617 (2018).
 120. Matic, J., Deeg, J., Scheffold, A., Goldstein, I. & Spatz, J. P. Fine tuning and efficient T cell activation with stimulatory aCD3 nanoarrays. *Nano Lett.* **13**, 5090–5097 (2013).
 121. Guasch, J., Hoffmann, M., Diemer, J., Riahinezhad, H., Neubauer, S., Kessler, H. & Spatz, J. P. Combining Adhesive Nanostructured Surfaces and Costimulatory Signals to Increase T Cell Activation. *Nano Lett.* **18**, 5899–5904 (2018).
 122. Deeg, J., Axmann, M., Matic, J., Liapis, A., Depoil, D., Afrose, J., Curado, S., Dustin, M. L. & Spatz, J. P. T cell activation is determined by the number of presented antigens. *Nano Lett.* **13**, 5619–5626 (2013).
 123. Friedl, P., Den Boer, A. T. & Gunzer, M. Tuning immune responses: Diversity and adaptation of the immunological synapse. *Nat. Rev. Immunol.* **5**, 532–545 (2005).
 124. Mossman, K. D., Campi, G., Groves, J. T. & Dustin, M. L. Altered TCR signaling from geometrically repatterned

- immunological synapses. *Science* **310**, 1191–1193 (2005).
125. Čemerski, S., Das, J., Giurisato, E., Markiewicz, M. A., Allen, P. M., Chakraborty, A. K. & Shaw, A. S. The Balance between T Cell Receptor Signaling and Degradation at the Center of the Immunological Synapse Is Determined by Antigen Quality. *Immunity* **29**, 414–422 (2008).
 126. Doh, J. & Irvine, D. J. Immunological synapse arrays: Patterned protein surfaces that modulate immunological synapse structure formation in T cells. *Proc. Natl. Acad. Sci. U. S. A.* **103**, 5700–5705 (2006).
 127. Yokosuka, T., Kobayashi, W., Sakata-Sogawa, K., Takamatsu, M., Hashimoto-Tane, A., Dustin, M. L., Tokunaga, M. & Saito, T. Spatiotemporal Regulation of T Cell Costimulation by TCR-CD28 Microclusters and Protein Kinase C θ Translocation. *Immunity* **29**, 589–601 (2008).
 128. Shen, K., Thomas, V. K., Dustin, M. L. & Kam, L. C. Micropatterning of costimulatory ligands enhances CD4⁺ T cell function. *Proc. Natl. Acad. Sci. U. S. A.* **105**, 7791–7796 (2008).
 129. Bashour, K. T., Tsai, J., Shen, K., Lee, J. H., Sun, E., Milone, M. C., Dustin, M. L. & Kam, L. C. Cross Talk between CD3 and CD28 Is Spatially Modulated by Protein Lateral Mobility. *Mol. Cell. Biol.* **34**, 955–964 (2014).
 130. Lee, J. H., Dustin, M. L. & Kam, L. C. A microfluidic platform reveals differential response of regulatory T cells to micropatterned costimulation arrays. *Integr. Biol.* **7**, 1442–1453 (2015).
 131. Min, S., Jeon, Y. S., Jung, H. J., Khatua, C., Li, N., Bae, G., Choi, H., Hong, H., Shin, J. E., Ko, M. J., Ko, H. S., Jun, I., Fu, H. E., Kim, S. H., Thangam, R., Song, J. J., Dravid, V. P., Kim, Y. K. & Kang, H. Independent Tuning of Nano-Ligand Frequency and Sequences Regulates the Adhesion and Differentiation of Stem Cells. *Adv. Mater.* **32**, 2004300 (2020).
 132. Zhu, C., Chen, W., Lou, J., Rittase, W. & Li, K. Mechanosensing through immunoreceptors. *Nat. Immunol.* **20**, 1269–1278 (2019).
 133. Sage, P. T., Varghese, L. M., Martinelli, R., Sciuto, T. E., Kamei, M., Dvorak, A. M., Springer, T. A., Sharpe, A. H. & Carman, C. V. Antigen Recognition Is Facilitated by Invadosome-like Protrusions Formed by Memory/Effector T Cells. *J. Immunol.* **188**, 3686–3699 (2012).
 134. Rossy, J., Laufer, J. M. & Legler, D. F. Role of mechanotransduction and tension in T cell function. *Front. Immunol.* **9**, 2638 (2018).
 135. Stanley, P., Smith, A., McDowall, A., Nicol, A., Zicha, D. & Hogg, N. Intermediate-affinity LFA-1 binds α -actinin-1 to control migration at the leading edge of the T cell. *EMBO J.* **27**, 62–75 (2008).
 136. Leslie, N. R. & Downes, C. P. PTEN function: How normal cells control it and tumour cells lose it. *Biochem. J.* **382**, 1–11 (2004).
 137. Whitlock, B. M. Enhancing cytotoxic T cell killing by PTEN depletion. [XXXXXXXXXXXXXXXXXXXX](#) (Ph.D. Thesis, Cornell University, 2018).
 138. Hui, K. L. & Upadhyaya, A. Dynamic microtubules regulate cellular contractility during T-cell activation. *Proc. Natl. Acad. Sci. U. S. A.* **114**, E4175–E4183 (2017).
 139. Tabdanov, E. D., Rodríguez-Merced, N. J., Cartagena-Rivera, A. X., Puram, V. V., Callaway, M. K., Ensminger, E. A., Pomeroy, E. J., Yamamoto, K., Lahr, W. S., Webber, B. R., Moriarity, B. S., Zhovmer, A. S. & Provenzano, P. P. Engineering T cells to enhance 3D migration through structurally and mechanically complex tumor microenvironments. *Nat. Commun.* **12**, 2815 (2021).
 140. Tamzalit, F., Tran, D., Jin, W., Boyko, V., Bazzi, H., Kepecs, A., Kam, L. C., Anderson, K. V. & Huse, M. Centrioles control the capacity, but not the specificity, of cytotoxic T cell killing. *Proc. Natl. Acad. Sci. U. S. A.* **117**, 4310–4319 (2020).
 141. de la Zerda, A., Kratochvil, M. J., Suhar, N. A. & Heilshorn, S. C. Review: Bioengineering strategies to probe T cell

- mechanobiology. *APL Bioeng.* **2**, 021501 (2018).
142. Krieg, M., Fläschner, G., Alsteens, D., Gaub, B. M., Roos, W. H., Wuite, G. J. L., Gaub, H. E., Gerber, C., Dufrêne, Y. F. & Müller, D. J. Atomic force microscopy-based mechanobiology. *Nat. Rev. Phys.* **1**, 41–57 (2019).
 143. Perica, K., Tu, A., Richter, A., Bieler, J. G., Edidin, M. & Schneck, J. P. Magnetic Field-Induced T Cell Receptor Clustering by Nanoparticles Enhances T Cell Activation and Stimulates Antitumor Activity. *ACS Nano* **8**, 2252–2260 (2014).
 144. Liu, Z., Liu, Y., Chang, Y., Seyf, H. R., Henry, A., Mattheyses, A. L., Yehl, K., Zhang, Y., Huang, Z. & Salaita, K. Nanoscale optomechanical actuators for controlling mechanotransduction in living cells. *Nat. Methods* **13**, 143–146 (2016).
 145. Douplik, A., Saiko, G., Schelkanova, I. & Tuchin, V. V. *The response of tissue to laser light. Lasers for Medical Applications: Diagnostics, Therapy and Surgery* (Woodhead Publishing Limited, 2013).
 146. Carovac, A., Smajlovic, F. & Junuzovic, D. Application of Ultrasound in Medicine. *Acta Inform. Med.* **19**, 168–171 (2011).
 147. Pan, Y., Yoon, S., Sun, J., Huang, Z., Lee, C., Allen, M., Wu, Y., Chang, Y. J., Sadelain, M., Shung, K. K., Chien, S. & Wang, Y. Mechanogenetics for the remote and noninvasive control of cancer immunotherapy. *Proc. Natl. Acad. Sci. U. S. A.* **115**, 992–997 (2018).
 148. Park, J. H., Rivière, I., Gonen, M., Wang, X., Sénéchal, B., Curran, K. J., Sauter, C., Wang, Y., Santomasso, B., Mead, E., Roshal, M., Maslak, P., Davila, M., Brentjens, R. J. & Sadelain, M. Long-term follow-up of CD19 CAR therapy in acute lymphoblastic leukemia. *N. Engl. J. Med.* **378**, 449–459 (2018).
 149. Met, Ö., Jensen, K. M., Chamberlain, C. A., Donia, M. & Svane, I. M. Principles of adoptive T cell therapy in cancer. *Semin. Immunopathol.* **41**, 49–58 (2019).
 150. Levine, B. L., Miskin, J., Wonnacott, K. & Keir, C. Global Manufacturing of CAR T Cell Therapy. *Mol. Ther. - Methods Clin. Dev.* **4**, 92–101 (2017).
 151. Bufi, N., Saitakis, M., Dogniaux, S., Buschinger, O., Bohineust, A., Richert, A., Maurin, M., Hivroz, C. & Asnacios, A. Human primary immune cells exhibit distinct mechanical properties that are modified by inflammation. *Biophys. J.* **108**, 2181–2190 (2015).
 152. Lühr, J. J., Alex, N., Amon, L., Kräter, M., Kubánková, M., Sezgin, E., Lehmann, C. H. K., Heger, L., Heidkamp, G. F., Smith, A. S., Zaburdaev, V., Böckmann, R. A., Levental, I., Dustin, M. L., Eggeling, C., Guck, J. & Dudziak, D. Maturation of monocyte-derived DCs leads to increased cellular stiffness, higher membrane fluidity, and changed lipid composition. *Front. Immunol.* **11**, 590121 (2020).
 153. Comrie, W. A., Li, S., Boyle, S. & Burkhardt, J. K. The dendritic cell cytoskeleton promotes T cell adhesion and activation by constraining ICAM-1 mobility. *J. Cell Biol.* **208**, 457–473 (2015).
 154. Leithner, A., Altenburger, L. M., Hauschild, R., Assen, F. P., Rottner, K., Stradal, T. E. B., Diz-Muñoz, A., Stein, J. V. & Sixt, M. Dendritic cell actin dynamics control contact duration and priming efficiency at the immunological synapse. *J. Cell Biol.* **220**, e202006081 (2021).
 155. Bhingardive, V., Kossover, A., Iraqi, M., Khand, B., Le Saux, G., Porgador, A. & Schwartzman, M. Antibody-functionalized nanowires: A tuner for the activation of T cells. *Nano Lett.* **21**, 4241–4248 (2021).
 156. Skocaj, M., Filipic, M., Petkovic, J. & Novak, S. Titanium dioxide in our everyday life; Is it safe? *Radiol. Oncol.* **45**, 227–247 (2011).
 157. Park, K. S., Min, K. M., Jin, Y. H., Seo, S. D., Lee, G. H., Shim, H. W. & Kim, D. W. Enhancement of cyclability of urchin-like rutile TiO₂ submicron spheres by nanopainting with carbon. *J. Mater. Chem.* **22**, 15981–15986 (2012).

158. Liu, C. S. C., Raychaudhuri, D., Paul, B., Chakrabarty, Y., Ghosh, A. R., Rahaman, O., Talukdar, A. & Ganguly, D. Cutting Edge: Piezo1 Mechanosensors Optimize Human T Cell Activation. *J. Immunol.* **200**, 1255–1260 (2018).
159. Michalick, L. & Kuebler, W. M. TRPV4—A Missing Link Between Mechanosensation and Immunity. *Front. Immunol.* **11**, 413 (2020).
160. Zhang, X., Kim, T. H., Thauland, T. J., Li, H., Majedi, F. S., Ly, C., Gu, Z., Butte, M. J., Rowat, A. C. & Li, S. Unraveling the mechanobiology of immune cells. *Curr. Opin. Biotechnol.* **66**, 236–245 (2020).
161. Bahng, J. H., Yeom, B., Wang, Y., Tung, S. O., Hoff, J. D. & Kotov, N. Anomalous dispersions of ‘hedgehog’ particles. *Nature* **517**, 596–599 (2015).
162. Totaro, A., Panciera, T. & Piccolo, S. YAP/TAZ upstream signals and downstream responses. *Nat. Cell Biol.* **20**, 888–899 (2018).
163. Zhou, H., Kim, J. P., Bahng, J. H., Kotov, N. A. & Lee, J. Self-assembly mechanism of spiky magnetoplasmonic supraparticles. *Adv. Funct. Mater.* **24**, 1439–1448 (2014).
164. Chen, H. J., Hang, T., Yang, C., Liu, G., Lin, D. A., Wu, J., Pan, S., Yang, B. R., Tao, J. & Xie, X. Anomalous dispersion of magnetic spiky particles for enhanced oil emulsions/water separation. *Nanoscale* **10**, 1978–1986 (2018).
165. Bedford, E. E., Méthivier, C., Pradier, C. M., Gu, F. & Boujday, S. Nanostructured and spiky gold shell growth on magnetic particles for sensors applications. *Nanomaterials* **10**, 1–19 (2020).
166. Wang, H. & Mooney, D. J. Biomaterial-assisted targeted modulation of immune cells in cancer treatment. *Nat. Mater.* **17**, 761–772 (2018).
167. Eil, R., Vodnala, S. K., Clever, D., Klebanoff, C. A., Sukumar, M., Pan, J. H., Palmer, D. C., Gros, A., Yamamoto, T. N., Patel, S. J., Guittard, G. C., Yu, Z., Carbonaro, V., Okkenhaug, K., Schrumpp, D. S., Linehan, W. M., Roychoudhuri, R. & Restifo, N. P. Ionic immune suppression within the tumour microenvironment limits T cell effector function. *Nature* **537**, 539–543 (2016).
168. André, P., Denis, C., Soulas, C., Bourbon-Caillet, C., Lopez, J., Arnoux, T., Bléry, M., Bonnafous, C., Gauthier, L., Morel, A., Rossi, B., Remark, R., Bresó, V., Bonnet, E., Habif, G., Guia, S., Lalanne, A. I., Hoffmann, C., Lantz, O., Fayette, J., Boyer-Chammard, A., Zerbib, R., Dodion, P., Ghadially, H., Jure-Kunkel, M., Morel, Y., Herbst, R., Narni-Mancinelli, E., Cohen, R. B. & Vivier, E. Anti-NKG2A mAb is a checkpoint inhibitor that promotes anti-tumor immunity by unleashing both T and NK cells. *Cell* **175**, 1731–1743 (2018).
169. Cross, S. E., Jin, Y. S., Rao, J. & Gimzewski, J. K. Nanomechanical analysis of cells from cancer patients. *Nat. Nanotechnol.* **2**, 780–783 (2007).
170. Fritsch, A., Höckel, M., Kiessling, T., Nnetu, K. D., Wetzel, F., Zink, M. & Käs, J. A. Are biomechanical changes necessary for tumour progression? *Nat. Phys.* **6**, 730–732 (2010).
171. Swaminathan, V., Myhre, K., Tim O’Brien, E., Berchuck, A., Globe, G. C. & Superfine, R. Mechanical Stiffness grades metastatic potential in patient tumor cells and in cancer cell lines. *Cancer Res.* **71**, 5075–5080 (2011).
172. Alibert, C., Goud, B. & Manneville, J. B. Are cancer cells really softer than normal cells? *Biol. Cell* **109**, 167–189 (2017).
173. Händel, C., Schmidt, B. U. S., Schiller, J., Dietrich, U., Möhn, T., Kießling, T. R., Pawlizak, S., Fritsch, A. W., Horn, L. C., Briest, S., Höckel, M., Zink, M. & Käs, J. A. Cell membrane softening in human breast and cervical cancer cells. *New J. Phys.* **17**, 083008 (2015).
174. Köster, D. V. & Mayor, S. Cortical actin and the plasma membrane: Inextricably intertwined. *Curr. Opin. Cell Biol.* **38**, 81–89 (2016).
175. Byfield, F. J., Aranda-Espinoza, H., Romanenko, V. G., Rothblat, G. H. & Levitan, I. Cholesterol depletion increases membrane stiffness of aortic endothelial cells. *Biophys. J.* **87**, 3336–3343 (2004).

176. Khatibzadeh, N., Gupta, S., Farrell, B., Brownell, W. E. & Anvari, B. Effects of cholesterol on nano-mechanical properties of the living cell plasma membrane. *Soft Matter* **8**, 8350–8360 (2012).
177. Behnke, O., Trantum-Jensen, J. & Van Deurs, B. Filipin as a cholesterol probe. II. Filipin-cholesterol interaction in red blood cell membranes. *Eur. J. Cell Biol.* **35**, 200–215 (1984).
178. Jambhekar, S. S. & Breen, P. Cyclodextrins in pharmaceutical formulations I: Structure and physicochemical properties, formation of complexes, and types of complex. *Drug Discov. Today* **21**, 356–362 (2016).
179. Zidovetzki, R. & Levitan, I. Use of cyclodextrins to manipulate plasma membrane cholesterol content: Evidence, misconceptions and control strategies. *Biochim. Biophys. Acta - Biomembr.* **1768**, 1311–1324 (2007).
180. Vahabikashi, A., Park, C. Y., Perkumas, K., Zhang, Z., Deurloo, E. K., Wu, H., Weitz, D. A., Stamer, W. D., Goldman, R. D., Fredberg, J. J. & Johnson, M. Probe sensitivity to cortical versus intracellular cytoskeletal network stiffness. *Biophys. J.* **116**, 518–529 (2019).
181. Guo, M., Pegoraro, A. F., Mao, A., Zhou, E. H., Arany, P. R., Han, Y., Burnette, D. T., Jensen, M. H., Kasza, K. E., Moore, J. R., Mackintosh, F. C., Fredberg, J. J., Mooney, D. J., Lippincott-Schwartz, J. & Weitz, D. A. Cell volume change through water efflux impacts cell stiffness and stem cell fate. *Proc. Natl. Acad. Sci. U. S. A.* **114**, E8618–E8627 (2017).
182. Otto, O., Rosendahl, P., Mietke, A., Golfier, S., Herold, C., Klaue, D., Girardo, S., Pagliara, S., Ekpenyong, A., Jacobi, A., Wobus, M., Töpfner, N., Keyser, U. F., Mansfeld, J., Fischer-Friedrich, E. & Guck, J. Real-time deformability cytometry: On-the-fly cell mechanical phenotyping. *Nat. Methods* **12**, 199–202 (2015).
183. Lekka, M. Discrimination between normal and cancerous cells using AFM. *Bionanoscience* **6**, 65–80 (2016).
184. Butcher, D. T., Alliston, T. & Weaver, V. M. A tense situation: Forcing tumour progression. *Nat. Rev. Cancer* **9**, 108–122 (2009).
185. Zhu, M., Zhao, X., Chen, J., Xu, J., Hu, G., Guo, D., Li, Q., Zhang, X., Chang, C. C. Y., Song, B., Xiong, Y., Chang, T. & Li, B. ACAT1 regulates the dynamics of free cholesterol in plasma membrane which leads to the APP- α -processing alteration. *Acta Biochim. Biophys. Sin.* **47**, 951–959 (2015).
186. Yang, W., Bai, Y., Xiong, Y., Zhang, J., Chen, S., Zheng, X., Meng, X., Li, L., Wang, J., Xu, C., Yan, C., Wang, L., Chang, C. C. Y., Chang, T. Y., Zhang, T., Zhou, P., Song, B. L., Liu, W., Sun, S. C., Liu, X., Li, B. L. & Xu, C. Potentiating the antitumour response of CD8⁺ T cells by modulating cholesterol metabolism. *Nature* **531**, 651–655 (2016).
187. Bryan, D. S., Stack, M., Krysztofiak, K., Cichoń, U., Thomas, D. G., Surcel, A., Schiffhauer, E. S., Beckett, M. A., Khodarev, N. N., Xue, L., Poli, E. C., Pearson, A. T., Posner, M. C., Robinson, D. N., Rock, R. S. & Weichselbaum, R. R. 4-Hydroxyacetophenone modulates the actomyosin cytoskeleton to reduce metastasis. *Proc. Natl. Acad. Sci. U. S. A.* **117**, 22423–22429 (2020).
188. Barry, M. & Bleackley, R. C. Cytotoxic T lymphocytes: All roads lead to death. *Nat. Rev. Immunol.* **2**, 401–409 (2002).
189. Golstein, P. & Griffiths, G. M. An early history of T cell-mediated cytotoxicity. *Nat. Rev. Immunol.* **18**, 527–535 (2018).
190. Chow, C. W., Rincón, M. & Davis, R. J. Requirement for transcription factor NFAT in interleukin-2 expression. *Mol. Cell. Biol.* **19**, 2300–2307 (1999).
191. Oeckinghaus, A. & Ghosh, S. The NF- κ B family of transcription factors and its regulation. *Cold Spring Harb. Perspect. Biol.* **1**, a000034 (2009).
192. Style, R. W., Boltyanskiy, R., German, G. K., Hyland, C., Macminn, C. W., Mertz, A. F., Wilen, L. A., Xu, Y. & Dufresne, E. R. Traction force microscopy in physics and biology. *Soft Matter* **10**, 4047–4055 (2014).
193. Weder, G., Hendriks-Balk, M. C., Smajda, R., Rimoldi, D., Liley, M., Heinzelmann, H., Meister, A. & Mariotti, A.

- Increased plasticity of the stiffness of melanoma cells correlates with their acquisition of metastatic properties. *Nanomed.-Nanotechnol. Biol. Med.* **10**, 141–148 (2014).
194. Luo, Q., Kuang, D., Zhang, B. & Song, G. Cell stiffness determined by atomic force microscopy and its correlation with cell motility. *Biochim. Biophys. Acta - Gen. Subj.* **1860**, 1953–1960 (2016).
 195. Liu, Y., Zhang, T., Zhang, H., Li, J., Zhou, N., Fiskesund, R., Chen, J., Lv, J., Ma, J., Zhang, H., Tang, K., Cheng, F., Zhou, Y., Zhang, X., Wang, N. & Huang, B. Cell softness prevents cytolytic T-cell killing of tumor-repopulating cells. *Cancer Res.* **81**, 476–488 (2021).
 196. Blanchoin, L., Boujemaa-Paterski, R., Sykes, C. & Plastino, J. Actin dynamics, architecture, and mechanics in cell motility. *Physiol. Rev.* **94**, 235–263 (2014).
 197. Vaahtomeri, K., Brown, M., Hauschild, R., De Vries, I., Leithner, A. F., Mehling, M., Kaufmann, W. A. & Sixt, M. Locally triggered release of the chemokine CCL21 promotes dendritic cell transmigration across lymphatic endothelia. *Cell Rep.* **19**, 902–909 (2017).
 198. Stack, T., Vincent, M., Vahabikashi, A., Li, G., Perkumas, K. M., Stamer, W. D., Johnson, M. & Scott, E. Targeted delivery of cell softening micelles to Schlemm’s canal endothelial cells for treatment of glaucoma. *Small* **16**, 2004205 (2020).
 199. Zhuang, L., Lin, J., Lu, M. L., Solomon, K. R. & Freeman, M. R. Cholesterol-rich lipid rafts mediate Akt-regulated survival in prostate cancer cells. *Cancer Res.* **62**, 2227–2231 (2002).
 200. Mollinedo, F. & Gajate, C. Lipid rafts as signaling hubs in cancer cell survival/death and invasion: Implications in tumor progression and therapy. *J. Lipid Res.* **61**, 611–635 (2020).
 201. Vorselen, D., Wang, Y., de Jesus, M. M., Shah, P. K., Footer, M. J., Huse, M., Cai, W. & Theriot, J. A. Microparticle traction force microscopy reveals subcellular force exertion patterns in immune cell–target interactions. *Nat. Commun.* **11**, 20 (2020).
 202. Janmey, P. A. & McCulloch, C. A. Cell mechanics: Integrating cell responses to mechanical stimuli. *Annu. Rev. Biomed. Eng.* **9**, 1–34 (2007).
 203. Quezada, S. A., Simpson, T. R., Peggs, K. S., Merghoub, T., Vider, J., Fan, X., Blasberg, R., Yagita, H., Muranski, P., Antony, P. A., Restifo, N. P. & Allison, J. P. Tumor-reactive CD4⁺ T cells develop cytotoxic activity and eradicate large established melanoma after transfer into lymphopenic hosts. *J. Exp. Med.* **207**, 637–650 (2010).
 204. Cachot, A., Bilous, M., Liu, Y. C., Li, X., Saillard, M., Cenerenti, M., Rockinger, G. A., Wyss, T., Guillaume, P., Schmidt, J., Genolet, R., Ercolano, G., Protti, M. P., Reith, W., Ioannidou, K., de Leval, L., Trapani, J. A., Coukos, G., Harari, A., Speiser, D. E., Mathis, A., Gfeller, D., Altug, H., Romero, P. & Jandus, C. Tumor-specific cytolytic CD4 T cells mediate immunity against human cancer. *Sci. Adv.* **7**, eabe3348 (2021).
 205. Hanahan, D. & Weinberg, R. A. Hallmarks of cancer: The next generation. *Cell* **144**, 646–674 (2011).
 206. Huse, M. Mechanical forces in the immune system. *Nat. Rev. Immunol.* **17**, 679–690 (2017).
 207. Moffat, J., Grueneberg, D. A., Yang, X., Kim, S. Y., Kloepper, A. M., Hinkle, G., Piqani, B., Eisenhaure, T. M., Luo, B., Grenier, J. K., Carpenter, A. E., Foo, S. Y., Stewart, S. A., Stockwell, B. R., Hacohen, N., Hahn, W. C., Lander, E. S., Sabatini, D. M. & Root, D. E. A lentiviral RNAi library for human and mouse genes applied to an arrayed viral high-content screen. *Cell* **124**, 1283–1298 (2006).
 208. Rosen, K., Shi, W., Calabretta, B. & Filmus, J. Cell detachment triggers p38 mitogen-activated protein kinase-dependent overexpression of Fas ligand: A novel mechanism of anoikis of intestinal epithelial cells. *J. Biol. Chem.* **277**, 46123–46130 (2002).
 209. Hawley, T. S. & Hawley, R. G. *Flow Cytometry Protocols*. (Humana Press, New York, 2018).
 210. Tse, J. R. & Engler, A. J. Preparation of hydrogel substrates with tunable mechanical properties. *Curr. Protoc. Cell*

- Biol.* **47**, 1–16 (2010).
211. Tseng, Q., Duchemin-Pelletier, E., Deshiere, A., Balland, M., Guilloud, H., Filhol, O. & Théry, M. Spatial organization of the extracellular matrix regulates cell-cell junction positioning. *Proc. Natl. Acad. Sci. U. S. A.* **109**, 1506–1511 (2012).
 212. Fleige, E., Quadir, M. A. & Haag, R. Stimuli-responsive polymeric nanocarriers for the controlled transport of active compounds: Concepts and applications. *Adv. Drug Deliv. Rev.* **64**, 866–884 (2012).
 213. Lu, Y., Sun, W. & Gu, Z. Stimuli-responsive nanomaterials for therapeutic protein delivery. *J. Control. Release* **194**, 1–19 (2014).
 214. Meng, H., Xue, M., Xia, T., Zhao, Y. L., Tamanoi, F., Stoddart, J. F., Zink, J. I. & Nel, A. E. Autonomous in vitro anticancer drug release from mesoporous silica nanoparticles by pH-sensitive nanovalves. *J. Am. Chem. Soc.* **132**, 12690–12697 (2010).
 215. Su, J., Chen, F., Cryns, V. L. & Messersmith, P. B. Catechol polymers for pH-responsive, targeted drug delivery to cancer cells. *J. Am. Chem. Soc.* **133**, 11850–11853 (2011).
 216. Li, Z., Clemens, D. L., Lee, B. Y., Dillon, B. J., Horwitz, M. A. & Zink, J. I. Mesoporous silica nanoparticles with pH-sensitive nanovalves for delivery of moxifloxacin provide improved treatment of lethal pneumonic tularemia. *ACS Nano* **9**, 10778–10789 (2015).
 217. Wu, M., Meng, Q., Chen, Y., Zhang, L., Li, M., Cai, X., Li, Y., Yu, P., Zhang, L. & Shi, J. Large Pore-Sized Hollow Mesoporous Organosilica for Redox-Responsive Gene Delivery and Synergistic Cancer Chemotherapy. *Adv. Mater.* **28**, 1963–1969 (2016).
 218. Patel, K., Angelos, S., Dichtel, W. R., Coskun, A., Yang, Y. W., Zink, J. I. & Stoddart, J. F. Enzyme-responsive snap-top covered silica nanocontainers. *J. Am. Chem. Soc.* **130**, 2382–2383 (2008).
 219. Han, H., Valdepérez, D., Jin, Q., Yang, B., Li, Z., Wu, Y., Pelaz, B., Parak, W. J. & Ji, J. Dual enzymatic reaction-assisted gemcitabine delivery systems for programmed pancreatic cancer therapy. *ACS Nano* **11**, 1281–1291 (2017).
 220. Wang, B., Van Herck, S., Chen, Y., Bai, X., Zhong, Z., De Swarte, K., Lambrecht, B. N., Sanders, N. N., Lienenklaus, S., Scheeren, H. W., David, S. A., Kiessling, F., Lammers, T., De Geest, B. G. & Shi, Y. Prolonged innate immune activation by enzyme-sensitive imidazoquinoline TLR7/8 agonist prodrug vesicles. *J. Am. Chem. Soc.* **142**, 12133–12139 (2020).
 221. Scott, E. A., Stano, A., Gillard, M., Maio-Liu, A. C., Swartz, M. A. & Hubbell, J. A. Dendritic cell activation and T cell priming with adjuvant- and antigen-loaded oxidation-sensitive polymersomes. *Biomaterials* **33**, 6211–6219 (2012).
 222. Li, Y., Li, Y., Ji, W., Lu, Z., Liu, L., Shi, Y., Ma, G. & Zhang, X. Positively Charged Polyprodrug Amphiphiles with Enhanced Drug Loading and Reactive Oxygen Species-Responsive Release Ability for Traceable Synergistic Therapy. *J. Am. Chem. Soc.* **140**, 4164–4171 (2018).
 223. Chen, Q., Chen, G., Chen, J., Shen, J., Zhang, X., Wang, J., Chan, A. & Gu, Z. Bioresponsive Protein Complex of aPD1 and aCD47 Antibodies for Enhanced Immunotherapy. *Nano Lett.* **19**, 4879–4889 (2019).
 224. Barthes, J., Mertz, D., Bach, C., Metz-Boutigue, M. H., Senger, B., Voegel, J. C., Schaaf, P. & Lavalle, P. Stretch-induced biodegradation of polyelectrolyte multilayer films for drug release. *Langmuir* **28**, 13550–13554 (2012).
 225. Zhang, Y., Yu, J., Bomba, H. N., Zhu, Y. & Gu, Z. Mechanical force-triggered drug delivery. *Chem. Rev.* **116**, 12536–12563 (2016).
 226. Wang, J., Kaplan, J. A., Colson, Y. L. & Grinstaff, M. W. Mechanoresponsive materials for drug delivery: Harnessing forces for controlled release. *Adv. Drug Deliv. Rev.* **108**, 68–82 (2017).

227. Davies, P. F. Hemodynamic shear stress and the endothelium in cardiovascular pathophysiology. *Nat. Clin. Pract. Cardiovasc. Med.* **6**, 16–26 (2009).
228. Agha, R., Ogawa, R., Pietramaggiore, G. & Orgill, D. P. A review of the role of mechanical forces in cutaneous wound healing. *J. Surg. Res.* **171**, 700–708 (2011).
229. Holme, M. N., Fedotenko, I. A., Abegg, D., Althaus, J., Babel, L., Favarger, F., Reiter, R., Tanasescu, R., Zaffalon, P. L., Ziegler, A., Müller, B., Saxer, T. & Zumbuehl, A. Shear-stress sensitive lenticular vesicles for targeted drug delivery. *Nat. Nanotechnol.* **7**, 536–543 (2012).
230. Tomasek, J. J., Gabbiani, G., Hinz, B., Chaponnier, C. & Brown, R. A. Myofibroblasts and mechano: Regulation of connective tissue remodelling. *Nat. Rev. Mol. Cell Biol.* **3**, 349–363 (2002).
231. Coulie, P. G., Van Den Eynde, B. J., Van Der Bruggen, P. & Boon, T. Tumour antigens recognized by T lymphocytes: At the core of cancer immunotherapy. *Nat. Rev. Cancer* **14**, 135–146 (2014).
232. Durgeau, A., Virk, Y., Cognac, S. & Mami-Chouaib, F. Recent advances in targeting CD8 T-cell immunity for more effective cancer immunotherapy. *Front. Immunol.* **9**, 14 (2018).
233. Roca-Cusachs, P., Conte, V. & Treppe, X. Quantifying forces in cell biology. *Nat. Cell Biol.* **19**, 742–751 (2017).
234. Auletta, T., De Jong, M. R., Mulder, A., Van Veggel, F. C. J. M., Huskens, J., Reinhoudt, D. N., Zou, S., Zapotoczny, S., Schönherr, H., Vancso, G. J. & Kuipers, L. β -Cyclodextrin Host-Guest Complexes Probed under Thermodynamic Equilibrium: Thermodynamics and AFM Force Spectroscopy. *Journal of the American Chemical Society* vol. 126 1577–1584 (2004).
235. Wang, X. & Ha, T. Defining single molecular forces required to activate integrin and Notch signaling. *Science* **340**, 991–994 (2013).
236. Moreno-Villoslada, I., Jofré, M., Miranda, V., Chandía, P., González, R., Hess, S., Rivas, B. L., Elvira, C., San Román, J., Shibue, T. & Nishide, H. π -Stacking of rhodamine B onto water-soluble polymers containing aromatic groups. *Polymer (Guildf)*. **47**, 6496–6500 (2006).
237. Mandelkern, M., Elias, J. G., Eden, D. & Crothers, D. M. The dimensions of DNA in solution. *J. Mol. Biol.* **152**, 153–161 (1981).
238. Chowdhury, F., Li, I. T. S., Leslie, B. J., Doğanay, S., Singh, R., Wang, X., Seong, J., Lee, S. H., Park, S., Wang, N. & Ha, T. Single molecular force across single integrins dictates cell spreading. *Integr. Biol.* **7**, 1265–1271 (2015).
239. Pascual, L., Baroja, I., Aznar, E., Sancenón, F., Marcos, M. D., Murguía, J. R., Amorós, P., Rurack, K. & Martínez-Mañez, R. Oligonucleotide-capped mesoporous silica nanoparticles as DNA-responsive dye delivery systems for genomic DNA detection. *Chem. Commun.* **51**, 1414–1416 (2015).
240. Zhang, Y., Yuan, Q., Chen, T., Zhang, X., Chen, Y. & Tan, W. DNA-capped mesoporous silica nanoparticles as an ion-responsive release system to determine the presence of mercury in aqueous solutions. *Anal. Chem.* **84**, 1956–1962 (2012).
241. Piper, J. W., Swerlick, R. A. & Zhu, C. Determining force dependence of two-dimensional receptor-ligand binding affinity by centrifugation. *Biophys. J.* **74**, 492–513 (1998).
242. Ranallo, S., Prévost-Tremblay, C., Idili, A., Vallée-Bélisle, A. & Ricci, F. Antibody-powered nucleic acid release using a DNA-based nanomachine. *Nat. Commun.* **8**, 15150 (2017).
243. Stejskalová, A., Oliva, N., England, F. J. & Almquist, B. D. Biologically inspired, cell-selective release of aptamer-trapped growth factors by traction forces. *Adv. Mater.* **31**, 1806380 (2019).
244. Tu, J., Boyle, A. L., Friedrich, H., Bomans, P. H. H., Bussmann, J., Sommerdijk, N. A. J. M., Jiskoot, W. & Kros, A. Mesoporous Silica Nanoparticles with Large Pores for the Encapsulation and Release of Proteins. *ACS Appl. Mater. Interfaces* **8**, 32211–32219 (2016).

245. Nouredine, A., Maestas-olguin, A., Saada, E. A., Labauve, A. E., Agola, J. O., Baty, K. E., Howard, T., Sabo, J. K., Sandoval, C. R., Doudna, J. A., Schoeniger, J. S., Butler, K. S., Negrete, O. A., Brinker, C. J. & Serda, R. E. Engineering of monosized lipid-coated mesoporous silica nanoparticles for CRISPR delivery. *Acta Biomater.* **114**, 358–368 (2020).
246. Natkanski, E., Lee, W. Y., Mistry, B., Casal, A., Molloy, J. E. & Tolar, P. B cells use mechanical energy to discriminate antigen affinities. *Science* **340**, 1587–1590 (2013).
247. Wang, J., Chen, H., Hang, T., Yu, Y., Liu, G., He, G., Xiao, S., Yang, B., Yang, C., Liu, F., Tao, J., Wu, M. X. & Xie, X. Physical activation of innate immunity by spiky particles. *Nat. Nanotechnol.* **13**, 1078–1086 (2018).
248. Thevendran, R., Sarah, S., Tang, T. H. & Citartan, M. Strategies to bioengineer aptamer-driven nanovehicles as exceptional molecular tools for targeted therapeutics: A review. *J. Control. Release* **323**, 530–548 (2020).
249. Crompton, J. G., Sukumar, M. & Restifo, N. P. Uncoupling T-cell expansion from effector differentiation in cell-based immunotherapy. *Immunol. Rev.* **257**, 264–276 (2014).
250. Hinz, B. The extracellular matrix and transforming growth factor- β 1: Tale of a strained relationship. *Matrix Biol.* **47**, 54–65 (2015).
251. Zhao, B., Li, N., Xie, T., Bagheri, Y., Liang, C., Keshri, P., Sun, Y. & You, M. Quantifying tensile forces at cell-cell junctions with a DNA-based fluorescent probe. *Chem. Sci.* **11**, 8558–8566 (2020).
252. Tseng, P., Judy, J. W. & Di Carlo, D. Magnetic nanoparticle-mediated massively parallel mechanical modulation of single-cell behavior. *Nat. Methods* **9**, 1113–1119 (2012).
253. Kamble, H., Barton, M. J., Jun, M., Park, S. & Nguyen, N. T. Cell stretching devices as research tools: Engineering and biological considerations. *Lab Chip* **16**, 3193–3203 (2016).
254. Solis, A. G., Bielecki, P., Steach, H. R., Sharma, L., Harman, C. C. D., Yun, S., de Zoete, M. R., Warnock, J. N., To, S. D. F., York, A. G., Mack, M., Schwartz, M. A., Dela Cruz, C. S., Palm, N. W., Jackson, R. & Flavell, R. A. Mechanosensation of cyclical force by PIEZO1 is essential for innate immunity. *Nature* **573**, 69–74 (2019).
255. Northcott, J. M., Dean, I. S., Mouw, J. K. & Weaver, V. M. Feeling stress: The mechanics of cancer progression and aggression. *Front. Cell Dev. Biol.* **6**, 17 (2018).
256. Chaudhuri, P. K., Low, B. C. & Lim, C. T. Mechanobiology of tumor growth. *Chem. Rev.* **118**, 6499–6515 (2018).
257. van der Woude, L. L., Gorris, M. A. J., Halilovic, A., Figdor, C. G. & de Vries, I. J. M. Migrating into the Tumor: A Roadmap for T Cells. *Trends in Cancer* **3**, 797–808 (2017).
258. Kim, S. H. J. & Hammer, D. A. Integrin cross-talk modulates stiffness-independent motility of CD4⁺ T lymphocytes. *Mol. Biol. Cell* **32**, 1749–1757 (2021).
259. Kwon, K. W., Park, H., Song, K. H., Choi, J.-C., Ahn, H., Park, M. J., Suh, K.-Y. & Doh, J. Nanotopography-Guided Migration of T Cells. *J. Immunol.* **189**, 2266–2273 (2012).
260. Kwon, K. W., Park, H. & Doh, J. Migration of T cells on surfaces containing complex nanotopography. *PLoS One* **8**, e73960 (2013).
261. Song, K. H., Park, S. J., Kim, D. S. & Doh, J. Sinusoidal wavy surfaces for curvature-guided migration of T lymphocytes. *Biomaterials* **51**, 151–160 (2015).
262. Wolf, K., Müller, R., Borgmann, S., Bröcker, E. B. & Friedl, P. Amoeboid shape change and contact guidance: T-lymphocyte crawling through fibrillar collagen is independent of matrix remodeling by MMPs and other proteases. *Blood* **102**, 3262–3269 (2003).
263. Gaylo, A., Schrock, D. C., Fernandes, N. R. J. & Fowell, D. J. T cell interstitial migration: Motility cues from the inflamed tissue for micro- and macro-positioning. *Front. Immunol.* **7**, 428 (2016).

264. Ueda, H., Zhou, J., Xie, J. & Davis, M. M. Distinct Roles of Cytoskeletal Components in Immunological Synapse Formation and Directed Secretion. *J. Immunol.* **195**, 4117–4125 (2015).
265. Henke, E., Nandigama, R. & Ergün, S. Extracellular Matrix in the Tumor Microenvironment and Its Impact on Cancer Therapy. *Front. Mol. Biosci.* **6**, 160 (2020).
266. Goley, E. D. & Welch, M. D. The ARP2/3 complex: An actin nucleator comes of age. *Nat. Rev. Mol. Cell Biol.* **7**, 713–726 (2006).
267. Zhao, Y., Lee, C. K., Lin, C. H., Gassen, R. B., Xu, X., Huang, Z., Xiao, C., Bonorino, C., Lu, L. F., Bui, J. D. & Hui, E. PD-L1:CD80 Cis-Heterodimer Triggers the Co-stimulatory Receptor CD28 While Repressing the Inhibitory PD-1 and CTLA-4 Pathways. *Immunity* **51**, 1059-1073.e9 (2019).
268. Ma, R., Kellner, A. V., Ma, V. P. Y., Su, H., Deal, B. R., Brockman, J. M. & Salaita, K. DNA probes that store mechanical information reveal transient piconewton forces applied by T cells. *Proc. Natl. Acad. Sci. U. S. A.* **116**, 16949–16954 (2019).
269. van 't Wout, A. B., Swain, J. V., Schindler, M., Rao, U., Pathmajeyan, M. S., Mullins, J. I. & Kirchhoff, F. Nef induces multiple genes involved in cholesterol synthesis and uptake in Human Immunodeficiency Virus Type 1-infected T Ccils. *J. Virol.* **79**, 10053–10058 (2005).
270. Ehrlich, A., Uhl, S., Ioannidis, K., Hofree, M., TenOever, B. R. & Nahmias, Y. The SARS-CoV-2 transcriptional metabolic signature in lung epithelium. *SSRN* (2020) doi:10.2139/ssrn.3650499.
271. Binnewies, M., Roberts, E. W., Kersten, K., Chan, V., Fearon, D. F., Merad, M., Coussens, L. M., Gabrilovich, D. I., Ostrand-Rosenberg, S., Hedrick, C. C., Vonderheide, R. H., Pittet, M. J., Jain, R. K., Zou, W., Howcroft, T. K., Woodhouse, E. C., Weinberg, R. A. & Krummel, M. F. Understanding the tumor immune microenvironment (TIME) for effective therapy. *Nat. Med.* **24**, 541–550 (2018).
272. Anderson, N. R., Minutolo, N. G., Gill, S. & Klichinsky, M. Macrophage-based approaches for cancer immunotherapy. *Cancer Res.* **81**, 1201–1208 (2021).
273. Myers, J. A. & Miller, J. S. Exploring the NK cell platform for cancer immunotherapy. *Nat. Rev. Clin. Oncol.* **18**, 85–100 (2021).
274. Jain, N., Moeller, J. & Vogel, V. Mechanobiology of Macrophages: How Physical Factors Coregulate Macrophage Plasticity and Phagocytosis. *Annu. Rev. Biomed. Eng.* **21**, 267–297 (2019).
275. Yuen, G. J., Demissie, E. & Pillai, S. B lymphocytes and cancer: A love–hate relationship. *Trends in Cancer* **2**, 747–757 (2016).
276. Tullia Bruno, C. B cells to the forefront of immunotherapy. *Nature* **577**, 474–476 (2020).
277. Wan, Z., Chen, X., Chen, H., Ji, Q., Chen, Y., Wang, J., Cao, Y., Wang, F., Lou, J., Tang, Z. & Liu, W. The activation of IgM- or isotype-switched IgG- and IgE-BCR exhibits distinct mechanical force sensitivity and threshold. *Elife* **4**, e06925 (2015).
278. Tolar, P. Cytoskeletal control of B cell responses to antigens. *Nat. Rev. Immunol.* **17**, 621–634 (2017).
279. Spillane, K. M. & Tolar, P. B Cell Antigen Extraction is Regulated by Physical Properties of Antigen Presenting Cells. *J. Cell Biol.* **216**, 217–230 (2017).
280. Zeng, Y., Yi, J., Wan, Z., Liu, K., Song, P., Chau, A., Wang, F., Chang, Z., Han, W., Zheng, W., Chen, Y. H., Xiong, C. & Liu, W. Substrate stiffness regulates B-cell activation, proliferation, class switch, and T-cell-independent antibody responses in vivo. *Eur. J. Immunol.* **45**, 1621–1634 (2015).
281. Zhang, Q. wen, Liu, L., Gong, C. yang, Shi, H. shan, Zeng, Y. hui, Wang, X. ze, Zhao, Y. wei & Wei, Y. quan. Prognostic significance of tumor-associated macrophages in solid tumor: A meta-analysis of the literature. *PLoS One* **7**, e50946 (2012).

-
282. DeNardo, D. G. & Ruffell, B. Macrophages as regulators of tumour immunity and immunotherapy. *Nat. Rev. Immunol.* **19**, 369–382 (2019).
283. Patel, N. R., Bole, M., Chen, C., Hardin, C. C., Kho, A. T., Mih, J., Deng, L., Butler, J., Tschumperlin, D., Fredberg, J. J., Krishnan, R. & Koziel, H. Cell Elasticity Determines Macrophage Function. *PLoS One* **7**, e41024 (2012).
284. Okamoto, T., Takagi, Y., Kawamoto, E., Park, E. J., Usuda, H., Wada, K. & Shimaoka, M. Reduced substrate stiffness promotes M2-like macrophage activation and enhances peroxisome proliferator-activated receptor γ expression. *Exp. Cell Res.* **367**, 264–273 (2018).
285. Zhuang, Z., Zhang, Y., Sun, S., Li, Q., Chen, K., An, C., Wang, L., van den Beucken, J. J. J. P. & Wang, H. Control of Matrix Stiffness Using Methacrylate-Gelatin Hydrogels for a Macrophage-Mediated Inflammatory Response. *ACS Biomater. Sci. Eng.* **6**, 3091–3102 (2020).
286. Scott, R. A., Kiick, K. L. & Akins, R. E. Substrate stiffness directs the phenotype and polarization state of cord blood derived macrophages. *Acta Biomater.* **122**, 220–235 (2021).
287. Seneviratne, A. N., Cole, J. E., Goddard, M. E., Park, I., Mohri, Z., Sansom, S., Udalova, I., Krams, R. & Monaco, C. Low shear stress induces M1 macrophage polarization in murine thin-cap atherosclerotic plaques. *J. Mol. Cell. Cardiol.* **89**, 168–172 (2015).
288. Chu, S. Y., Chou, C. H., Huang, H. Da, Yen, M. H., Hong, H. C., Chao, P. H., Wang, Y. H., Chen, P. Y., Nian, S. X., Chen, Y. R., Liou, L. Y., Liu, Y. C., Chen, H. M., Lin, F. M., Chang, Y. T., Chen, C. C. & Lee, O. K. Mechanical stretch induces hair regeneration through the alternative activation of macrophages. *Nat. Commun.* **10**, 1524 (2019).
289. Shan, S., Fang, B., Zhang, Y., Wang, C., Zhou, J., Niu, C., Gao, Y., Zhao, D., He, J., Wang, J., Zhang, X. & Li, Q. Mechanical stretch promotes tumoricidal M1 polarization via the FAK/NF- κ B signaling pathway. *FASEB J.* **33**, 13254–13266 (2019).
290. Dong, L., Song, Y., Zhang, Y., Zhao, W., Wang, C., Lin, H., Al-ani, M. K., Liu, W., Xue, R. & Yang, L. Mechanical stretch induces osteogenesis through the alternative activation of macrophages. *J. Cell. Physiol.* **236**, 6376–6390 (2021).
291. Meli, V. S., Veerasubramanian, P. K., Atcha, H., Reitz, Z., Downing, T. L. & Liu, W. F. Biophysical regulation of macrophages in health and disease. *J. Leukoc. Biol.* **106**, 283–299 (2019).
292. Adams, S., Wuescher, L. M., Worth, R. & Yildirim-Ayan, E. Mechano-immunomodulation: Mechanoresponsive changes in macrophage activity and polarization. *Ann. Biomed. Eng.* **47**, 2213–2231 (2019).

Curriculum Vitae

CONTACT INFORMATION

Work address/telephone : ME D1 2926, Station 9, 1015 Lausanne, Switzerland/+41216934398
Email/cell phone : kewen.lei@epfl.ch/+41786379078

PERSONAL INFORMATION

Family Name, First name : Lei, Kewen
Date/place of birth : Jul. 4, 1991/China
Google Scholar ID : Kewen Lei (EPFL)
Linkedin profile : <https://www.linkedin.com/in/kewen-lei-398b0b90/>

EDUCATION

2017 – Now	Ph.D.	Materials Science and Engineering École polytechnique fédérale de Lausanne (EPFL) , Lausanne, Switzerland Advisor: Prof. Li Tang
2014 – 2017	M.Sc.	Macromolecular Chemistry and Physics Fudan University , Shanghai, China Advisors: Prof. Lin Yu and Prof. Jiandong Ding
2010 – 2014	B.Sc.	Macromolecular Science and Engineering Fudan University , Shanghai, China

AWARDS

2017	Award for Outstanding Graduate Student, Fudan University, China
2017	Award for Outstanding Student of Master Degree, Fudan University, China
2015	LORD Scholarship, Fudan University, China
2014	Award for Outstanding Student of Bachelor Degree, Fudan University, China

PUBLICATIONS

1. **K. Lei**, A. Kurum, M. Kaynak, M. Gao, Y.Q. Xie, Y. Guo, M. T.M. Hannebelle, Y. Wu, G. Zhou, G. E. Fantner, M. S. Sakar, L. Tang. Cancer-cell stiffening via cholesterol depletion enhances adoptive T-cell immunotherapy, **Nat. Biomed. Eng.**, **2021**, 5, 1411-1425. *Highlighted: Editorial of Nature Biomedical Engineering Issue 13 December; EPFL News; Radio Television Suisse; MedicalXpress.*
2. **K. Lei**, L. Tang. T cell force-responsive delivery of anticancer drugs using mesoporous silica microparticles, **Mater. Horiz.**, **2020**, 7, 3196–3200. *Cover story of Materials Horizons Issue 12 December. Highlighted: EPFL News; Materials Horizons Emerging Investigator Series.*
3. **K. Lei**, A. Kurum, L. Tang. Mechanical immunoengineering of T cells for therapeutic applications. **Acc. Chem. Res.**, **2020**, 53, 2777–2790.

4. M. Gao, Y.Q. Xie, **K. Lei**, Y. Zhao, A. Kurum, S. V. Herck, Y. Guo, X. Hu, L. Tang. A manganese phosphate nanocluster activates the cGAS-STING pathway for enhanced cancer immunotherapy, *Adv. Ther.*, **2021**, 4, 2100065.
5. H. Yang[#], **K. Lei**[#], F. Zhou, X. Yang, Q. An, W. Zhu, L. Yu, J. Ding. Injectable PEG/polyester thermogel: A new liquid embolization agent for temporary vascular interventional therapy, *Mater. Sci. Eng. C*, **2019**, 102, 606-615. ([#]Co-first authors)
6. **K. Lei**, L. Tang. Surgery-free injectable macroscale biomaterials for local cancer immunotherapy, *Biomater. Sci.*, **2019**, 7, 733-749.
7. Y. Guo, **K. Lei**, L. Tang. Neoantigen vaccine delivery for personalized anticancer immunotherapy, *Front. Immunol.*, **2018**, 9, 1499.
8. **K. Lei**, Y. Chen, J. Wang, X. Peng, L. Yu, J. Ding. Non-invasive monitoring of *in vivo* degradation of a radio-paque thermoreversible hydrogel and its efficacy in preventing postoperative adhesion, *Acta Biomater.*, **2017**, 55, 396-409.
9. Q. Ma, **K. Lei**, J. Ding, L. Yu, J. Ding. Design, synthesis and ring-opening polymerization of a new iodinated carbonate monomer: a universal route towards ultrahigh radiopaque aliphatic polycarbonates, *Polym. Chem.*, **2017**, 8, 6665-6674.
10. **K. Lei**, Q. Ma, L. Yu, J. Ding. Functional biomedical hydrogels for *in vivo* imaging, *J. Mater. Chem. B*, **2016**, 4, 7793-7812.
11. Y. Chen, J. Luan, W. Shen, **K. Lei**, L. Yu, J. Ding. Injectable and thermosensitive hydrogel containing liraglutide as a long-acting antidiabetic system, *ACS Appl. Mater. Interfaces*, **2016**, 8, 30703-30713.
12. **K. Lei**, W. Shen, L. Cao, L. Yu, J. Ding. An injectable thermogel with high radiopacity, *Chem. Commun.*, **2015**, 51, 6080-6083. [Cover story of Chemical Communications Issue 28 April.](#)
13. J. Luan, W. Shen, C. Chen, **K. Lei**, L. Yu, J. Ding. Selenium-containing thermogel for controlled drug delivery by coordination competition, *RSC Adv.*, **2015**, 5, 97975-97981.

PATENTS

- 2015 L. Yu, **K. Lei**, J. Ding. "An X-ray opaque thermogel and the preparation approaches thereof", CN 201510053193.1.

PRESENTATIONS

1. **Oral Presentation**, 10th Faculty & Staff Annual Retreat Swiss Cancer Center Leman, Nov. 22-23, 2021, Lausanne, Switzerland.
2. **Poster Presentation**, ISREC-SCCL Symposium 2021: Hallmarks of Cancer - 21 Years On, Aug. 28-31, 2021, Lausanne, Switzerland.
3. **Oral Presentation (eTalk)**, 2021 Europe's Cancer Immunotherapy Meeting (18th CIMT Annual Meeting), Oct. 10-12, 2021, Mainz, Germany.
4. **Oral Presentation**, 2019 EDMX Materials Science and Engineering Research Day, Nov. 29, 2019, Lausanne, Switzerland.
5. **Poster Presentation**, 2019 Biomedical Engineering Society Annual Meeting, Oct. 16-19, 2019, Philadelphia, US.

6. **Poster Presentation**, 1st International Conference of Molecular Engineering of Polymers, Oct. 13-16, 2016, Shanghai, China.
7. **Oral Presentation**, Chinese Biomaterials Congress & China-US Joint Forum on Innovation and Regulation of Biomaterials, Nov. 19-22, 2015, Haikou, China.

PROFESSIONAL MEMBERSHIPS

- 2021 – Now **Member**, The Association for Cancer Immunotherapy (CIMT)
- 2017 – Now **Member**, European Academy of Tumour Immunology (EATI)

SUPERVISION OF STUDENTS

Master Students

- 2020 – 2021 Thibault De La Taille (EPFL-Life Sciences Engineering), Semester project
- 2019 – 2020 Sara De Grandis (Technical University of Denmark-Biomedical Engineering), Exchange semester project
- 2019 – 2020 Stéphane Costa Borges (EPFL-Chemical Engineering & Biotechnology), Master thesis
- 2018 – 2019 Giulia Crivello (EPFL-Life Sciences Engineering), Semester project

Bachelor Students

- 2019 – 2020 Michael Halim (The University of British Columbia-Chemical & Biological Engineering), Exchange semester project
- 2018 – 2019 Jingfei Ren (Nanyang Technological University-Materials Science & Engineering), Exchange semester project